INSTITUTE OF EARTH AND ENVIRONMENTAL SCIENCE

Camera Monitoring at volcanoes: Identification and characterization of lava fountain activity and near-vent processes and their relevance for early warning systems

Tanja Ivonne Witt
13. November 2018

Cumulative dissertation
to obtain the academic degree
"doctor rerum naturalium" (Dr. rer. nat.)
in the scientific discipline Geophysics

Submitted to the
Faculty of Mathematics and Natural Sciences
at the University of Potsdam, Germany

Hauptbetreuer: Priv. Doz. Dr. Thomas R. Walter
Zweitbetreuer: Prof. Dr. Bernd Zimanowski

Gutachter: Prof. Dr. Magnus Tumi Gudmundsson
Dr. Helge Gonnermann

Prüfungskommision: Prof. Dr. Thorsten Dahm
Priv. Doz. Dr. Thomas R. Walter
Prof. Dr. Magnus Tumi Gudmundsson
Prof. Dr. Max Wilke

URN urn:nbn:de:kobv:517-opus4-421073
http://nbn-resolving.de/urn:nbn:de:kobv:517-opus4-421073

Erklärung

Hiermit erkläre ich, dass ich die vorliegende Arbeit selbstständig verfasst und keine weiteren außer den angegebenen Quellen und Hilfsmittel verwendet habe.

Diese Erklärung bezieht sich explizit auch auf die in der Arbeit enthaltenen Graphiken, Zeichnungen, Kartenskizzen und bildliche Darstellungen.

Author's declaration

I hereby confirm that I have written the accompanying thesis by myself, without contributions from any sources other than those cited in the text, the references, and the acknowledgements.

This applies explicitly to all graphics, drawings, maps and images included in the thesis.

Tanja Witt

Friday 7th December, 2018

Abstract

Basaltic fissure eruptions, such as on Hawai'i or on Iceland, are thought to be driven by the lateral propagation of feeder dikes and graben subsidence. Associated solid earth processes, such as deformation and structural development, are well studied by means of geophysical and geodetic technologies. The eruptions themselves, lava fountaining and venting dynamics, in turn, have been much less investigated due to hazardous access, local dimension, fast processes, and resulting poor data availability.

This thesis provides a detailed quantitative understanding of the shape and dynamics of lava fountains and the morphological changes at their respective eruption sites. For this purpose, I apply image processing techniques, including drones and fixed installed cameras, to the sequence of frames of video records from two well-known fissure eruptions in Hawai'i and Iceland. This way I extract the dimensions of multiple lava fountains, visible in all frames. By putting these results together and considering the acquisition times of the frames I quantify the variations in height, width and eruption velocity of the lava fountains. Then I analyse these time-series in both time and frequency domains and investigate the similarities and correlations between adjacent lava fountains. Following this procedure, I am able to link the dynamics of the individual lava fountains to physical parameters of the magma transport in the feeder dyke of the fountains.

The first case study in this thesis focuses on the March 2011 Pu'u'Ō'ō eruption, Hawai'i, where a continuous pulsating behaviour at all eight lava fountains has been observed. The lava fountains, even those from different parts of the fissure that are closely connected, show a similar frequency content and eruption behaviour. The regular pattern in the heights of lava fountain suggests a controlling process within the magma feeder system like a hydraulic connection in the underlying dyke, affecting or even controlling the pulsating behaviour.

The second case study addresses the 2014–2015 Holuhraun fissure eruption, Iceland. In this case, the feeder dyke is highlighted by the surface expressions of graben-like structures and fault systems. At the eruption site, the activity decreases from a continuous line of fire of ~60 vents to a limited number of lava fountains. This can be explained by preferred upwards magma movements through vertical structures of the pre-eruptive morphology. Seismic tremors during the eruption reveal vent opening at the surface and/or pressure changes in the feeder dyke. The evolving topography of the cinder cones during the eruption interacts with the lava fountain behaviour. Local variations in the lava fountain height and width are controlled by the conduit diameter, the depth of the lava pond and the shape of the crater. Modelling of the fountain heights shows that long-term eruption behaviour is controlled mainly by pressure changes in the feeder dyke.

This research consists of six chapters with four papers, including two first author and two co-author papers. It establishes a new method to analyse lava fountain dynamics by video monitoring. The comparison with the seismicity, geomorphologic and structural expressions of fissure eruptions shows a complex relationship between focussed flow through dykes, the morphology of the cinder cones, and the lava fountain dynamics at the vents of a fissure eruption.

Zusammenfassung

Basaltische Spalteneruptionen, wie auf Hawai’i oder Island, werden vermutlich durch die laterale Ausbreitung von Förderdikes und damit verbundener Grabenbildung verursacht. Prozesse der festen Erde sind mittels geophysikalischer und geodätischer Technologien gut erforscht. Die Ausbrüche selbst, d.h. die Lavafontänen und die Ventdynamik wiederum wurden aufgrund des gefährlichen Zugangs, der lokalen Dimension, der schnellen Prozesse und der daraus resultierenden schlechten Datenverfügbarkeit kaum untersucht.

Diese Arbeit liefert ein detailliertes quantitatives Verständnis über Form und Dynamik von Lavafontänen und der morphologischen Veränderungen an ihren jeweiligen Eruptionsstellen. Mittels Bildverarbeitungstechniken, einschließlich Dronen und festen Kameras, wurden von mir die Videoframes von zwei bekannten Spaltausbrüchen auf Hawaii und Island ausgewertet. Auf diese Weise extrahiere ich die Dimensionen mehrerer Lavafontänen, die in allen Frames sichtbar sind. Durch die Zusammenstellung dieser Ergebnisse und unter Berücksichtigung der Erfassungszeiten quantifiziere ich die Schwankungen in Höhe, Breite und Eruptionsgeschwindigkeit. Dann analysiere ich diese Zeitreihen im Zeit- und Frequenzbereich und untersuche die Ähnlichkeiten und Zusammenhänge zwischen benachbarten Lavafontänen. Anschließend verknüpfte ich die Dynamik der einzelnen Lavafontänen mit den physikalischen Parametern des Magmatransports im Förderdike.

Die erste Fallstudie dieser Arbeit konzentriert sich auf die Pu’u’Ō’ō Ausbruch, Hawaii im März 2011, bei der ein kontinuierliches pulsierendes Verhalten an allen Lavafontänen beobachtet werden konnte. Lavafontänen verschiedener Teilsegmenten der Spalte sind eng miteinander verbunden, sie weisen Ähnlichkeiten im Frequenzgehalt und Ausbruchsverhalten auf. Das regelmäßige Muster in den Lavafontänenhöhen deutet auf eine hydraulische Verbindung im darunter liegenden Dike als steuernden Prozess innerhalb des Magma-Fördersystems hin.

Die zweite Fallstudie befasst sich mit dem Holuhraun-Ausbruch 2014/2015. In diesem Fall wird der horizontale Förderdike durch grabenartige Strukturen und Bruchsysteme an der Oberfläche hervorgehoben. An der Ausbruchsstelle nimmt die Aktivität von einer kontinuierlichen Feuerlinie auf einzelne Lavafontänen ab. Dies lässt sich durch eine bevorzugte Aufwärtsbewegung des Magmas durch vertikale Strukturen der prä-eruptiven Morphologie erklären. Seismische Erschütterungen während des Ausbruchs zeigen Ventöffnungen an der Oberfläche und/oder Druckveränderungen im Förderdike. Die sich während des Ausbruchs entwickelnde Topographie der Schlackenkegel interagiert mit dem Verhalten der Lavafontänen. Lokale Schwankungen in Höhe und Breite der Lavafontäne werden jedoch durch den Schlotdurchmesser, die Tiefe des Lavaponds und die Form des Kraters gesteuert. Die Modellierung der Fontänenhöhe zeigt, dass das langfristige Ausbruchsverhalten vor allem durch Druckänderungen im Förderdike gesteuert wird.

Diese Forschungsarbeit besteht aus sechs Kapiteln mit je zwei Papern als Erst- bzw. Co-Autor. Es etabliert eine neue Methode zur Analyse der Dynamik von Lavafontänen durch Videoüberwachung. Der Vergleich mit der Seismizität, den geomorphologischen und strukturellen Ausprägungen von Spalteneruptionen zeigt einen komplexen Zusammenhang zwischen der Dikeströmung, der Vulkanmorphologie und der Dynamik der Lavafontänen an einer Spalteneruption.

Contents

Chapter 1

Introduction

1.1 Motivation

Volcanic eruptions affect population, traffic and economy across borders, as demonstrated in 2010 when the Eyjafjallajökull eruption caused economical losses of about 1.7 billion Euros due to the interruption of the air traffic (Budd et al., 2011). Nearly 11 % of the world's population lives within 100 km of a volcano, and around 3 % lives closer than 30 km to one of them (Brown et al., 2015). The objective of volcano monitoring is to forecast and assess volcanic hazards, as well as to acquire data for research to increase the knowledge of the underlying physics and mechanisms. One of the difficulties in observation, is the vast number of active volcanoes, as around 50 - 60 out of over 1 500 volcanoes erupt every year, leading to fatalities and damages (Brown et al., 2015). Although volcanoes in developed countries are well monitored with the help of expensive geophysical instrumentation, many of the recent eruption hazards occurred at poorly monitored volcanoes. This is due to the high number of volcanoes which makes it impossible to monitor all, e.g., in the U.S. five observatories monitor about one third of the volcanoes in this area. Therefore, even very fundamental qualities about the height and scale of important eruptions that occurred during the last years is missing.

The scale of the eruptions is important, as it is associated to the scale of hazards. At the flanks of volcanoes, lava flows, lahars or pyroclastic density currents (PDCs) are recognised; while at the vent region, dome collapses, rock falls and ballistics are possible. In the cloud, volcanic gases, ash and tephra can be transported over large distances. Secondary hazards are landslides, tsunamis and floods. Beside the scale of the eruption, the type of volcanoes have an influence on the potential risks of an eruption.

Based on the their main rock type the volcanoes can be clustered. Over 50 % of all known volcanoes are basaltic ones or include basaltic products. They are associated with a magmatic reservoir that feed the eruption by dykes and conduits; and occur in all shape and volcano types (Walker, 1993) from mid-ocean ridge volcanoes (Sinton and Detrick, 1992), shield-/stratovolcanoes (Cronin, 2013; Hildreth et al., 1984; Michon et al., 2007) to fissure eruptions. In this thesis, the focus is on basaltic fissure eruptions.

Fissure eruptions have been observed at different volcanic settings (see Figure 1.1). They are predominant on ocean islands, such as Kilauea and Mauna Loa (Lundgren et al., 2013; Poland et al., 2008), and at divergent plate margins or rift zones, such as Iceland (e.g., Krafla, Hekla, Askja - Acocella et al., 2000; Rubin and Pollard, 1988) and the East African Rift (e.g., Dabbahu by Field et al., 2012). Fissure eruption can also occur at convergent margins and in intraplate settings. They can be connected to a volcano, as seen in Iceland (e.g., Reykjanesskagi Einarsson and Douglas, 1994, or Bárðarbunga) and Hawai'i (e.g., Kilauea). They also can occur independent from a volcano, such as Alu (Etiopia) or Mount Tarawera (New Zealand). If the fissure eruption is connected to a volcano, the eruption can take place at the flank of that volcano (e.g., Etna - Andronico and Corsaro, 2011; Vergniolle and Ripepe, 2008) or even kilometres away from the summit (e.g., Kilauea or Bárðarbunga - Lundgren et al., 2013; Poland et al., 2008; Sigmundsson et al., 2015) to which they are connected via crustal flow paths rather than forming a continuous fissure at the surface. Fissure eruptions are also of interest as they can produce large effusive eruptions with a line of cones. The eruption, the dyke intrusion and the associated fault can change the surrounding morphology (Rubin and Pollard, 1988), e.g., the Laki fissure in 1783–1785 produced 14.7 km^3 of flood basalts and several cones, forming the whole surrounding area (Reynolds et al., 2016; Thordarson and Self, 1993).

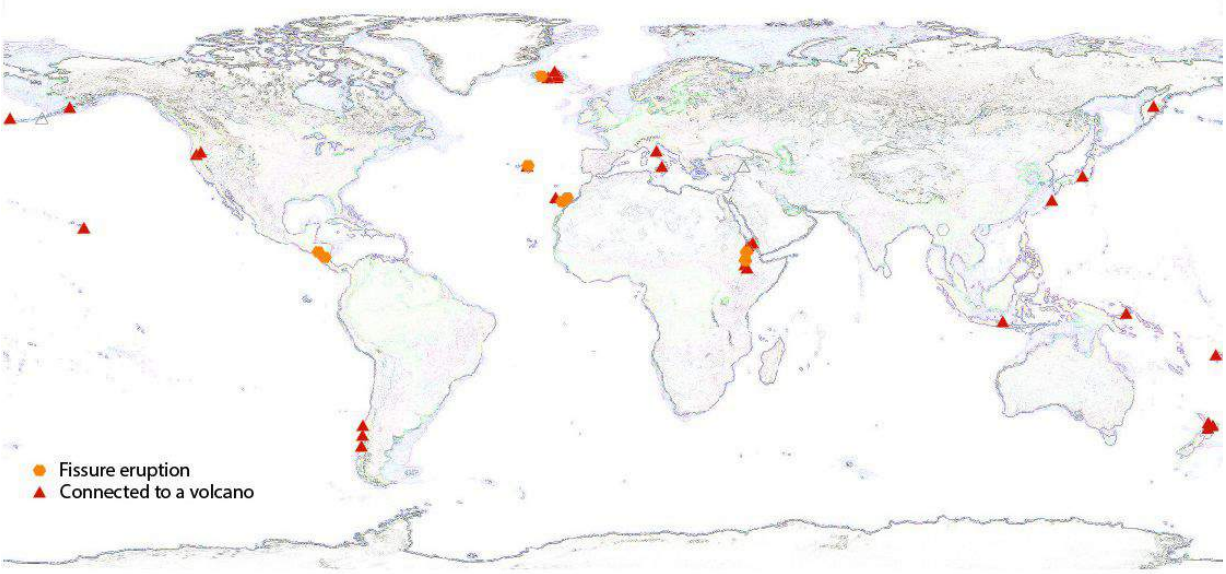

Figure 1.1: Map of selected fissure eruptions of the last two millenniums Fissure eruptions belonging to a volcano are represented as red triangles, while orange hexagons stand for fissure eruptions that are disconnected to a central volcano. The list based on the GMPV database.

The location of a fissure is controlled by the crustal stress field, which is in turn related to the existing morphology, material heterogeneities and magma buoyancy (Acocella and Neri, 2003; McGuire and Pullen, 1989). Consequently, the knowledge of the dyke is mainly based in geophysical data (seismicity and deformation) and modelling. This does not allow interpretation of interactions between eruption vents and complexities in the magma path. The link between the feeder dyke and the surface activity is often less clear, and may be associated with elongated fissures or more isolated conduits (see Figure 1.2). While geodetic data commonly suggests an extensive dike with rather uniform openings at depth (the upper edge often 1-3 km beneath the surface), at the surface segmented fissures or even isolated vents occur (Lundgren et al., 2013; Wylie et al., 1999a). This activity at the vents is associated with lava fountains that show a complexity of distinct venting activity - often in pulsating form - and the development of characteristic morphologic expressions, such as scoria or spatter cones. Most of the activity is Hawaiian and Strombolian eruptions (Valentine and Gregg, 2008), but rarely also Plinian fissure eruptions can occur (Lara et al., 2004). This process from a line of lava fountains to distinct vents is rarely studied, but can be observed well with video monitoring techniques.

Volcano monitoring is the discipline of detecting signs of changes due to reawakening of volcanoes and leading to an enhancement of the understanding of volcanic behaviour (Sparks, 2003). Modern volcano monitoring is commonly based on collecting multiple data which are ground-based or space-based. One of the most important ground-based methods is the seismology measurement. Seismicity reveals fluid pathways, crustal processes, the sources and changes in the pressure and stress field (e.g., Benson et al., 2008; Chouet, 1996; McNutt, 1996; Scarpa and Gasparini, 1996). Furthermore, geodetic data (Global Positioning System and Interferometric Synthetic-Aperture Radar) provides information about the ground deformation associated with magma movements (Dzurisin, 2007). Changes in the magma chamber can also be seen in microgravity measurements (Rymer, 1996) and changes in the degassing (Oppenheimer et al., 2003). The chemical composition of the magma and erupted gases provide an indication of the magma origin, the driving mechanism and on the volcanic processes. Space-based measurements provide information about ground deformation, thermal anomalies or the volcanic cloud depending on the used wavelength (Francis et al., 1996). Satellite systems provide a good global coverage, but they are limited in data collection during eruptions due to a scanning interval (partially multiple days) and a spatial resolution in meter range.

Due to rapid improvements in photogrammetric data, drones and other unmanned areal vehicles (UAVs) are becoming more important. These technologies enable the development of digital elevation models of the vent area and plume (Amici et al., 2013b; Darmawan et al., 2018; Gomez and Kennedy, 2017; Gomez and Purdie, 2016). Based on two elevation models with a time-shift, the deformation can be calculated and interpreted with models. Consequently, collapse of lava domes (Walter, 2011), changes in the volcanic topography (Cecchi et al., 2003) and deformation patterns can be observed.

Many volcano observatories use web cameras for real time viewing of the volcanoes, but commonly no quantitative analysis is applied. In this thesis, the potential of optical cameras as one part of an early warning system is explored. This technology could be used to identify and characterise lava fountain dynamics and underlying activity near-vent processes at fissure eruptions. The lava fountain dynamics and morphology can provide important eruption parameters, such as duration, pressure and activity changes, and dimension parameters of the conduit and lava pond.

This dissertation is realized by using video monitoring (e.g., from webcams at volcano observatories) in combination with other methods to analyse ongoing eruptions. Video monitoring has a range of application opportunities at high spatial and temporal resolution. Based on the data, small deformations prior to an eruption or due to dome building can be analysed (Darmawan et al., 2018; Salzer et al., 2016; Walter et al., 2013b) and compared to other geophysical data, such as seismicity. New developments in UAVs and photogrammetry facilitate the analysis of the flow field and velocity of a volcanic plume (Björnsson et al., 2013; Diefenbach et al., 2012; Dürig et al., 2015). To date, photogrammetric monitoring has mainly been done with thermal cameras (e.g., James et al., 2006; Patrick et al., 2007; Stevenson and Varley, 2008) or high-speed cameras (e.g., Taddeucci et al., 2012b) at Etna (e.g., Behncke et al., 2006; Scollo et al., 2014), Stromboli (e.g., Andronico et al., 2008) and Kilauea (e.g., Patrick et al., 2011a). Many of these studies focus on the erupted material, mainly on lava fountains. Therefore, the lava fountains remained to be analysed on their overall activity and height. While, a detailed analysis of the fountain amplitude with a time-resolution of seconds to minutes, or the relationship to the topography is missing.

Following, a general view of video monitoring, especially with optical cameras and their application in monitoring of volcanic activity and in the analysis of morphology is presented. Furthermore, a short introduction to lava fountains is given. This chapter is finished by the addressing research questions and providing details on the specific contributions to the papers that arose from this dissertation.

1.2 Video monitoring

Optical surveillance by camera monitoring provides continuous data in high resolution at reasonable costs (Diefenbach et al., 2012; Walter, 2011). Based on the acquisition, a wide range of time scales and spatial coverage, from broad to local surface processes, can be covered. While the precision can be high, in some situations ground-based surveying techniques are performed at a higher precision (Diefenbach et al., 2012). Results of video monitoring are small deformations at the crater due to volcanic eruptions (Patrick et al., 2010), extrusions (Major et al., 2009), velocities of the pyroclasts (Gaudin et al., 2014; Taddeucci et al., 2012b), changes in the lava level (Spampinato et al., 2011), lava flow flux variations (James et al., 2007) and fumarole activities (Stevenson and Varley, 2008). Digital image correlation (DIC), particle image velocity (PIV) or optical flow can then be used to estimate the volume changes, extrusion rates, and other quantitative information on the geomorphic evolution of volcanoes (Walter et al., 2013b). The preferred technique is strongly dependent on the eruption site and the data set. Furthermore, feature and manual point tracking allows qualitative information about rock and ballistics trajectories to be obtained.

The techniques from photogrammetry can provide important information on volcano activity and on the morphology of the volcanic area. However, it also contains various sources of errors. Potential error sources during acquisition and image analysis can be minimized by carefully designing the photogrammetric survey and acquisition geometry, as well as choosing the optimal optics and camera characteristics (Diefenbach et al., 2013; Major et al., 2009). Other errors such as those caused by atmospheric conditions are not as easy to isolate. Poor atmospheric conditions are in particular troublesome when monitoring lava fountain dynamics with optical cameras. This dissertation provides mathematical concepts and algorithms to optimize the volcano monitoring by video observation and addresses the limitations in detail as well.

1.3 Lava fountains, fissures and vents

A lava fountain is a jet of lava that is erupted into the air. They are caused by a rising mixture of gas bubbles and magma to the surface. As the mixture ascends, the bubbles expand rapidly, and burst at the surface (Parfitt, 2004). Typically, heights of lava fountains range from a few meters, to a few hundred meters. Highly energetic fountain pulses can reach heights of up to 1500 m (Allard et al., 2005). Lava fountains occur at isolated vents, along fissure eruptions, or within lava lakes. The activity of lava fountains can range from a series of short pulses to a continuous lava fountain, which are suggestive of different mechanisms in the source region (Houghton and Gonnermann, 2008).

Currently, two conceptual models of lava fountain dynamics are discussed. One model suggests that the bubbles get trapped in a storage region prior to the eruption, and then collapse, coalesce or ascend as an annular two-phase flow of gas and melt through the conduit (Collapsing foam model, e.g., Jaupart and Vergniolle, 1988, 1989; Vergniolle and Jaupart, 1986, 1990; Vergniolle and Mangan, 2000). The other model assumes that the bubbles are attached to the magma, and during the journey to the surface, a highly vesicular foam is produced which gets disrupted due to bubble overpressure (Rise Speed Dependent Model, e.g., Fagents and Wilson, 1993; Head and Wilson, 1987; Parfitt and Wilson, 1995; Parfitt, 2004; Parfitt and Wilson, 1994, 1999; Parfitt et al., 1995). Both conceptual models are end-member models. A combination of these two mechanisms, most likely contributes to the formation of lava fountains (Houghton and Gonnermann, 2008).

Many studies can be found that describe the strong relationship between those lava fountain dynamics and the height of the lava fountain and the flow processes within the vertical dykes (e.g., Manga, 1996; Parcheta et al., 2013; Pioli et al., 2012; Polacci et al., 2006; Slezin, 2003; Vergniolle and Jaupart, 1986). Besides the exsolved gas content of the magma, the eruptive volume flux, the magma rise speed, and the degree to which bubble coalescence effectively depletes the magma of gas. The morphology and outer conditions, such as the amount of re-entrainment of degassed lava, magma level fluctuations and wind, influences the height of fountains (Parfitt et al., 1995). Models of lava fountains include different factors to evaluate which ones are the most important for the underlying system (e.g., Gonnermann and Manga, 2013; Wilson, 1993; Wilson et al., 1995; Woods, 2013). The relevance of the factors can vary due to eruption style and setting of the eruption, such as fissure eruption, isolated vent or lava lake.

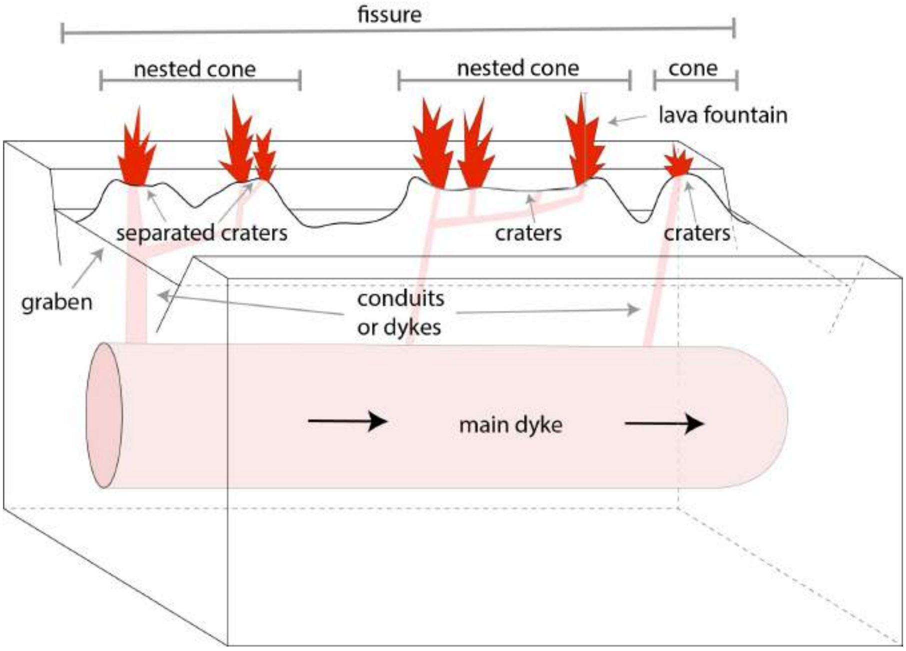

Figure 1.2: Area of a cone-building fissure eruption. Due to an underlying, laterally propagating, feeder dyke the crust is extending and a graben structure is formed. The details on how the dyke feeds the conduits and the lava fountains erupting at surface vents are unclear. Various types of cones may form at the surface.

In this dissertation, the focus is on lava fountains at fissure eruptions.
Cones may be formed depending on the pre-existing topography, magma properties and eruptive behaviour. The magma supply of a feeding conduit is connected to an underlying horizontal dyke (see Figure 1.2). However, as the link between this underlying dyke and the activity at the surface is often not well studied, it may range between an elongated fissure and isolated conduits. Above the horizontal feeding dyke a graben structure is formed, and can be observed at the surface (Ruch et al., 2016). When the dyke or smaller conduits from the dyke reach the surface, opening of fissures can be observed. This can occur at more than one location. If multiple of these opening structures are found, they are divided into segments, which are large scale clusters of such smaller fissures (Lundgren et al., 2013). The segments themselves, can be divided in small-scale features, which are named depending on the resulting topography. If no cones are formed, closely spaced lava fountains are called a group (e.g., at Pu’u’Ō’ō in Chapter 2). In cases of cone-building these groups are within the cones and therefore are labelled as cones (Reynolds et al., 2016; Thordarson and Self, 1993). The morphology and characterization of the cones depend on internal factors, such as eruption height, eruption parameters and tectonics, as well as on environmental conditions and pre-existing topography, and range from cinder cones over scoria cones to half cones (Reynolds et al., 2016). Cones can host one or several craters with sometimes several fountains. Each of these fountains occurs at a certain location within this small-scale feature, the vents.

1.4 Main questions and outline

The primary goal of this thesis is to better understand fissure eruptions, in particular their focusing, dynamics and morphology. Using video monitoring can support answering several questions regarding fissure eruptions. The following chapters will introduce the methods used and will explain how to combine the information from the lava fountain analysis with other data, such as seismicity and morphology data. Therefore, this thesis can be separated into technical and geoscientific aspects. All the papers in the following chapters, except for Chapter 5, are already published as articles in peer-reviewed journals and therefore can be read separately. The following section lists the research questions of the dissertation and briefly summarizes each chapter and addresses the research questions.

The research first focuses on the development of a novel method to extract the dimensions and dynamics of lava fountain activity at fissure eruptions. The result of that technical aspects is used to answer geoscientific aspects targeting different sub-themes, as the eruption dynamic at fissure eruptions, topographic aspects, such as morphology of the cones and the feeder dyke area, and (structural) interaction. In terms of the eruption dynamics, we focus on the activity of lava fountains, and address the following questions:

1) How can the dimensions and velocities at lava fountains be measured by optical video monitoring? Do aligned fountains show similar behaviour or is their behaviour randomly distributed? What can we learn from the lava fountain behaviour about the underlying system of the fissure eruption?

In Chapter 2, a new method for the detection of lava fountain heights and their analysis is presented. The used method and its limitations are discussed. Based on the colour information of the image (BGR value) and with an edge detection algorithm the fountain can be masked and therefore the height is extracted. The analysis of the time-series data of the lava fountain heights, includes comparisons of aligned fountains based on their frequency content and the correlation between their height time-series. Analysing videos from the Pu’u’Ō’ō eruption in March 2011, revealed a high correlation and similar frequency pattern suggesting an interaction of the fountains rather than a random distribution. Based on further calculations, a dependency on the underlying system is seen and parameters, such as pressure waves within the underlying dyke, were discussed.

The topography can be divided in structural changes seen at the surface, such as graben formation and lava flow, and structural changes seen below the surface, such as the vertical feeder dyke. Here, I start with changes seen on the surface and afterwards discuss aspects occurring beneath the surface, to answer following questions.

2) Which structural changes occur at the surface during an fissure eruption? Which complexities arise and how relevant are pre-existing structures?

In Chapter 3, the concept of digital elevation models (DEMs) based on aerial photographs is introduced. Based on these DEMs the area of the Holuhraun eruption is analysed. Beside the morphology changes due to cone building and the lava field, a graben structure has formed. The graben structure is dominated by oblique opening and was influenced by the pre-existing topography. This graben structure provides conclusions on dyke parameters, such as depth and dyke opening.

3) How are lava fountains on fissure eruptions dominated by other geophysical structural changes as shown by seismicity? Can changes in lava fountains be used to explain changes in seismic data signals? How is the feeding dyke connected to the surface vents?

In Chapter 4, the Holuhraun eruption is analysed. Using the methods described in Chapter 2, the lava fountain height is compared to tremor data. Tremor data can be obtained by various sources. Here, the tremor was produced by the vents parameters, the lava flow and the dyke intrusions. The vent parameters, which are one of the sources, also effect the lava fountains. An analysis of the vent parameters can provides more information regarding the source. The tremor in the beginning of the eruption is focused at the location of the later vents, and therefore at the most active lava fountains. We see that an increase in the lava fountain activity, and therefore an opening and/ or pressure change, are the most reasonable source for an increase of the tremor regime.

As a last sub-theme, the interaction between the described eruption dynamics and the structural and morphologic changes is studied. The research is focused on following questions.

4) How are the lava fountain behaviour and the morphology of the eruption site influenced by each other? How do the lava pond depth and the feeder conduit diameter influence the height of a lava fountain?

In Chapter 5, the fountain height evolution, which was described in 4, is combined with the morphology data of the cones, which was shortly discussed in Chapter 3. The methods of Chapter 3 were used to get a detailed final morphology, while additional video data provides information about the earlier morphology. This video data was also used for the calculation of lava fountain heights. Therefore, the relationship between morphology and fountain behaviour can be investigated at two example cones. Modelling the height of the lava fountains afterwards, highlights the influence of the conduit radius and the depth of the lava pond within the crater, and show that variability in the feeder conduit diameter results in similar lava pond depths for the given eruption parameters.

In Chapter 7, the concluding remarks of this thesis and the outlook for the future research is discussed.

1.5 Author's contributions and publications

The Chapters 2- 4 of this thesis are each a peer-reviewed article in a scientific journal. The chapter 5 is in preparation and will be soon submitted. These articles and the author's contributions therein are listed below:

- Chapter 2:

  Witt, T., Walter, T. R. (2017): Video monitoring reveals pulsating vents and propagation path of fissure eruption during the March 2011 Pu'u'Ō'ō eruption, Kilauea volcano - Journal of Volcanology and Geothermal Research, 330, 43-55. doi:10.1016/j.jvolgeores.2016.11.012

  - The author, T. Witt, developed the mathematical concepts in this article, prepared the associated MATLAB codes wrote up the manuscript, implementing comments from her Ph.D. adviser and co-author, T.R. Walter

- Chapter 3: Müller, D., Walter, T. R., Schöpa, A., Witt, T., Steinke, B., Gudmundsson, M. T., Dürig, T. (2017): High-Resolution Digital Elevation Modeling from TLS and UAV Campaign Reveals Structural Complexity at the 2014/2015 Holuhraun Eruption Site, Iceland - Frontiers in Earth Science, 5, 59. doi:10.3389/feart.2017.00059

  - The co-author, T. Witt, participated in the GPS data acquisition and processing, and joined the field work. Furthermore, she contributed to the discussion of the results and commented on the manuscript.

- Chapter 4:

  Eibl, E. P. S., Bean, C. J., Jónsdóttir, I., Höskuldsson, A., Thordarson, T., Coppola, D., Witt, T., Walter, T. R. (2017): Multiple coincident eruptive seismic tremor sources during the 2014-2015 eruption at Holuhraun, Iceland - Journal of Geophysical Research, Solid Earth, 122(4), 2972-2987. doi:10.1002/2016JB013892

  - This article is an application of the height analysis, which is elaborated on in Chapter 2 of this thesis. T. Witt recorded video data in the field, performed the fountain height calculations and contributed the height-related text and figures. Together with the first author E. Eibl, she discussed the correlation between fountain height results and the tremors at the vent region.

- Chapter 5:

  Witt, T., Walter, T.R., Müller, D., Schöpa, A., Gudmundsson, M.T.: The relationship between lava fountaining and vent morphology at the 2014–2015 Holuhraun eruption, Iceland, analysed by video monitoring and topographic mapping - in preparation

  - The author, T. Witt, acquired the field data and analysed the height and morphology data, calculated and discussed the lava fountain height model and wrote the manuscript, implementing comments from her Ph.D. adviser and co-author, T.R. Walter. The co-author, D. Müller, processed the DEMs used for morphology analysis. Other co-authors contributed field or overflight data.

Chapter 2

Video monitoring reveals pulsating vents and propagation path of fissure eruption during the March 2011 Pu'u'Ō'ō eruption, Kilauea volcano

Abstract

Lava fountains are a common eruptive feature of basaltic volcanoes. Many lava fountains result from fissure eruptions and are associated with the alignment of active vents and rising gas bubbles in the conduit. Visual reports suggest that lava fountain pulses may occur in chorus at adjacent vents. The mechanisms behind such a chorus of lava fountains and the underlying processes are, however, not fully understood.

The March 2011 eruption at Pu'u'Ō'ō (Kilauea volcano) was an exceptional fissure eruption that was well monitored and could be closely approached by field geologists. The fissure eruption occurred along groups of individual vents aligned above the feeding dyke. We investigate video data acquired during the early stages of the eruption to measure the height, width and velocity of the ejecta leaving eight vents. Using a Sobel edge-detection algorithm, the activity level of the lava fountains at the vents was determined, revealing a similarity in the eruption height and frequency. Based on this lava fountain time series, we estimate the direction and degree of correlation between the different vents. We find that the height and velocity of the eruptions display a small but systematic shift in time along the vents, indicating a lateral migration of lava fountaining at a rate of 11 m/s from W to E. This finding is in agreement with a propagation model of a pressure wave originating at the Kilauea volcano and propagating through the dyke at 10 m/s from W to E. Based on this approach from videos only 30 s long, we are able to obtain indirect constraints on the physical dyke parameters, with important implications for lateral magma flow processes at depth. This work shows that the recording and analysis of video data provide important constraints on the mechanisms of lava fountain pulses. Even though the video sequence is short, it allows for the confirmation of the magma propagation direction and a first-order estimation of the dyke dimensions. [1]

---

[1] Originally published as: Witt, T., Walter, T. R. (2017): Video monitoring reveals pulsating vents and propagation path of fissure eruption during the March 2011 Pu'u'Ō'ō eruption, Kilauea volcano. - Journal of Volcanology and Geothermal Research, 330, 43-55. doi:10.1016/j.jvolgeores.2016.11.012

2.1 Introduction

Fissure eruptions have been observed at Hekla (1947, 1970), Askja (1961), Mauna Loa (1984), Kilauea (1983 – 2015, continuing), Dabbahu (2005), Reunion (2006), Tolbachik (2013), and many other volcanoes in past decades (Project, 2016; Siebert et al., 2011). Commonly referred to as "Hawaiian-type eruptions", they are predominant on ocean islands and at divergent plate margins but also occur at convergent margins and in intraplate settings (Valentine and Gregg, 2008). Fissure eruptions can occur kilometers away from the volcano summit to which they are connected via crustal flow paths rather than forming a continuous fissure at the surface. At Mauna Loa (Hawai'i), fissure eruptions have opened at distances exceeding 15 km from the volcano summit (Lockwood et al., 1985). The location of a fissure interacts with the crustal stress field (Walter and Amelung, 2006). At Etna volcano (Italy), fissure eruptions may occur close to inhabited areas on the lower slope of the volcanic edifice (Acocella and Neri, 2009). The end-member mechanisms of these lateral and eccentric fissures are (i) horizontal dyke propagation or (ii) divergence of a magma path at great depth followed by predominantly vertical dyke ascent. Distinguishing between these two mechanisms is often difficult (Acocella and Neri, 2003), which is why observation of a lateral-flow mechanism is so important to understanding the link between fissure eruptions and their source region.

Here, we demonstrate the utility of video monitoring in the study of fissure eruptions. We consider an exceptionally well-monitored case example of a fissure eruption that occurred at Kilauea, Hawai'i (Poland, 2014). In March 2011, a fissure eruption occurred in the East Rift Zone of Kilauea and was located at a distance of over 17 km from the Kilauea summit crater (Orr et al., 2015). Specifically, the eruption occurred along several aligned vents, which followed the surface expression of a geodetically and seismically inferred dyke intrusion (Lundgren et al., 2013). A lateral magma flow is geometrically hypothesized because the eruption vents formed at a significant lateral distance from Kilauea (Lundgren et al., 2013). Additionally, fluctuations in the lava lake level at Kilauea were coincident with activity changes at Pu'u'Ō'ō (Poland, 2014), suggesting a hydraulic connection (Montagna and Gonnermann, 2013). However, to date, no direct observations have tested or quantified the lateral magma flow concept based on vent activity at an erupting fissure. Because fissures open sequentially and show venting activity that appears to be correlated to those fissures (Björnsson, 1985; Jackson et al., 1975; Mangan et al., 1993), lateral magma propagation may continue to dominate the subterranean system.

The pulsating behaviour of vents can be investigated in detail via video analysis, as this study shows. Video analyses have been performed elsewhere to investigate volcanic processes because camera monitoring facilitates continuous footage at reasonable costs and in high resolution (Diefenbach et al., 2012; Walter, 2011). This monitoring technique is flexible over a wide range of time scales and allows both a broad spatial coverage and a precise measurement of local surface processes (e.g., Bluth and Rose, 2004; Honda and Nagai, 2002). However, for many applications, it has a lower precision than ground-based surveying techniques (Diefenbach et al., 2012). The methods used for video monitoring are separated into satellite-, aerial- and terrestrial-based methods (Walter et al., 2013a), in which quantitative image analysis, digital flow-field computation, image sequence matching and other photogrammetric and computer vision algorithms are applied (e.g., Baldi et al., 2000; James et al., 2007, 2006; Julio Miranda and Granados, 2003). Common applications in volcanology have included the study of deforming craters (Patrick et al., 2010), extrusion (Major et al., 2009) and collapse of lava domes (Walter, 2011), changes in the volcanic topography (Cecchi et al., 2003), deformation patterns, displacement vectors (Major et al., 2009) and other physical parameters, such as ejection velocities of pyroclasts (Taddeucci et al., 2012a,b). Using thermal cameras a lava flow flux variations (James et al., 2007), cyclic rising and falling of a lava lake surface during unrest (Spampinato et al., 2011), dome building (Schneider et al., 2008), fumarole activity (Stevenson and Varley, 2008) and many other volcanic processes can also be examined. Subsequent digital image correlation can then be used to estimate the volume, extrusion rates, and other quantitative information on the geomorphic evolution of volcanoes (Walter et al., 2013a).

Photogrammetric calculations can provide information on changes in volcanic topography (Cecchi et al., 2003), deformation patterns, and displacement vectors (Major et al., 2009). Therefore, camera monitoring, both optical and thermal, combined with modern image processing algorithms might allow researchers to gather valuable information on erupting fissures, as well. Volcanic fissures and associated venting activity have frequently been recorded by video systems, but a detailed analysis using modern techniques has not yet been performed.

In this paper, we first summarize the mechanisms responsible for Hawaiian lava fountains and the March 2011 Pu'u'Ō'ō eruption. Then, we describe the video data and the methods applied to analyse the video images and explain the results of the image processing, including vent activity levels and the correlation between adjacent vents aligned along the Pu'u'Ō'ō fissure. The results show a pulsation behaviour that occurs chronologically at adjacent vents, often with a clear phase shift. A reasonable dataset in space and time can provide important clues on the formation of pulsating vents due to sub-surface processes and indicate the direction of magma flow at depth. This work highlights the scientific value of video analysis at fissure eruptions and its possible use for obtaining information on processes at depth.

2.2 Lava fountains and the March 2011 Pu'u'Ō'ō eruption

Lava fountains develop when a magma-bearing fissure opens, leading to low-viscosity magma extrusion at the surface (Swanson et al., 1976). Lava fountains are characterized by pulses and jets of a mixture of magmatic gas, magma and pyroclastic products. The height of a fountain can reach hundreds of meters. The dynamics of lava fountains may be governed by gas bubble layers that either form during magma rise or previously accumulate at depth and drive the intensity of the eruption (Allard et al., 2005; Manga, 1996). So far, this description has considered only the vertical dynamics, but fissure eruptions represent structures with a considerable horizontal extent. Therefore, we attempt here to investigate the horizontal dynamics as well.

2.2.1 Hawaiian lava fountains and venting activity

The classic type of lava fountaining can be regularly observed on Hawai'i and is therefore often referred to as "Hawaiian type". Highly energetic fountain pulses can reach heights of up to 1500 m (Allard et al., 2005). Lava fountains are thought to be caused by the rise of a mixture of gas bubbles and low-viscosity magma to the surface (Parfitt, 2004). The gas bubbles may be formed at different depths due to volumetric expansion of volatiles and may be trapped in storage regions prior to eruption.

Different conceptual models of lava fountain dynamics suggest different gas compositions (proportion of CO_2 or H_2O), formation mechanisms and bubble accumulation zones (Parfitt, 2004). The collapsing foam model (CF, e.g., Jaupart and Vergniolle, 1988, 1989; Vergniolle and Jaupart, 1986, 1990; Vergniolle and Mangan, 2000) assumes that CO_2 is the driving gas. Between the conduit and the magma storage zone, bubbles form and become trapped. The bubbles accumulate as a foam (Parfitt, 2004) or a layer of gas (Allard et al., 2005) at a significant depth, as much as 1.5 km beneath the surface. Some bubbles collapse, coalesce or ascend as an annular two-phase flow of gas and melt through the conduit, with the two phases exhibiting significantly different flow velocities. The eruption style depends on whether the foam is collapsing instantaneously or gradually and therefore on the viscosity of the magma. In contrast, the Rise Speed Dependent Model (RSD, e.g., Fagents and Wilson, 1993; Head and Wilson, 1987; Parfitt and Wilson, 1995; Parfitt, 2004; Parfitt and Wilson, 1994, 1999; Parfitt et al., 1995) assumes that H_2O is the driving gas and argues that the buoyant rise of the bubbles is coupled to the melt because bubbles are slow relative to the melt phase. Consequently, the bubbles are bound to the magma from which they exsolved, and the bubble-gas mixture behaves as a single phase (Parfitt, 2004). During ascent, a highly vesicular foam is produced that is disrupted when the bubble overpressure exceeds the tensile strength of the bubble-separating film of melt (Houghton and Gonnermann, 2008). Due to the high degree of coupling associated with the ascent velocity of the bubbles, the eruption style (Hawaiian or Strombolian eruptions) depends on the ascent velocity of the magma beneath the eruption vent (Parfitt, 2004). These two conceptual models are end-member models, a combination of these two mechanisms, including both CO_2 and H_2O bubbles, most likely contributes to the formation of lava fountains (Houghton and Gonnermann, 2008).

During bubble and magma ascent, the pressure inside the bubbles relative to the surrounding pressure becomes increasingly important as the bubbles approach the surface (James et al., 2009). The bubbles start to nucleate and grow via diffusion and expansion or via coalescence. The gas bubbles rise buoyantly and push the column of degassed magma up the conduit. During ascent, further syneruptive nucleation of bubbles in the magma surrounding the ascending gas bubbles occurs (Polacci et al., 2006). The magma vesicularity increases with increasing gas volume flow rates and decreasing conduit diameter until a threshold value of 45 vol % is reached (Pioli et al., 2012). Viscous and inertial forces hinder further bubble expansion, resulting in overpressurization of the bubbles. However, the pressure is reduced by lengthening and spacing of the bubbles (James et al., 2009) and by increasing gas flow rates, which are controlled by the vesicularity of the magma (Pioli et al., 2012). Depending on the timing and depth of the formation and growth processes of the bubbles, fountains can be low, intermediate or high (Parcheta et al., 2013). Pulsating fountains may result from the formation of layers or waves of bubbles during ascent. The distance between the layers is set by the balance between bubble growth and hydrodynamic self-diffusion (Manga, 1996).

Studying lava fountain pulses might provide greater insight into the flow processes of a bubbly magma. Previous studies have mainly focused on flow processes that are directed upward in a vertical conduit (e.g., Manga, 1996; Parcheta et al., 2013; Pioli et al., 2012; Polacci et al., 2006; Slezin, 2003; Vergniolle and Jaupart, 1986). However, in a horizontal dyke, magma flow processes also occur along the dyke. Therefore, additional horizontal flow has to be considered.

Hawaiian lava fountains can develop in rift zones tens of kilometres away from the conduit. Therefore, our testable hypothesis is as follows: a lateral pulse of magma can be quantified by careful recording of the pulsating behaviour of lava fountains.

2.2.2 The March 2011 Pu'u'Ō'ō eruption

Pu'u'Ō'ō is a cinder and spatter cone volcano located in the East Rift Zone (ERZ) of the Kilauea volcano (Hawai'i), which has erupted almost continuously since 1983. The Pu'u'Ō'ō crater, a 500 × 300 m wide and up to 100 m deep depression, refilled after large eruptions in early 2011 (Orr et al., 2015). On 5th March 2011, the crater floor collapsed along with increased seismicity, as shown by time-lapse camera data (Orr et al., 2015). Lava began to erupt between the Napau crater and the Pu'u'Ō'ō crater, marking the start of the 2011 Kamoamoa fissure eruption (see Fig. 2.1). In the beginning of the eruption on 5th March 2011, a single 100 m long fissure opened in the eastern segment (E-segment), and lava fountains with estimated eruption heights of approximately 20 m developed (Lundgren et al., 2013). Over the next 12 h the eruption activity propagated bilaterally to the north-east and the south-west, and reached

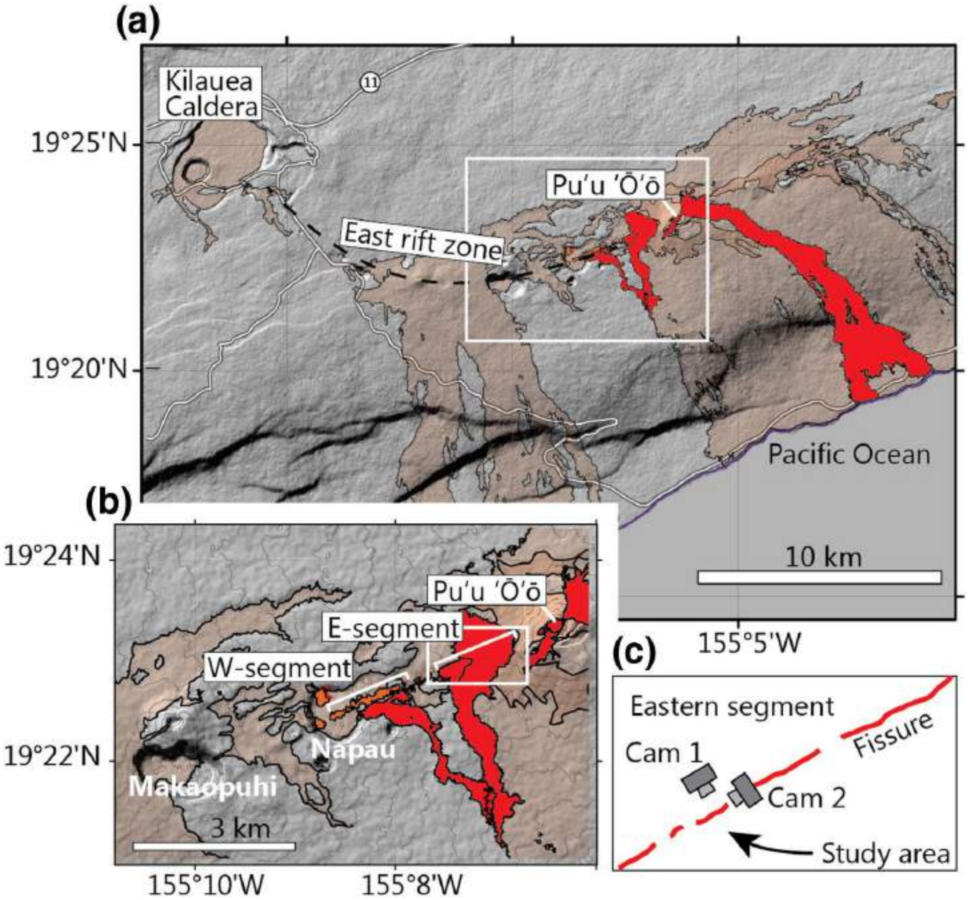

Figure 2.1: Maps of Hawai'i, the Kilauea volcanic system, and the Kamoamoa eruption area (a) East Rift Zone of the Kilauea volcanic system on the Island of Hawai'i with the position of the Kilauea Caldera and Pu'u'Ō'ō Crater. Lava flows are shown in red. (b) Region of the Kamoamoa fissure eruption (episode 59) between the Napau and Pu'u'Ō'ō craters. The western and eastern segments of the fissure are highlighted. (c) Location of the eastern fissure with the position of the two cameras (Cam 1 and Cam 2) at the end of the eastern segment E3.

a length of approximately 2.3 km (Orr et al., 2015). On 6th March 2011, the fountain heights increased to 25 - 30 m, as estimated visually (Orr et al., 2013). After some hours, the western segment (W-segment) became active, while the area between the segments showed no activity (see Fig. 2.1b). On 8th March 2011, activity along the E-segment decreased. In the evening of March 9th, 2011, the fissure eruption also ceased along the W-segment, and the Kamoamoa eruption was over after 4 days (Orr et al., 2015).

Although the Kamoamoa eruption (episode 59) occurred 17 km away from the deforming Kilauea summit crater (Richter et al., 2013), these distant sites are thought to be hydraulically connected (Lundgren et al., 2013; Poland, 2014). A dyke (or pipe) possibly connects Kilauea and Pu'u'Ō'ō (and the associated fissure eruption) (Lundgren et al., 2013; Orr et al., 2015). Satellite radar interferometry data revealed significant ground displacements associated with the dyke, which was constrained to a length of approximately 15 km and a depth from the surface of 3 - 5 km (Lundgren et al., 2013). The width of the dyke opening at the surface was found to increase from nearly 1.5 m to over 2.8 m during the eruption, and was constrained to < 3 km beneath the surface (Lundgren et al., 2013). Lava flows covered the surface immediately surrounding the vents, which is why no geodetic data exist there and why the details of the connection between the dyke at depth and the vents remain hypothetical. The multiple pulses of the lava fountains remain to be studied in this context.

2.3 Video recording and image analysis methods

2.3.1 Camera set-up

During the Kamoamoa eruption, two short videos (both ~ 30 s long) were recorded at the eastern fissure eruption segment E-3 on 5th March 2011 (see Fig. 2.1). The videos were made almost simultaneously but from different viewing directions (Orr et al., 2015). The fissure started erupting at 17:22 and appeared to stop propagating to the north-east at 17:38 (all times are given in Hawaiian time). The camera observations suggest that the activity stopped or was very low at 21:55. The fissure reactivated at 2:42 the next day and finally stopped erupting before 3:00 (Orr et al., 2015).

The videos we used were recorded at a frequency of 30 frames/s and at a resolution of 640 × 360 pixels. Video #1 records a view perpendicular to the vents. It shows lava spattering at the vents, which started erupting shortly before the start of the video (see Fig. 2.2 left - initial activity at the fissure in the front, Fig. 2.1 Cam 1). The fissure eruption can be separated into two groups of vents, each with lava fountains at four individual vents (see Fig. 2.4). Video #1 is ideally suited for our investigation due to its field of view and geometry with respect to the fissure. Video #2 was recorded in front of the propagating fissure with a viewing direction parallel to the fissure during fissure propagation at 17:31 (Orr et al., 2015). The video succeeds in capturing the fissure propagation from SW to NE; however, the field of view makes a more quantitative analysis challenging.

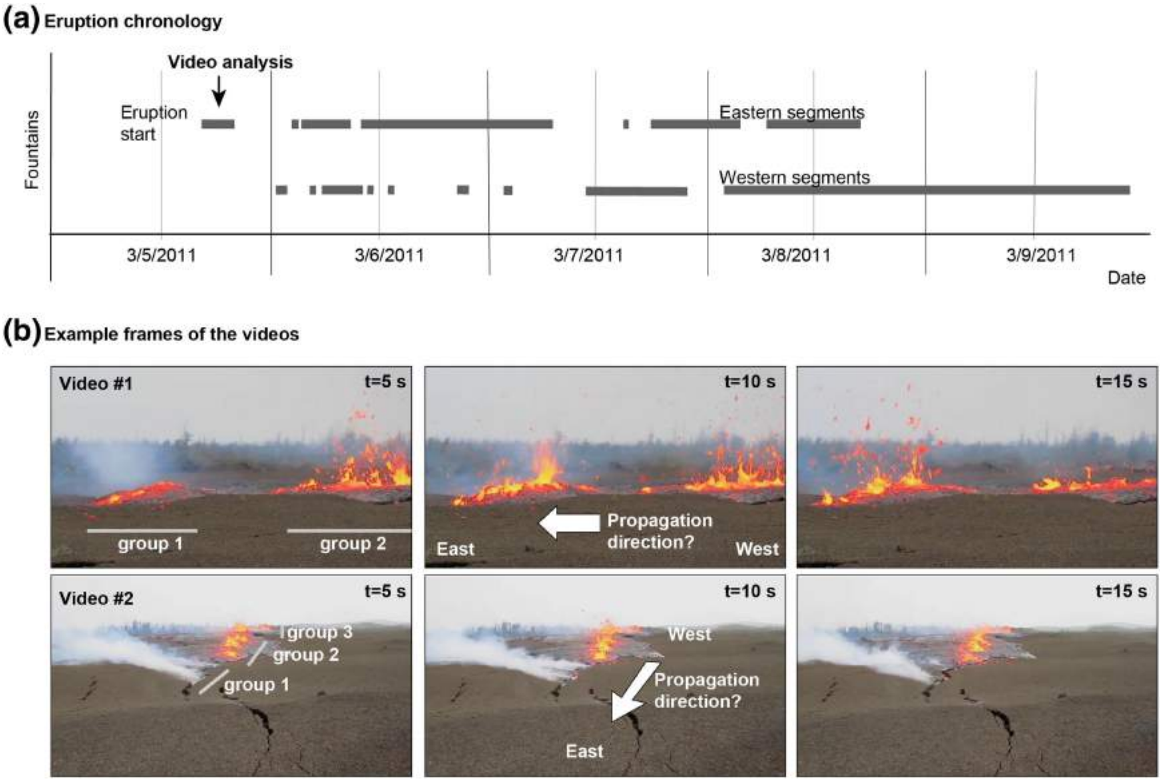

Figure 2.2: Timing of fountain activity and frame example (a) fountain activity along the western and eastern fissures throughout the Kamoamoa eruption. The time of the recorded video is marked, and the time is in Hawaiian time. (b) Example frames from both cameras with a timestep of 5 s between the frames. The upper row show frames of video #1 recorded by Cam 1 from the north of the fissure; the lower row depict frames of video #2 recorded by Cam 2 from the east of the fissure.

The vents are identifiable in both videos and are arranged in a line, which is indicative of a near-linear fissure at depth feeding these vents. Two to three groups of fountains are distinguishable (see Fig. 2.2). Each group is defined by 3 - 5 vents that are closely spaced at < 2 m. The groups are separated by a nearly 4-m-long zone with nearly no activity.

Scaling of the videos was performed by analysis of the falling particles, as detailed further below. The timing of the video images was recorded by an internal intervalometer.

2.3.2 Video analysis

The aims of the video analysis are to reliably measure the dynamics of the fountains, its pulsating behaviour and to test if there is a relationship between the different vents.

To analyse the video of the lava fountains, we develop a method to measure velocity and height in the image time series. Before calculating the height and velocity, each frame is converted into a grey-scale image that is based either on one of the colour channels of the camera or on a combination of colour channels. The weight of the different colour channels is based on the setting and is chosen in such a way as to visually improve the contrast between the background, the steam and the foreground. In our case the red channel was weighted the highest. The velocity measurement involves a modified mpiv-Code (Mori and Chang, 2003), a Matlab Particle Image Velocimetry toolbox. The code is based on the Particle Image Velocimetry (PIV) method, which allows the calculation of the difference between two images by cross-correlation (Raffel et al., 2007; Westerweel, 1997). The image is divided into several quadratic search windows, so-called subregions with side lengths larger than the expected maximum displacement between pairs of images. The subregions overlap by 50 %. Based on the maximum heights of the fountains (approximately 5 to 6 m), we expected a maximum displacement in the vertical direction of 17 pixels/frame. Due to additional horizontal displacement we expect total displacements of up to 20 pixels/frame; therefore, a sub-region size of 32×32 pixels was chosen. Consequently, we have an overlap of 16 pixels. The displacement of the correlation peaks of these sub-regions is calculated in mpiv. Based on the spatial and temporal scaling, the velocities are computed between the images for each sub-region. Here, the falling particle velocities are used for scaling only.

The height of the venting activity was measured using two entities, the maximum height and the height of the main body of the lava fountain. The maximum height H_{max} is the height of the highest magma clasts above the vent, whereas the height of the main body is the height of the lava fountain before fragmentation near the vent becomes detectable in the video data (see Fig. 2.3). Due to this fragmentation, we differentiate between the main body of the fountain and the spatters (fragmented material).

The height measurements are achieved using a Sobel edge detection algorithm (Vincent and Folorunso, 2009). This algorithm works on two-dimensional matrices; consequently, the algorithm is channel-based. As the fountains show clear signals in the red colour channel, we based our channel-based edge detection approach on that channel. After detecting the edges of the eruption at each vent within each frame, the areas surrounded by these edges are evaluated. All areas that have strong edges are labelled by the regionprops algorithm of MATLAB. To select the region of the maximum height of the fountain, the position of the fissure vent in the image is manually defined as the reference level for the lower edge of the main body of the fountains (see Fig. 2.3, red line). This level also defines the lower edge of the fountains, whereas the upper edge is the highest pixel among all the selected areas. Using the edge detection method, the borders of the particles and the main fountains are identified. Converting these edges to a binary file with filled borders, the regionprops algorithm provides us with the properties of each individual area. The maximum or main height can be calculated based on the distance between the highest pixel and the lowest pixel of all areas or specific areas, respectively. As a result, in the time series, both the spatter and the main body of

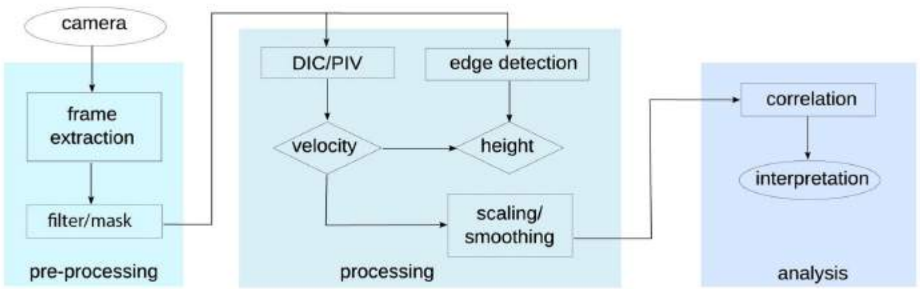
(a) **Method flowchart**

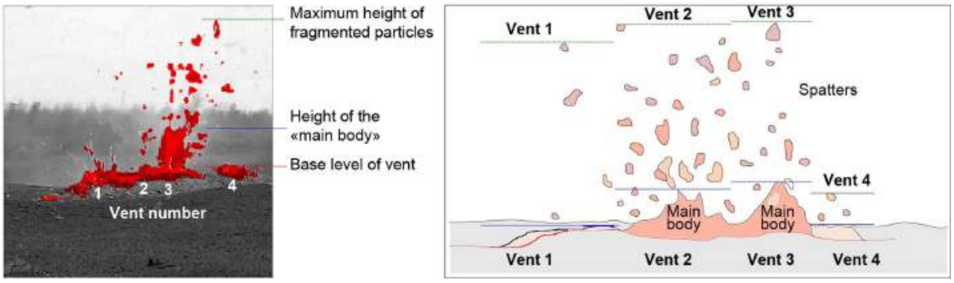
(b) **Method of vent height definition**

Figure 2.3: Processing scheme and height definition (a) method flowcharts detailing the processing from video recording to velocity and height analysis. (b) Basic illustration of the different heights: the maximum height of particles ejected by the fountain (green), the height of the main body of the lava fountain (blue), and the pixels that define the level of the vents (red). The different heights are shown for the eastern group as an example.

the lava fountains are detected (see Fig. 2.3, green line). The reference level of the manually defined vent location is used to identify the area of the main body of the fountain. Because the level is defined as the lower edge of the main body, all areas that include pixels associated with this reference level are connected to the vent. Therefore, only the regions of these areas are analysed to calculate the height of the main body of the fountain, i.e., h_{body} (see Fig. 2.3, blue line). By performing this procedure for all images separately, a fissure height time series can be produced.

At high frequencies ($>10\,\mathrm{Hz}$), the signal-to-noise ratio in the heights is higher, resulting in limited imaging data information. On one hand, the increase in the signal-to-noise ratio is likely due to both the stabilizer of the camera and the JPEG compression, where blocks of 8×8 characters are coded together, which leads to initial detection inertia (Tu et al., 2013). Higher-quality cameras and videos (higher frame rates, higher resolutions, and use of a calibrated lens) might improve these limits. On the other hand, this limitation may arise from our definition of the main body of the fountains. As the main body does not include the spatters, we observe sharp decreases in the height when the spatters become disconnected from the main body. To reduce the influence of this effect, we use a 7th-order Butterworth low-pass filter with a cut-off frequency of 3 Hz. Due to the transfer function of the filter, frequencies larger than half the Nyquist frequency ($\frac{1}{2}\ \mathrm{f}_{Ny} = 7.5\,\mathrm{Hz}$) are neglected. Thus, the filtering also reduces artefacts arising from the camera resolution and frame rate. The very long- and short-term trends are filtered out by an additional 7th-order Butterworth high-pass filter with a cut-off frequency of $f_L = 0.15\,Hz$, which is a tenth of the main frequency. Consequently, we emphasize the pulses of the fountains, and we can measure the height variation using a channel-based edge detection algorithm and a low-pass filter.

2.3.3 Statistical tests

To analyse the image time series, we calculate the frequencies and the cross-correlation between the different fountains by utilizing the channel-based edge detection results. As a first step, we calculate the frequency content of the time series of each vent. This indicates whether the eruptive pulses at the different vents show similar patterns and are thus somehow connected to each other. Then, we use the main frequency of the vents to calculate the range of frames per period N. The last step is to correlate the pulses of the aligned vents with each other. We correlate the whole time series to obtain a time shift between two vents and to examine single pulses, which allows us to investigate the temporal variations in the time shift (i.e., the time-dependent correlation). Importantly, if the behaviour of the fountains is unstable and changing, monotone pulses are not present. In the case of a time-dependent correlation, we calculate the cross-correlation between the fountains of two neighbouring vents. The correlation is based on N points of the first time series with $N + 2 \cdot N_{shift}$(with N_{shift} mostly equal to $0.5 \cdot N$) of the second time series. We assume that the time delay is not more than one period forward or backward. Thus, we select the second time series such that the sequence starts at $t_{shift} = N_{shift}/N \cdot T[\,s]$ before the first time series sequence and finishes at t_{shift} after. As a result, we obtain the correlation between two time series that are measured at separated eruption vents.

2.3.4 Scaling

The videos are taken as a sequence of images at a known interval, and the spatial scale of the field of view is measured in pixels. To estimate a pixel-to-meter conversion, we use the PIV method. The method gives us the velocity of particles, as described above, in pixels/s. Therefore, by measuring the falling velocity of particles (spatters) over 10 to 15 frames, assuming free fall conditions, we are able to calculate the corresponding velocity in m/s. Based on the comparison of both velocities of the falling particles (a measured velocity in pixel/s and a calculated velocity in m/s), we can calculate the scaling factor. However, by neglecting the friction and drag, we may overestimate the velocity and consequently overestimate the height. Comparison with the maximum height measured in the field (Orr et al., 2015), reveals that our calculated scales are acceptable. To minimize the error, we analysed 25 particles, starting at their highest point and detecting their position during the falling process. As a result, we obtain a scaling factor of 43.5 ± 2.6 pixels/m for video #1, and geometric distortions in the camera field of view (FOV) were not corrected further. Video #2 was taken at an oblique angle, and scaling was not possible. Similar scaling approaches were used in other studies elsewhere, e.g., at Mount St. Helens (Voight et al., 1983).

The temporal resolution is given by the camera setting of 30 frames/s. The spatial resolution depends on the accuracy of the edge detection divided by the scaling factor, as determined above. Consequently, the mean spatial resolution is assumed to be 7.8 cm. In terms of velocity, we detected a maximum velocity of 52.0 m/s and an accuracy of 0.5 pixels; therefore, the velocity is limited to a resolution of 4.2 m/s.

The errors in the height variation are parameter based. Varying the pre-processing parameters (such as the weighted sum of the R, G, and B components to calculate the grey value and the threshold for the edge detection) and the edge-detection parameters may affect the error and precision. For example, the beginning of the eruption along the western fissure features a relatively large error caused by heavy steaming and therefore a lower contrast in the grey value between background and the fountain in the foreground. In the following, we demonstrate our method by applying it to the Pu’u’Ō’ō eruption. Details on the limitations of the method and the context of the example results are further elaborated in the Discussion section 2.5.

2.4 Results

Both videos show a variation in the height of the fountains. The data sets are analysed with respect to their frequency content and by correlation methods to evaluate vent pulsation.

Video #1 shows eight vents, four in each group. The maximum height of the fountain eruption (H_{max}) is ~5 m. The height of the mean fountain body varies between 1.8 and 3.9 m for the different vents. Due to the pulses, the mean height of the main body ranges between 0.3 and 1.4 m. Video #1 shows a lower image structure for the main body and a higher image structure for the spatters. Therefore, the edge of the main body and the velocity of the spatters can be well constrained. The trajectories of different spatters are not oriented entirely vertically. Instead, we find a horizontal component that is especially large for those vents located at the ends of the fountain groups (the eastern group 1 and the western group 2). The mean value of the spatter velocity is 5.3 ± 1.4 m/s. The upward detected velocity is between 0.1 and 15 m/s. The highest velocities are observed for the spatters that have vertical trajectories. The horizontal component varies widely and is quantified to between 36 % and 196 % of the maximum vertical velocity. Therefore, the horizontal component is often much higher than the vertical displacement component.

Video #2 shows three groups of fountains with different activity. The group in the front consists of relatively small connected vents that start to fountain during the recording of the video. The fissure propagates towards the observer, which is also why a longer video sequence is not available (T. Orr, pers. comm. 2015). In the beginning, no activity is observed along the vent, but abundant steam is present. After 10 s, lava reaches the surface, and continuous lava fountain pulses are observed 2 s later. The central group (see Fig. 2.3, right frames) consists of three vents and exhibits lava fountain activity throughout the remaining video. During the first seconds of the video, the activity of the fountaining increased, resulting in taller fountains. With the initiation of fountaining in the front group, the activity decreases, and the height slightly decreases. The activity of the farthest group of fountains, in which two vents can be distinguished, appears to remain relatively stable.

2.4.1 Height of the pulsating eruptions

The main fountain body height (h_{body}) can be calculated for each of the eight vents separately. The results for the eastern group (group 1) and the western group (group 2) are shown in Fig. 2.4. In both groups, the two central vents (vents 2, 3 and 6, 7) exhibit the highest fountains and the most activity. The eastern group (Fig. 2.4b) exhibits less activity at the beginning (< 0.75 m), especially along the outer vents (< 0.5 m), and then exhibits an increase in activity (> 0.75 m) after 15 s. In contrast, the activity of the western group is high (~ 1.5 - 2.25 m) in the beginning of the video and subsequently decreases (< 1 m).

The maximum height calculation of the spatters shows a pulsating behaviour. Nearly simultaneous height peaks are visible for the eastern group at several times, such as at 6 s, 16 s, and 26 s, which are labelled (i), (ii) and (iii), respectively. Notably, the almost simultaneous peaks appear to occur slightly earlier at vents 4 and 3 than at vents 2 and 1. Additionally, in the western group, we observe height peaks with only a small time lag, such as the peak at 11 s (labelled (iv) in Fig. 2.4). The vents on the western side appear to show this eruption peak slightly earlier than the vents on the eastern side. To address this apparent shift in more detail, we provide a detailed frequency and correlation analysis in the following section.

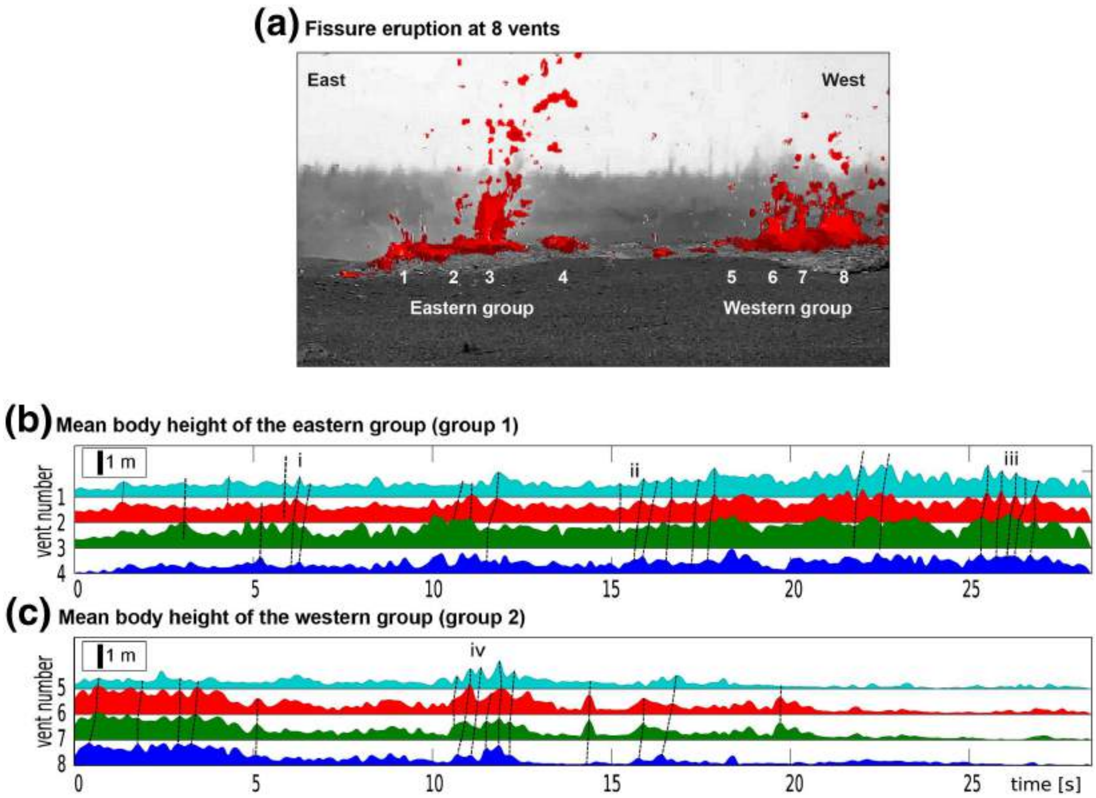

Figure 2.4: Height variations over time in video #1 (a) the vents are named and separated into two groups. The camera was located north-northwest of the fissure segment E3. (b and c) Smoothed height of the main body time series of video #1 for (b) the eastern group (vents 1 – 4) and (c) the western group (vents 5 – 8). Dashed lines link the time of maximum eruption height at adjacent vents for several pulses.

2.4.2 Frequency, correlation and velocity

2.4.2.1 Frequencies

Bandpass filtering allows us to emphasize the different pulses of the fountains and to reduce artefacts arising from the camera resolution and frame rate. The frequency spectrum over time for selected vents is shown in Fig. 2.5 (further frequency spectra are accessible in the supplementary material). From this analysis, we again observe an increase in activity in the eastern group and a decrease in activity in the western group.

In the frequency domain, we observe pulses, i.e., regions with higher energy, over a range of frequencies in comparison to the low-energy background. Depending on the contrast with the background, we define significantly higher values as high venting activity. During periods of low venting activity, the contrast is lower, and the energy decreases with increasing frequency.

Short venting pulses and repeated pulsation are identified as a high-frequency pattern, e.g., at seconds 22 – 24 at vents 2 and 3. Low venting activity and low pulsating behaviour are considered a low-frequency pattern, e.g., at seconds 19 – 24 at vents 7 and 8. Within the groups (each with 4 vents), we observe a high degree of similarity in pulsating behaviour. However, the pulsating behaviour of the eastern group clearly differs from that of the western group. The activity of the eastern group is higher in frequency at the end of the video, whereas the activity of the western group is lower at the end of the video.

The pulsating behaviour appears to be evident in terms of both height (Fig. 2.4) and frequency (Fig. 2.5). Height changes are therefore associated with frequency changes. We interpret this frequency increase to be associated with a higher velocity, which leads to greater eruption

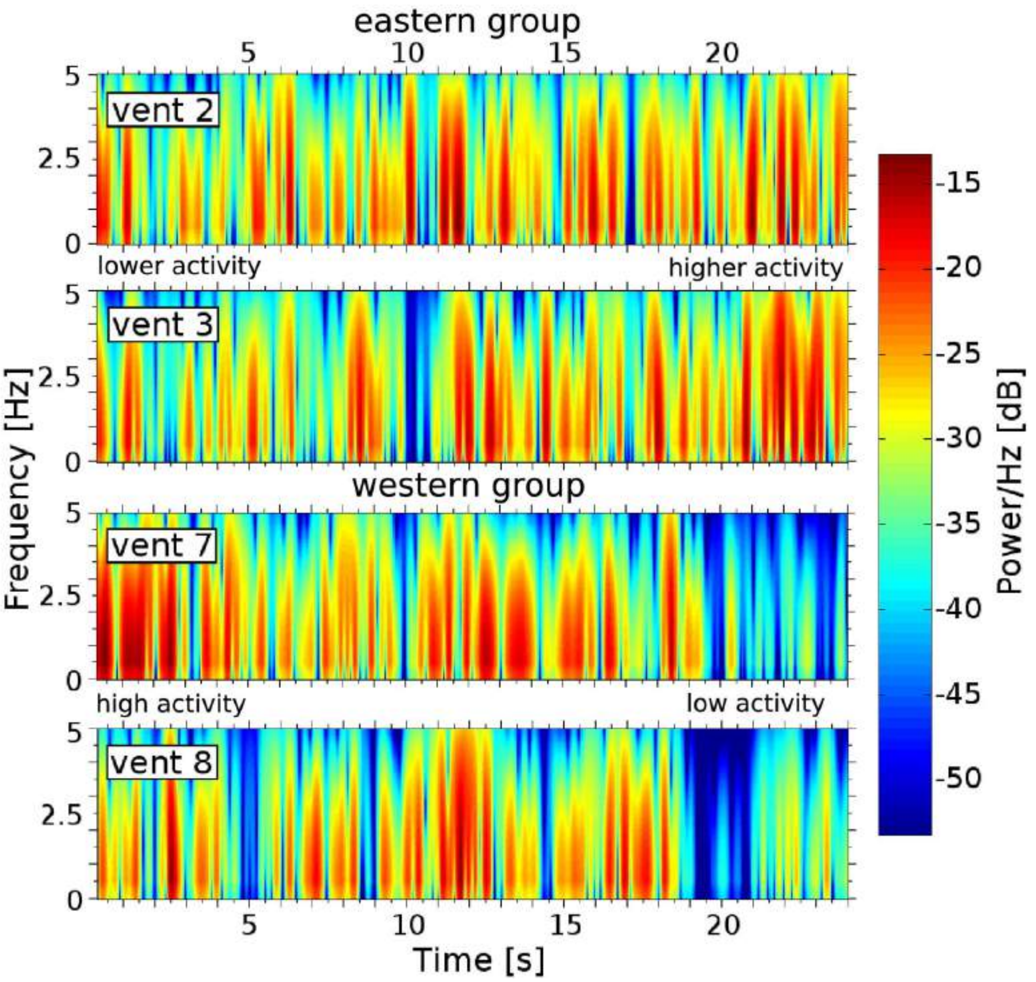

Figure 2.5: Time vs frequency variation plots for vents 2 and 3 (eastern group) and for vents 7 and 8 (western group). The different pulses are clearly indicated by a high concentration of frequencies of 3 to 5 Hz. Additionally, a lower activity of the fountains in the beginning (eastern group) with respect to the end (western group) is also observable.

heights. Therefore, monitoring the frequency-dependent variations of fissure eruptions provides a constraint on the eruption height and ejecta velocity.

Counting the number of pulses for the individual vents, we find that a total of approximately 50 pulses occur in the video, varying slightly between 48 and 53 pulses for the different vents. A closer examination reveals that the pulses that are observed at different vents do not occur in chorus. Instead, a short temporal delay is observed between vents farther to the west and vents farther to the east.

For the eastern fissure (see Fig. 2.5, upper row), all the vents (vents 1 to 4) show a main frequency of 1.47 Hz ($T = 0.68$ s). For the western fissure (see Fig. 2.5, lower row), the vents exhibit greater variations. In total, the main frequency is calculated to be 1.57 ± 0.27 Hz, resulting in a period of $T = 0.63 \pm 0.11$ s. This information will be of use for the correlation analysis below.

2.4.2.2 Correlation

As we have shown above, the amplitude spectrum of each fountain is similar to the amplitude spectra of the other fountains, and the main frequencies are quite similar. Now, we discuss the correlation of these pulsating behaviours. We perform a cross-correlation in time and space, to analyse the behaviour of the eight vents in space and the changes in time shifts between

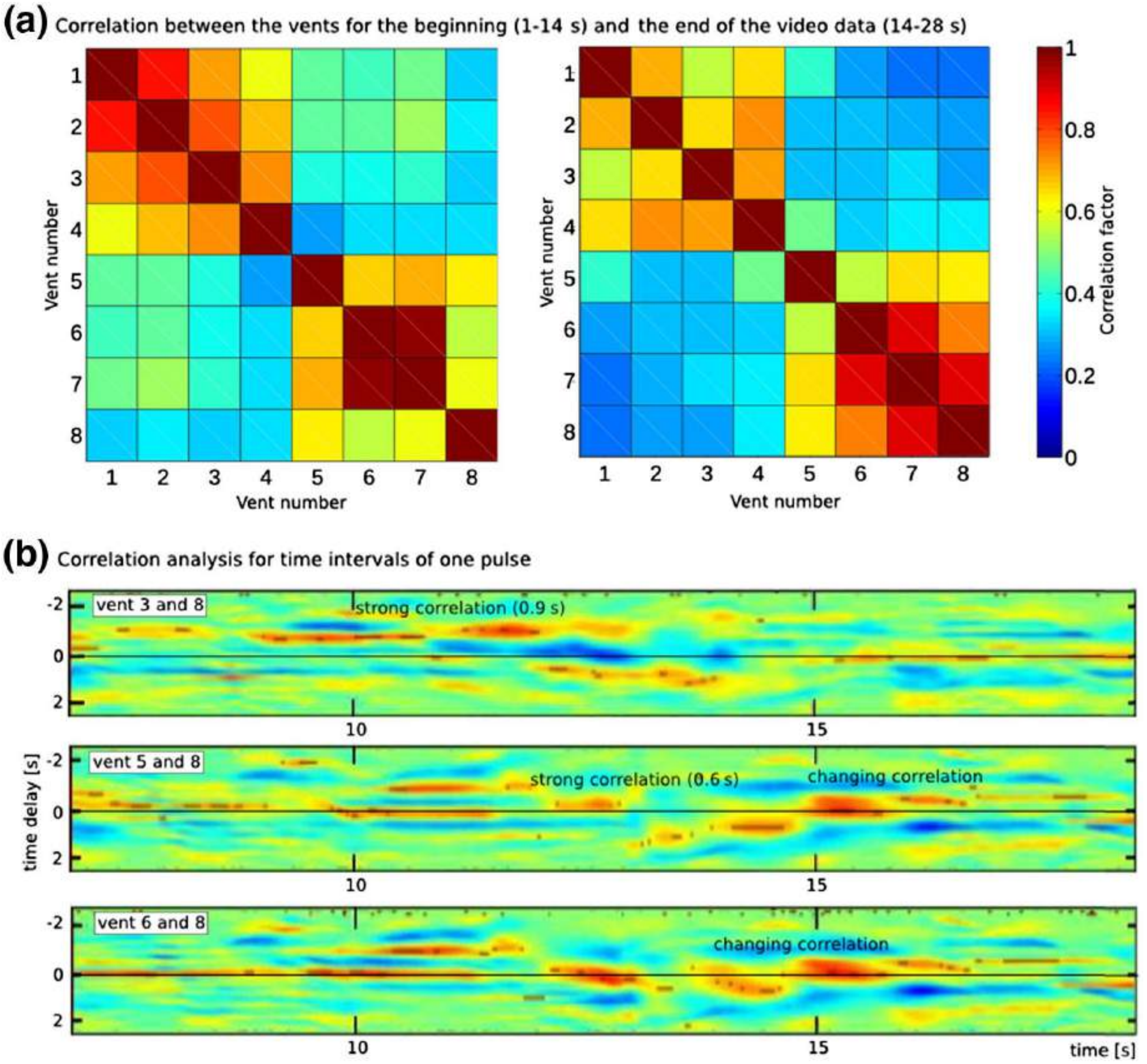

Figure 2.6: Correlation analysis (a) cross-correlation matrix between all eight vents for the first 14 s of the video (left) and the last 14 s of the video (right). The diagonal band of high correlation is the auto-correlation. (b) Correlation between neighbouring vents as a function of time. The correlations are between vent 8 (western group) and three other vents: vents 3 (eastern group), 5 and 6 (western group). Changes in the correlation behaviour and a high correlation between the vents at longer time delays with increasing distance between vents can be observed.

the pulses. The results are displayed in Fig. 2.6. The cross-correlation matrix between all eight vents, shown as a heat map (Fig. 2.6a), shows a high correlation within each group of four vents. Among the 8×8 cells, we clearly identify four distinguished quadrants, two of which have high correlations (shown by red colours) and two with lower correlations (blue). This is evident for the entire time series, although the correlation within the western group is higher at the beginning of the time series, whereas the correlation within the eastern group is higher in the second half of the time series. We observe that nearby vents generally have a high correlation factor that decreases with increasing vent distance. Therefore, vents belonging to the same group show a similar lava fountaining behaviour. Proximal vents exhibit a more pronounced synchrony than those that are farther away. The beginning of the time series shows a generally stronger correlation of adjacent vents than the second half of the time series.

By considering selected vents and shorter intervals, we can study the cross-correlations in time. Fig. 2.6b shows the correlation between vent 8 and other selected vents (additional correlation figures are provided in the supplementary material). The illustration allows the visualization of the time delay in the pulsating behaviour at these selected vents. We find that a clear and systematic time shift in the pulsating behaviour exists between the analysed vents. At 12 s, the vents that are closely spaced (vents 6 and 8 in Fig. 2.6b) feature a dominant time lag of 0.2 s. The vents that are farther spaced (vents 3 and 8 in Fig. 2.6b) feature a dominant time lag of 0.9 s. This suggests that the time lag increases with distance.

We also see episodes during which large changes in the correlation behaviour occur and other episodes during which no correlation is evident. Large changes occur during periods of activity change in the two groups, as identified earlier (Figs. 2.4 & 2.5). During these periods of activity change, the venting frequency increases in the eastern group and decreases in the western group (e.g., at 12 s in Fig. 2.6b). During these times, the correlation analysis reveals jumps in the time delay between the different vents. The correlation between vents in different groups decreases to nearly zero. The correlation between vents in the same group increases, and no time lag is observed (e.g., at 16 s in Fig. 2.6b).

2.4.2.3 Velocity

Based on the time separation observed above and the distance between the identified vents (Table 2.1), we can estimate a velocity. To do so, we consider the time lags of the identified correlated pulses for all four vents within each group (eastern group = green, western group = blue) and for all the vents between both groups (black). The calculation paths and results are shown in Fig. 2.7.

In general, we find that those vents that are closely spaced display a shorter time separation. The fissure eruption time separation for vents adjacent to each other is generally < 1 s. As the distance between the vents increases, the time separation increases. Comparing the time separation for vents that are far from each other, we observe delay times exceeding 1 s. The time separations within a group (Fig. 2.7b) exhibit smaller standard deviations and, consequently, smaller variations throughout the video. The western group is more stable in terms of correlation behaviour. The standard deviation of the time separations between the two groups increases with increasing distance between the vents.

Based on the time separation, we compute the velocity. We refer to this velocity as the apparent venting velocity, and the results are shown in Fig. 2.7c. We find a remarkably stable velocity for the entire fissure. The overall venting velocity calculated from the correlation is -10.6 ± 3.3 m/s. Therefore, the vents in the western group erupt before the eastern vents. Despite relatively large velocity variations between nearby vents, the velocity between the two groups is stable. The larger variations are due to the small time delay and its variations during

Table 2.1: Distance between the vents the calculated distance between the different vents in meters. These distances are needed to calculate the velocities.

	1	2	3	4	5	6	7	8
1	0.0	1.4	2.9	5.0	8.8	10.2	11.4	12.4
2	1.4	0.0	1.5	3.6	7.4	8.9	10.0	11.0
3	2.9	1.5	0.0	2.1	5.9	7.4	8.5	9.5
4	5.0	3.6	2.1	0.0	3.8	5.2	6.4	7.4
5	8.8	7.4	5.9	3.8	0.0	1.5	2.6	3.6
6	10.2	8.9	7.4	5.2	1.5	0.0	1.2	2.2
7	11.4	10.0	8.5	6.4	2.6	1.2	0.0	1.0
8	12.4	11.0	9.5	7.4	3.6	2.2	1.0	0.0

(a) Time separation between vents

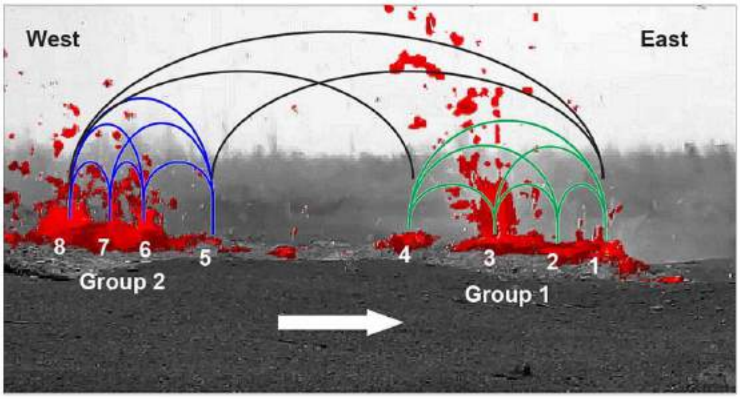

(b) Eruption chronology

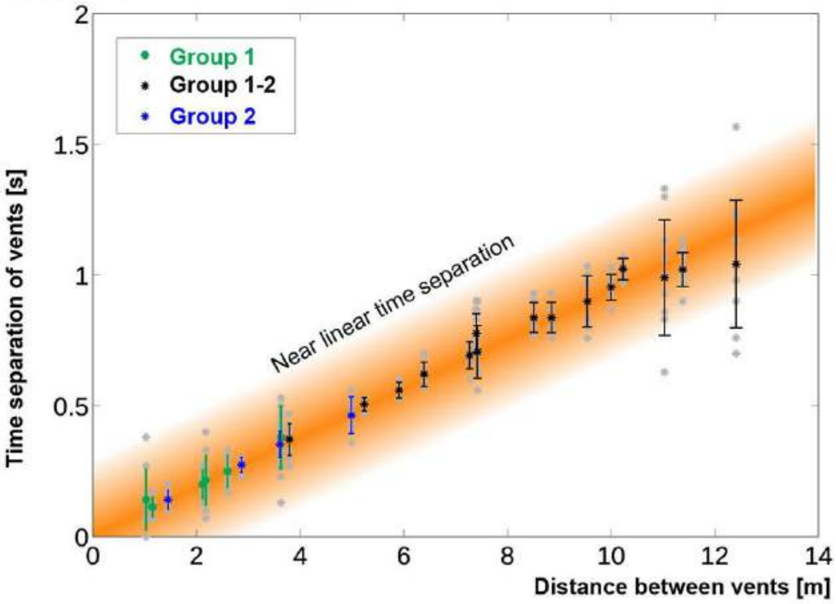

(c) Velocity

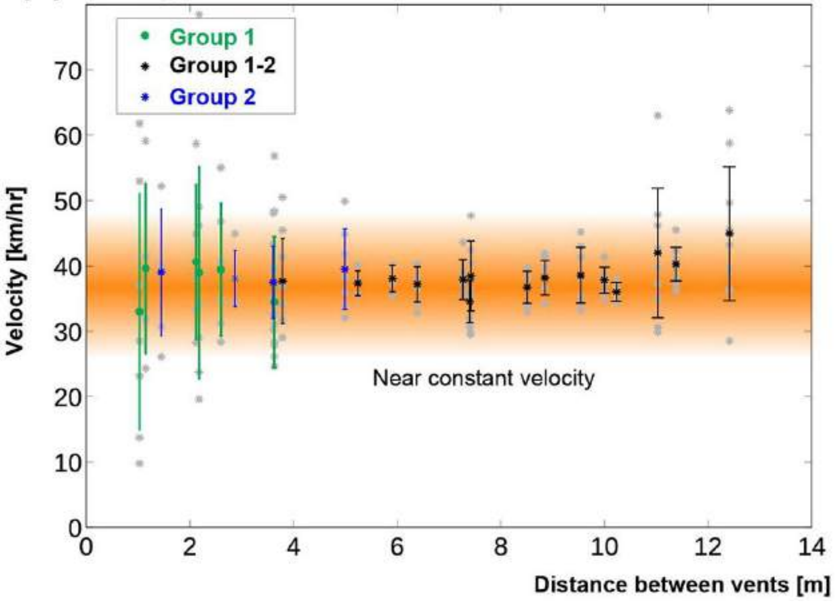

Figure 2.7: Time differences in eruption behaviour and resulting velocities (a) time separation between vents, with the calculation path given for all four vents within each group (eastern group = green, western group = blue), and for all vents between both groups (black). (b) Time delay between fountain pulses of distinct vents as a function of the distance between these vents, calculated by correlating the main body heights of the fountains. (c) The previously determined time delay is converted into velocity. Velocity variations are greater for very small distances and distant vents.

the eruption. We interpret this time lag between pulses to depend on the spacing and timing of the eruption-triggering gas bubbles of the aligned vents.

In video #2, the propagation of magma can be observed in the front group (group 1; see Fig. 2.2b). First, steam rises from the distal edge of the group and propagates to the proximal edge over the course of 21 s (from second 3 to second 24). Then, magma starts to reach the surface. Based on this observation, we can roughly estimate the velocity of fissure propagation to be $0.23 \pm 0.07\,\mathrm{m/s}$. Consequently, the fissure propagation velocity at the surface is significantly lower than the apparent venting velocity derived from correlated pulsating behaviour. The interesting implications of this result are discussed further below.

2.5 Discussion

To test our method for video analysis, we applied it to a well-monitored eruption. We observed pulsating behaviour in the lava fountains occurring in chorus at adjacent vents. By analysing the height of the vents in terms of frequency and the correlation between the vents, a closer investigation revealed propagation of the pulses over time from west to east. This rate of propagation was found to be constant throughout the investigated video sequence, which may imply that the conditions leading to pulsating fountains also remained stable.

The connections among distinct groups in a fissure eruption are usually difficult to quantify. To analyse the connection between lava fountains, we show that our photogrammetric method may allow the investigation of adjacent vent connectivity. By analysing the correlations of both height and frequency, we suggest that a coupling exists between vents that belong to a single group. In addition, we also find a coupled relationship between vents in adjacent groups, although it is less pronounced. This finding is in agreement with the geodetically constrained subsurface model of Lundgren et al. (2013), where the fissures are connected at depth by the same dyke. We observe that pulses of higher and lower activity propagate from west to east. This west-to-east propagation is observed from one fissure to its adjacent fissure, as well as between the vents.

We observe that the correlation regime can change episodically and sporadically. Based on analysis of the two videos, the pulsating nature of the vents is obvious and is characteristic of the lava fountains. During some periods, adjacent vents, separated by up to 12 m, exhibit synchronized activity. This behaviour sometimes features small temporal lags (0.03 to 1.67 s) when one vent is somewhat behind its neighbouring vent.

Despite changes in the correlation regime, the lava pulse frequency, the eruption frequency and the rest time between the pulses remain similar for contiguous lava fountains, implying a controlling process in the magma feeder system itself. Because the individual vents exhibit the propagation, we conjecture that the root cause is related to the feeder dyke, similar to the larger-scale hypothesis based on geodetic and geologic data (Lundgren et al., 2013; Orr et al., 2015). Before describing the implications of these results further, we describe the limitations of the observations and analysis techniques.

2.5.1 Limitations

Photogrammetric analysis contains various sources of errors - both systematic and non-systematic. Potential error sources include the design of the photogrammetric survey, optics and camera characteristics, temporal and pixel resolutions, acquisition geometry, precision of the measurements in the images, random factors (such as atmospheric conditions, e.g., steam or cloud cover), and operator errors occurring during recording (e.g., shaking or camera position) and/or during image analysis (Diefenbach et al., 2013; Major et al., 2009).

Difficulties in video analysis may therefore arise from technical aspects (an uncalibrated camera with poor resolution), from the travel path (steam and hot air) and from user aspects (camera shaking), as well as from the viewing geometry (obliquity to the target or distorted field of view). One of the main sources of errors during data collection is the camera itself. For instance, the lens can produce distortions of the image, the impact of which is hard to quantify. These lens effects are related to the distance between the object and the camera and are dependent upon the focal length (Formenti et al., 2003). Here, the cameras were situated a few tens of meters from the vents; thus, the resulting distortions are assumed to be small.

The videos were not recorded at exactly the same time, and the timing and geometry of acquisition were not optimal. Both videos are only ~30 s long; thus, we can only resolve short temporal disparities and small spatial variations. Although we observe very stable results during this period, we cannot determine whether these variations remain stable over longer periods of time. An optimal configuration of the two cameras would show the same features from slightly different viewing positions (here, features were hardly comparable because the camera positions were at ~90 ° with respect to each other and because Cam 2 was perpendicular to the fissure). However, although the videos were short, we demonstrated that important information can be retrieved.

Errors due the scaling may also propagate into velocity errors because there are no concrete measurements for the pixel size. Therefore, we can only approximate a scaling factor. That means that the height is not an absolute value and is instead a relative value. Additionally, accurate estimates of ground sample distances are difficult to achieve from oblique photographs (video #2) because there is a large difference in scale between the foreground and background. As a result, pixels in different parts of an image can represent very different heights (Diefenbach et al., 2012). Therefore, changes in the fountain heights of distant groups (see Fig. 2.2B, groups 2 and 3) cannot be observed quantitatively.

Sub-pixel variability, related to changes in the surface characteristics (e.g., colour or shape) and to rotational movements of the irregular spatters can affect the results of our imaging technique (Walter et al., 2013a). Especially in the velocity analysis, changes in the brightness and shape of fragmented particles can result in an underestimation of the particle parameters. With decreasing particle brightness (due to cooling of the lava), the pixels can become categorized as background and not as particles. Consequently, the size and height might be underestimated. Therefore, we cannot rule out the possibility that particles with a higher brightness value will eventually lead to a higher similarity. As a result, the calculated velocity may be underestimated due to changes in the analysed particles. Furthermore, velocity underestimation occurs due to the simultaneous upward and downward movement of two particles within one sub-area because the PIV technique cannot distinguish between different particles within one window. This method performs its search after the movement of the whole sub-window. Due to the small area of the fountains and the relatively large time step between the images, each fountain features only a few velocity vectors. Consequently, the variation in the pixel values at the bottom of the fountain might be too large to correlate, i.e., the velocity of the rising gas bubbles cannot be approximated.

The eastern vents exhibit persistent steaming. As a result, fragmented particles are more difficult to detect in this region than in the western part. This mostly affects the results of the maximum height and velocity measurements. In the maximum height measurements, magma ejected from adjacent vents is also detected. Consequently, the pulses of one vent may interfere with the pulses of adjacent vents, and the results of individual vents can be biased by spatters from adjacent vents. Therefore, we analysed the maximum height of the entire group in total, and we use only this calculation as an approximation of the activity of the whole fissure.

In future work, the results of the maximum height might be improved by recording at higher resolutions and by using Particle Image Velocimetry to track particles starting from the vent and by combining several views. The height of the main body of the lava fountain analysed here shows the characteristic decrease in the height as the lava fragments and falls as spatters. As a result, it does not belong to the main body of the lava fountain anymore and is considered a stable result. In addition, a comparison of the video data and seismic data would be interesting. Based on the limited video and seismic data available, only one earthquake with a magnitude > 2 occurred nearby (half an hour before the video recording). Therefore, we were unable to study this question. Additional data, such as infrasound data, might be compared to the video analysis to elaborate the dynamics of the described pulsating behaviour of the fountains in greater detail.

2.5.2 Implications for pressure wave velocity and dyke width

We find a major discrepancy between the velocity observed at the surface by the propagation of the fissure (video #2) and the venting velocity calculated by the correlation (video #1). The venting velocity is almost 50 times larger than the velocity of the surface cracking. These rates represent different processes that are associated with brittle failure and fluid flow. These findings may further support the fact that the process controlling the venting velocity is rooted more deeply.

Lava fountains occur due to rising gas bubbles, foams or layers of gas (Allard et al., 2005; Parfitt, 2004; Vergniolle and Jaupart, 1986, 1990). Differences exist because present models mainly consider the rise of gas bubbles within a centralized conduit. The fissure eruption investigated here is fed by a 25-km-long dyke connected to the conduit/chamber at Kilauea (Poland, 2014); thus, we conjecture that heterogeneities in the bubbly melt are transported laterally. We assume a vesicularity of 44 - 76 vol % (mean: 66 vol %). The bubbles are spherical with diameters of 0.01 to 0.7 cm, which are homogeneously distributed overall but locally clustered (Mangan et al., 1993), forming thin layers of bubbles. These layers are seen as the heterogeneities and differ slightly in bubble size distribution and vesicularity. A similarity in the pulsating behaviour observed at adjacent vents may indicate that the pulses are generated by the same heterogeneities in the dyke. These heterogeneities may be due to different compositions and/or relative proportions of volatile and melt phases, and may have formed at depth before being transported vertically and laterally. The exact nature of bubbly regions remains unclear, and their characteristics may be revealed once longer video sequences are available. During an eruption, the pressure changes markedly. Therefore, with longer video sequences and acquisitions at different stages of an eruption, we might be able to identify such variations. Furthermore, one could combine visible observations at the surface with other data, such as seismic, infrasound or deformation data, to produce physical models based on the independent observations.

The propagation direction of a dyke is of interest for understanding many geophysical parameters. The paths of propagating dykes are controlled by the surrounding stress field (Maccaferri et al., 2011), and the paths of these dykes determines the location of volcanotectonic earthquakes (Walter and Amelung, 2006). Previous studies have focused on understanding dyke ascent and propagation mechanisms (Karlstrom et al., 2009; Segall et al., 2001; Spence and Turcotte, 1985; Weertman, 1970). The propagation of pressure variations through the dyke in the East Rift Zone was called upon to explain the delay times between the deflation/inflation of the Pu'u'Ō'ō summit and the Kilauea summit during early eruptive episodes (1983 - 1985)

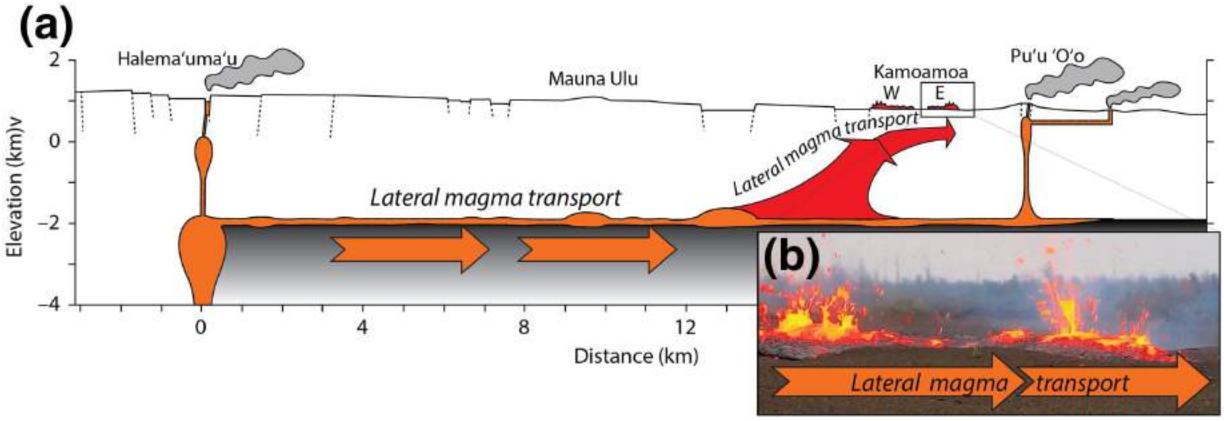

Figure 2.8: Conceptual model of the lateral propagation path in the East Rift Zone (a) Cross section through Kilauea and the East Rift Zone. (b) Close-up of the eastern fissure segment of the Kamoamoa eruption. The magma feeder system is after Lundgren et al. (2013), and the cross-sectional sketch has been modified from Orr et al. (2015).

(Montagna and Gonnermann, 2013). Based on these changes, the lateral velocities of magma pressure waves and the opening of the dyke were calculated.

Montagna and Gonnermann (2013) show that one-dimensional models of magma flow in an elastic-walled dyke can reproduce the spatio-temporal pattern of the tilt. Based on the simplifying assumptions of idealized uniform dyke geometry and an incompressible magma, the momentum and mass continuum can be reduced and analysed. The eruption at Kilauea is an ongoing eruption; therefore, we assume that a pre-existing dyke system was reactivated for the studied Kamoamoa eruption. Consequently, we use the same parameters as Montagna and Gonnermann (2013), except for the parameters we can calculate from the tilt data at Kilauea and Pu'u'Ō'ō and the changes in the lava lake level (Orr et al., 2015). With these parameters, we can test whether a similar calculation is valid for the Kamoamoa eruption and is confirmed by our optical images. First, we calculate the lateral velocity of the magma pressure front to compare it with the velocity we calculated from the image analysis. The delay time between the decrease in tilt signals at the Pu'u'Ō'ō summit and the Kilauea summit was approximately 25 min (Orr et al., 2015). This difference implies a lateral velocity of the magma pressure wave of 10 m/s. This compares well to our velocity of 10.6 ± 3.3 m/s, calculated from the video monitoring data and phase shifts of correlated pulsating venting activity. In addition to the velocity, the calculated direction is also in agreement with the directions from other studies. The dyke model of Lundgren et al. (2013) suggests a dyke feeds the eruption and originates in the west (see Fig. 2.8). The similarities between the results are remarkable, allowing us to hypothesize that the time differences between the activity of adjacent vents can be used to detect lateral magma flow in a pre-existing dyke due to pressure changes caused by changes in magma withdrawal or supply in the magma storage region. The proportionality constant between the magma flow rate and the pressure gradient, which is a characteristic magma transport efficiency, is based mainly on the dyke width.

The velocity of the magma in the dyke is dependent on the diameter of the dyke. Assuming only a variation in the dyke width, the velocity u and dyke width b are related by

$$u = -\frac{b^2}{\mu\gamma}\partial p_x \tag{2.1}$$

where μ is the magma viscosity, γ is the friction coefficient, and p is the magma pressure (Montagna and Gonnermann, 2013). Based on the results of this study and the initial dyke width of 1.6 m proposed by Montagna and Gonnermann (2013), we obtain a dyke opening of 1.36 to 2.37 m. A similar dyke opening was obtained from surface displacement data (Lundgren et al., 2013), which yielded an opening of approximately 1.5 m to over 2.8 m from the first day to the end of the eruption, respectively. Although we only analyse a very short video that spans only a small section of the whole eruption area, our estimated dyke opening is in agreement with that result.

Video monitoring is a rapidly growing field in volcanology, and this study shows that underlying physical conditions can be interpreted from video data. In addition, the pulsating nature and associated feeder system might be used to improve our understanding of why fissures actually exhibit a pulsating behaviour. Future studies will further elaborate and test existing concepts of venting activity at Hawai'i and elsewhere, and video data might be compared to other independent data sets in greater detail.

2.6 Conclusions

The Kamoamoa fissure eruption (episode 59) was recorded by video cameras for only few tens of seconds. Nevertheless, the data allows us to better understand the pulsating behaviour of eruptive vents and their connections at depth. A frequency analysis was performed to test the pulsating behaviour of eight vents. The analysis revealed a high degree of similarity between vents that are closely spaced and a lower degree of similarity between groups and fissures. Eruption vents that belong to the same fissure exhibit a very high degree of similarity in the frequency pattern and also feature pronounced eruption peaks that appear to happen in chorus. A closer examination of this correlated behaviour, however, reveals a small but systematic and significant phase shift. The vents that are located closer to the volcano Kilauea, which supplies the magma, show peaks in eruptions before the vents that are located farther away. This pattern is highly systematic and stable over the period of the video. Larger distances between the vents are correlated with larger phase shifts in eruption activity. Based on the time lag, we calculate a velocity of $11 \pm 3\,\mathrm{m/s}$, which is very consistent with previous independent studies.

Despite small changes in the correlation regime, the frequency of lava pulses and eruptions and the length of rest periods between the pulses remain similar for adjacent lava fountains. These patterns imply that the controlling process lies in the magma feeder system itself. If all individual vents show the same propagation, we conjecture that the cause is rooted deeply in the feeder dyke and represents a hydraulic connection. We propose a conceptual model of lateral flow of a bubbly magma along a feeding dyke from west to east.

The study of the videos of the Kamoamoa eruption can be considered as a promising example. The results demonstrate the high value of video analysis, image correlation and edge detection for investigating processes associated with lava fountains. Future work, and especially longer and higher quality video sequences in combination with other data, may potentially reveal further details on the similarity of fountains at adjacent vents and may aid our understanding of the geometric and dynamic characteristics of the subsurface magma feeder system.

Acknowledgements

Discussions with partners of the Futurevolc project are greatly appreciated. T. Witt was financially supported by the EU FP7 project FUTUREVOLC under grant agreement 308377. This research is also a contribution to VOLCAPSE, a research project funded by the European Research Council under the European Union's H2020 Programme/ERC consolidator grant no. [ERC-CoG 646858]. The earthquake data used in this work are available in the ANSS catalogue.

Discussions with Michael Poland, Tim R. Orr and Paul Lundgren are greatly appreciated. The paper was greatly improved by the constructive and accurate reviews provided by N. Varley and an anonymous reviewer.

Chapter 3

High-Resolution Digital Elevation Modeling from TLS and UAV Campaign Reveals Structural Complexity at the 2014/2015 Holuhraun Eruption Site, Iceland

Abstract

Fissure eruptions are commonly linked to magma dikes at depth and are associated with elastic and inelastic surface deformation. Elastic deformation is well described by subsidence occurring above the dike plane and uplift and lateral widening occurring perpendicular to the dike plane. Inelastic deformation is associated with the formation of a graben, which is bordered by graben parallel faults that might express as sets of fractures at the surface. Additionally, secondary structures, such as push-ups, bends and step overs, yield information about the deforming domain. However, once these structures are formed during fissure eruptions, they are rarely preserved in nature, due to the effects of rapid erosion, sediment coverage or overprinting by other faulting events. Therefore, simple normal fault displacements are commonly assumed at dikes. At the 2014/2015 Holuhraun eruption sites (Iceland), increasing evidence suggests that developing fractures exhibited variations in their displacement modes. In an attempt to investigate these variations, a fieldwork mapping project combining Terrestrial Laser Scanning (TLS) and Unmanned Aerial Vehicle (UAV)-based aerophoto analysis was undertaken. Using these data, we generated local high-resolution Digital Elevation Models (DEMs) and a structural map that facilitated the identification of kinematic indicators and the assessment of the observed structures. We identified 315 fracture segments from these satellite data. We measured the strike directions of single segments, including the amount of opening and opening angles, which indicate that many of the measured fractures show transtensional dislocations. Of these, ~81 % exhibit a significant left-lateral component and only ~17% exhibit a right-lateral component. Here, we demonstrate that the local complexities in these fracture traces and geometries are closely related to variations in their transtensional opening directions. Moreover, we identified local changes in fracture azimuths and offsets close to eruption sites, which we speculate are associated with geometric changes in the magma feeder itself. The results highlight that the opening of fractures associated with an erupting fissure may record transtensional modes with both, left-lateral and right-lateral components. These results further highlight the value of

using UAV-based high-resolution data to contribute to the integrity of the observations of the structural complexities produced by local geologic events. [1]

---

[1] Originally published as: Müller D, Walter TR, Schöpa A, Witt T, Steinke B, Gudmundsson MT and Dürig T (2017) High-Resolution Digital Elevation Modeling from TLS and UAV Campaign Reveals Structural Complexity at the 2014/2015 Holuhraun Eruption Site, Iceland. Front. Earth Sci. 5:59. doi:10.3389/feart.2017.00059

3.1 Introduction

Dike intrusions and fissure eruptions are associated with elastic and inelastic deformation at the surface. While the effects of elastic deformation can be identified from a distance using remote sensing techniques (Dzurisin et al., 1984), the effects of inelastic deformation appear locally, may exhibit complexities at smaller scales and may be rapidly obscured by weathering; consequently, they have been less thoroughly investigated. Commonly observed is the formation of a graben, i.e., a depression bordered by inward-dipping normal faults that may be expressed as a series of complex fractures at the surface. However, reverse slip has also been reported (Gudmundsson and Loetveit, 2005) and reproduced in analog models (Gudmundsson et al., 2008; Trippanera et al., 2015b). Faults associated with dike intrusions and rifted margins may develop in both oblique and normal spreading conditions. However, there is still debate about the vertical propagation direction of faults (Grant and Kattenhorn, 2004; Gudmundsson, 1992; Opheim and Gudmundsson, 1989; Trippanera et al., 2015a), thus demonstrating the need for detailed structural analysis in extensional regions.

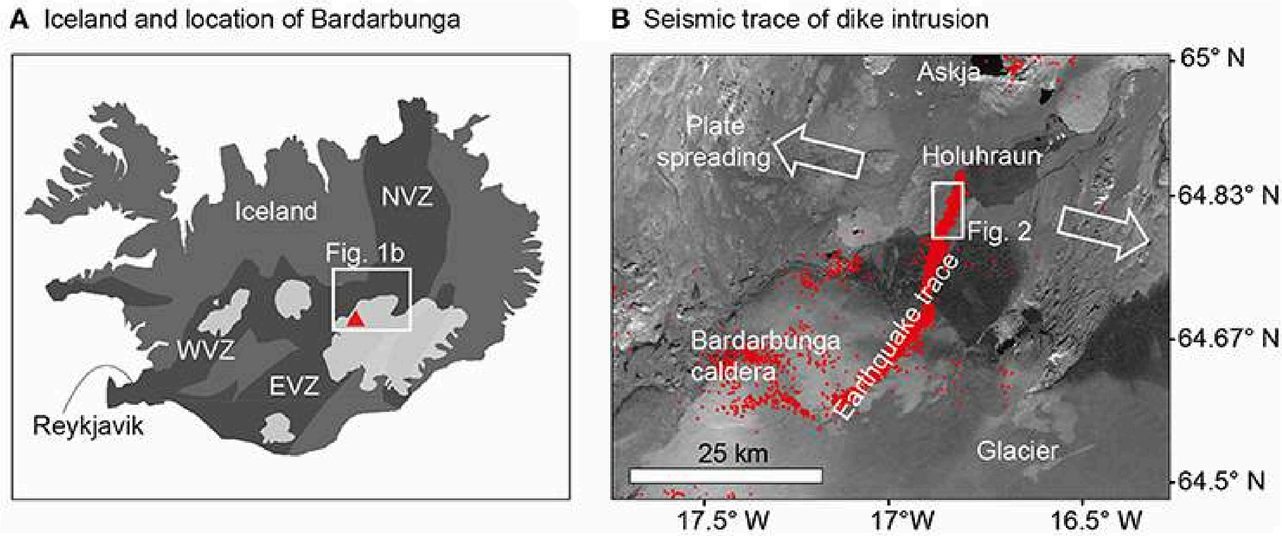

Figure 3.1: Study area (A) Iceland and locations of the volcanic zones, namely, the Northern Volcanic Zone (NVZ), Western Volcanic Zone (WVZ) and Eastern Volcanic Zone (EVZ). The red triangle depicts the location of the Bárðarbunga central volcano, under Vatnajökull glacier (glaciers are light gray). (B) Northern sector of Vatnajökull glacier within the Bárðarbunga caldera. Red dots depict earthquake locations (Icelandic Meteorological Office) recorded over a time span of 3 weeks, indicating the path of the intruding dike. The 2014/2015 Holuhraun eruption occurred at its northern end and produced lava flows covering 86 km2 (dark gray areas). Background image: WorldView-2, September 2015. The white box outlines the region shown in Figure 3.2D.

The results of previous detailed studies performed at volcanoes indicate that extensional structures may exhibit high complexity (Peacock and Parfitt, 2002). The active rift in Iceland provides very recent examples of structures associated with intrusion-related faulting in an extensional regime that may accommodate significant strike-slip movement, as was recently evidenced by divergence that was oblique with respect to the direction of the underlying dike (Ruch et al., 2016). To better understand the development of extensional faulting structures, here, we study the geomorphology and structural geology of the 2014/2015 Holuhraun eruption site, which is the site of the most recent rifting episode in Iceland. By analyzing Terrestrial Laser Scanning (TLS) derived Digital Elevation Models (DEMs), together with Unmanned Aerial Vehicle (UAV) based high resolution aerophoto mosaics, we were able to identify local structures, such as step overs, push-ups and en echelon arrays, that confirm a component of strike-slip motion. We show that the strike-slip component is locally highly heterogeneous and that the reactivation of preexisting structures, topography and heterogeneities have played important roles in developing the observed complexity of the structural arrangement.

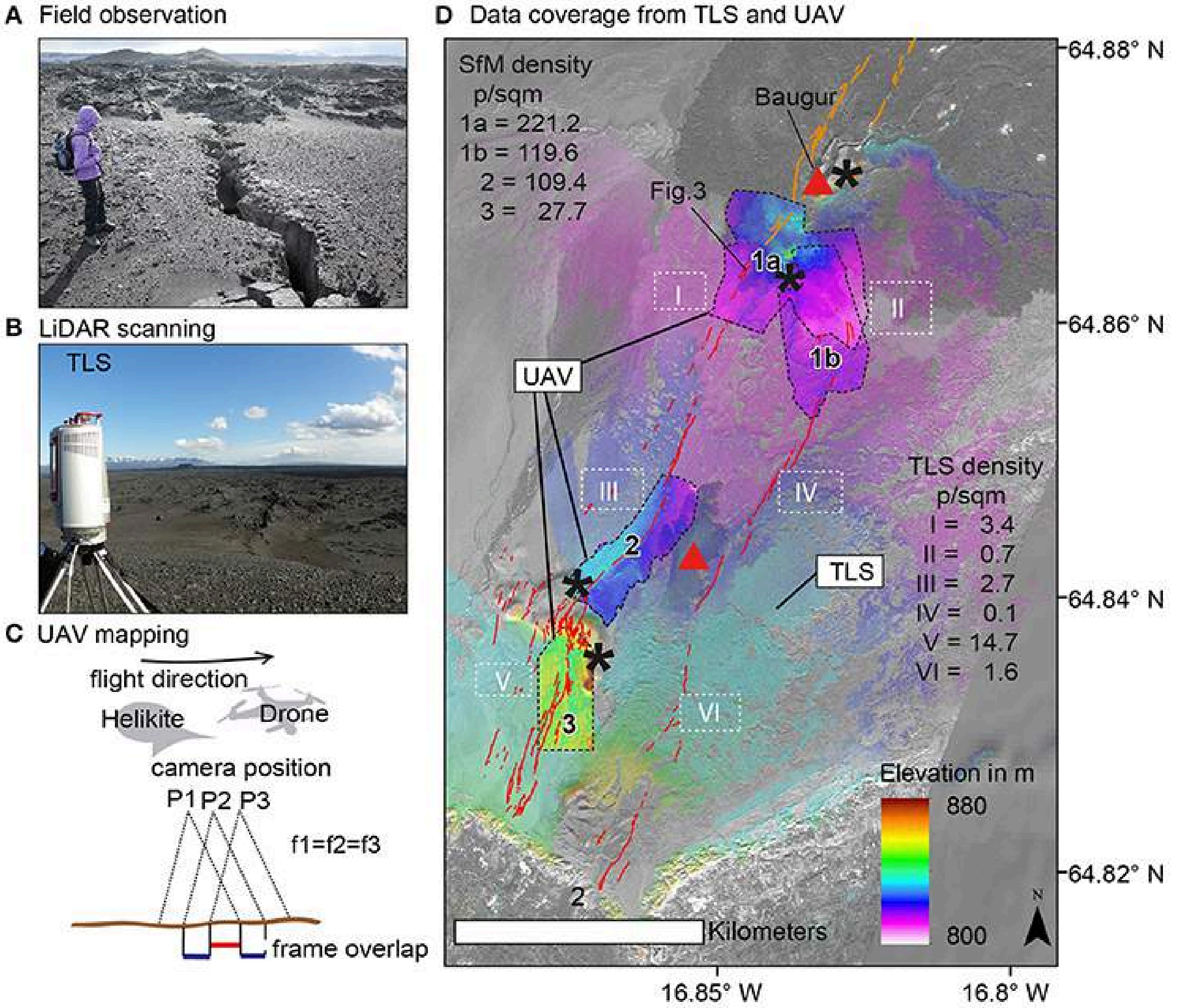

Figure 3.2: Methods (A) Field observations in August 2015. (B) LiDAR scanning was performed using a TLS device, a Riegl VZ-6000 instrument, with a scanning distance of up to 6 km. (C) Sketch of UAV data acquisition. We used either a balloon kite or drones, equipped with cameras, moving in loops over the ground and constantly acquiring photos. (D) Data coverage of the used acquisition techniques. The colored point cloud in the background shows the topographic data set acquired by TLS, with black stars depicting single scan positions spanning an area of almost 20 km^2. Colored point clouds with higher intensities are areas where UAV imaging data were acquired. Point densities (in points per square meter) are indicated. Red lines indicate fractures observed from our data. Orange lines indicate fractures buried by lava as observed by Hjartardóttir et al. (2016).

The area studied here is a part of the Bárðarbunga volcanic system, which is located in the extensional Eastern Volcanic Zone (EVZ in Figure 3.1A), a tensional tectonic environment in central Iceland (Sigmundsson, 2006). The Bárðarbunga system consists of a central volcano and large fissure swarms (extending 55 km toward the NNE and 115 km toward the SE). The central volcano (Figure 3.1B) is located under the northwestern sector of Vatnajökull glacier, from which a magma-filled crack propagated to the northeast in August – September 2014 to feed the 2014/2015 Holuhraun eruption (Sigmundsson et al., 2015). The dike intrusion preceding the eruption was connected to the Bárðarbunga caldera; this intrusion was exceptionally well monitored by multinational research projects and was instrumentally recorded using scientific infrastructure (http://futurevolc.vedur.is/).

The Holuhraun eruption, which lasted for 6 months (August 2014 – February 2015), involved the mobilization of ~ 1.9 ± 0.3 km3 of magma (Gudmundsson et al., 2016). Petrologic data and seismic records obtained by the Icelandic Meteorological Office (Figure 3.1B) suggest that the ascent of magma beneath the Bárðarbunga central volcano was followed by the lateral transport of magma through the upper crust over a distance of ~ 45 km to the Holuhraun eruption site (Geiger et al., 2016; Sigmundsson et al., 2015). Based on the analysis of seismic data, this lateral magma propagation was associated with normal faulting, as well as strike-slip faulting at variable depths (Ágústsdóttir et al., 2016). Seismic records reflect the presence of dominantly left-lateral slip components, as well as some right-lateral slip components (Ágústsdóttir et al., 2016); a relatively high number of right-lateral seismic events occurred close to the Holuhraun eruption site in the north, at depths of 5 - 8 km. Geodetic and field surveys revealed that dominantly left-lateral slip and only minor right-lateral slip occurred prior to the onset of the main eruption on 29th August 2014 (Ruch et al., 2016). These differences might be associated with the depths and resolutions by which the used methods are constrained.

The eruptive vents of the 2014/2015 Holuhraun eruption can be grouped, based on their locations and eruptive characteristics, into three distinct clusters, namely, (i) the main Holuhraun eruption site, which reactivated the 1797/98 crater row and was active for over 6 months; (ii) a row of small craters that formed to the east of the main fissure; and (iii) the 5th September 2014 eruption site, which formed 2.5 km to the south of the main fissure along a series of en echelon segments and was active for only 2 days. Satellite radar data allowed the survey of these structures at a resolution of better than 10 m (Floricioiu et al., 2015; Rossi et al., 2016); these data revealed details about the crater row and the eruptive fissure. Compared to the crater row of the previous eruption in 1797/98, its final shape is composed of only four major vents along the main fissure, the highest of which (Baugur crater, Figure 3.2D) reached a height of ~ 100 meters. Photographic analysis revealed that the orientation of the newly formed craters resembles that of the old crater row of the 1797/98 eruption (Hjartardóttir et al., 2016).

The high-resolution structural analysis of the 2014/15 Holuhraun eruption site should yield a better understanding of the structures that resulted from the lateral propagation of a dike through crust that was previously affected by earlier faulting and oblique rifting processes (Ruch et al., 2016). To accomplish this, we mapped and analyzed the 2014/15 Holuhraun eruption site. Here, we identify the locations of 315 fractures and trace their extend. At the northern tip of the dike, the displacements of fractures are quantified and their orientations and relationships to the general rifting direction are analyzed. This local analysis is then placed into the context of the 2014/15 Holuhraun rifting episode and compared to other sites exhibiting similar structural complexities.

3.2 Data and Methods

We used satellite data to obtain an overview of the 2014/15 Holuhraun eruption site both before and after the eruption, which occurred between 29th August 2014 and 27th February 2015. To investigate further details about the fractures identified in this area, we acquired high-resolution TLS data and aerial photographs using cameras mounted on UAVs during a field campaign in August 2015, 6 months after the end of the eruption.

3.2.1 Satellite Data

The structural overview presented here is based on the analysis of satellite imagery and the results of the TanDEM-X satellite mission (Floricioiu et al., 2015; Rossi et al., 2016). For further details on the TanDEM-X data, we refer to those publications. The presented elevation change is based on the differences between the pre-eruptive and co-eruptive DEMs, which were acquired on 21st November 2011 and 9th September 2014, respectively. In addition, we used the available WorldView-2 data, which were acquired on 12th July 2014 (immediately prior to the onset of the seismic crisis) and 25th September 2015 (6 months after the termination of the eruption), with off-nadir angles of 12.4 and 26.8° , respectively. These data are panchromatic and have a spatial resolution of ~0.6 m.

3.2.2 Close Range Aerial Photographs from UAV

The use of UAVs facilitates the acquisition of high-resolution photo data, which represent much higher resolution data than the morphological and structural data obtained by recent satellite systems (Amici et al., 2013c; Mancini et al., 2013; Nakano et al., 2014). Commonly used UAVs include multicopters, kites and balloons (Carrivick et al., 2016), which allow for especially wide applications in the fields of photogrammetry and remote sensing if equipped with cameras or other sensors. The use of optical cameras carried by UAVs over certain terrains permits the application of modern computer vision approaches; here, they allow for the derivation of digital terrain models at unprecedented levels of detail (James and Varley, 2012).

We mounted lightweight cameras on two quadcopter drones and a helium-filled balloon-kite (Figure 3.2C) flying at a height of 100 - 150 m. This combination of UAVs was selected because it allowed us to efficiently record images on both calm and windy days. We acquired all data presented here on 2 days (14th and 15th August 2015). The UAVs used were Phantom 2 quadcopters from DJI, which were equipped with 12 Megapixel GoPro Hero 3+ cameras and H3-3D gimbals (camera suspension system) to avoid shaking. The cameras typical fish-eye distortion was significantly reduced by replacing the original lens (a 170 ~wide-angle lens) with an OST 10 mp 5.4 mm IR CUT Replacement Lens with a 60° objective. The helikite used here (by Allsopp Helikites Limited, UK) is a helium-filled balloon-kite that is attached via a Dyneema line to a field scientist walking along a desired path on the ground. A helium volume of 2 m3 carried our modified GoPro cameras and allowed them to remain stable in wind speeds of up to 35 km/h. The cameras were placed in time-lapse mode. The drone-based cameras, flying at a speed of 5 m/s, used a setting of 1 fps (frame per second) whereas the cameras on the helikite, which traveled at a walking speed of <1 m/s, used a setting of 0.2 fps. In total, we acquired over 7,000 images of the Holuhraun eruption site and its associated graben structure.

We first visually inspected the images and deleted those that were out of focus or otherwise of low quality. The remaining images were grouped into chunks of distinct regions and were then photogrammetrically processed using the Structure from Motion (SfM) approach (Carrivick et al., 2016; Westoby et al., 2012). The SfM technique, which is able to reproduce high-resolution 3D surfaces from 2D photographs, was applied using the Agisoft PhotoScan Professional commercial software package (version 1.2.6). The ideal conditions of data acquisition are a constant focal length during the overflight, perpendicular target acquisition geometry, sufficient overlap in the images (which was ~80 % on average in our study), and the measurement of Ground Control Points (GCPs) for georeferencing purposes. The processing of these images is based on the identification of corresponding pixels in different images and consists of three steps, namely, (i) image alignment, (ii) dense cloud construction and (iii) surface generation. This process yields a dense cloud of points defining the most likely positions for corresponding points in a 3D space, as well as geolocated photo mosaics and DEMs. Following this rationale, we focused on the following four regions: the western and eastern graben faults close to the vent region (areas 1a and 1b), a bent segment of the western fault system at the 5th September eruption site (area 2) and the southern part of the western fault system, which is located near a pronounced hill (area 3). These locations are detailed in Figure 3.2D.

3.2.3 Laser Scanning

Terrestrial Laser Scanning (TLS) is based on the principles of LiDAR (Light Detection and Ranging), which measures the time delay between emitted laser pulses and their echo receptions (Fornaciai et al., 2010; Richter et al., 2016). We used a Riegl VZ-6000 scanner (Figure 3.2B), which features a rotating head scanner with a horizontal field of view of 360° and a vertical field of view of -30 to 30°. It operates using near-infrared wavelengths, with a pulse rate between 30 and 300 kHz. The scanner is equipped with an internal GPS antenna, an internal leveling device and an optical camera. The Riegl VZ-6000 has a maximum range of 6 km and an angle measurement resolution of 0.0005°. Although the range of 6 km theoretically covers most of the area of interest between the eruption site and the glacier, we selected different viewing points and merged their data in order to increase the density of scans in the far field and reduce shadowing problems. Scans were acquired from four different scan positions (Figure 3.2D) that exhibited some overlap; they were then merged using point cloud matching techniques. To geocode the TLS scans, we used reflectors (recognized in the scans) that were placed around the scanning position and measured using differential GPS. Each TLS scan thus yielded a point cloud containing tens of millions of data points. The data processing of each scan was performed using Riegl RiSCAN Pro 2.0.2 (http://www.riegl.com), which is a commercial software designed to process TLS point cloud data.

3.2.4 Point Cloud Density and Referencing

As graphically illustrated in Figure 3.2D, from the UAV data, we were able to derive 237 m points for area 1a (221 points/m^2), 82 M points for area 1b (119 points/m^2), 55 M points for area 2 (109 points/m^2) and 11 M points for area 3 (27 points/m^2). The obtained resolutions range from 0.067 to 0.19 m (Table 3.1). Thus, the resolutions of drone based photos are ~3 - 8 times higher than those of the WorldView-2 satellite-derived optical data (Figure 3.3). The drone-based DEMs have resolutions that are 60 to 180 times higher than the already high 12 m resolution derived from the TanDEM-X mission.

The dense point clouds obtained from UAV data processing were georeferenced based on the TLS data. This was achieved in two steps: first, rough tie-point matching was performed; second, the Multi-Station Adjustment module, as implemented in the RiSCAN Pro 2.0.2 software package, was applied. The Multi-Station Adjustment tool calculates the best fit of the coarsely aligned SfM point cloud to the reference point cloud (which, in our case, represents the TLS data) by rotating, translating and scaling the data. In this way, we minimized the spatial offset between the point clouds. Using the highly consistent TLS data with millions of possible GCPs for the registration of our SfM point clouds made the additional measurement of GCPs in the field redundant. Therefore, the procedure of referencing one point cloud against another reference point cloud is similar to that described in Richter et al. (2016) . This technique was beneficial, as placing GCPs on sharp fresh lava flow surfaces is difficult. After meshing the dense clouds, we produced mosaics and DEMs from these data.

Table 3.1: Data comparison for different areas using the methods described in the text.

Data	**SfM**				**TLS**	**WorldView-2**	**TanDEM-X**
Region	1a	1b	2	3	Whole region	Whole region	Whole region
Date of acquisition	08/2015	08/2015	08/2015	08/2015	08/2015	12.07.2014 25.09.2015	21.11.2011 09.09.2014
Point count p	237 m	82 m	55 m	11 m	93 m	No data	No data
Area km^2	1.07	0.69	0.51	0.40	33.00	48	~1,180
Density p/km^2	221.16	119.57	109.42	27.68	2.82	1.78	0.08
Resolution m	0.067	0.091	0.095	0.19	0.6	0.56	~12

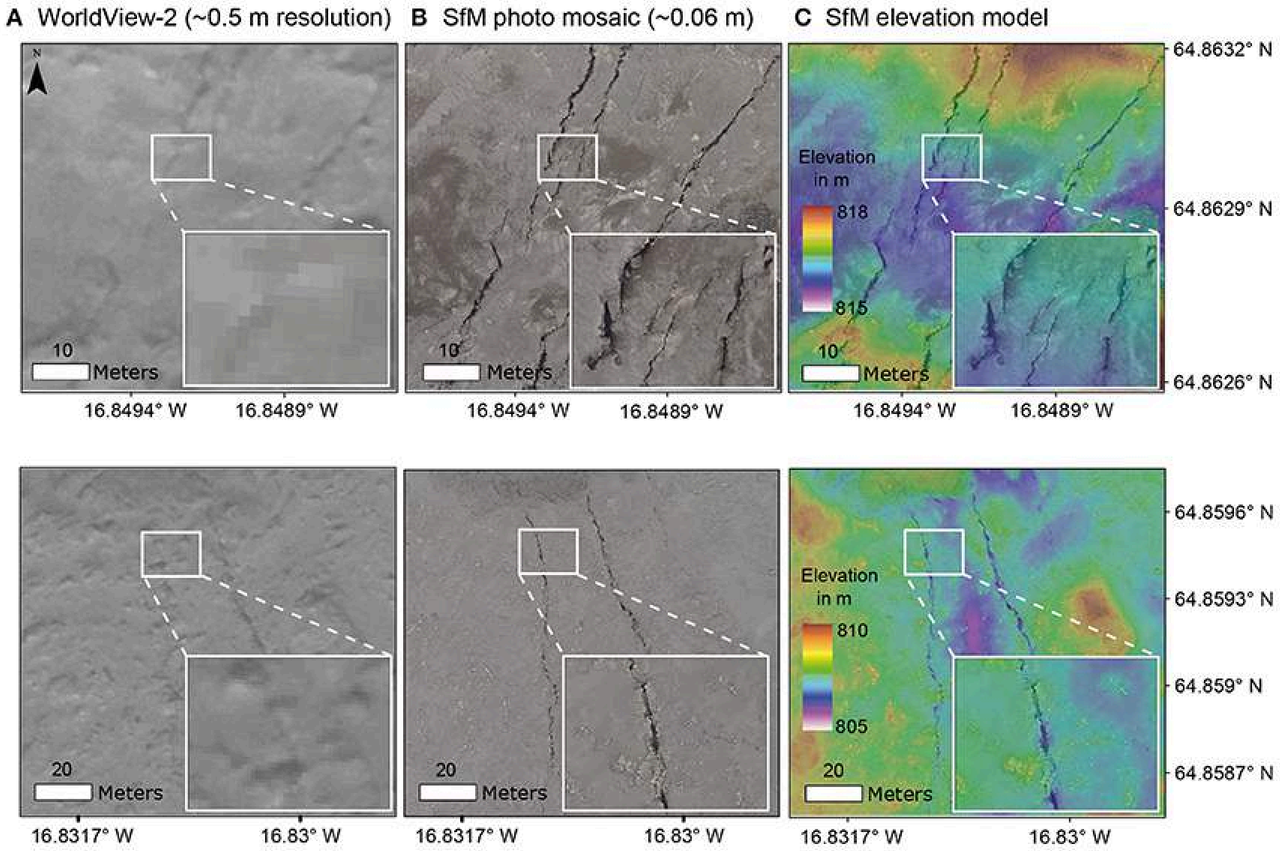

Figure 3.3: Resolution (A) WorldView-2 panchromatic data with a spatial resolution of ~0.6 m, (B) UAV-based SfM photo mosaic with a resolution of 0.067 m, and (C) UAV-based photo mosaic draped over the DEM obtained from SfM. Locations are inside areas a1 and a2 in Figure 3.4B. The upper row (area a1) shows the fracturing close to the 2014 Holuhraun eruption site at the western graben fault; the lower row (area a2) shows the fracturing at the eastern graben fault.

The data collected from satellite images, UAV photographs and TLS produced a very high-resolution topography database, slope maps and aerophoto mosaics that allowed us to perform structural mapping and directly measure displacements at fracture traces (Figure 3.4). The mosaic was first visually analyzed in order to locate compressional or restraining structures. Then, the horizontal displacements in the photo mosaic were measured. We identified locations where fault traces were clearly detectable and displacements could be quantified. By linking several cohesive points on either side of the fractures using polylines (providing start and end coordinates) in ArcGIS, we were able to determine the amount and directions of opening (heave). Comparing these data to the azimuths of the respective fracture segments allowed us to assess whether their horizontal slip was right-lateral or left-lateral. Vertical displacements (throw), in turn, were assessed using our high-resolution DEMs, based on profiles that were normal to the observed fractures. The strike directions and lengths of fractures were obtained in a similar manner and were then sampled at intervals of 5 m.

3.2.5 Data Limitations

The densities of TLS point clouds strongly depend on the distance to the scanning system and the chosen scan frequency. We observed a density of 2,000 points per m^2 in the near-field region of our scans but a density of only 0.1 points per m^2 at the maximum distance of our scans. This difference may become an issue when attempting to automatically align different scans. In particular, because the density in overlapping areas (e.g., in the area of the 5th September

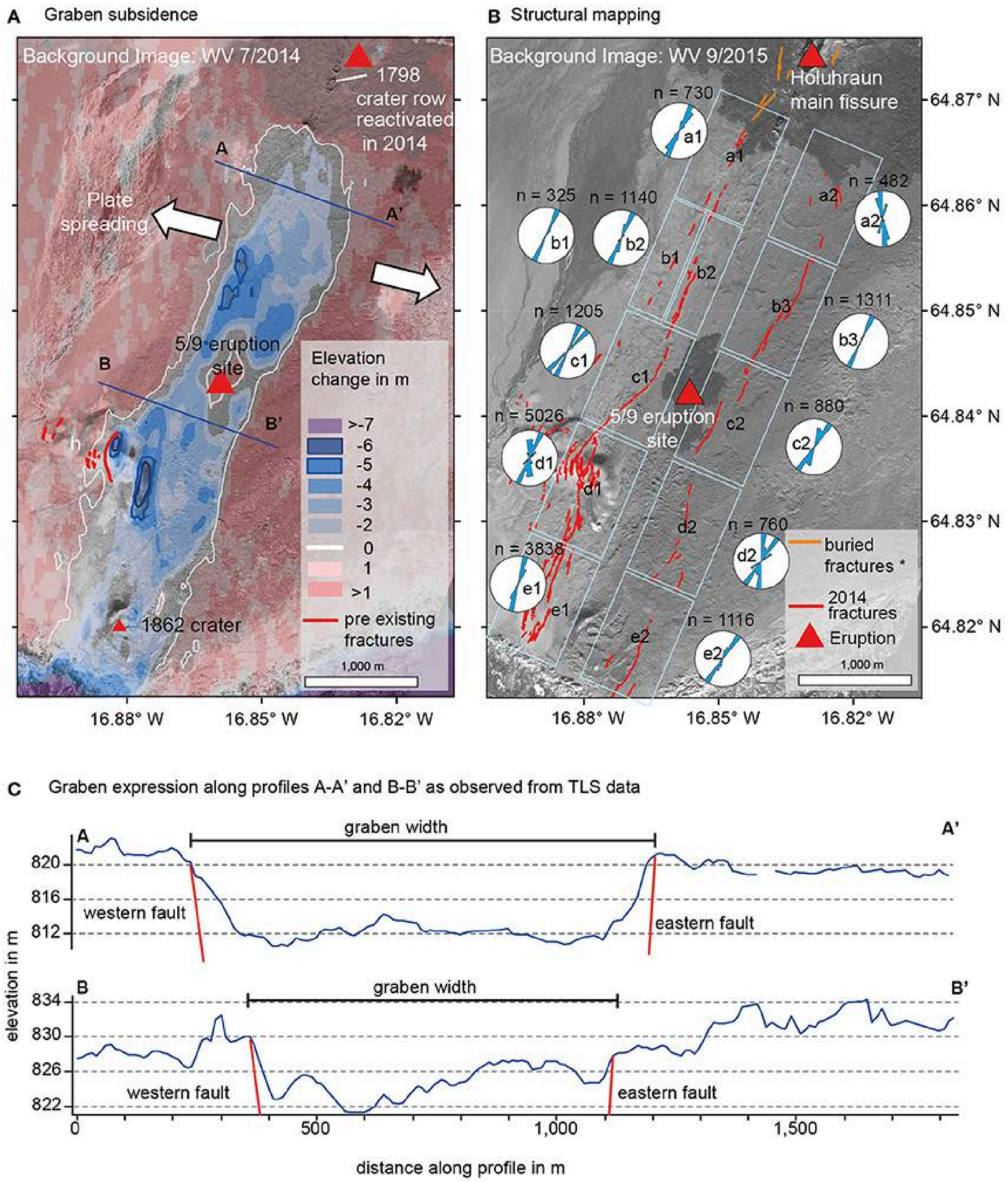

Figure 3.4: Graben subsidence and structural mapping of (A) uplift (in red) and graben subsidence (in blue) based on a comparison of TanDEM-X data from November 2011 and September 2014. The background image is a WorldView-2 image acquired prior to the eruption in July 2014. Note that the location of the old crater row in the north corresponds exactly to the site of the 2014 Holuhraun fissure. The red lines indicate fractures that were identified using pre-eruptive WorldView-2 data. The average plate spreading direction (104° azimuth) is indicated by white arrows. (B) Structure lineament mapping results and associated strike directions of fractures, grouped (light blue boxes) along both boundary faults on either side of the graben. The red lines indicate the newly formed fractures, as observed from WorldView-2 post-eruptive data (acquired in September 2015), and orange lines indicate the pre-eruptive fractures observed by Hjartardóttir et al. (2016). Note the hourglass-like fracture convergence at the 5th September eruption site and the fracture convergence toward the 2014 Holuhraun main eruptive site in the north. The strike directions of the fracture groups are shown by rose plots in 10 degree classes, weighted by fracture length, where n corresponds to the accumulated fracture segment length for this fracture group in m. (C) Graben profiles drawn normal to the graben along A - A' and B - B' display variations in graben width and shape. While the graben has a symmetric shape in the northern profile, it comprises a tilted block or half graben formation in the southern profiles, thus confirming that reactivation and higher deformation have occurred on the western fault.

eruption site) was very low, it was difficult to accurately align the different scans in these regions.

Structure from Motion (SfM) data must be acquired using proper acquisition geometries. Changing acquisition geometries may introduce perspective effects to the data, as was identified in region 3 (Figure 3.2D). Therefore, region 3 is not assessed further in the fracture displacement analysis. In general, the fact that SfM point clouds tend to bend at their edges must be taken into consideration. Nevertheless, in the central regions of the SfM point clouds, the accuracy is usually on the order of a few cm. The flight height of 100 - 150 m used for acquisition here is appropriate for covering large areas but limits the resolution and, thus, the accuracy of 3D model reconstruction. This limited resolution may become an issue when analyzing vertical objects, such as fracture traces. Therefore, our data allow us to only partly measure displacements in 3D.

3.3 Results

First, we provide a structural overview of the region; then, we detail its structural geology.

The WorldView-2 satellite imagery, as well as the elevation changes calculated from the data of the TanDEM-X satellite mission, reveal the clear structural boundaries of a graben system (Figure 3.4A). Comparing the WorldView-2 data set collected in 2014 (immediately prior to the onset of the seismic swarms preceding the Holuhraun eruption) to those collected in 2015 (6 months after the termination of the eruption) allows us to identify major fractures and distinguish between preexisting fractures and those that developed during the intrusion in 2014. On either side of the graben, graben bounding faults are expressed as single or multiple sub-parallel fractures. More fracture segments (260) were identified on the western graben fault (Figure 3.4B) than on the eastern fault (55). Here, single fractures have rather large throws (on the order of m) compared to those of multiple fracture arrangements. In the case of two parallel fractures, the throw at the fracture trace is usually small (<0.2 m), but the central regions of the blocks located in between these fractures exhibit bending and sagging. A dominant preexisting fault is located on a hill that is made of pillow lava rising above the Holuhraun lava field at the western graben fault (hill h in Figure 3.4A). At this location, steep scarps can be observed in the images (red lines in Figure 3.4A) obtained prior to the 2014 dike intrusion. These scarps deepened during the 2014 intrusion.

A comparison of the image quality and resolution of the WorldView-2 satellite data and the UAV data shows that the traces of major fractures can generally be identified in the WorldView-2 satellite data, whereas small-scale fractures with widths that are below 0.5 m cannot easily be identified. The UAV images allow us to not only identify more and smaller fractures (Figure 3.3) but also to measure the displacements and complexities of these fractures, as well as the morphologies associated with them. The UAV results are discussed in the following sections.

3.3.1 Topographic Expression

Changes in elevation observed in the near-field regions of the dike range from +1.5 m uplift outside the graben (Figure 3.4A) to -4 m slip for central parts of the graben, which locally even exceed -5 m, for instance north of the 5th September 2014 eruption site (red triangle in Figure 3.4A) and at the fractured hill in the southwest (h in Figure 3.4A). Generally, elevation changes appear to be concentrated on the western side of the graben, where slightly higher uplift and slip values are recorded. In contrast, the uplift outside the graben remains almost constant at 1 - 1.5 m in the near-field region of the graben, where variations in graben slip were observed from south to north along the graben. We note that due to the local scale analyzed in this study, a decrease in uplift with distance to the graben (cf. Sigmundsson et al., 2015) is not seen in Figure 3.4A. In terms of the dislocation recorded at the graben faults, which starts at -4 m at the edge of the glacier (S), the graben slip decreases to -3 m at the location of the 1862 crater (southern red triangle in Figure 3.4A). At the intersection with hill h (Figure 3.4A), the graben slip reaches an average value of 4.5 m and increases to the north of the 5th September eruption site, where the maximum slip values occur. Closer to the main eruption site, the graben slip decreases and finally reaches -1 to -2 m close to the main eruption site (N). Hence, the displacements of the graben faults decrease as the faults approach the main eruption site. At the second and smaller eruption site (5/9 eruption site in Figure 3.4B), the topographic changes are rather large.

On a local scale, the topographic expressions associated with the graben faults comprise restraining and releasing bends and push-up structures (Figure 3.5). In general, the UAV-based topographic data confirm that in the north, the topographic throw at the graben faults is relatively small and is generally below 1 m (Figures 3.5B,C). In turn, clear topographic steps are found in regions that are closer to the 5th September eruption site (Figure 3.5E). Interestingly, the widespread appearance of very local push-up structures occurs at sites where changes in azimuth can be identified (Figure 3.5D).

The topographic expression of the graben therefore varies on a larger scale (decreasing closer to the main Holuhraun eruption site) and on a local scale (at restraining bends). In summary, the analysis of topographic expressions reveals that the sections of the western graben fault display larger changes in elevation, which may mean that the reactivation of preexisting structures occurred on the western graben fault in a similar manner as that described above for the fractured hill (area 3).

3.3.2 Fractures and Their Azimuths

Comparing the WorldView-2 data (obtained before and after the eruption) to the SfM data reveals that the emergence of intrusion-related fractures occurred in 2014 (red lines in Figure 3.4B). Manually tracing these fractures clearly depicts the outline of the graben. These fractures are concentrated in the southwestern region of the study area. Here, we distinguish 260 fractures on the western side of the graben and 55 fractures on the eastern side of the graben. The total fracture segment lengths are 13.3 km on the western side of the graben and 4.6 km on the eastern side of the graben.

The fractures of the graben system have an average strike direction of N20°. Changes in azimuth were mainly observed (i) where fractures intersect with local topography on the western side of the graben, (ii) in the southern region of the eastern graben fault and iii) close to the Holuhraun main eruption site, where fractures on the western side of the graben are directed to the NE and fractures on eastern side are directed to the N or even NW. On the western side of the graben, the mean deviation from the general trend of the fractures toward the eruptive fissure is +12° (positive direction is clockwise); therefore, the fractures are rotated compared to the fracture segments located further south. On the eastern side, the trend of the fractures is rotated in an anticlockwise direction up to -60°. This creates an hourglass pattern, with varying strike directions on either side of the graben (Figure 3.4B). Because the center axis of the graben has a mean strike of N23°, the fractures identified in 2014 slightly deviate from that trend, as they record an average strike direction of N20°.

Additionally, although the 5th September 2014 eruption site is located in the center of a 600 m wide graben, the fissure of the Holuhraun main eruption site is located in the center of a narrower graben (260 - 400 m) that is only collinear with the western graben fault. Therefore, the

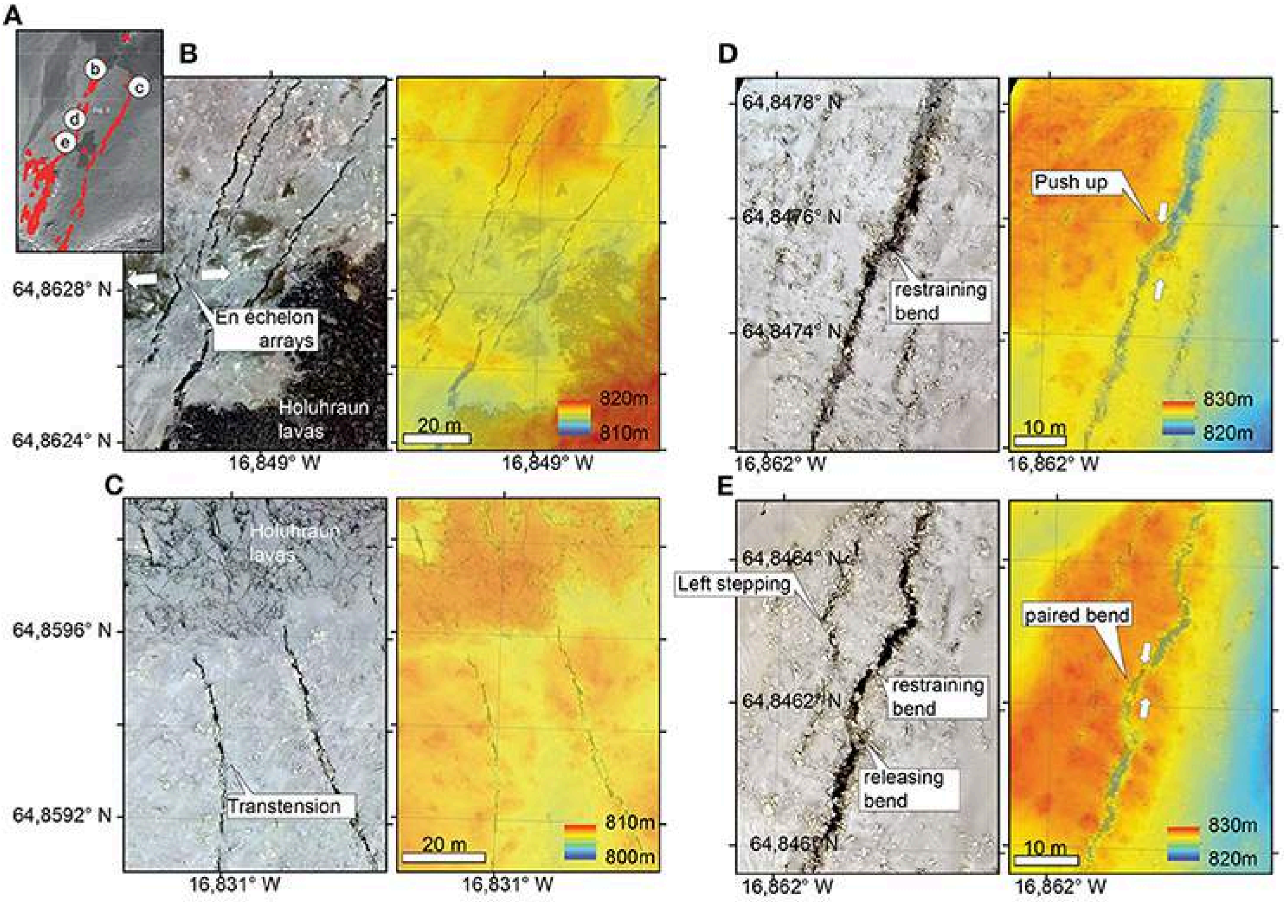

Figure 3.5: Local structural examples (A) Fracture overview map together with close-up view locations as shown in insets b-e (SfM photo mosaic and SfM DEM model). Red triangles show the 2014 Holuhraun and 5 September 2014 eruption sites. (B) Photo mosaic showing en echelon arrays of surface fractures commonly associated with strike-slip kinematics. The DEM shows no dominant vertical throw and the observed fractures mainly opened horizontally. (C) Curved fractures directed to the NNW and partly covered by lavas. Field data and aerophotos suggest a transtensional type of fracturing. (D) Local restraining bends lead to push-up structures that are visible in photo mosaic and DEM. (E) Local bending fracture traces lead to releasing bends and restraining bends as topographic complexities.

fractures of the western graben fault maintain a nearly constant azimuth (box a1 in Figure 3.4B), while fractures of the eastern graben fault display a counterclockwise curvature of up to -60°, with an azimuth that points directly toward the main eruptive fissure (box a2 in Figure 3.4B), thus again resembling an hourglass pattern close to the eruption site. The same trend can also be observed at the smaller eruption cones that are located at the intersection of a bent segment of the eastern fault and the fractures that are parallel to the main fissure (secondary fissure in Figure 3.6A).

Comparing the mean fracture azimuth (N20°), the mean rift axis (N25°) and the mean rifting direction (N104°) reveals that fracture patterns are not simply parallel to the rift axis, but are instead rotated with respect to the expected rifting trend. Fracture trends that are not simply perpendicular to the stretching vector have previously been identified as being typical products of oblique rifting in brittle-ductile systems (Tron and Brun, 1991); a similar conceptual model may thus apply here.

3.3.3 Horizontal Fracture Offsets and Strike-Slip Component

The obtained photo mosaics allow us to study the modes of opening in more detail by using structural geologic and kinematic criteria. In total, we identify 143 sites at areas 1a and 1b (Fig-

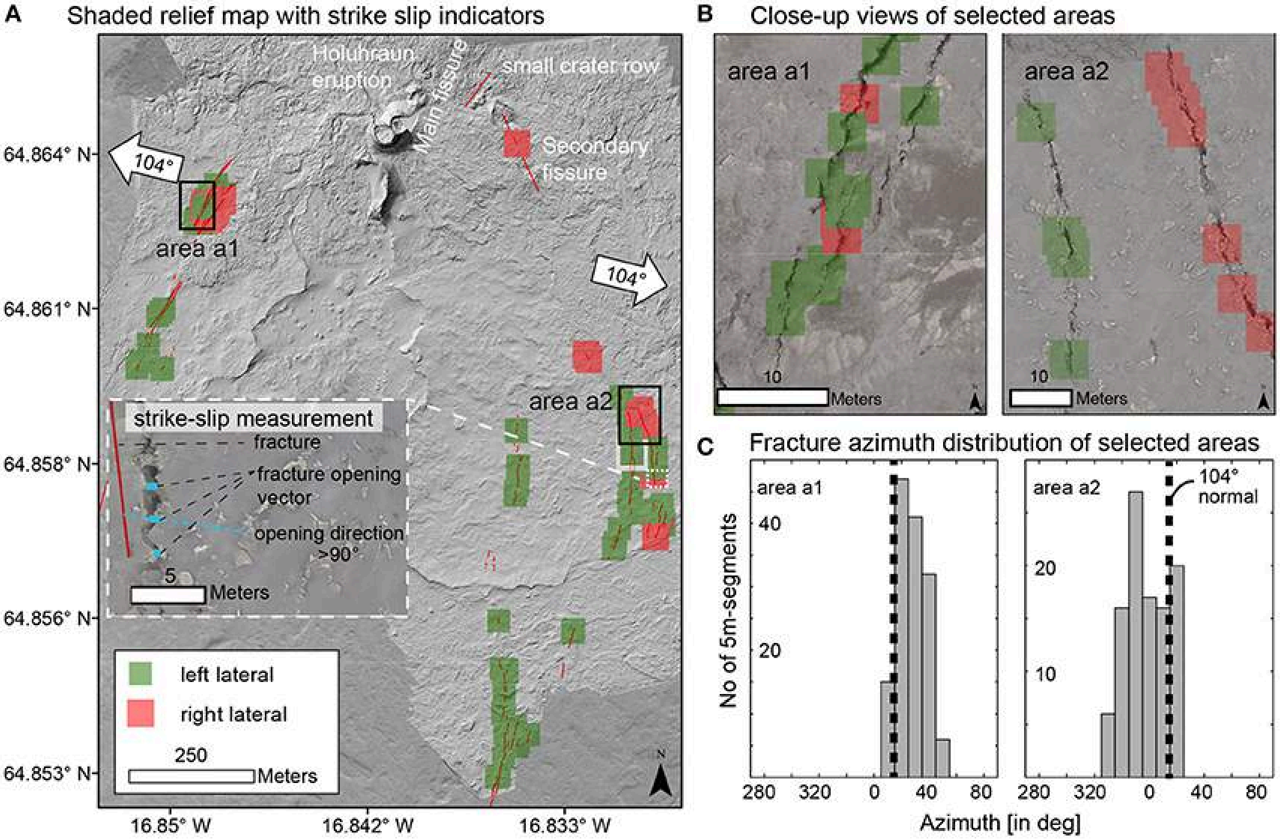

Figure 3.6: Assessment of strike-slip components (A) Strike-slip components measured at 143 positions, indicated by red and green boxes in areas a1 and a2 (Figure 3.4B), showing the dominance of left-lateral motion (green boxes). Right-lateral slip (red boxes) and tensile opening components (no color at fracture) can also be observed. Systematic analysis reveals the consistency of kinematics along distinct fracture traces as well as local complexities, such as opposite motions at adjacent fracture traces. The inset indicates how strike-slip was determined. (B) Close-up views of selected areas a1 and a2. Note that although both left-lateral and right-lateral components can be observed in our data close to this eruption site, the left-lateral transtensional mode is clearly dominant. (C) Histogram analysis and comparison of the strike directions of the two areas against the rift-normal direction; a uniform rifting of 104° is assumed.

ure 3.2D) where we could differentiate between faults with right-lateral and opening, left-lateral and opening and faults with purely extensional components (Figure 3.6). In transtensional regions located close to the main eruption site, 81 % of faults contain left-lateral components, 17 % contain right-lateral components, and 2 % do not exhibit clear strike-slip components. These results are in agreement with those of independent studies (Ágústsdóttir et al., 2016), as they reflect the presence of both left-lateral and right-lateral transtensional components at the surface, which Ágústsdóttir et al. (2016) observed at depth.

The spatial distribution of the identified transtensional fractures is not uniform. For instance, fractures located to the S and SE of the Holuhraun eruption site and near the lavas exhibit dominantly right-lateral and opening components (Figure 3.6B, area a2). Fractures located ~2 km to the south of the Baugur crater, in turn, exhibit dominantly left-lateral and opening modes (Figure 3.6A). Fractures located within the western graben show similar patterns, exhibiting right-lateral and left-lateral motions; however, they become dominantly left-lateral with increasing distance to the eruption site (Figure 3.6B, area a1). We find that surface fracture kinematics are strongly site-specific and that their correct identification depends on determining from which fracture branch of a specific graben segment the data were acquired.

Approximately 68 % of the identified faults that have a right-lateral component strike to the NW. Only 16 % of the faults that have left-lateral components strike to the NW, while most strike to the NE. This difference implies that strike-slip motion may be related to the average strike direction of its respective fracture segment. Using UAV photographs, we were able to determine the amount of opening occurring at tensional fractures, as well as the amount of strike-slip occurring at transtensional fractures. Measurements collected along profiles close to the 2014/15 eruption site indicate that the cumulative fracture opening measured throughout the entire graben is 3.8 m and that its cumulative strike-slip motion is ~0.4 m.

3.4 Discussion

The 2014/15 Holuhraun eruption was associated with a dike intrusion in a segment of a rift zone located between the central volcanoes of Askja and Bardabunga. This eruption caused extensive surface rupturing, with an average azimuth that is rotated with respect to the mean rifting direction of N104°E (Figure 3.6C). Details of these surface ruptures were investigated using satellite imagery, TLS and drone-based close-range photogrammetry, which revealed a locally complex pattern of surface fractures and delimited the extent of the graben above the inferred eruption feeder dike. We observed a non-uniform spatial distribution of strike-slip and opening mode components, as well as the presence of both left-lateral and right-lateral fault components, among which the former is dominant. Therefore, these results agree with those of seismic (Ágústsdóttir et al., 2016), geodetic and structural field studies (Ruch et al., 2016). Preexisting topography, earlier fault locations and the locations of eruption sites close to that of an eruption in 1797/98 produced highly variable transtensional displacement with primarily left-lateral strike-slip indicators. Before discussing the implications of this work and its relationship to those of independent studies further, we provide details about the limitations of the methods used here, the collected data and their analytical techniques in the following sections.

3.4.1 Limitations

Based on the analysis of these data, we identified a number of limitations that are further discussed here. The fractures identified using the WorldView-2 data are rather large, as the highest resolution of these data is ~0.6 m. In contrast, the drone-based data yield centimeter-scale resolutions but are limited in that they could not be used to map the entire area to the south of the 2014/2015 Holuhraun eruption site. We selected key areas close to the two eruption sites that were systematically overflown and where closer studies of the kinematics could also be performed. As a consequence, large parts of the graben fault systems were not imaged by our drone cameras. We solved this problem by combining the drone-based results with a TLS campaign in which the TLS instrument with a scan range of up to 6 km provided the reference data. By doing so, we were able to generate a topographic data set with a resolution of 10 m throughout the graben region and to obtain close-range drone-based mosaics and DEMs with resolutions ranging from 0.067 to 0.19 m at selected key areas. Nevertheless, the resolutions of the drone-based data are 8--180 times higher than those of the satellite-based mosaics and DEMs derived from the WorldView and Tandem-X data sets, respectively.

During our field observations, we walked in between fractures and realized that fine-grained, wind-blown sand often partially covered or obscured fractures. The analysis of additional photographs that we acquired from an airplane during the eruption reveals that even more fractures were initially present in this region (Figure 3.7). Specifically, small-scale fractures that are clearly traceable in aerial images from September 2014 appear only as isolated sinkholes and short fractures in UAV images from August 2015. Therefore, we reiterate that the timing of UAV mapping projects is crucial for obtaining complete structural analyses and that rapid

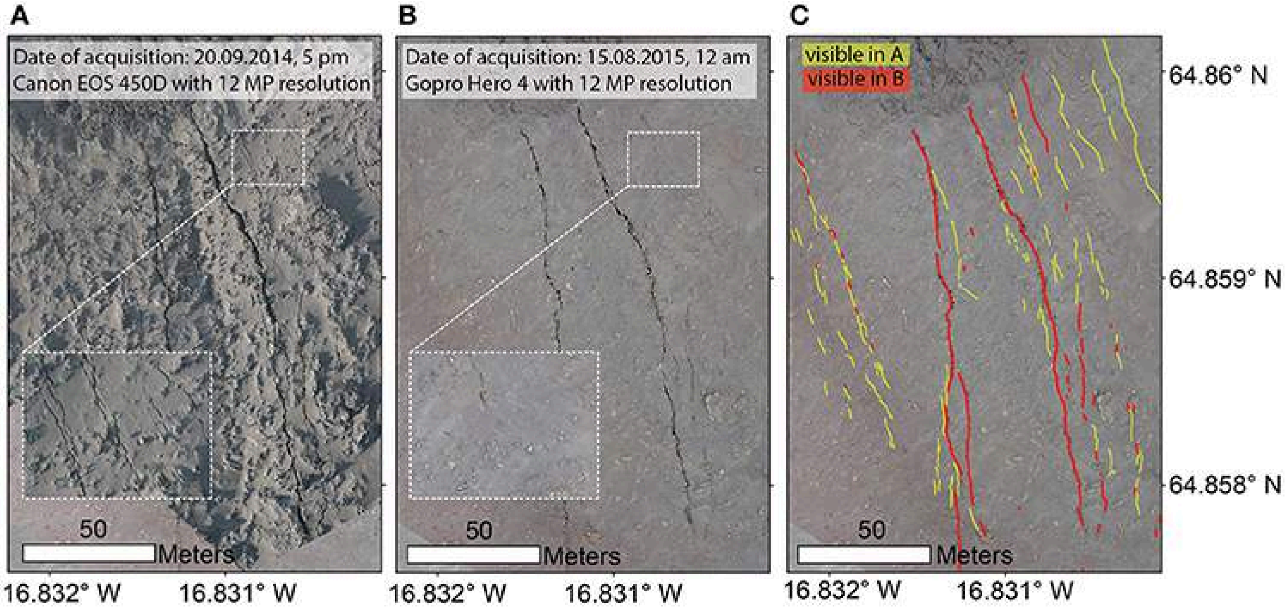

Figure 3.7: Example of limitations (A) Close-range aerial image taken during the eruption in September 2014, showing multiple small-scale fractures near the two main larger fractures. Image taken using hand held digital SLR camera with 16 megapixels in the early morning hours. (B) UAV camera images used in this study show larger fractures in detail; however, small-scale fractures are hard to identify. Image taken using GoPro camera at noon. Differences between (A) and (B) are due to camera type, time of image acquisition, and time lag between fracture formation and image acquisition. (C) Lineament map of the two images illustrates differences. Especially in small-scale fractures, local sinkholes and disconnected fractures are predominant, while large parts of the fractures are obscured and hidden by fine-grained deposits (i.e., ash and sand).

UAV-based campaigns are needed immediately following eruptions. Therefore, although drone-based morphological and structural mapping is a highly efficient tool for the analysis of small areas, acquiring data directly after or even during an eruption could yield even better results and could be used to analyze temporal changes in the years following an eruption. However, these temporal changes, which are also associated with the cooling of magma bodies, were not the focus of our field campaign.

3.4.2 Graben Expression and Vertical Throw

Due to the large dimensions, a good overview of the morphological expressions of the graben is given by satellite-based DEMs, such as those that were earlier presented (Floricioiu et al., 2015; Rossi et al., 2016) or in our study. Given the identified reactivation of preexisting faults (Ruch et al., 2016), we can only speculate about their offset prior to our measurement campaign. Reactivation has played an important role, as is evidenced by the fact that the eruption occurred at exactly the same site as an earlier eruption, as well as the fact that the largest fault offset occurred at exactly the same site as those of earlier faults at the hill in the south. The graben has an average strike of 23°, which coincident with the general strike directions of fissures in the Northern Volcanic Zone. In comparison to the mean spreading direction of N104°, the graben is non-normal to the tectonic trend expected for a pure rift opening. The subsidence area of the graben is clearly bounded by fracture sets on both of its sides; it also exhibits variable widths, ranging from <400 m to more than 1,000 m (Figure 3.4A). Starting in the south, with a width of 900 m, the subsidence area of the graben increases slightly toward the north, where it reaches a maximum width of 1,100 m at its intersection with a hill in the southwestern region. To the north of the hill, the subsidence area of the graben narrows and reaches a local minimum of ~600 m at the 5th September 2014 eruption site. Assuming that the dike location did not change substantially following the formation of the graben faults, this width change may suggest

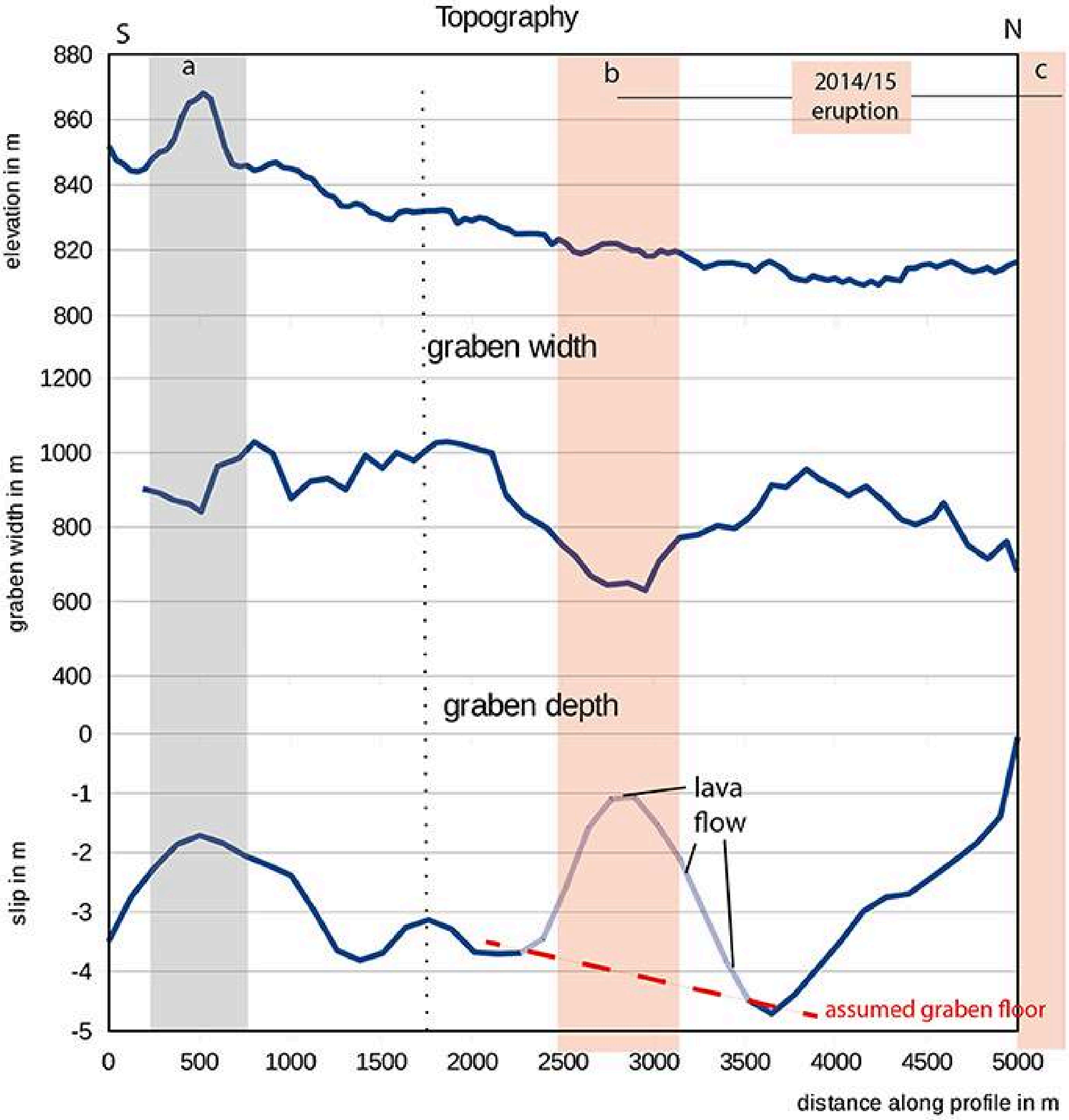

Figure 3.8: Comparison of topography and relevant graben parameters The elevation profile was drawn in the center of the graben from south (edge of the glacier) to north (Holuhraun eruption site). Graben depth and width were measured along parallel profiles (at a distance of 100 m from each other), normal to the graben. Area a depicts the location of the 1862 crater, b depicts the location of the 5th September 2014 eruption site and c depicts the location of the Holuhraun main eruption site. The influence of the upward migrating dike segment at location b is clearly visible.

that the vertical flow of magma occurred from a dike at a depth of several hundreds of meters extending to the surface vents. Further north, between the two eruption sites, the width of the graben subsidence area increases again to more than 1,000 m. Next, moving toward the main fissure in the north, the fault systems bend and cause the graben to narrow to widths of 400 m or less. The narrowing of the graben near the eruption sites resembles an hourglass pattern and may be related to the changing geometry or depth of the magma feeder or the depth of the dike tip. The latter could strongly influence the geometry of the graben (Figure 3.8). A shallower dike segment would locally narrow the graben and would likely be associated with an increasing cumulative throw. However, while we do observe a narrowing in the width of the graben, we find that the fault throw is only ~1--2 m and is therefore relatively small close to the main eruption site (N). Further south, at the 5th September eruption site, we observe a different fault throw pattern, which increases to over 4.5 m and locally reaches 6 m. The vertical throw therefore ranges from 1 to 2 m in the northeastern region of the study area to ~6 m at the 5th

September eruption site; we speculate that this reflects the complex deviation of the upper edge of the propagating dike. Finger-like magma paths originating from a deeper dike could potentially produce less surface deformation and fault throw than a continuous dike opening at a shallow depth would create (Figure 3.9). The presence of finger-like connections linking surface vents to a crustal dike was also recently suggested based on the analysis of tremor data (Eibl et al., 2017a) collected near the Holuhraun eruption site.

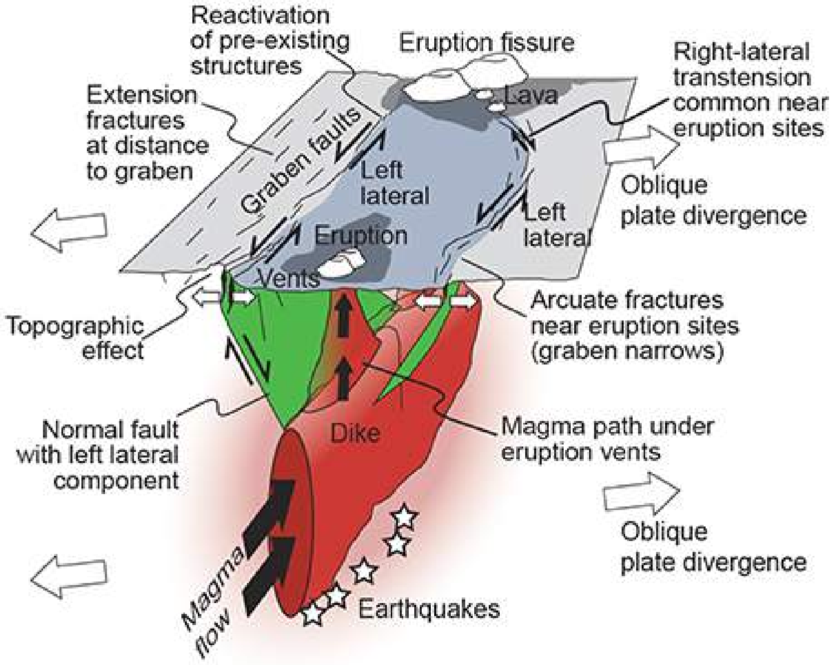

Figure 3.9: Sketch illustrating the structural relations at the Holuhraun eruption sites Graben subsidence is identified above the feeder dike (red color), and delimited by graben faults (green color) and smaller fractures at distance (black lines). At the surface, the graben faults show transtensional dislocations with predominantly (>80 %) left-lateral component, which is similarly identified in seismic focal mechanisms (white star symbology) during the dike intrusion at depth (Ágústsdóttir et al., 2016). Near the surface, the graben faults appear near vertical in dip, and show large slip and splays close to pre-existing topographic highs ("topographic effect") and reactivation of other pre-existing structures and weak zones (e.g., associated with the 1797/98 vents in the north). The strike variation of graben faults show convergence toward eruption sites, yielding an arcuate expression, often associated with en-echelon arrays and step overs. This hourglass fracture convergence toward the eruption sites leads to fractures are rotated with respect to the plate divergence direction, so that they have a right-lateral component. Changes in the fault strike and formation of arcuate graben faults and an hourglass appearance close to the eruption sites are allegedly associated to a change in dike geometry at depth, either due to the presence of a locally shallower dike, or the establishment of a conduit-like magma path feeding the eruption vents, as suggested in Eibl et al. (2017a).

3.4.3 Fracture Azimuth and Mode Changes

Changes in the azimuths and numbers of fractures have been demonstrated in regions where fractures interact and change their azimuthal directions toward topographic heights or volcanic edifices (Belousov et al., 2005; Kervyn et al., 2009). Fractures located closer to the Holuhraun eruption site display complex distributions of mixed modes, where the sinistral direction is generally dominant. As these complexities are observed close to the Holuhraun eruption site, the propagation and rise of magma could have led to the formation of one or more sets of fractures. During the further propagation of the feeder system or the drain back and cooling of the dike, fracture modes recording different senses of motion could have developed.

We identified that 81 % of the faults in regions 1a/b contain a left-lateral component and that 17 % contain a right-lateral component. These results are in agreement with the inferred seismic focal mechanisms of earthquake events during the dike intrusion identified in this region (Ágústsdóttir et al., 2016), of which 85 % are left-lateral and 15 % are right-lateral. However, our results are only locally representative, as we did not analyze all of the eastern and western fracture systems; additionally, in many cases, surface ruptures were too intense to allow for the identification of any distinct cohesive points on either side. However, the surface expressions of the fracture kinematics identified from our drone data match the seismic observations, despite the fact that the seismic data mainly represent the deeper proportions of the intruding dike whereas we can only measure the surface effects. This similarity suggests that the stress conditions and rupture processes at depth might be comparable to those observed at the surface.

In addition, we observed a change toward more right-lateral components in fractures located close to the main 2014/15 Holuhraun eruption site, which we explain by changing strike directions.

Although displacement components at the graben faults were identified using geodetic and structural field data (Ruch et al., 2016; Sigmundsson et al., 2015), as well as the results of seismic studies (Ágústsdóttir et al., 2016), some differences are evident. For example, while geodetic studies suggest that an oblique opening recording dominant left-lateral motion occurred throughout the study area, with only minor right-lateral events (Ruch et al., 2016; Sigmundsson et al., 2015), earlier seismic studies (Ágústsdóttir et al., 2016) suggested that this region records the presence of both left-lateral (85 %) and right-lateral (15 %) kinematics. Our results record both opening and dominantly left-lateral motions, as well as a locally increased right-lateral component. Therefore, the results of these three studies agree well with each other. The observed differences are likely related to the different depths from which these data were collected. While seismic data mainly originate at depths of 5 to 8 km, our observations and those of Ruch et al. (2016) are limited to the surface, where the horizontal component (lateral widening) also becomes relevant. Ruch et al. (2016) used these surface observations to constrain a dike dislocation model, thus indicating that the large fault throw at the surface is linked to the opening of a large dike at shallow levels. In our study, we also find that fault throw and fault width differ from those in their surrounding areas at the 5th September eruption site. Therefore, the interpretation that fault throw is larger closer to the eruption site may be biased by the larger dike width. Seismic tremors marked the arrival of the dike in the shallow crust, as was recently illustrated by Eibl et al. (2017a).

GPS and direct point wise field measurements are advantageous because they produce high-precision, locally robust data. The SAR technique yields spatial measurements of hundreds of thousands of points with a pixel scale of several meters. Our study demonstrates the added value of using high-resolution near-field photogrammetry derived from UAV platforms with centimeter-scale resolutions, which can be used to identify local deformation structures. Ideally, a combination of these data is realized and obtaining consistent results is best, as is demonstrated by the comparison of our data to those of previous studies.

Geodetic data suggest a mean dike opening of 4.5 meters and a mean left-lateral component of 1 m, which compare well to the identified historical slip deficit values of 4 and 0.7 m, respectively (Ruch et al., 2016; Sigmundsson et al., 2015). Our results indicate a fracture opening of up to 3.8 m and recorded a strike-slip of ~0.4 m. The fracture opening and strike-slip kinematics identified in our data somewhat underestimate those estimated by the analysis of geodetic data, which may be due to the sedimentation and coverage of a number of surface fractures (see also Figure 3.7). Minor fractures may be lacking, which may explain the 20 % difference between our results and those obtained from the analysis of satellite geodetic data.

However, the quantification of strike-slip values must be handled with care, as measurements obtained directly at the fracture trace are not very distinct and may even lead to misinterpretations. Underestimated values may be produced because we observe processes happening in very near-field regions, whereas satellite geodesy techniques, such as InSAR (e.g., Sigmundsson et al., 2015), observe mid- to far-field displacement. Techniques, such as pixel tracking allow faults in both the far field and the near field to be analyzed, as was shown for the Holuhraun eruption by Ruch et al. (2016). As the fault slip values given by Ruch et al. (2016) are comparable to those determined using the drone-based data we presented, their results and implications appear to be sound and valid. We note that our interpretations of only the brittle deformation component at the surface are simplistic, whereas the entire deformation regime encompasses more complex elastic-brittle-ductile behavior with different relevance at different depths. This depth-dependent complexity may also have contributed to the production of fractures during the eruption.

Nevertheless, our results are consistent with those of geodetic and historical investigations indicating that the amount of fracture opening is ~5 - - 6 times larger than the amount of strike-slip motion. We note that our results suggest that the identification of the opening and strike-slip motion strongly depend on the location where measured and therefore close-range photogrammetric data can be applied to contribute to the analyses of local geologic processes.

3.4.4 Reactivation

The presence of preexisting fractures played a significant role during the 2014/2015 Holuhraun eruption, as was previously demonstrated by the analysis of satellite and airborne imaging data (Hjartardóttir et al., 2016) and geodetic and field data (Ruch et al., 2016). The 2014 Holuhraun eruption occurred exactly where a major eruption occurred in the 1797; this older crater row is also visible in the satellite image taken before the 2014 eruption (Figure 3.4A). Earlier studies (Sigurdsson and Sparks, 1978) suggested that the so-called Holuhraun 1 or Kvislahraun lavas formed during an eruption originating in the Askja volcanic system. Later workers propose, based on the analysis of the geochemical composition of the lavas, that Holuhraun 1 is likely to have formed during two separate eruptions and are rather related to the Veidivötn volcanic system (Hartley and Thordarson, 2013). Structurally, as proposed by Hjartardóttir et al. (2016), the inferred 2014/2015 dike plane is in line with these older lineaments. The old Holuhraun 1 crater row was made up of at least ten small vents that were covered by the 2014/2015 Holuhraun eruption. These old cones did not lie along a straight line, as our data and those of previous studies demonstrate (Ruch et al., 2016). Instead, the old crater row exhibits a segmented structural orientation. Therefore, the graben fault systems and eruption fissures could display a similar segmentation that might be predisposed to existing structural weaknesses.

3.5 Conclusions

The 2014/2015 Holuhraun eruption site exhibits complex topographic and structural surface expressions that were analyzed by combining satellite imagery, TLS and UAV-based close-range photogrammetry. We derived a high-resolution DEM and photo mosaic data set that allowed us to identify sites of fault reactivation and the delineation of structures that formed during this eruption and its preceding dike intrusion. We find that the azimuths of fractures vary locally and that the fracture sets record transtensional motion, with 81 % of the fractures exhibiting a left-lateral component and 17 % of the fractures exhibiting a right-lateral component. These results are in agreement with those of independent geophysical monitoring and modeling studies, which suggest that the surface fracture expression is in agreement with indirect constraints at depth. We find an hourglass-shaped narrowing of the expression of the surface fractures close to the eruption sites, which might be interpreted as the shallower upper edge of a feeding dike at a depth of several hundred meters. We also identify a larger fault throw closer to the 5th September eruption site, which might be associated with a larger dike opening. Moreover, this work demonstrates that the flexible use of UAV techniques, together with the use of other remote sensing methods, can be applied to study large areas. Additionally, this work demonstrates that the rapid implementation of campaigns can be used to obtain high-resolution imagery of the kinematics of volcano-tectonic events.

Author Contributions

DM collected the helikite data, performed the analysis on data and led the writing of the manuscript. TRW collected multicopter data and analyzed data, and coordinated writing of the manuscript. AS collected and processed TLS data. BS collected drone data. TW collected and processed the dGPS data. MG was involved in data interpretation and the writing of the manuscript. TD contributed by airborn photography and visual descriptions of the event.

Conflict of Interest Statement

The authors declare that the research was conducted in the absence of any commercial or financial relationships that could be construed as a potential conflict of interest.

Acknowledgments

This work contributed to and was partially supported by the FUTUREVOLC project. We especially thank IMO for releasing detailed monitoring information from the Holuhraun eruption. Financial support came from an expedition fund of the GFZ Potsdam. This is a contribution to VOLCAPSE, a research project funded by the European Research Council under the European Union's H2020 Programme/ERC consolidator grant ERC-CoG 646858. The TanDEM-X data analysis in this work is considered to be a contribution to the Helmholtz Alliance EDA. We thank Armann Höskuldsson for support during our field work. Moreover, we thank the DLR for providing the TanDEM-X data set that was used to derive a topographic base map of the region.

Chapter 4

Multiple coincident eruptive seismic tremor sources during the 2014 - 2015 eruption at Holuhraun, Iceland

Abstract

We analyze eruptive tremor during one of the largest effusive eruptions in historical times in Iceland (2014/2015 Holuhraun eruption). Seismic array recordings are compared with effusion rates deduced from Moderate Resolution Imaging Spectroradiometer recordings and ground video monitoring data and lead to the identification of three coexisting eruptive tremor sources. This contrasts other tremor studies that generally link eruptive tremor to only one source usually associated with the vent. The three sources are (i) a source that is stable in back azimuth and shows bursts with ramp-like decrease in amplitude at the beginning of the eruption: we link it to a process below the open vents where the bursts correlate with the opening of new vents and temporary increases in the lava fountaining height; (ii) a source moving by a few degrees per month while the tremor amplitude suddenly increases and decreases: back azimuth and slowness correlate with the growing margins of the lava flow field, whilst new contact with a river led to fast increases of the tremor amplitude; and (iii) a source moving by up to 25° southward in 4 days that cannot be related to any observed surface activity and might be linked to intrusions. We therefore suggest that eruptive tremor amplitudes/energies are used with caution when estimating eruptive volumes, effusion rates, or the eruption explosivity as multiple sources can coexist during the eruption phase. Our results suggest that arrays can monitor both the growth of a lava flow field and the activity in the vents. [1]

Plain Language Summary

We analyzed a type of earthquake that is long lasting, has no sudden start but is slowly getting stronger, and is recorded during eruptions. This so-called tremor is usually thought to be merely caused below the vent where the magma moves up toward the surface. Therefore, it was, for example, used to estimate how much magma and how fast the magma erupts, how high, and where the erupted magma would go. However, using a dense network of seismometers at only 15 km distance from the erupting magma-during the Holuhraun eruption in Iceland in 2014/2015 - we found three areas where tremor is caused. These are (i) below the vent where the magma moves up toward the surface, (ii) at the cooling sides of the growing lava flow field, and (iii) probably at less than 2 km depth where the Earth's crust breaks and magma moves

---

[1] Originally published as: Eibl, E. P. S., C. J. Bean, I. Jónsdóttir, A. Höskuldsson, T. Thordarson, D. Coppola, T. Witt, and T. R. Walter (2017), Multiple coincident eruptive seismic tremor sources during the 2014–2015 eruption at Holuhraun, Iceland, J. Geophys. Res. Solid Earth, 122, 2972–2987, doi:10.1002/2016JB013892

horizontally. We warn other scientists to be careful when using the tremor amplitude but also show that we can with our instruments watch in real time where the lava flow field is growing.

4.1 Introduction

Volcano monitoring commonly includes seismological records and allows the distinction between different types of signals that are characteristic of volcanoes. A long-lasting, emergent signal-tremor-is usually observed during eruptions (McNutt, 1992) and often starts and ends with the extrusion of magma (Battaglia et al., 2005; Langer et al., 2011; Soosalu et al., 2005). However, the precise mechanism that generates eruptive tremor is poorly understood because of limited on-site observations and measurements of sufficient quality (Langer et al., 2011; Senyukov et al., 2015) and poor constraints on tremor locations especially at depth.

Published tremor source models can be broadly grouped into four different classes: (i) the normal modes of a linear oscillator with open or closed ends are excited (e.g., Chouet, 1988), (ii) fluid flow excites the conduit walls (e.g., Julian, 1994), (iii) evenly spaced pulses continuously repeat (e.g., Hotovec et al., 2013; Neuberg et al., 2000), and (iv) hydrothermal boiling (e.g., Cannata et al., 2010; Leet, 1988).

As an attempt to find a possible tremor model, the tremor is usually correlated with other direct observations. For example, a correlation between tremor amplitude and the height of lava fountains (Alparone et al., 2003; Koyanagi et al., 1987; McNutt, 1987) has been attributed to a resonating source. Tremor generated by fluid flow was assumed when the tremor amplitude correlated with the gas content in the magma (Tárraga et al., 2014), the constriction of the conduit (Tárraga et al., 2014) or conduit geometry (Julian, 1994), or the intensity of the eruption (Belousov et al., 2015; Falsaperla et al., 2005; Julian, 1994; Langer et al., 2011; Soosalu et al., 2005; Tárraga et al., 2014). For correlations of the tremor amplitude and SO2 emission rate (Nadeau et al., 2011; Palma et al., 2008) or with infrasonic pressure (Ripepe et al., 2009) or correlations of tremor bursts and spattering episodes (Coppola et al., 2005; Patrick et al., 2011b) the tremor source was related to boiling activity.

While correlations were established in the above mentioned cases, this was not always the case. Eaton et al. (1987) found evidence that tremor amplitude and fountain height did not correlate except for times when the fissure was forced open at the beginning of an eruption episode. Similarly, Aki and Koyanagi (1981) observed a high correlation between tremor and volume of erupted material merely at the beginning of an eruption. Subsequently, Aki and Koyanagi (1981) described that the tremor amplitude decreased while the amount of erupted material remained high. Such a lack of correlation might be due to more than one simultaneously active tremor source, as Battaglia et al. (2005) suggested at Piton de la Fournaise based on the tremor locations they derived using an amplitude-based location method. Other studies do not attempt to resolve the tremor source model but focus more on forecasting/monitoring eruptions. McNutt (1994), for example, suggested the use of the tremor amplitude in order to estimate the size of an eruption and the amount of ash that will be ejected (see also Bernard et al., 2016). This idea is supported by studies suggesting that the tremor amplitude or energy and the effusion rate are linked (Battaglia et al., 2005; Coppola et al., 2009; Falsaperla et al., 2005; Koyanagi et al., 1987). However, others like Coppola et al. (2009) and Allard et al. (2011) also find that high tremor amplitudes occur when the magma discharge is low (<0.3 m^3/s) and link this to a change in eruptive style.

Here we present the eruptive tremor that accompanied the 2014–2015 fissure eruption at Holuhraun, fed from Bárðarbunga volcano in Iceland (Sigmundsson et al., 2015). The tremor data were recorded with a seismic array at about 15 km distance from the fissure (Figure 4.1) and compared to effusion rate estimates derived from Moderate Resolution Imaging Spectroradiometer (MODIS) sensor, lava fountain height measurements as derived from video records, and the growing lava flow field.

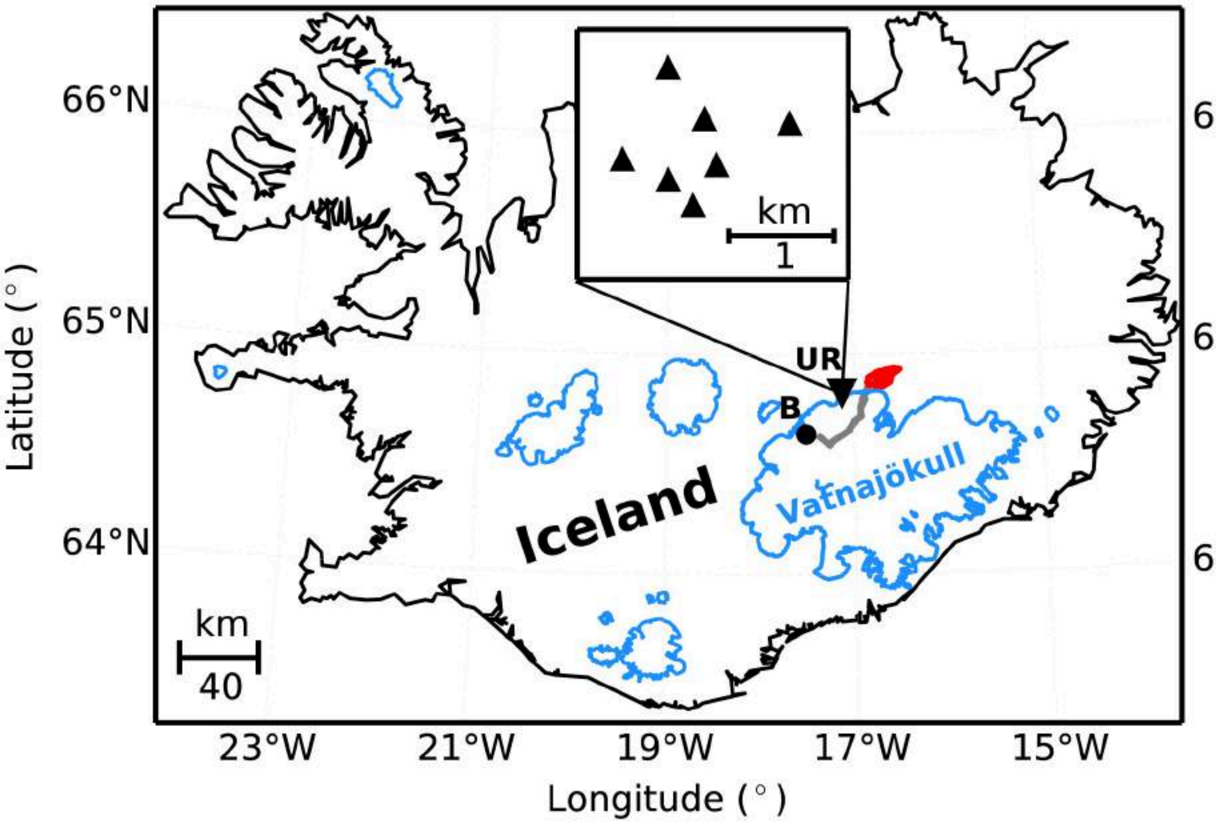

Figure 4.1: Geometry (inset) and location of seismometers arranged as a seven-element array UR northwest of Vatnajökull glacier, Iceland Glaciers (blue), the 2014 formed dyke segments as described in Sigmundsson et al. (2015) (grey), and the erupted lava flow field in Holuhraun (red) and Bárðarbunga volcano (B, black dot) are marked.

4.2 Overview of the Eruption

4.2.1 General Overview of the Fissures

From 16 August 2014 seismicity at 3 to 8 km depth propagated 48 km from beneath the ice-covered Bárðarbunga volcano first toward the southeast then north-northeast (Sigmundsson et al., 2015). At 0:02 UTC on 29 August a 4 h long eruption started near the northern end of this migrating seismicity at Holuhraun - about 5 km north of the glacier's northern rim. On 31 August 2014 a fissure opened at the same place, with lava production that continued for 6 months until 27 February 2015. Additionally, a new fissure opened beneath the glacier on 3 September (Eibl et al., 2017b) and 2 km north of the ice on 5 September. The latter eruption was detected at 7:00 UTC by a news reporter and ended in the afternoon of 7 September. The vigour of the activity at the fissure from 5 to 7 September was much less than on the main vent system. A brief overview is given here of the evolution of the vent activity and the progressive growth of the lava flow field.

4.2.2 Vent Activity

The eruptions on 29 and 31 August began along a 600 m and 1.9 km long fissure, respectively (Hjartardóttir et al., 2016). They started with a continuous, aligned curtain of lava fountaining (Thordarson et al., 2015) with higher activity on the southern and middle parts of the fissure. On 1 September the activity on the fissure began to localize along specific vents. By 2 September the activity was concentrated on the vents named Norðri and Suðri located on the northern and southern end of the original fissure as well as the vents Heimasætan and Baugur situated along

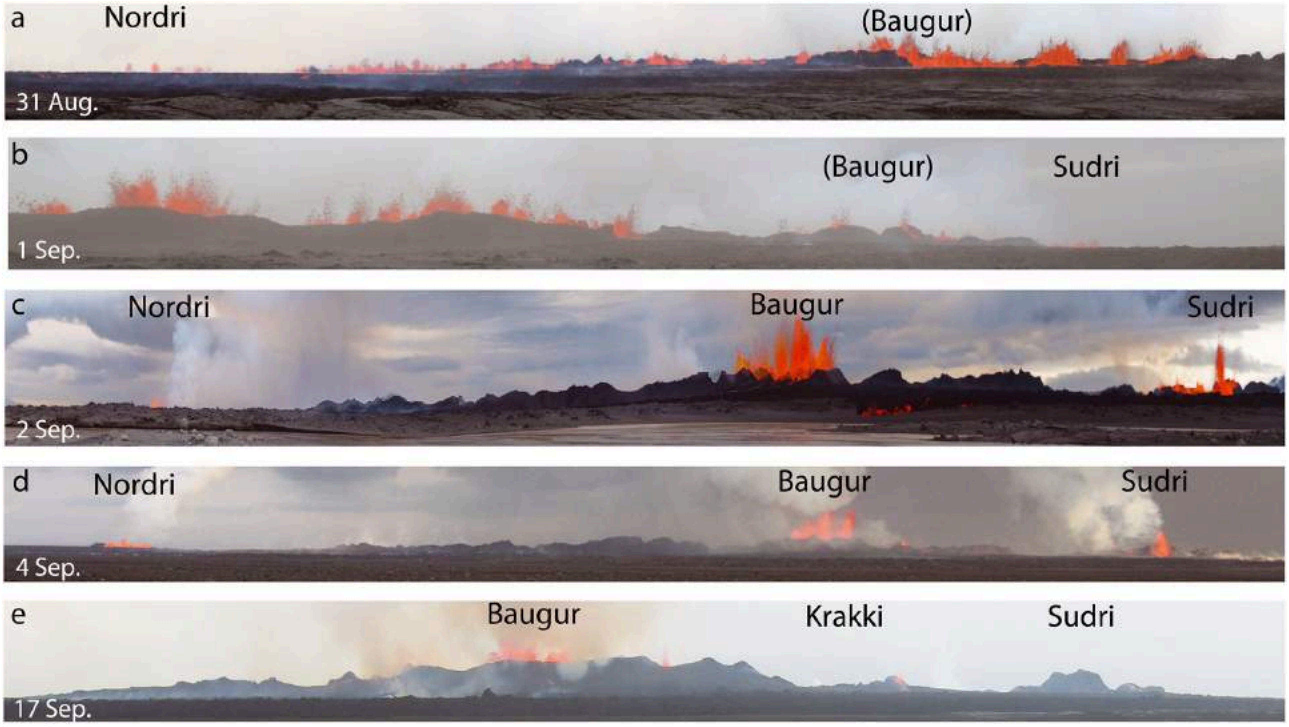

Figure 4.2: Vent activity along the fissure viewed from the west between 31 August and 17 September 2014 For an overview of vent locations and geometries see Figure 4.3. (a) On 31 August the activity is continuously visible along the fissure. The southern end is not shown. Photo: Ármann Höskuldsson. (b) On 1 September the activity along the fissure started to focus. The northern end is not shown. Photo: Johanne Schmith. (c) On 2 September the activity focused on Norðri, Suðri, and an elongated middle part consisting of Heimasætan and Baugur. Three feeding channels are visible in Baugur. Photo: Daniel Müller. (d) On 4 September the vent activity is as in Figure 4.2c. Photo: Ármann Höskuldsson. (e) On 17 September merely Baugur and Krakki are active. Norðri and Suðri show no superficial activity. Photo: Águst Thór Gunnlaugsson.

the middle segment of the original fissure (see Figures 4.2 and 4.3). Within a few days, the ramparts of Heimasætan and Baugur merged into a single structure with at least three vents surrounded by an elongated rampart. We will refer to the middle part as Baugur hereafter. In the next few days Norðri, Suðri, and Baugur built up ramparts. Norðri shut down between 11 and 12 September. No surface activity was seen from Suðri from 13 September (Figure 4.2). Apart from two short-lived new vents Krakki (14 to 20/22 September) and an unnamed vent east to the fissure (14 to 16 September), the system stabilized from 22 September when Baugur was the only active part of the fissure with three feeding vents. From early February the lava level in Baugur dropped until the eruption stopped on 27 February 2015.

4.2.3 Growth of the Lava Flow Field

The growth of the lava flow field (Figure 4.3) (Pedersen et al., 2017) was mapped in detail using GPS instruments in the field and data from satellites TERRA, AQUA, NOAA (daily), Landsat-8, Landsat-7, EO-1, SENTINEL-1, TerrasarX TandemX Radarsat 2, Cosmo Skymed (weekly), and radar images from the Icelandic coastguard. The extruding basaltic lava initially flowed toward the northeast. It reached the river Jökulsá á Fjöllum on 7 September but continued northeastward until 15 September (Figure 4.3). Up until 26 September substantial lateral growth of the lava flow field took place both at the northwestern and southeastern margins. Thereafter, the growth was confined to the southeastern margins with minor activity in late October to mid-November along the northern margins. New lava flows south of and

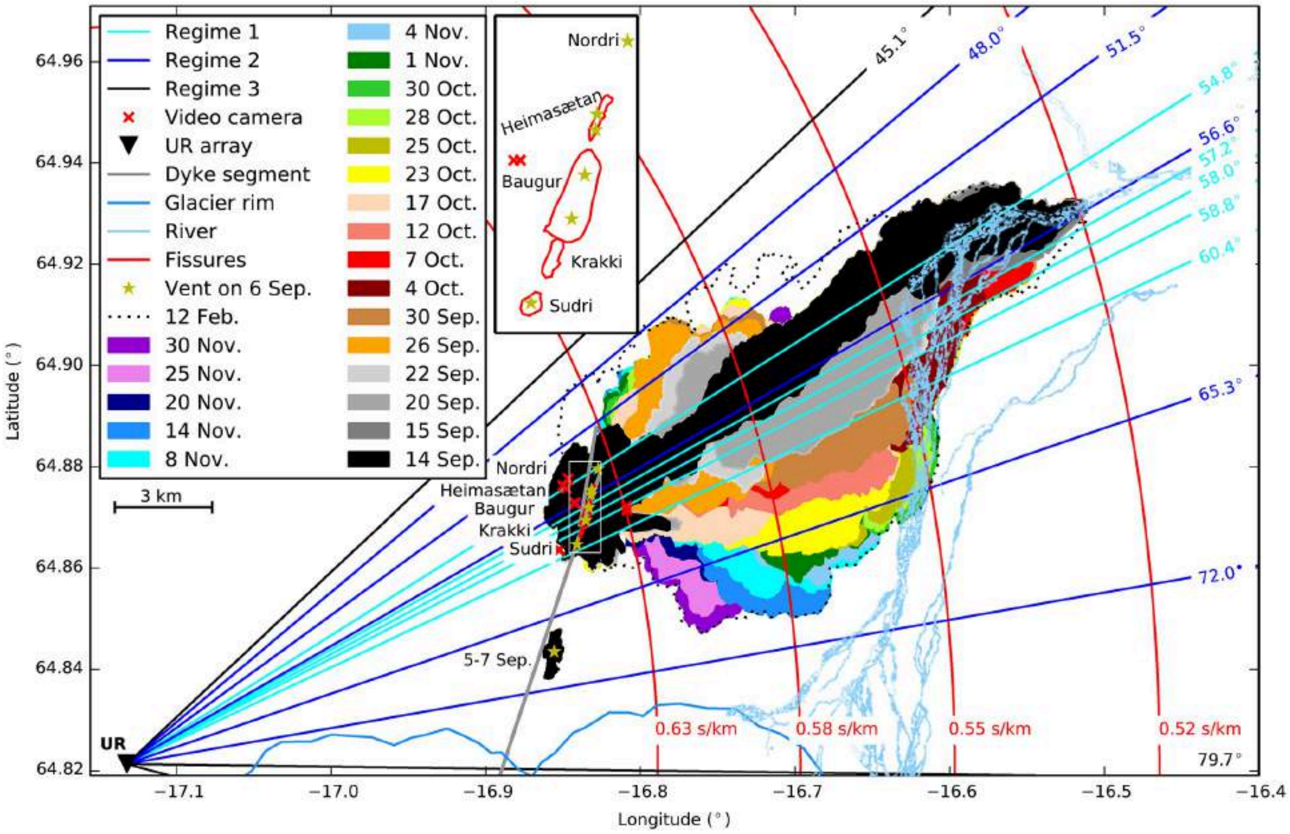

Figure 4.3: Growth of the lava flow field between 14 September and 30 November 2014 Lines mark the dyke segments as in Sigmundsson et al. (2015) (grey), the outline of Vatnajökull glacier (blue), Jökulsá á Fjöllum river (light blue), and the shape of the vents (red) as present in February, i.e., Norðri, Heimasætan, Baugur, Krakki, Suðri, and the fissures active during 5 to 7 September. Red crosses mark the location of the cameras used for lava fountain height calculation. Yellow stars mark the active vents on 6 September, i.e., Norðri, Heimasætan (twice), Baugur (twice), and Suðri (see also inset). To ease comparison with Figure 4.6, cyan, blue, and black lines mark back azimuths with respect to seismic array UR. All back azimuths are corrected so that the 60.4° back azimuth aligns with Suðri (70.27°) (see text). Cyan lines mark the five back azimuths in Regime 1. Blue lines mark the minimum and maximum back azimuth in Regime 2 until 15 September, the southernmost one between 15 September and 21 October, the overall southern maximum, and the overall northern maximum. Black lines mark the minimum and maximum back azimuth observed for sources in Regime 3. Red circles mark locations on the surface with identical slownesses at UR. Slownesses given are based on a comparison of observed slownesses in Regime 2 and actively growing flow front at the same time (see Figure 4.6d).

parallel to the first one formed from 15 September, 22 September, 7 October, 12 October, and 31 October.

The key elements of the flow field growth are (i) the lava transport system and (ii) the active flow fronts. While lateral growth of the flow field takes place at the active flow front, growth via inflation takes place within the lava flows and in particular over the internal pathways feeding lava to the active parts of the flow. When the eruption stopped on 27 February 2015, the lava had covered an area of 85 km^2 and reached a height of 62 m in the vicinity of the fissure and an average lava thickness of 17 m (Thordarson et al., 2015).

4.3 Methods

4.3.1 Frequency-Wave Number Analysis With Array Data

We installed an array (Figure 4.1) from 30 August to 24 November 2014 in order to locate and track eruptive tremor sources spatially and temporally. An array is required as tremor does not have any clearly identifiable P and S wave arrivals but is recorded as coherent waveforms on different stations in the array. The array initially consisted of seven three-component Güralp 6TDs (30 s to 100 Hz), of which four were replaced by Güralp 3ESPCD (60 s to 50 Hz) on 26 September. From late November only one station in the array continued to record. The array had an aperture of 1.63 km, a minimum station distance of 360 m, no angular dependence, and was designed to resolve frequencies between 0.4 and 6 Hz based on a typical P wave velocity in the volcanic zone in Iceland of 2.5 km/s (Flóvenz and Gunnarsson, 1991).

We subdivide the recording of the vertical component in 1 h long, not overlapping time windows. We detrend, taper, instrument correct, and downsample to a sampling frequency of 20 Hz. Then we perform a frequency-wave number (FK) analysis between 0.8 and 2.0 Hz with a moving time window of 20 periods (14.3 s) in length and 20% overlap as implemented in Beyreuther et al. (2010) and Megies et al. (2011).

The FK analysis performs a grid search in a horizontal slowness grid with, in our case, a limit of ± 1.0 s/km and a stepsize of a fourth of the width of the main lobe (0.02 s/km), chosen based on the array response function and the properties of our data. The result is a time series of absolute power, semblance, and jointly inverted back azimuth and slowness. We require a minimum semblance of 0.25 and use the time series of the back azimuth to create histograms with 0.8° wide bins. The dominant back azimuth is picked automatically and the median slowness calculated. By calculating histograms of the back azimuths, we ensure that back azimuths from different sources are not averaged but that we pick the back azimuth associated with the dominating tremor source in each time window.

The back azimuth describes the angle between north and the direction toward the epicenter. The slowness is defined as the inverse of the apparent velocity of the wavefront and contains information about the wave type and potentially the source-receiver distance. We estimate the error of each back azimuth and slowness value based on the shape and location of the main lobe of the array response function in the horizontal slowness grid. We find all points with a power of at least 95% of the maximum, determine their corresponding slowness and back azimuth, and calculate the standard deviation of these values (La Rocca et al., 2008). Our errors in back azimuth and slowness are 5.5 to 8° and 0.045 to 0.051 s/km, respectively.

4.3.2 Effusion Rate Derivation From Space-Based Thermal Data

MIROVA (Middle Infrared Observation of Volcanic Activity) is an automated global hot spot detection system run at the UnivsersitÃă di Torino (Coppola et al., 2016) based on near-real-time ingestion of Moderate Resolution Imaging Spectroradiometer (MODIS) data. The system completes automatic detection and location of high-temperature thermal anomalies and provides a quantification of the volcanic radiant power (VRP) within 1 to 4 h of each satellite overpass (Coppola et al., 2016). During the 2014/2015 Holuhraun eruption, MIROVA provided a first-order indication of the ongoing effusive trend (Coppola et al., 2017).

Satellite-based thermal data rely on the observed relationship between lava discharge rate, lava flow area, and thermal flux (e.g., Harris, 2013; Pieri and Baloga, 1986; Wright et al., 2001, , and references therein). For any given eruptive condition, this relationship allows VRP to be set as proportional to the time-averaged lava discharge rate (TADR), where the coefficient of proportionality (c_{rad}=VRP/TADR) takes into account the appropriate rheological, insulation, and topographic conditions of the observed lava flow (Coppola et al., 2013).

The best fit coefficient (c_{rad}±50%) for the Holuhraun eruption has been calculated (Coppola et al., 2017) on the basis of the silica content of the erupted lava as $c_{rad} = 6.45{\cdot}10^{2}5(X_{SiO_2})^{-10.4}$. By setting $X_{SiO_2} = 50.5$ wt% (http://earthice.hi.is/ bardarbunga_2014), we obtain a radiant density of 0.6 - 1.8 · 108 J m^{-3} which is considered to incorporate the appropriate emplacement conditions for the lava flow. This range of values allowed us to provide a mean (Figure 4.7b), upper and lower boundary limits for lava discharge rate calculation.

4.3.3 Lava Fountain Height Estimation From Video Records

Video recordings allow the monitoring of eruption sites and venting activity at high spatial and temporal resolution. In order to quantify changes in fountain height at the Holuhraun fissure during the first few days, we set up daytime video cameras recording the activity. The best locations (except on the first day of the eruption) were northwest of the fissure (see Figure 4.3). Due to weather conditions, wind direction, and the area covered by lava, the camera had to be moved slightly every day. Its distance was 0.5 to 2 km from the fissure, and it had a field of view of 140 m × 80 m to 320 m × 180 m at the distance of the observed fissures. The length of the videos varied from several minutes up to 2 h. The JVC GC-PX10 and Nikon D5100 cameras had a recording frequency set to 50 frames/s and 25 frames/s, respectively. All videos were recording at a resolution of 1920 × 1080.

In order to calculate the height of the lava fountains in Baugur, Suðri, and Norðri (see Figure 4.3), we first convert each frame of a video into a gray scale image mainly based on the red channel of the camera. The red channel enabled us, for this particular case of fountaining, to better distinguish between lava, cloud, and steam. Using a Sobel edge detection algorithm (Jin-Yu et al., 2009), we calculate the edges of the erupted lava fountain of each vent. All areas that are surrounded by strong edges are labeled by the regionprops algorithm of MATLAB. The difference between the lowest pixel of all areas of one fountain and the highest pixel of the same fountain is the calculated height.

The videos are scaled by the distance to the lens and the lens type. Furthermore, we validated the resulting scaling by analysis of falling particles (assuming frictionless conditions) as inWitt and Walter (2017). Due to different focal lenses and distances to the vents, the minimum size of detectable particles varied for every video, being in the range of 0.07 to 0.17 m pixel size. To compare the different heights, we only calculated heights of particles larger than âĹij20 cm. We give the error of the mean height as one standard deviation. The error of the maximum height is based on the accuracy of the edge detection (±2 pixel unless the picture is very noisy) and the corresponding scaling from pixel to meter.

4.4 Results

The eruption was accompanied by harmonic, seismic tremor strongest between 0.7 and 1.5 Hz with overtones at a spacing of 0.1 Hz (Figure 4.4). It was present throughout the whole eruption and with a constant frequency pattern.

The seismic array results (see Figures 6b and 6c) indicate that the tremor came from a northeasterly direction during our 3 month long record. Upon closer inspection of the back azimuth we subdivided the eruptive tremor into three regimes. Tremor in these three regimes had identical characteristics in the seismograms and spectrograms recorded at UR at 15 km distance. The regimes are active at the same time, are differentiated based on their source location and speed of source movement, and are described in the following.

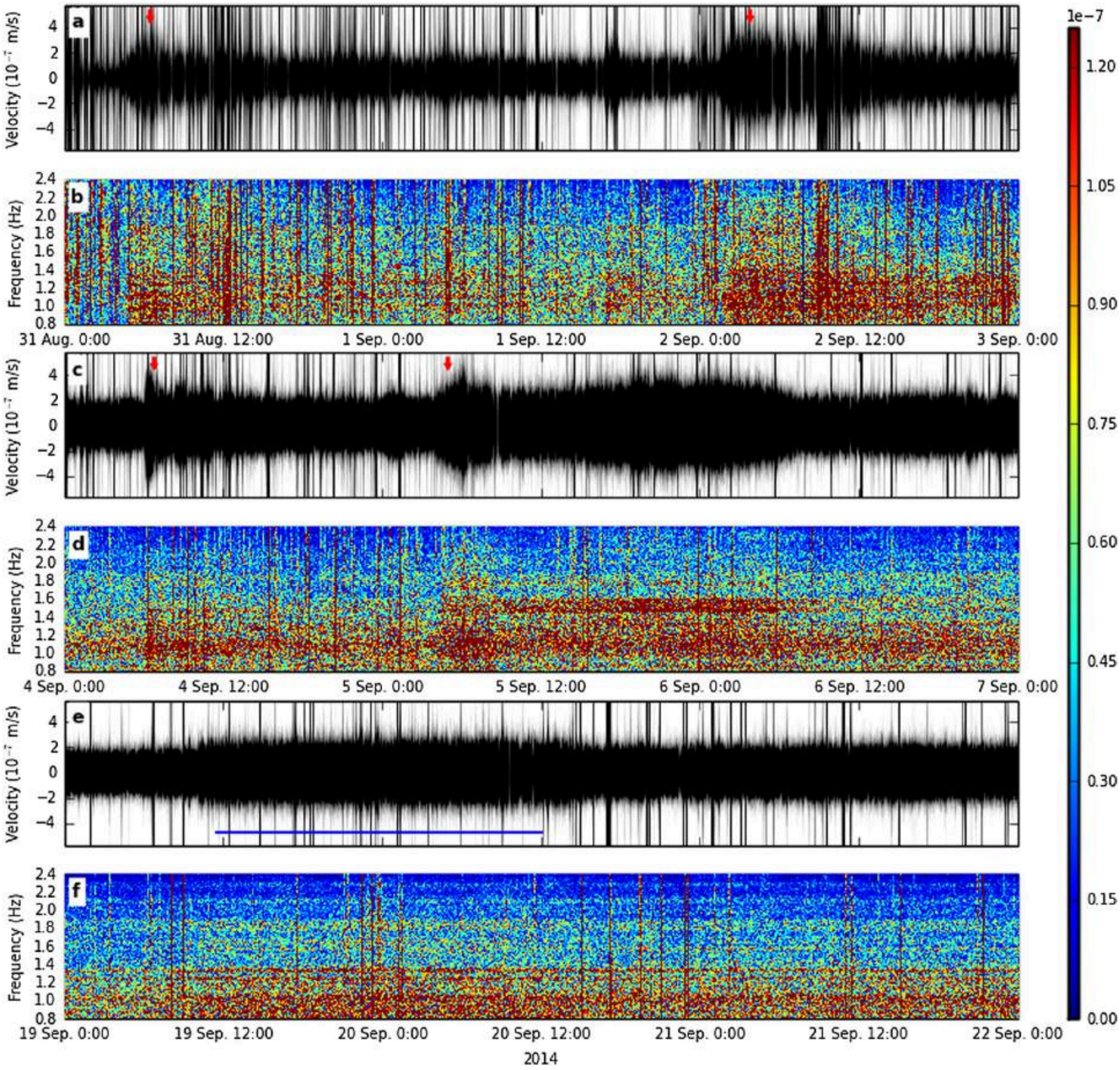

Figure 4.4: Instrument-corrected seismogram and amplitude spectrogram of the eruptive tremor at UR array filtered between 0.8 and 2.4 Hz The earthquakes appearing as vertical lines are mostly from the dyke and the continuing Bárðarbunga caldera collapse. We show all four tremor bursts in Regime 1 (red arrows) from (a and b) 31 August to 3 September and (c and d) 4 to 7 September. (e and f) One exemplary sudden increase and decrease in tremor amplitude in Regime 2 between 19 and 22 September is shown, while the visually verified lava contact with the river is marked with a blue horizontal line.

4.5 Correlation of the Vent Activity and Tremor Regime 1

The eruptive tremor started on 31 August at 4:14 UTC which we assume is the time when the fissure reopened. The open fissure was confirmed by recordings of a webcamera located on a hill 16 km northeast of the vents at 5:51 UTC when the fog had lifted.

In the time domain the tremor signal in Regime 1 shows five strong, 4 to 26 h long pulses (Figures 4.4a-4.4d) during the first 8 days of the eruption (see Table 4.1). The initial increase is sudden, while the following decrease in amplitude is exponential. The first pulse can be linked to the opening of the fissure on 31 August and the fourth one to the opening of the southern fissures on 5 September. The third pulse is not further described here as it is associated with a

Table 4.1: Comparison of Back Azimuths in Regime 1 With the Active Vents and Times of Tremor Bursts With Lava Fountain Height and Opening Fissures[a]

Date (Time) [UTC]	Tremor Amplitude	Back Azimuth [°]	Slowness [s/km]	Mean (Max) Fountain Height [m] [2]	Tremor Source in Regime 1
31 Aug to 16 Sep		54.8			Norðri
31 Aug to 26 Nov		57.2			Baugur
31 Aug to 22 Nov		58.0			Baugur
1 Sep to 20 Nov		58.8			Baugur
31 Aug to 26 Sep		60.4			Suðri
31 Aug (4:14-9:00)	Peak, exp.	57.2	0.59-0.63	N: 6.9 ± 2.4 (15.0 ± 0.2)	New fissure
	decrease				opened
“	“	“	“	B/S: 46.5 ± 6.6 (91.5 ± 0.4)	“
1 Sep	Low			B: 64.1 ± 12.4 (91.5 ± 0.3)	-
“	“	“	“	N: 48.7 ± 5.7 (84.8 ± 0.4)	“
2 Sep	Peak, exp.	57.2	0.56-0.63	B: 92.2 ± 6.9 (105.7 ± 0.5)	Higher lava
	decrease		“		fountains
“	“	“	“	N: 62.9 ± 10.8 (108.9 ± 0.6)	“
“	“	“	“	S: 28.7 ± 7.1 (69.8 ± 0.6)	“
3 Sep	Peak, exp.	119-134	0.57-0.75	B: 96.9 ± 13.3 (109.2 ± 0.2)	Shallow dyke
	decrease				formed
“	“	“	“	“	subglacially
“	“	“	“	“	Eibl et al. (2017b)
4 Sep	Peak, exp.	57.2	0.53-0.60	B: 126.4 ± 4.2 (133.0 ± 0.7)	Higher lava
	decrease		“		fountains
5 Sep (4:20) to	Two peaks	63-71	0.48-0.55		New fissure
6 Sep (6:00)			“		opened
“	“	“	“	“	2 km north of the ice

[2] N, B, and S denote Norðri, Baugur, and Suðri, respectively.

pre-eruptive, shallowing tremor source beneath the glacier that is interpreted as the formation of a new dyke at less than 2 km depth (Eibl et al., 2017b).

Camera monitoring of the fountain heights at the distinct vents suggests that the other two tremor bursts (see Figures 4.4a-4.4d) coincide with increases in fountain height. We observed a strong increase in lava fountain height at Baugur and Norðri from 31 August to 1 September (see Table 4.1) when the activity focused on fewer vents. At the same time the tremor amplitude decreased from the initial peak amplitude on 31 August (Figure 4.5a) while parts of the fissure became inactive. The fountain height at Baugur and Norðri increased further on 2 September coinciding with an increase in tremor amplitude. Following a slight decrease in lava fountain height and tremor amplitude until 3 September, both increased on 4 September. The fountain height of Suðri seems to decrease between 31 August and 2 September. However, as the fountaining on 31 August is continuous, the fountain height in Suðri cannot be separated from Baugur.

Apart from an increase in tremor, the opening of the southern fissures on 5 September is visible as an increase of back azimuth, a decrease in slowness (see Table 4.1), and higher-frequency content between 1.3 and 1.8 Hz. Although these fissures remained active until 7 September, no

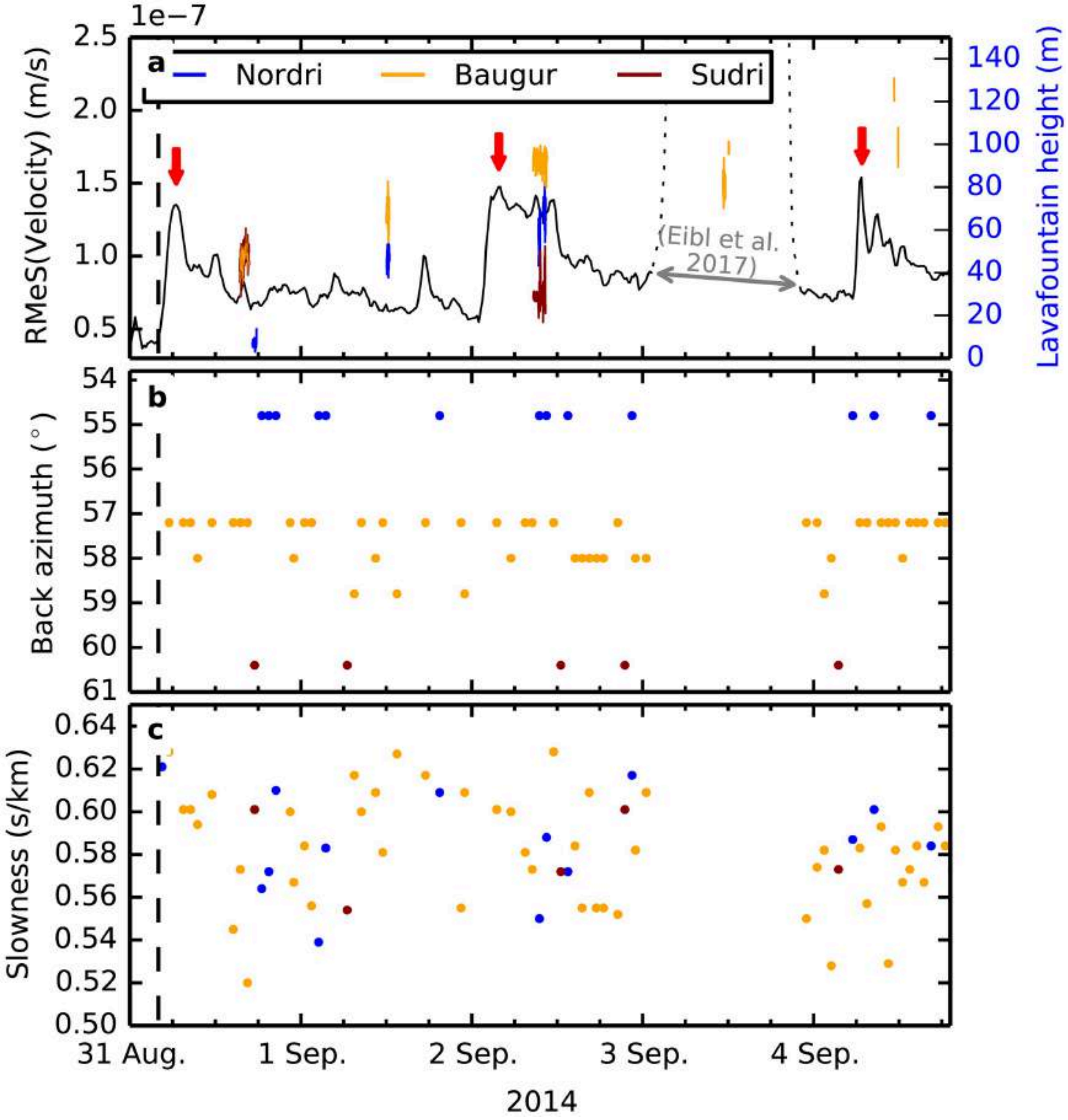

Figure 4.5: Tremor amplitude in comparison to the lava fountain height from 31 August to 5 September 2014 (a) The black line shows the tremor Root Median Square (RMeS) of the vertical component of station URB filtered between 0.8 and 2.0 Hz. Red arrows as in Figure 4.4. The vertical, black, dashed line marks the start of the eruption. The RMeS on 3 September is dotted and truncated as this is shown and interpreted in Eibl et al. (2017b). The blue, orange, and dark red lines show the lava fountain height in Norðri, Baugur, and Suðri, respectively. (b) Colored dots mark each 1 h long time window where one of the five stable back azimuths in Regime 1 is dominating. Dots are colored according to the vents in Figure 4.5a. (c) Same as in Figure 4.5b but showing the associated slownesses.

tremor signal related to their activity was detected after 4:00 UTC on 6 September primarily because of more intense activity in the northern fissure. However, the tremor indicates that the fissures opened around 4:20 UTC on 5 September, 2 h and 40 min before it was detected by a news reporter.

The back azimuth from UR array was - even in the first 24 h of the eruption - stable in the range of 54.8 to 60.4°. This is about 10° off the vents. In other studies a systematic offset between the actual source and array back azimuths was observed (Krüger and Weber, 1992; Schweitzer, 2001). The reasons for this might be topographic features or heterogeneities in the bedrock that bend the seismic rays. In our case the systematic offset was stable in time and consistent for Regimes 1 and 2 where the tremor location can be well constrained.

The tremor in Regime 1 (see Table 4.1) is characterized by five stable back azimuths (54.8, 57.2, 58.0, 58.8, and 60.4°) and slownesses in the range of 0.53 to 0.61 s/km (see Figure 4.6b). We correct for array squinting by adding about 10° to the back azimuths and can align the back azimuths in Regime 1 with Norðri, the three lava fountains in Baugur and Suðri. This squint correction also aligns the back azimuths on 5/6 September with the eruption on 5 to 7 September.

The activity in the three main ramparts fits to the visibility of the back azimuths in Regime 1. This regime was the dominating tremor source until 15 September. The northern tremor source in Regime 1 became less visible shortly after Norðri stopped erupting in mid-September. The lava fountain activity in Baugur slowed down to vigorous boiling with periodic bursting of bubbles in October, while the three middle back azimuths were visible from time to time (see Figure 4.6b). The highest lava fountains were, in general, associated with Baugur which is consistent with the fact that the middle three back azimuths dominated (Figure 4.5b).

Apart from the above mentioned correlations between vent activity and tremor back azimuths in Regime 1, Suðri did not show any surface activity from mid-September although the southernmost tremor source in Regime 1 continued to be active (see Figure 4.6b). It is, however, possible that the tremor source after mid-September was generated in the lava flow field as it points to a location where the feeding channels changed multiple times.

4.5.1 Correlation of the Lava Flow Field Growth and Tremor Regime 2

The tremor back azimuths in Regime 2 (see Table 4.2) gradually changed a few degrees southward per month (see Figure 4.6c). This regime dominated from 15 September to 21 October and from 2 to 24 November. From mid-September the back azimuth gradually changed from around 62.5 to 65.5° (southward), while back azimuths from 2 November were in the range of 64 to 70°. We subdivided the back azimuths in Regime 2 with five blue lines (see Figure 4.6c). These lines are also shown in Figure 4.3 in order to ease comparison. It can be seen that the tremor back azimuths correlate with the growth of the lava flow field. For example, from 15 September when the back azimuths indicate a gradual southward movement (see Figure 4.6c), lava flows were emplaced farther and farther south (Figure 4.3).

Slownesses scattered over 0.05 s/km but increased on average from around 0.55 to 0.6 s/km between 11 and 25 September, decreased back to 0.55 s/km until 5 October, and increased again to 0.6 s/km until 21 October. From 2 November slownesses ranged from 0.51 to 0.59 s/km (see Figure 4.6d). These gradual changes in slowness correlate with changes in distance between the newly formed lava flow field and UR array (Figure 4.6d). In September and October increasing slownesses coincided with decreases in distance whilst decreases in slowness coincided with increases in distance. As the tremor source moves away from UR, body waves travel through deeper regions and arrive at UR more steeply and therefore at lower slownesses. This correlation supports a tremor source at the growing margins of the lava flow field at the surface of the bedrock.

In the time domain fast increases in tremor amplitude in Regime 2 occurred on 7, 19, 27, and 29 September, decreases on 15, 20, and 28 September and 7 and 17 October (see Figures 4.4e and 4.4f). On-site observations show that new lava flows flowed into Jökulsá á Fjöllum River four times (see Figures 4.3 and 4.6a and Table 4.2 for the exact times). The first three contacts were accompanied by sudden increases and decreases in the tremor amplitude (see Figure 4.6) without any change in slowness or back azimuth. The fourth contact cannot be seen as the tremor source in Regime 3 dominated. One decrease on 17 October could not be attributed to a source.

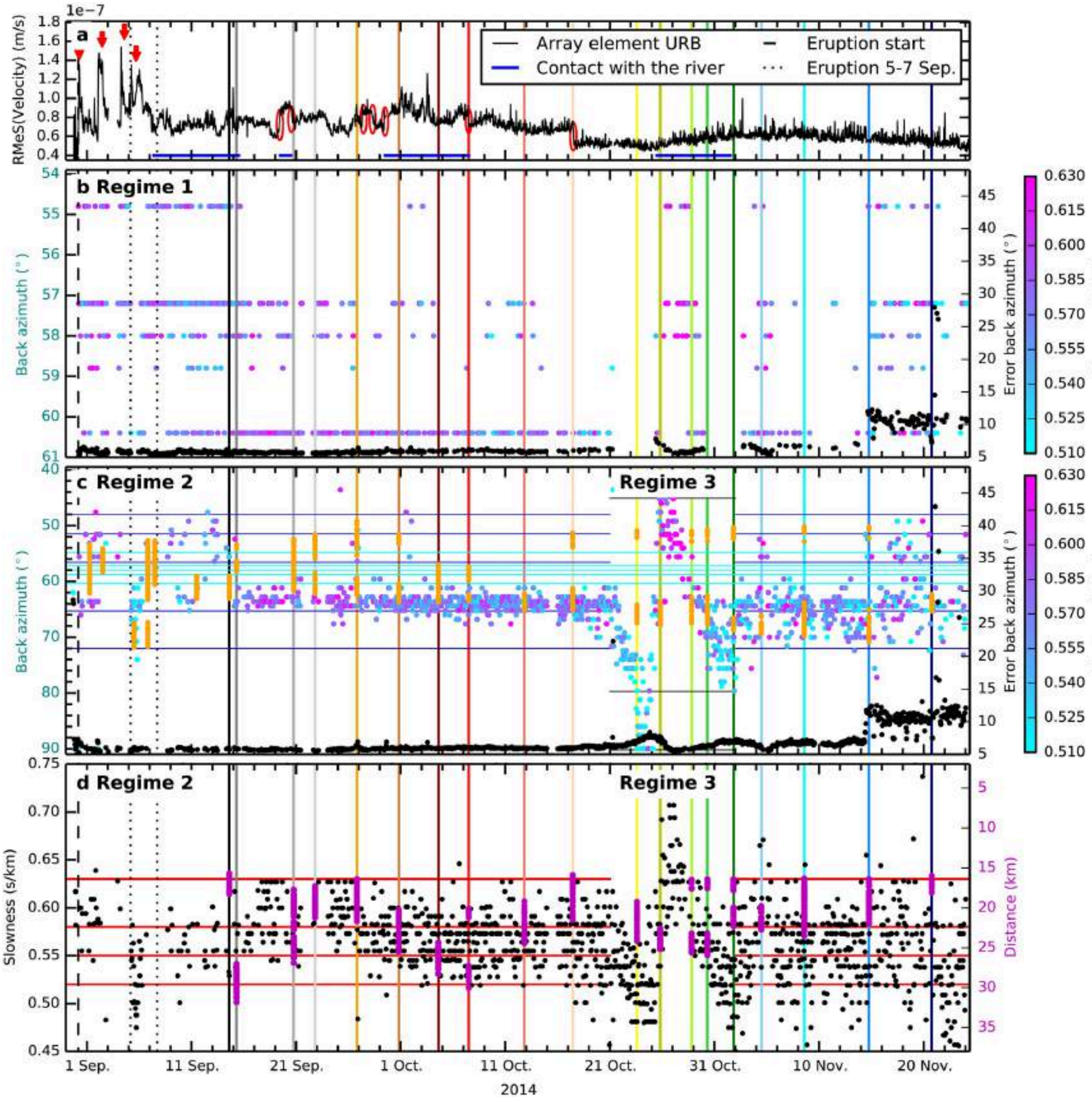

Figure 4.6: Separation of tremor sources based on the back azimuth between 31 August and 24 November 2014 (a) RMeS (black), black dashed line, and red arrows as in Figure 4.5. Red ellipses mark sudden increases or decreases in tremor amplitude, and blue horizontal lines mark when the lava flow field flowed into Jökulsá á Fjöllum River. Dotted lines mark the start and end of the eruption on 5-7 September. Colored vertical lines indicate when the lava flow field was mapped with colors corresponding to Figure 4.3. (b) Dots colored according to slowness mark each 1 h long time window where one of the five stable back azimuths in Regime 1 is dominating. Black dots indicate the corresponding error of the back azimuth. It increased on 14 November when stations started to fail. Black and colored vertical lines as in Figure 4.6a. (c) Dots colored according to slowness mark each 1 h long time window in Regimes 2 and 3 where the back azimuth is none of the five stable directions in Regime 1. Black dots as in Figure 4.6b; colored and black vertical lines as in Figure 4.6a. Orange dots indicate the back azimuth of the actively growing flow front. Cyan horizontal lines mark the five stable directions in Regime 1, and black lines mark the minimum and maximum back azimuths in Regime 3. Blue lines mark the overall northernmost direction, northern and southernmost directions before 15 September, the southernmost direction between 15 September and 21 October, and the overall southernmost direction in Regime 2. Projections are shown in Figure 4.3. (d) Same as Figure 4.6c but for slowness instead of back azimuth marked with black dots. Red horizontal lines mark minimum and maximum slowness observed before 21 October, minimum slowness on 23 September and on 27 September to 1 October, and are projected in Figure 4.3. Magenta dots mark the distance between the newly formed lava flow field and UR array as visible in Figure 4.3.

Table 4.2: Comparison of Back Azimuths and Slownesses in Regime 2 With the Growing Lava Flow Field and Times of Sudden Increases and Decreases in Tremor Amplitude With the Contact With the River

Date [Time in UTC]	Tremor Amplitude	Back Azimuth [°]	Slowness [s/km]	Features of the Growth of the Lava Flow Field (Regime 2)
11 Sep to 25 Sep		62.5 → [3]	0.55 → 0.6	Flow field grows toward UR
25 Sep to 5 Oct		...	0.6 → 0.55	Flow field grows away from UR
5 Oct to 21 Oct		→ 65.5	0.55 → 0.6	Flow field grows toward UR
2 Nov to 15 Nov		64-70	0.51-0.59	
7 Sep (18:20)	Increase			River reached
15 Sep (3:20)	Decrease	64	0.55 ± 0.02	River left
19 Sep (10:55)	Increase	63	0.59 ± 0.04	River reached
20 Sep (16:30)	Decrease	63	0.58 ± 0.03	River left
27 Sep (8:35)	Increase	63.8	0.57 ± 0.02	First snow
28 Sep (8:35)	Decrease	63.8	0.57 ± 0.02	
29 Sep (10:05)	Increase	63.8	0.57 ± 0.03	River reached
7 Oct (11:45)	Decrease	64.2	0.56 ± 0.04	River left
17 Oct (12:25)	Decrease	64.2	0.58 ± 0.03	

[3] Arrows indicate gradual movements in back azimuth or slowness.

4.5.2 Regime 3: Back Azimuth Changes Up To 25° in 4 Days

Tremor from Regime 3 dominated from 21 October to 2 November and is characterized by back azimuths that changed up to 25° in 4 days (see Figure 4.6c). There are two fast southward movements from 21 to 25 October (65 to 90°) and from 26 October to 2 November (45 to 74°). These movements correspond to a minimum horizontal movement (at the distance of the fissure) of about 10 km.

The corresponding slownesses gradually decrease from 0.58 to 0.48 s/km and 0.70 to 0.51 s/km, respectively (Figure 4.6d). Decreasing slownesses indicate that the tremor source either moved away from UR or that it is composed of more body waves. Consequently, we assume that the tremor source either deepened in time or moved at the same depth laterally toward the southeast away from the vents (and UR array). A combination of both is also possible.

No change in tremor amplitude is visible at that time.

4.5.3 Correlation of Effusion Rate and Tremor Amplitude

The array - installed on 30 August - detected harmonic tremor from 4:14 UTC on 31 August to about 24 February. Apart from four peaks in the tremor within the first 8 days and erratic sudden increases or decreases, the tremor amplitude decreased gradually with time with occasional increases or decreases in amplitude. However, on 2 February the tremor amplitude increased and only reached the detection threshold of our array at 15 km distance from the fissures about 3 days before the eruption was officially declared over.

A general decrease in both effusion rate derived from satellites and tremor amplitude over 6 months can be observed (Figure 4.7). On a smaller scale the effusion rate peaked from 7 to 11 September and around 5 October, whilst the tremor amplitude was highest on 31 August to 5 September and 2 October. Excluding the increases and decreases in tremor amplitude, for example, on 29 September, which are due to the contact with the river, the peak in tremor amplitude on 2 October is not as prominent as the peak in effusion rate. The offset between

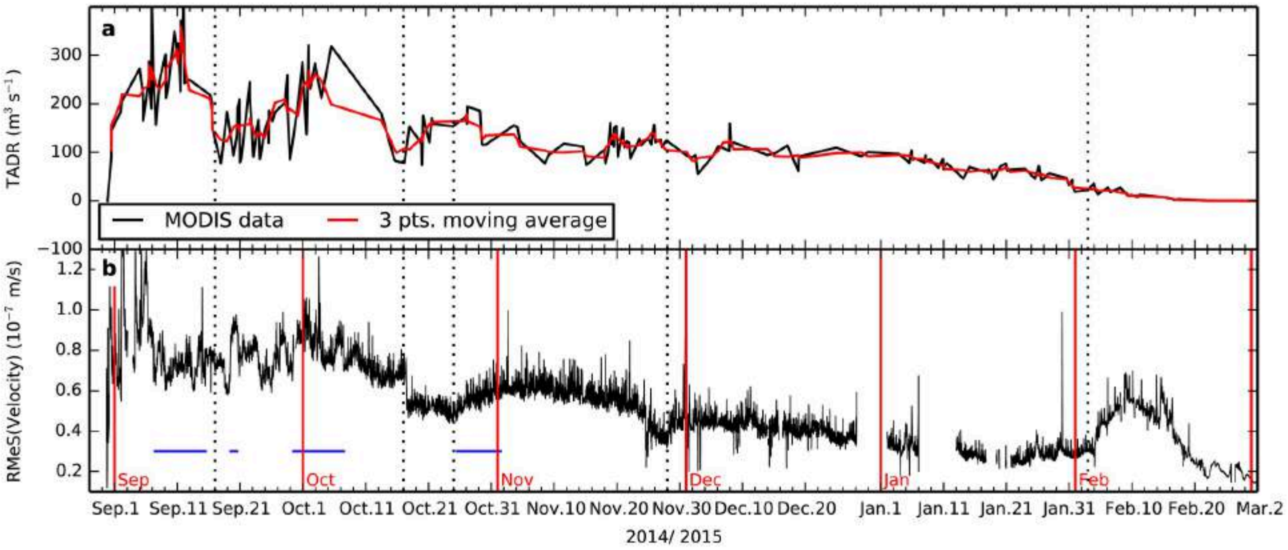

Figure 4.7: Comparison of RMeS of the tremor with effusion rate from 31 August 2014 to 2 March 2015 Dotted lines are for orientation. (a) MODIS-derived Time Averaged lava Discharge Rate (TADR). (Coppola et al., 2017) (b) RMeS of array station URB (black line). Blue horizontal lines mark times of contact between the growing lava front with Jökulsá á Fjöllum River. Red vertical lines mark the beginning of months.

the MODIS-derived effusion rates and the tremor amplitude during sources in Regime 1 might be due to the fact that the satellite-based effusion rates assume that the lava flow has reached a steady state thermal state (Garel et al., 2012). In basaltic flows this generally takes a few hours to a few days so that sharp variations in the lava flux are not immediately reflected by sharp variation of the radiant output.

In contrast, lows in effusion rate and tremor amplitude broadly coincide in mid-September and mid-October. From then on small-scale fluctuations of tremor amplitude and effusion rate do not seem to correlate. However, the tremor increase by a factor of 3 in February roughly coincided with the deviation of the effusion rate from an exponential decreasing trend on 27 January (Coppola et al., 2017) and was also observed by Allard et al. (2011) on Piton de la Fournaise. A lack of correlation might be due to multiple coincident tremor sources or a dominant tremor source not related to processes in the vents.

4.6 Discussion

Eruptive tremor is usually interpreted to be associated with only one source in the literature. In contrast, we found three coexisting tremor sources in the eruptive tremor during a well-recorded eruption in Iceland. Below we discuss possible tremor generation models and implications for studies that use the tremor amplitude or energy to estimate input parameters for other models, for example, plume height models.

4.6.1 Regime 1: Vent Tremor Model

We summarize our observations regarding tremor Regime 1 below in order to find a possible vent tremor model:

1. The eruptive tremor started/ended with the opening/closing of the fissure (see Figure 4.7c).
2. Tremor was very narrow banded, harmonic ($\Delta f = 0.1$ Hz), and strongest from 0.7 to 1.5 Hz (see Figure 4.4).

3. There were no frequency glidings or frequency jumps during these 6 months of eruption (see Figure 4.4).
4. The vents (especially Baugur) had a temporary lava pond on top, which exhibited lava fountaining and spattering over the rampart.
5. The tremor was generated locally below open vents, not while magma flowed horizontally in the 48 km long dyke (see Figure 4.3).
6. Although a 1.9 km long fissure opened on the first day, the tremor source was already focused on certain directions where Norðri, Suðri, and Baugur formed subsequently (see Figure 4.6b).
7. Tremor was stronger when a new vent opened, and lava fountains were higher (see Figure 4.5a).
8. In the first few days of the eruption there were peaks in the tremor amplitude as well as in the effusion rate (see Figures 7b and 7c).
9. Comparing the slownesses with the slownesses on 3 September (Eibl et al., 2017b), we suggest that the tremor source was at less than 2 km depths, but not on the surface.

Based on GPS and interferometric synthetic aperture radar (InSAR) data (Andrew Hooper, personal communication, 2016) and mapping of superficial faults (Hjartardóttir et al., 2016), the dyke was inferred to be as shallow as 300 m below the eruptive site on the day before the eruption. Tremor was from the very first day generated in five distinct regions presumably at a few hundred meters depth, above which vents formed later. Two scenarios regarding the evolution of the feeding system are possible:

1. The dyke remained at about 300 m depth whilst magma was fed through five distinct "fingers" to the surface. Three of these fingers feed Baugur, whilst two feed Norðri and Suðri. The initial 1.9 km long fissure was fed sideways from these fingers reflecting merely the weakness of the crust, not the feeding system.
2. The whole dyke reached the surface visible as a 1.9 km long fissure. However, from day 2 merely regions with more or faster flow remained open, whilst other parts of the dyke shut down. These five regions generated tremor beneath Baugur, Norðri, and Suðri (illustrated in Figure 4.8). The latter scenario seems more likely to us given that the dyke reached at least 300 m depth and that the lava fountains increase with the focusing on single vents on day 2.

As eruptive tremor started only once the fissure opened, it might be related to degassing processes as suggested, for example, by Soosalu et al. (2005). Ripepe and Gordeev (1999) proposed that the tremor is the result of a viscoelastic response of the magma to a sudden pressure drop that is generated when bubbles coalesce. As decompression dominates over diffusion in the uppermost few hundred meters of the dyke, bubble growth speeds up. They propose that tremor is generated in a region merely 100 to 200 m beneath the surface. Based on a clear correlation between eruption type (effusive-Strombolian-lava fountain-sustained column) and tremor amplitude (increasing), Alparone et al. (2003) suggested similarly that the tremor is generated at shallow depth. They observed systematic depth changes of the tremor source and link it to rising magma that starts to fragment and allows gas bubbles to coalesce and migrate.

An alternative model might be flow in the conduit as favored by Hibert et al. (2015) when they found a correlation between extrusion rate and tremor energy but no correlation with the

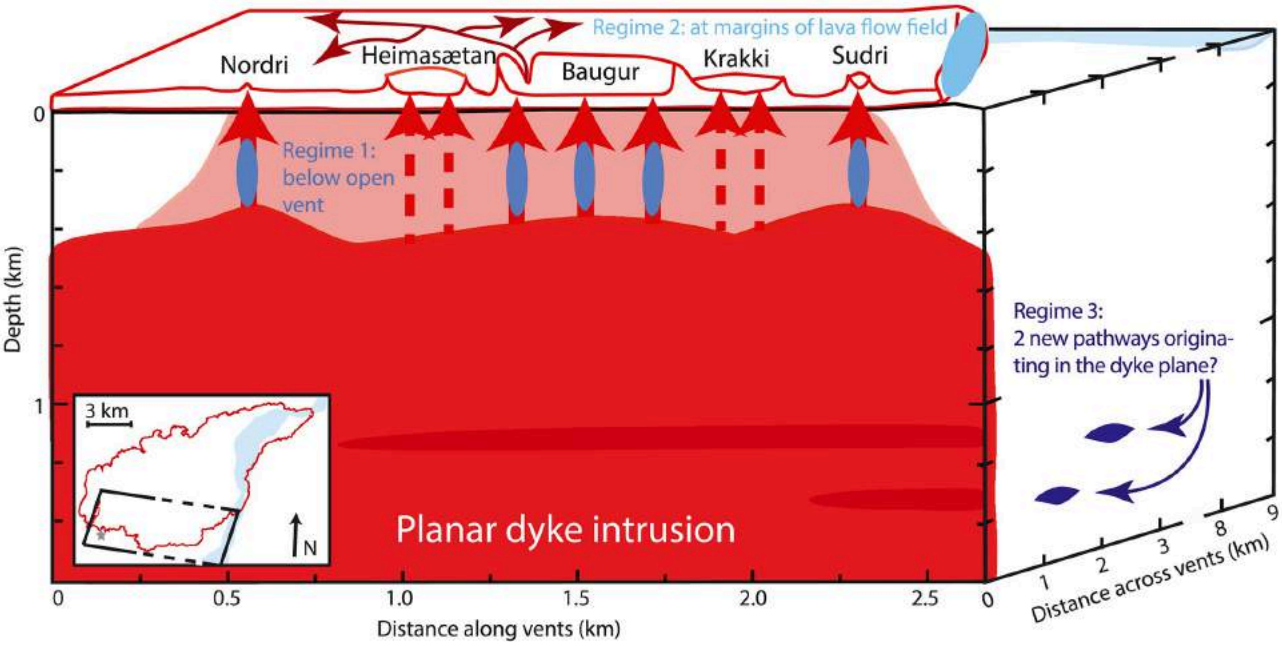

Figure 4.8: Schematic illustration of the locations of the three tremor regimes It was inferred from InSAR, GPS, and superficial fault mappings that the tip of the dyke (red plane) was located at a few hundred meters depth beneath the eruptive site on the day before the eruption started. In the first 24 h the whole dyke might have reached the surface as indicated by the light red region. The vents that remain open from day 2 are marked with red, solid arrows. Red dashed lines mark regions that fed vents for a few days only and generated no or weak tremor. Light, medium, and dark blue regions mark the array located tremor source regions. This is mainly at the margins of the lava flow field (Regime 2), shallow in the open vents (Regime 1), and potentially whilst new intrusions happened (Regime 3). Note that even on the first day tremor is preferably generated in the medium blue regions and that the dark blue tremor in Regime 3 appears red when it is located behind the planar dyke intrusion. Dark red arrows indicate the main feeding system in the lava flow field. The inset indicates the illustrated part of the lava flow field and vent area where the gray star marks the location of oblique superficial fractures (Ásta Rut Hjartardóttir, personal communication, 2016).

infrasonic signal. However, as there were no infrasonic recordings in early September when the tremor in Regime 1 dominated, we cannot comment on the applicability here.

4.6.2 Regime 2: Lava Flow Field Tremor Model

We summarize our observations in tremor Regime 2 in order to discuss sources related to the lava flow field:

1. The tremor amplitude increased when lava was in contact with water from the river Jökulsá á Fjöllum (see Figure 4.6a).
2. Although the lava flow field inflated and lava flowed in open or roofed channels, the tremor back azimuth (see Figure 4.6c) and slowness (see Figure 4.6d) correlated with the growing margins of the lava flow field (see Figure 4.3).
3. Tremor was very narrow banded, harmonic ($\triangle f = 0.1$ Hz), and strongest from 0.7 to 1.5 Hz (see Figure 4.4).

The observed correlations indicate that the tremor in Regime 2 was generated at the surface of the bedrock (Figure 4.8). As changes in height were less than 60 m at a distance of 15 km to 30 km from UR array, changes in slowness were mainly caused by horizontal changes in distance as visible in Figure 4.6d.

If the hot lava comes in sudden contact with cold water from the river, the water beneath the flow is converted into steam. This hydrothermal boiling is a viable tremor source as observed, for example, at Old Faithful Geyser (Kedar et al., 1998). However, at Old Faithful Geyser the associated tremor amplitude at 30 m distance was less than $2 \cdot 10^-10$ m/s. We therefore doubt that tremor from hydrothermal boiling could be recorded at more than 15 km distance.

Once the lava reaches the surface, it forms a lava flow field that is mainly cooled by the contact with air, water, and the ground. While lava is continuously fed into the lava flow field, it inflates until margins start to fail. This failure of newly formed viscoelastic crust creates repeated microcracks that might merge into low-frequency tremor. Tremor is generated on all surfaces of the lava flow field but, in contact with water the steam, can migrate up through cooling cracks and enhance the cooling of the lava flow, therefore allowing larger microearthquakes and stronger tremor from the sides. Rock deformation in the form of regularly repeating earthquakes was observed as a possible source of tremor in Hotovec et al. (2013) and Eibl et al. (2017b).

During other eruptions the appearance of a lava flow was not seen to affect the tremor amplitude (Alparone et al., 2003). Lava flows were also observed at times when no change in the tremor amplitude occurred (Battaglia et al., 2005; Langer et al., 2011) or when tremor amplitude was low (Soosalu et al., 2005). Here we similarly observed no change in tremor amplitude at times when the array results suggest a change from vent-related to lava flow field-related tremor.

4.6.3 Regime 3: Dyke Intrusions

The dominating tremor source in Regime 3 showed two fast southward movements (see Figures 4.6 c and 4.6 d). This tremor source dominated over the tremor from the vents and lava flow field although the overall tremor amplitude increased only slightly. The slownesses indicate that these fast southward movements happened farther from UR array (slowness of 0.48 - 0.58 s/km) than the lava flow field-related tremor in the month before (0.55 - 0.60 s/km).

As this tremor source moved about 10 km southward in 4 days - much more than the extent of the lava flow field - we suggest that they might be related to processes in the subsurface such as further dyke formations (see Figure 4.8). A tremor source at depth can also easily explain lower associated slownesses as it creates more body waves than a superficial tremor source. However, it seems unlikely to us that a shallow tremor source would move downward. We therefore speculate that the tremor source moved laterally toward the southeast with a slight decrease in depth to explain the slowness pattern.

According to the back azimuths, the dykes originated at different locations: at depth north of Norðri and in the region below Suðri (see Figure 4.8). Oblique, curved, slightly widening faults, originating around Suðri trending toward the south, are visible up to 200 m south of the lava field about 1 km east of Suðri (Ásta Rut Hjartardóttir, personal communication, 2016, gray star in the inset of Figure 4.8). They might mark the location of these slightly deepening intrusions on the surface. It was observed that the seismic expression of shallow dyke intrusions at less than 2 km depth is tremor and need not necessarily generate high-frequency earthquakes (Eibl et al., 2017b). However, InSAR data that could clearly detect deformation associated with the opening fissures on 31 August and 5 September do not show any sign of intrusions after September (StÃľphanie Dumont, personal communication, 2016). Alternatively, this tremor could be unrelated to the volcanic activity.

4.6.4 Possible Applications of the Tremor Amplitude

In the past the tremor amplitude/energy was used to find a suitable tremor source model, to estimate the effusive rate (Battaglia et al., 2005; Hibert et al., 2015), erupted volume (Battaglia et al., 2005; Hibert et al., 2015), to track changes in the degassing regime (Coppola et al., 2009) or to predict the explosivity index and amount of ash (Bernard et al., 2016; McNutt, 1994).

Studies that found a correlation between the tremor energy and effusion rate (Battaglia et al., 2005; Hibert et al., 2015) favored a tremor source representing flow of magma in the conduit. However, correlation of tremor amplitude and effusion rate (Coppola et al., 2009; Koyanagi et al., 1987) suggest that the degassing is the main tremor source (for underlying assumptions see Coppola et al., 2009). Coppola et al. (2009) also suggested that a lack of correlation between effusion rate and tremor amplitude reflects a change in the degassing regime. They suggest that changes between fast and slow flow regimes can be tracked by comparing effusion rate derived from MODIS sensors with tremor amplitude.

The three tremor sources during the Holuhraun eruption were active at the same time with similar frequency and time domain properties and similar slownesses and back azimuth ranges. We might expect a correlation between the tremor amplitude/energy linked to the vents (Regime 1) with explosivity, effusion rate, or the eruptive volume as suggested above. However, we would not expect a correlation with the overall tremor amplitude due to the tremor generation at the margins of the lava flow field (Regime 2) and its dependence on contact with water. In our case we cannot interpret the lack of correlation between effusion rate and tremor amplitude as a change in degassing regime as in Coppola et al. (2009).

4.7 Conclusions

We observed 6 months of continuous eruptive tremor during a basaltic fissure eruption that started and ceased with the opening/closing of the vent. The eruptive tremor was harmonic, continuous, and strongest between 0.7 and 1.5 Hz with no frequency changes. We used it to pinpoint the eruption starts to 4:14 UTC on 31 August and 4:20 UTC on 5 September 2014. Additionally, we identified three eruptive tremor sources which is exceptional: (i) below open vents, (ii) at the margins of the growing lava flow field, and (iii) migrating at less than 2 km depth beneath the surface. We speculate that the eruptive tremor was linked (i) to bubble generation, (ii) repeating microearthquakes, and (iii) to horizontal dyke formations. However, based on the spectral content of the three tremor sources, they cannot be separated.

We further note that even at the beginning of the eruption when a 1.9 km long fissure opened, the tremor focused in five regions where the vents formed later. This fast focusing from an elongated fissure to distinct vents was also visible in videos and photos of the lava fountaining.

Increases in tremor amplitude could be associated with different processes. Increases in vent-related tremor were associated with stronger lava fountaining activity and new opening vents. Increases in lava flow field-related tremor were associated with contact with water or snow. In order to get a first-order estimate of, for example, the effusion rate, only tremor sources related to the vents should be considered. However, our results suggest that if satellite data are not available (clouds, low repeat times), the region is not accessible, and the array is close enough, arrays can be used to monitor the growth of a lava flow field in addition to the activity in the vents.

Acknowledgments

The data were collected and analyzed within the framework of FutureVolc, which has received funding from the European Union's Seventh Programme for research, technological development and demonstration under grant agreement 308377. We thank Bergur H. Bergsson and Heiko Buxel for technical support; Magnús H. Steinarsson and Aoife Braiden for support in the field; and Andrew Hooper, Freysteinn Sigmundsson, and Ásta Rut Hjartardóttir for feedback on the schematic illustration. We thank Emmanuel Pagneux and Vincent Drouin for data. Seismic data are available via the website http://futurevolc.vedur.is. The array processing was performed using the freely available Python toolbox ObsPy.

Chapter 5

The relationship between lava fountaining and vent morphology for the 2014 – 2015 Holuhraun eruption, Iceland, analyzed by video monitoring and topographic mapping

Abstract

Fissure eruptions are associated with lava fountains which often show complex distinct venting activity in pulsating form, and the development of characteristic morphological features such as scoria or spatter cones. Most morphological studies are based on observations of old structures and are not related to direct observations and systematic records of vent activity, which are rare. The 2014 – 2015 Holuhraun eruption site, Iceland, offered an exceptional opportunity to study the location and evolution of these cones and their relationship to venting dynamics in unprecedented detail.

Here we analyze records from lava fountain activity at distinguished vents, captured during the 2014-2015 Holuhraun eruption, and compare them with the morphology of spatter cones that developed. We conducted a fieldwork mapping project combining terrestrial laser scanning (TLS) and unmanned aerial vehicle (UAV) aerophoto techniques to characterize the cone morphologies. We recorded videos of the eruption and used edge detection and particle image velocimetry to estimate venting heights and particle velocities.

We find that the number of active vents producing lava fountains decreases from 57 along the whole line of fire to 10 lava fountains at distinct vents during the first five days of the eruption. We suggest that this happens by channelling the magma supply in the subsurface developing conduits. Thereby we see that at the locations where spatter cone morphology developed, the strongest and the highest lava fountains with high ejection velocities were recorded on the very first days of the eruption. In addition, the sites that eventually developed moderate or weak cone morphologies were identified as less active lava fountain locations during the early stage of the eruption. The comparison of our topographic datasets shows that the spatter cones remained similar in shape but increased in size as the eruption progressed. In addition, we suggest that the observed changes in morphology may have affected lava ponding in the crater, which in turn strongly influenced the lava fountain heights. [1]

---

[1] Submitted as: Witt T, Walter TR, Müller D, Gudmundsson MT, and Schöpa A (excepted) The relationship between lava fountaining and vent morphology at the 2014 Holuhraun eruption, Iceland, analysed by video monitoring and topographic mapping, Frontiers.

Our results improve the general understanding of landscape evolution in rift zones and demonstrate the close relationship between cone morphology and lava fountain activity at the onset of an eruption.

5.1 Introduction

Graben morphology, tensile fractures, normal faults, and magmatic fissures together with aligned cones are common structural and morphological features of rift zones in Iceland and elsewhere. Typically, rifting events are associated with lateral dike intrusions that originate in a central volcano (Rubin, 1990) and associated eruption locations at fissures (Ferguson et al., 2010; Lipman, 1980; Medynski et al., 2016; Wright et al., 2006). At these fissures, a large number of vents may lead to lava fountaining and are thought to be closely related to the geometry and pressure fluctuations at the underlying feeder dike (Witt and Walter, 2017). A lava fountain is a mixture of magmatic gases and fragmented lava, which erupt vertically from a vent as a jet (Calvari et al., 2018). A vent is the surface feature from which the lava fountain occurs (see Figure 5.1 c). The lava fountain is formed when large amounts of volatiles are rapidly released from the magma while the magma is ascending and the pressure is reducing within the conduit (Calvari et al., 2018).

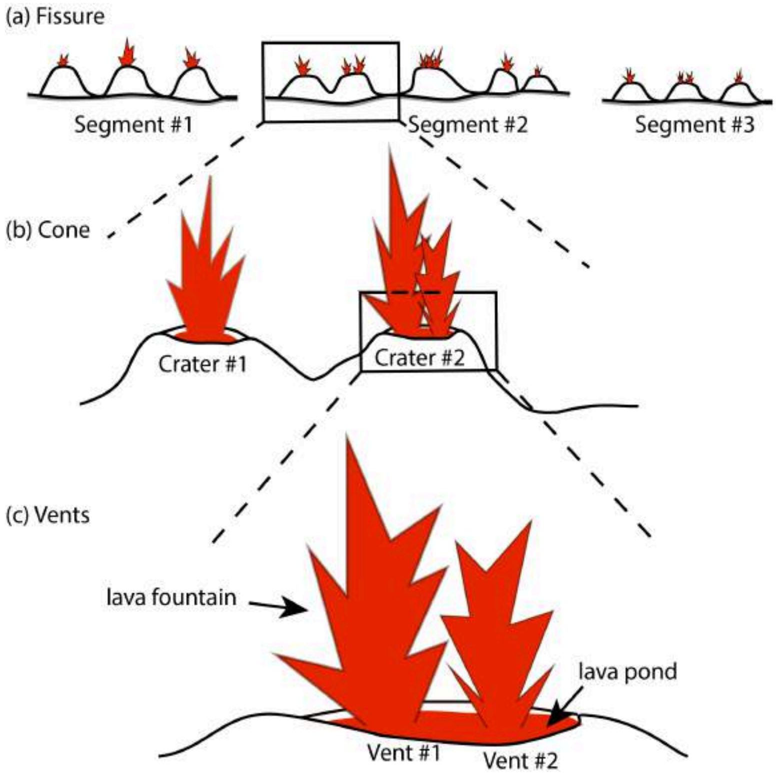

Figure 5.1: Definition of fissure, cone and vent. a - Elongated fissure divided into three segments. The fissure is the whole eruption site, and segments are parts of the fissure which are separated by small inactive areas. b - The erupted material from the volcanic eruptions sculps several cones (triangle-shaped hills) or ramparts. These cones hosted craters, vents, and lava fountains. c - Crater area with lava pond and vents. Each lava fountain occurs at an own vent, while the crater can host several vents.

Dike intrusions, eruptions, and associated faulting play an important role in the development of the geomorphology and topography of rift zones (Rubin and Pollard, 1988). Although rift zones are the most common magmatic environment on Earth, the opportunity to characterize rift-related volcanism is limited. Beneath normal faulting, magmatic injection plays a significant role within the rifting process, and the interaction of these two processes creates the rift morphology (Ferguson et al., 2010; Medynski et al., 2013). Therefore, magmatic injections are mainly responsible for rift zone extension, as seen at the Dabbahu rifting episode, Ethiopia (Medynski et al., 2016; Wright et al., 2006). Seismic and geodetic data available in Iceland indicate that the feeder dikes are commonly $<10\,\mathrm{m}$ thick, a few kilometers high, and may propagate along a rift for several tens of kilometers (Rubin, 1995). As most of these sheet intrusions become stuck beneath the surface, periods of volcanic unrest with sheet injections are more frequent than volcanic eruptions (Gudmundsson and Brenner, 2005). Similar recent examples occurred at Kilauea volcano (Lundgren et al., 2013), Fogo volcano (Bagnardi et al., 2016), Tolbachik (Lundgren et al., 2015) and Iceland (Sigmundsson et al., 2015). Dike intrusions along a rift zone are associated with subsidence of the central volcano, the establishment of harmonic tremor, and downrift migration of a swarm of earthquakes at rates of a few tens of centimeters per second, reflecting the migration of the magma-filled crack-tip (Gudmundsson et al., 2016; Rubin and Pollard, 1988). At the surface, the areas above erupting dikes develop volcanic landscapes with complex interfingering lava flows, scoria and spatter cones and fracture networks (Walker and Sigurdsson, 2000).

However, the link between the feeder dike and the surface activity is often unclear, and the eruption dynamics may be associated with segmented elongated fissures or more isolated conduits. While geodetic data commonly suggest an extensive dike with a rather uniform opening at depth (the upper edge often at 1-3 km depth beneath the surface; Lundgren et al., 2013), eruption at the surface occurs at aligned vents or even isolated vents (Witt and Walter, 2017; Wylie et al., 1999a). Gradual development may occur from the fissure to venting activity, which has been previously explained by the flow of hot magma through a crack-like fissure, leading to focused activity at only a few vents (Wylie et al., 1999a). Therefore, a high magma supply benefits the opening of single large vents within a cinder cone, while gradual changes in the eruption style (e.g., from lava fountains to mild Strombolian explosions) are determined by changes in the shallow dike feeding system (Spampinato et al., 2008). Our observations during the 2014 Holuhraun eruption further highlight the complex relationship between focused flow through dikes, morphology development, and dynamics of the vents of an eruptive fissure. The aim of this study is to understand the relationship between the height of lava fountains and cinder cone growth by comparing lava fountain activity with the morphology evolution of the corresponding cones. As our data from Iceland reveal, focused regions develop within the first days of an eruption, and the growing spatter cone is able to modulate the height and dynamics of the lava fountain.

5.1.1 Fissure morphology, different vent types and their controls

A rifting event is characterized by eruptive fissures at the surface, often in segmented and discontinuous alignment, with some fissures having an en-echelon array. Such irregularities may arise from reactivation of preexisting structures and stress field complexities (Parcheta et al., 2015). The dikes feeding the fissure can be divided into three types depending on the present volcano topography, tectonic setting and mean composition of the magma. These factors can also lead to the reorientation of the dike in the upper thickness of the dike (Acocella and Neri, 2009). The taller the volcano is, the longer the dikes with radial orientations (Acocella and Neri, 2009). Whether the dikes reach the surface and produce a fissure eruption depends mainly on the stress field in the volcano region (Gudmundsson and Brenner, 2005). Individual fissures may be hundreds of meters long, and host tens to hundreds of vents (see Figure 5.1). The fissure geometry strongly depends on preexisting structures, as evident for the 1969 Mount Ulu eruption of Kilauea, where fissure irregularities arise from weak zones at preexisting cooling joints (Parcheta et al., 2015). A further localization of the eruption activity and an increase in lava fountain height were interpreted as increase in the exit velocity at the surface due to cooling (Parcheta et al., 2015), solidification of some segments and thermal erosion in other segments of the dike, and/or varying eruption rates and volatile exsolution (Bruce and Huppert, 1990; Ida, 1996; Parcheta et al., 2015; Wylie et al., 1999b). Eruptions change the topography of the area and develop rifts and aligned fractures and cones (Müller et al., 2017). The link between fissure eruption and topography may even occur in two ways, as changing morphology may affect the dike geometry (Maccaferri et al., 2017) and type of eruption and change the direction of lava flows and tephra (Head III and Wilson, 1989; Rowland and Walker, 1990). Cones are normally classified based on stratigraphic and morphological data (e.g., Corazzato and Tibaldi, 2006; Dóniz-Páez, 2015) and described by parameters such as size, shape, slope, orientation and crater number and size (e.g., Grosse et al., 2009). The morphology of cones and craters along a fissure is strongly linked to the nature of the basaltic explosive eruption, forming cinder cones and spatter cones that often host lava ponds in their central crater and feed extensive lava flows (see Figure 5.1; Fedotov, 1981; Gudmundsson et al., 2016; Head III and Wilson, 1989; Parcheta et al., 2013; Thordarson et al., 2015; Valentine and Gregg, 2008; Wolfe et al., 1987). The cone parameters depend on the output rate, eruption volume, and fountain height, width, and clast size distribution, as well as instabilities within the summit region (Behncke et al., 2014; Calvari and Pinkerton, 2004; Head III and Wilson, 1989).

A decrease in the fountain height can result in a transition from a scoria to spatter cone. The spatter cones are then nested within the scoria cone and they predominantly develop by low lava fountain fallout, coalescence, and spatter flow, while scoria cones are dominated by agglutinated and coalesced deposits (Reynolds et al., 2016). The shape of the cones can be influenced by the wind strength and direction (Reynolds et al., 2016), structural setting, and local topography (Corazzato and Tibaldi, 2006), as well as, lava outflows which can lead to higher erosion at a portion of the cone (Calvari and Pinkerton, 2004).

The type and internal structure of the cones are also determined by the eruption duration, fountain height, magma flux, water content and variations in these factors (Carey and Sparks, 1986; Houghton and Gonnermann, 2008; Houghton and Schmincke, 1989; Németh, 2010; Németh et al., 2011; Parfitt and Wilson, 1994; Riggs and Duffield, 2008; Sumner, 1998). However, the evolution of cone morphology has rarely been addressed and with limited details (Reynolds et al., 2016; Thordarson and Self, 1998) due to difficult access of the data. Systematic measurements of lava fountain activity during eruption and changes in morphology may be linked to provide novel insights into the physical processes during eruption dynamics. To this aim, the parameters characterizing the morphology of the cones can be extracted from digital elevation models (DEMs). Aerial photos taken by camera drones allow the generation of high resolution DEMs (Amici et al., 2013a; Mancini et al., 2013; Müller et al., 2017; Nakano et al., 2014; Westoby et al., 2012) and can be used for poorly accessible volcanic terrain, such as lava flows (e.g., Favalli et al., 2010), volcanic domes (e.g., Darmawan et al., 2018) and large cone areas (Corazzato and Tibaldi, 2006; Dóniz-Páez, 2015).

To study the link between morphology and the eruption dynamics, we analyze the fountain behavior during the initial phase and model the lava fountain heights of the Holuhraun eruption (Iceland). In the following sections, we first describe the overall eruption episode and the methods used. Then, in section 5.4, the changes in the cinder cone morphology, analysis of the fountaining behavior, combination of the morphology and fountain height, and activity of the fountains are presented. Lastly, we model the fountain height to study the influence of i) a lava pond within the crater and ii) the conduit radius on the height.

5.1.2 Focused venting

Eyewitness accounts report that shortly after the onset of eruptive activity, fountain activity was focused at a few distinct vents that shaped the eruption site, with the formation of a cone morphology (Bruce and Huppert, 1989, 1990; Delaney and Pollard, 1982; Wylie et al., 1999a). The processes driving magma from a planar dike to feed surface eruptions at a few localized vents have long been a subject of debate. The focused flow was thought to occur as a feedback effect of the rate of solidification (McBirney and Murase, 1984) based on thermo-mechanical erosion and magma cooling (Bruce and Huppert, 1990), and/or be associated with solidification and changes in magma viscosity (Wylie et al., 1999b). In some areas, the cooling from the surrounding bedrock is higher than the heat flux from the magma. Therefore, the vents may be blocked by solidified magma, and thus, the fountain activity at this vent ends. At vents with high heat flux due to large vent diameters, magma may be able to erode and melt the surrounding bedrock, causing the conduit to widen until an equilibrium is reached (Bruce and Huppert, 1989, 1990). Extending earlier studies by Bruce and Huppert (1990); Delaney and Pollard (1982); Lister and Kerr (1991); Wylie et al. (1999a) demonstrated that both solidification and viscosity variations play a major role in the localization of flow in the fissure.

Tremor source location shows that long period earthquakes concentrate beneath the localized vents by day 2 from the start of the eruption (Eibl et al., 2017a), demonstrating that focused venting occurs early. The time from the opening of a fissure to focused venting varies from a few hours (e.g., 1959 Kilauea eruption with 2 hours - Richter et al., 1970) to several days (e.g., a few days at Krafla between 1974 and 1984 - Björnsson et al., 1979). Localized vents may rapidly build up characteristic cones, which are aligned in rows along the dike path and associated with Strombolian and Hawaiian eruptions (Németh et al., 2011).

Previous descriptions of focused venting along fissures and the formation of eruptive cones were mainly based on before-after eruption comparisons or sparse eyewitness observations. To monitor eruption sites and venting activity at high spatial and temporal resolution, video monitoring and computer vision tools (i.e., quantitative video analysis tools) are essential. Volcano monitoring has been achieved with thermal cameras (e.g., James et al., 2006; Patrick et al., 2007; Stevenson and Varley, 2008), high-speed cameras (e.g. Taddeucci et al., 2012b), and time-lapse cameras (Salzer et al., 2016; Walter, 2011). These observations have been made from safe distances at various types of volcanoes, such as at Etna, Italy (e.g., Behncke et al., 2006; Scollo et al., 2014), Stromboli, Italy (e.g., Andronico et al., 2013), Mount Saint Helens, USA (Major et al., 2009), and Kilauea, Hawai'i (e.g., Patrick et al., 2010). From these observations, the parameters of the fissure eruption, such as height, width, area, and perimeter (Behncke et al., 2006; Witt and Walter, 2017) can be determined. The dependency of fountain height on magma level fluctuation, vesicularity of the magma, backfilling and rheological changes can be inferred (Parcheta et al., 2013; Patrick et al., 2007). Here we use video records from the Holuhraun fissure eruption, to investigate focused venting with unprecedented detail.

5.2 Study area

Iceland is located on the boundary between the North American and Eurasian plates. These plates diverge from each other by 18.5 mm/year (Árnadóttir et al., 2008) in the N104°E direction (DeMets et al., 2010). Two characteristic transform fault zones are developed, defining the Eastern and the Northern Volcanic Zones, which are associated with several central volcanoes and attached fissure swarms (Thordarson and Larsen, 2007). During rifting events, the fissure swarms are fed by dikes that drive magma laterally away from the central volcanoes (e.g., Acocella and Trippanera, 2016; Medynski et al., 2016). These dikes generate large deformation and normal faulting, such as during the 2014 – 2015 Holuhraun eruption (Ruch et al., 2016; Sigmundsson et al., 2015).

Bárðarbunga (see the red triangles in Figure 5.2 a) is one of these central volcanoes and hosts the plumbing system associated with the most recent rifting event in Iceland. Bárðarbunga is located beneath the Vatnajökull ice cap (see the light gray area in Figure 5.2a) and has a 7×10 km wide and 700 m deep caldera (Gudmundsson and Högnadóttir, 2007) that subsided in the course of the 2014 – 2015 Holuhraun eruption (Gudmundsson et al., 2016). The Bárðarbunga fissure swarms are directed to the north and north-east (see Figure 5.2, new fis-

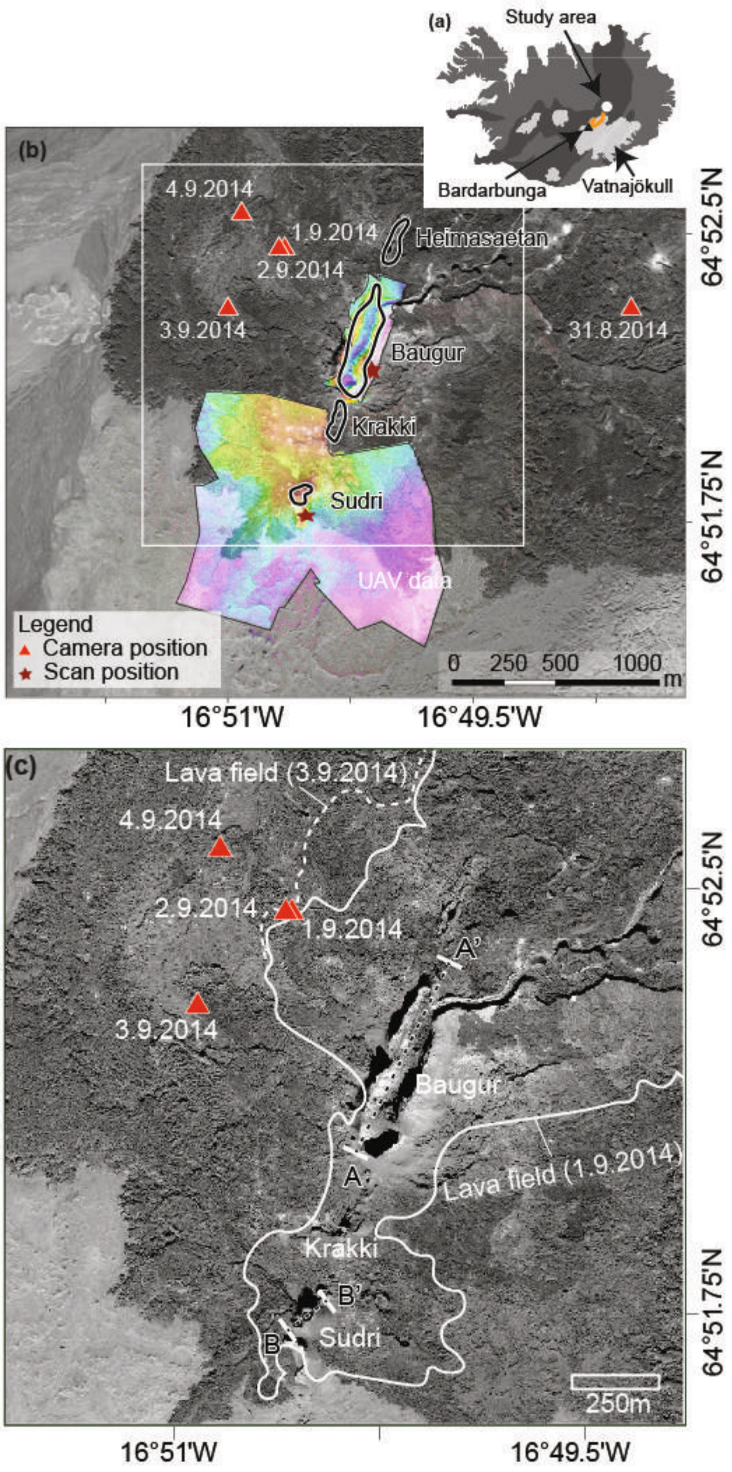

Figure 5.2: Area of the 2014 – 2015 Holuhraun fissure eruption. a - Map of Iceland with the study area highlighted by a white dot. The main rift zones of Iceland are shown in dark gray. The central volcano Barðarbunga, which is the origin of the feeder dike (orange line), is shown as a gray triangle and is located within the geyser Vatnajökull (light gray area). b âĂŞ Southern part of the Holuhraun eruption site, with the area covered by UAV data colored. The color indicates the topographic height of each data point. TLS data were obtained from two positions given by a star, and camera data were recorded from different locations (triangles). The data collection date of each site is also displayed next to the red triangle. c âĂŞ A closer look at the Baugur and Suðri cones with the outlines of the lava field on Sept 1-3. A-A' and B-B' show the profile lines for the morphologies of the cones shown in Figure 5.7.

sures in orange) and form an approximately 150 km long volcanic system, possibly intersecting with the Askja fissure swarms (Björnsson and Einarsson, 1990).

The 2014/2015 Holuhraun eruption was located at a similar place as the 1797/1798 eruption, in which the lava erupted from a 2 km long fissure about 15 km south of Askja (Hartley and Thordarson, 2013). The main eruption in 1797/1798 occurs in the winter season forming 19 cones in a line with an azimuth of N14°. Based on the geochemical analyses of the lava flows these could be assigned to the Barðarbunga volcano (Hartley and Thordarson, 2013).

The Holuhraun eruption, northeast of Bárðarbunga, is the largest eruption in Iceland by volume since the Laki eruption (1783 – 1784). On Aug 16, 2014, an intense seismic swarm started at Bárðarbunga caldera at 3:00 UTC, occurring in several clusters (Sigmundsson et al., 2015). Seismicity migrated northward for 41 km, located at a depth of 6 to 10 km, and stopped migrating within 2 weeks on Aug 27 (Ágústsdóttir et al., 2016; Sigmundsson et al., 2015). During this period, a graben structure and multiple fractures formed at the surface above the dike (Hjartardóttir et al., 2016; Müller et al., 2017; Ruch et al., 2016). On Aug 29, 2014, the first eruption, lasting for approximately 4 hours, started at a 600 m long fissure, at the same location where the Holuhraun lava field formed in 1797/1798 (see Figure 5.2; Gudmundsson et al., 2016). The connection between the diffused seismicity at 6-10 km depth, and the eruption locations at the surface was imaged using seismic array methods, which detected and located events clustering under the eruption vents (Caudron et al., 2018; Eibl et al., 2017a), possibly representing conduits connecting a deeper dike to the surface vents (Eibl et al., 2017a). The tremor and microseismicity at the dike remained high during dike propagation and eruption (Ágústsdóttir et al., 2016). On Aug 31, a second fissure eruption started at an ~ 1.5 km long fissure at the same location as the first eruption (Sigmundsson et al., 2015). This second eruption was associated with spatter-dominated scoria cone formation. The activity was characterized by large fountains that increased in mean lava fountain heights from 47 to 126 m during the first 4 days (Eibl et al., 2017a). The fountains became progressively focused at several vents in the following days. Therefore, the fountains at the largest cone (Baugur, see Figure 5.2b) show heights up to 130 m, while other cones hosted fountains with heights of ~ 100 m (Eibl et al., 2017a) and lava ponds in their center (Ruch et al., 2016). While the eruption initially occurred at many vents, only a few vents remained after the first few days. From south to north, the vents were named Suðri, Krakki, Baugur, Heimasætan, and Norðri, where Krakki and Heimasætan were formed later during the eruption and ended earlier (see Figure 5.3) than the main cones listed above. These main cones have reached heights between 40 m (Suðri) and approximately 100 m (Baugur), with the latter cones being the main source of the lava field (Müller et al., 2017; Pedersen et al., 2017). The different cones may contain multiple vents (see Suðri cone in Figure 5.2c). While satellite radar data have allowed studying the general morphology of the lava field (Dirscherl, 2016; Pedersen et al., 2017), small-scale features such as cones and craters have not been described in detail.

Sigmundsson et al. (2015) analyzed the deformation rate associated with the Barðarbunga central volcano and dike opening, and compare this geodetic signal to the eruption volume at the Holuhraun fissures. Therefore they were able to constrain and compare the inflow of magma into the dike and the eruption volume. After Sept 4, 2014, the inflow of magma into the dike was approximately equal to the magma outflow feeding the eruption (Sigmundsson et al., 2015). This time (Sept 4) represents the end of the initial phase of the eruption, while the eruption continued for ~ 6 months and ended on Feb 27, 2015. The eruption after the initial phase is characterized by fountaining activity restricted to the main cones. The total volume of the identified intruded and erupted magma was $1.9 \pm 0.3\,\mathrm{km}^3$ (Gudmundsson et al., 2016).

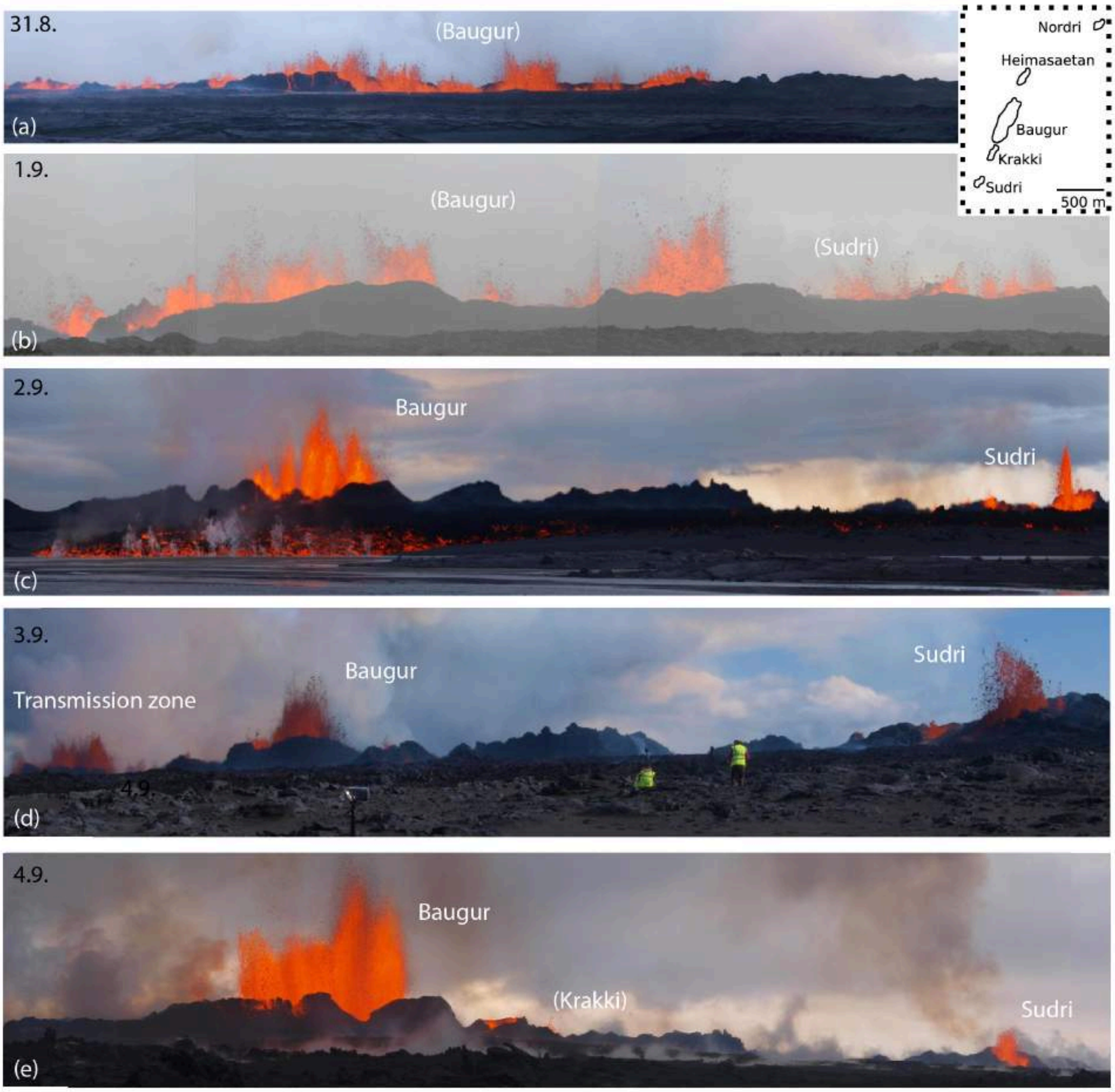

Figure 5.3: Evolution of the eruption. Examples from optical images for the first five days of the eruption. a - In the beginning, we observed several cones that were hard to separate and, therefore, were interpreted as a line of erupting vents. b - On the second day, the number of cones decreased, but the fountain heights increased. c-e - After Sept 2, the vents, Suðri and Baugur, emerged and remained fixed in their location until the end of activity (here, the location seems to change due to the change in camera position, see Figure 5.2c for comparison; the orientation for all images is NS).

5.3 Data collection and methods

5.3.1 Collected data

To investigate the relation between fountaining and vent morphology, we analyze the video data that we acquired during the first days of the 2014 – 2015 Holuhraun eruption. We compare the video data to a variety of available digital elevation models (DEMs). In the following section, we first describe the data and then the analysis methods. The timing and specifications of the data are provided in Table 5.1.

The morphological study comparing DEMs acquired before and after the eruption is based on (i) satellite imagery and results from the TanDEM-X and WorldView-2 satellite missions and

Table 5.1: Summary of different data sets used to analyse the fountaining behaviour and morphology.

Date (Time)	Date technique	Instrument	Technical details
21/11/2011 & 09/09/2014	Satellite	Terra SAR-X	12 m resolution
12/06/2014 & 25/09/2015	Satellite	World View-2	~0.6 m resolution off nadir angle: 12.4° & 16.8°
31/08 – 05/09/2014	Camera	JVC camera & Nikon D5000	0.1 – 0.25 m/pixels
13 – 16/08/2015	Laser	Riegl VZ-6000 scanner (near infra-red)	up to 6 km, 0.0005° angle resolution pulsating rate: 30 – 300 kHz FOV: horizontal 360° vertical -30° - 30°
14 – 15/08/2015	Drone SfM	12 M Pixel GoPro Hero 3+ camera	0.067 – 0.19 m resolution

(ii) field data attained at key locations by camera drones and terrestrial laser scanning (TLS). A detailed description of the TanDEM-X data, and our field data can be found in Floricioiu et al. (2015) and Rossi et al. (2016), and in Müller et al. (2017), respectively.

Table 5.2: Summary of different data sets used to analyse the fountaining behaviour and morphology.

UAV	weather conditions at surveillance	Flying speed → temporal resolution of camera
DJI Phantom 2 drone	calm weather conditions	5 m/s → 1 frame/s
Helium-filled helikite	calm & windy weather with wind speed up to 35 km/h	< 1 m/s → 0.2 frame/s

On Aug 14 and 15, 2015, we collected approximately 2000 close-range aerial photographs of the area around the southern vents and Baugur, covering an area of 1.07 km^2 (see the colored areas in Figure 5.2b). Additional information on the unmanned aerial vehicle (UAV) used can be found in Table 5.2. During the same field campaign, we collected a TLS dataset covering ~ 6 km^2, scanned from two elevated locations (see the stars near Baugur and Suðri in Figure 5.2b). While the drone data are mostly shadow free and allow, based on the high resolution, detailed structural and morphological analyses, the quality of the resulting mosaic and DEMs is strongly dependent on sufficient georeferencing (Müller et al., 2017). We therefore, performed georeferencing and distortion correction by point matching (tie point matching and multistation adjustment) of the Structure from Motion (SfM) data towards the TLS point cloud and yielded a high-quality dataset. Details of these datasets, their acquisition resolution, and the DEM processing can be found in Müller et al. (2017). In contrast to our paper, where the eruption area is studied, Müller et al. (2017) analyze the graben structure above the dike.

The cone morphology is compared to the fountaining dynamics. Fountaining was recorded by video cameras for the initial eruption phase (first four days). We used several video cameras and were hence able to record fountaining dynamics from different locations between Aug 30 and Sept 5, 2014. Due to the wind direction, haze and advancing lava flows, the locations of the cameras had to be adjusted regularly. The best locations (except the first day of the eruption) were on the northwest side of the fissure (see Figure 5.2). The cameras were mounted on stable tripods so that shaking artifacts were minimized. The distances between lava fountains and cameras were between 0.5 and 2 km with a Field of View (FOV) from 140 × 80 m to 320 × 180 m. The length of the videos varied from several minutes to 2 hours. The two different camera types used were consumer cameras (JVC GC-PX10 and Nikon D5100), which were set to record with a frequency of 50 frames/second and 25 frames/second, respectively. Both camera types were set to a resolution of 1920 × 1080 pixels. The timing of the video images was recorded by an internal intervalometer and synchronized with a computer.

5.3.2 Analytic methods

5.3.2.1 Morphology generation and difference

To generate a three-dimensional structure from the UAV photographs, we used the SfM approach (Carrivick et al., 2016; Westoby et al., 2012) using the commercial software package Agisoft PhotoScan Professional (version 1.2.6). After initial quality control, we generated a sparse and dense point cloud from the photographs covering the cones and craters of Holuhraun. The dense point cloud contained approximately 320 million points, only loosely placed in reference. The point cloud was then merged with a referenced TLS point cloud. The details of data processing are described by Müller et al. (2017), who used enlarged aerial and TLS data for analyzing the graben formation in the Holuhraun area, while our focus here is on the area of the eruptive vents and cones.

TLS is achieved by a ground-based Light Detection and Ranging (LIDAR) instrument, where the time delay between emitted laser pulses and its echo reception is measured (Fornaciai et al., 2010; Richter et al., 2016). By selecting different viewpoints and merging the data, we could increase the density of the scans in the far field and reduce shadowing problems (Müller et al., 2017). Therefore, we chose two different scan positions with overlap between the different scans and merged them with point cloud matching techniques as available in the Riscan Pro Software package. This method has the advantage of not needing to place ground control points (GCPs) on the difficult terrain of fresh, sharp lava flow surfaces.

The merged point cloud provides us with a very high-resolution posteruption topography database with a resampled resolution of 0.067 m, slope maps, and aerophoto mosaics that allow morphological analysis of the cones. The high-resolution data are acquired and analyzed for the Suðri and Baugur cones because we also acquired video data at these cones during the eruption.

We display the development of the morphology on one two-dimensional profile with different orientations (see Figure 5.2 and 5.4). This reprojection on AA' and BB' profiles (see Figure 5.2 c) was chosen to compare the morphology to the video observations that were taken from the given camera position. The initial morphology from the videos was extracted as the outline of the vents from camera records and overview images, which were recorded from similar angles. Due to small changes in the recording position (see Figure 5.2), we corrected the cone outline to a common viewing point and spatial resolution. Therefore, the studied initial morphology is limited to a N-S profile and can be compared to the final morphology by choosing the same profile orientation. Furthermore, we can observe the changes in morphology during the first several days. The results are displayed in ArcMap and ArcScene using ArcGIS.

The cone morphology is described by the basal cone diameter ($2r$), the cone height relative to the lowest topography (h), and the top cone diameter ($2t$; see Figure 5.4), as described by (Bemis et al., 2011). Furthermore, we calculated (after Favalli et al., 2009) the flatness $f = t/r$

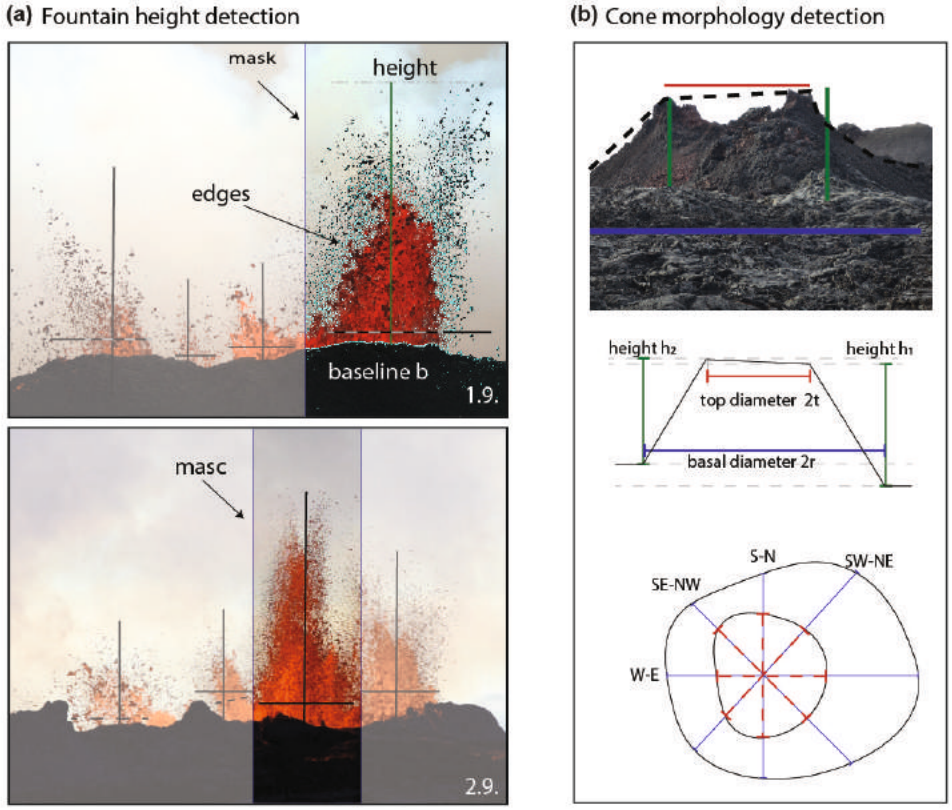

Figure 5.4: Methods a - Method for calculating the fountain height by edge detection (in cyan) on two example frames of the lava fountains at Baugur on Sept 1 and 2. After manual masking (box around fountain) the heights are extracted by the difference between the baseline and the highest fountain particles. b - Measurement of the morphological scales of cones shown in a photo from the side and from above. For elongated craters (e.g., Baugur), the top and basal diameters depend on the chosen profile. The height is a relative measure between the base and the top of a cone.

and the height-to-radius-ratio h/r by using:

$$\text{angle of slope} \qquad \angle_{slope} = \arctan \frac{h}{r-t} = \arctan \frac{h/r}{1-f} \tag{5.1}$$

$$\text{Volume} \qquad V = 1/3 \cdot \pi(h)(r^2 + r \cdot t + t^2) \tag{5.2}$$

Therefore, both the height-to-radius-ratio and the angle of the slope are characteristics of the constituent tephra. Due to posteruption colluvial fills and erosion, the height-to-radius-ratio decreases (Porter, 1972), which is why the morphology needs to be measured during and immediately after an eruption. Thus, the height is given with respect to the surrounding lava field, which is at an elevation of approximately 835 m. Morphologic asymmetry can be caused by persistent wind action, which leads to a locally higher deposition (Porter, 1972). Previous studies (Bemis et al., 2011; Bemis, 1995; Smith and Cann, 1992) have shown that three parameters are needed to describe the overall variance in the cone morphology: the height-to-radius ratio h/r, the flatness f, and a parameter to measure the size, such as height, top or basal radius or volume (Bemis, 1995). We therefore measured the diameters (top and base), height and slope angle. Based on the ratio of the minimum and maximum basal diameter, the cones (see Figure 5.4b) are separated into categories of circular (ratio of 1), subelliptical (ratio between 1 and 1.5), elliptical (ratio between 1.5 and 2), elliptical elongated (ratio between 2 and 2.5) and superelliptical (ratio > 2.5) (Dóniz-Páez, 2015).

5.3.2.2 Fountain dynamics by video analysis

Investigation of the fountain dynamics is based on videos taken at the beginning of the main eruption from Aug 31 to Sept 5. The FOV of all video data covers the entire region between the two main cones, Suðri and Baugur. Each video shows several fountains occurring at the different vents.

To reduce perspective distortions in the videos, we attempted to record perpendicular to the fissure azimuth. First, we identify the fountains by eye. We assume that the width of the fountains is equal to the vent diameter. If the fountains overlap with each other, we assumed a larger vent diameter (sum of both), i.d. a maximum estimate of the vent diameter. Regions where activity stops are counted as "inactive" vents, and the vent diameter is zero.

To calculate the height of the lava fountains, we first convert each frame of a video into an 8-bit image based on the red channel of the camera. The red channel was found to be advantageous for this particular case of fountaining to distinguish between lava, clouds and steam (cf., Witt and Walter, 2017). Using a Sobel edge detection algorithm (Jin-Yu et al., 2009), we calculate the edges of the erupted lava fountain of each vent. All areas that are surrounded by strong edges are labeled by the *regionprops* algorithm of MATLAB, which measures the properties of an image region. The difference between the lowest pixel of all areas of one fountain and the highest pixel of the same fountain is the calculated height.

From the pixel domain, we convert the results to meters. The videos are scaled by factor r [cm/pixels] calculated by considering the distance between the cones and camera d [cm], the sensor size of camera B [mm], the pixel resolution of image p [pixel] and the used focal lens f [mm] by

$$r = d \cdot \frac{B}{f \cdot p} \tag{5.3}$$

The heterogeneous scaling arising from the different distances of the regions imaged by pixels and their positions relative to the cameras was neglected. Additionally, distortions arising from atmospheric disturbances close to hot lava flows or from the camera lens were not corrected. However, we validated the general scaling results by the analysis of falling particles assuming frictionless conditions, as performed in other previous studies (e.g., Taddeucci et al., 2012a; Voight et al., 1983; Witt and Walter, 2017). Due to different focal lenses and distances to the vents, the scaling factor has to be calculated for each video separately, and the minimum size of detectable particles varied for every video. To compare the different heights, we calculated heights of only particles larger than 20 cm, which is the smallest particle that can be clearly detected in every video. For the width, the outline is calculated in the same way. Subsequently, the width of the fountains has to be picked manually (Figure 5.4 b), and has to be checked carefully due to overlap of the aligned fountains.

5.4 Results

5.4.1 General overview

The main 2014 – 2015 Holuhraun fissure eruption began on Aug 31, 2014, and started as a long fissure (see Figure 5.3 a) with an azimuth angle of N12°E. The length of the fissure is marked by near continuous fountaining activity, which is more than 1.9 km in length. The video records clearly show pulses at 57 fountains aligned along the fissure. In the north (later location of Norðri), the video records show that the fountains are slightly lower and more separated than in the south (later location of Suðri and Baugur). The highest and most powerful fountains are seen at the locations where the Baugur cone formed in the following days (see Figure 5.3 a and b).

On the second day, the activity started to concentrate at fewer distinct locations (see Figure 5.3 b), while the fountain height increased. The main activity had already concentrated at Suðri and Baugur on day 1 (see Figure 5.3 c). This trend of activity concentration continued in the following days (see Figure 5.3 d and e), gradually changing the morphology of the fissure from spatter ramparts along the active vents to cinder cones with few vents inside them. The fountains increased in height at Baugur between days 3 and 4 (Sept 2 and 3). At Suðri, in turn, fountain heights were stable.

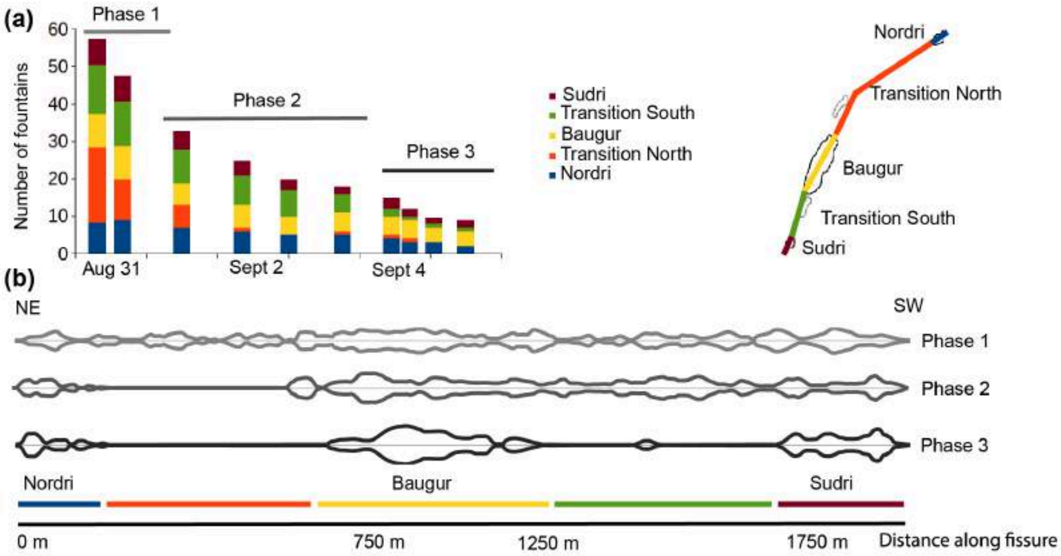

Figure 5.5: Numbers of fountains. a - Number of active fountains during the first few days of the 2014 – 2015 Holuhraun eruption. The different phases of the first five days of eruption are color coded in gray from light (Phase 1) to dark (Phase 3). The number of fountains for each segment is obtained from overview images. The segments are color coded with blue for Norðri, red for the transition zone in the northern part, yellow for Baugur, green for the transition zone in the southern part, and brown for Suðri. The position of the different segments is shown to the right. b - Vent distribution during the 3 different phases observed during the first days of the eruption in the overview images, as shown in Figure 5.3. The width of the different lines shows the diameter of the vent at that position. We assumed that the width of each fountain is equal to the diameter of the vent. Areas with no vents are defined as inactive. The segments are indicated by colored lines below the profiles. The decrease in the number of active vents is clearly seen. From Phase 1 to Phase 2, a decrease in the northern transition segment (red) can be observed. Between Phase 2 and Phase 3, a decrease in lava fountains occurs in the southern transition segment (green). Furthermore, the local distribution shows that the decrease in activity of lava fountains starts from the north and propagates to the south.

The change from an almost continuous line of fountains to fewer distinct vents consists of 3 phases that blend into each other. (i) The first phase started on Aug 31 at 4:00 UTC and lasted for 22 ±4 hours until Sept 1 at 2:00 UTC. This phase consisted of a nearly continuous line of fountains with a length of approximately 2 km. During that time, we identified 57 fountains (see Figure 5.3 a and 5.5 a). The number of fountains decreases quickly, with this trend being fastest in the northernmost part of the fissure (see Figure 5.5 b, blue line and Figure 5.3 c). (ii) The second phase started on Sept 1 at 2:00 ± 4:00 UTC and had a duration of 73 ± 7 hours until Sept 4 at 3:00 ± 3:00 UTC. This phase started with nearly continuous activity from 19 fountains for one day, and it is characterized by a zone with almost no activity between fewer large spatter cones in the north (later called Norðri) and the cones further to the south (see Figure 5.5 b, red line). During this phase, the activity at the southern part was also focused at some larger vents (later called Baugur and Suðri). (iii) The third phase started on Sept 4, and all the activity was concentrated at three main spatter cones (i.e., at Norðri, Baugur, and

Suðri) and some smaller unnamed vents (see Figure 5.5 a, green line and Figure 5.3) with a total of 10 lava fountains. On the last day of our fieldwork (Sept 5), two fountains were observed at Suðri, one at each vent. One fountain occurred at the later location of Heimasætan, four fountains at Baugur, and three fountains at Norðri. The decrease in the fountain number seems larger at the beginning of each phase (see Figure 5.5 a).

5.4.2 Morphology of the cones

The preexisting morphology, as measured from satellite data, allows the manual identification of 19 cones or remnants thereof oriented along a line with an azimuth of N14°. The 19 cones were made up of eleven small cones (see Figure 5.6 a, cones 4, 5, 9, 10, 12, 14, 15, 16, 17, 18, and 19) and eight large cones. Four of these large cones were well expressed and circular in outline (cones 3, 7, 8 and 13), with radii of 30 m (cone 8), 40 m (cone 13) and 50 m (cone 3 and 7). Cone 1 and cone 2 were partially overlapping at an azimuth angle of N116°, and thus, they were almost perpendicular to the overall cone trend of N14°. Cone 1, with dimensions of 115 × 85 m, was larger than cone 2, with dimensions of 70 × 60 m. Cone 6 was elongated N12° and had dimensions of 50 × 85 m. Cone 11 also had a similar long-axis azimuth angle (N10°) and dimensions of 40 × 25 m.

The 2014 – 2015 Holuhraun eruption caused significant changes in the preexisting cone morphologies of the 1797/1798 eruption that are observed in video and photogrammetric data, discussed in the following in more detail. The cones of the 2014 – 2015 Holuhraun eruption form a line with an azimuth angle of N12°. In the following section, we detail the changes in morphology from SW to NE in accordance with the FOV of the video cameras. The height of the cone morphology is calculated as the difference between the lowest topography and the highest rim of the cone (see Figure 5.4 b).

Table 5.3: Cone morphology of the two cones of Suðri The cones are described by the basal diameter (2r), top diameter (2t), and height (h).

Date	south-west cone			north-east cone			link	
	2r [m]	2t [m]	h [m]	2r [m]	2t [m]	h [m]	width [m]	height [m]
1 Sept	44.43	16.96	13.19 ± 0.90	26.36 ± 0.28	8.68 ± 0.17	14.26 ± 0.06	17.07 ± 0.23	4.70 ± 0.11
2 Sept	38.17	8.58	18.14 ± 0.36	32.72	5.86	16.50 ± 0.11	15.55	4.25 ± 0.99
4 Sept	42.62	9.49	19.49 ± 0.56	35.14	11.51	17.43 ± 0.73	7.07	5.23 ± 0.07
Aug '15 (final)	52.03 ± 7.95	38.04 ± 4.07	33.77 ± 4.72	54.76 ± 8.52	36.43 ± 3.39	37.84 ± 5.13	13.29	44.37 ± 0.27

Suðri: Suðri shows two distinct vents aligned N57°, differing from the general trend of the fissure eruption (N12°). Comparing the preeruption morphology (see Figure 5.6 b_1, cones 3 & 4) and the posteruption morphology (see Figure 5.6 b_2), we can observe that the orientation of cones 3 & 4 is the same as that of the two vents (see the gray lines in Figure 5.6 b_1 & b_2). The orientation is calculated by the azimuth of the connecting line of the center points of each vent. During the first day of the eruption (Aug 31, 2014), the different vents were not yet formed. The fissure morphology was nearly constant, and no large morphological variations were observed at this eruption site. On Sept 1, the cone morphology started to grow, as evidenced by the outline in the video data (see Figure 5.7). The highest rims of the Suðri cone were in the northeast, 14.3 ± 0.1 m, and in the southwest, 13.2 ± 0.9 m. During the next several days (Sept

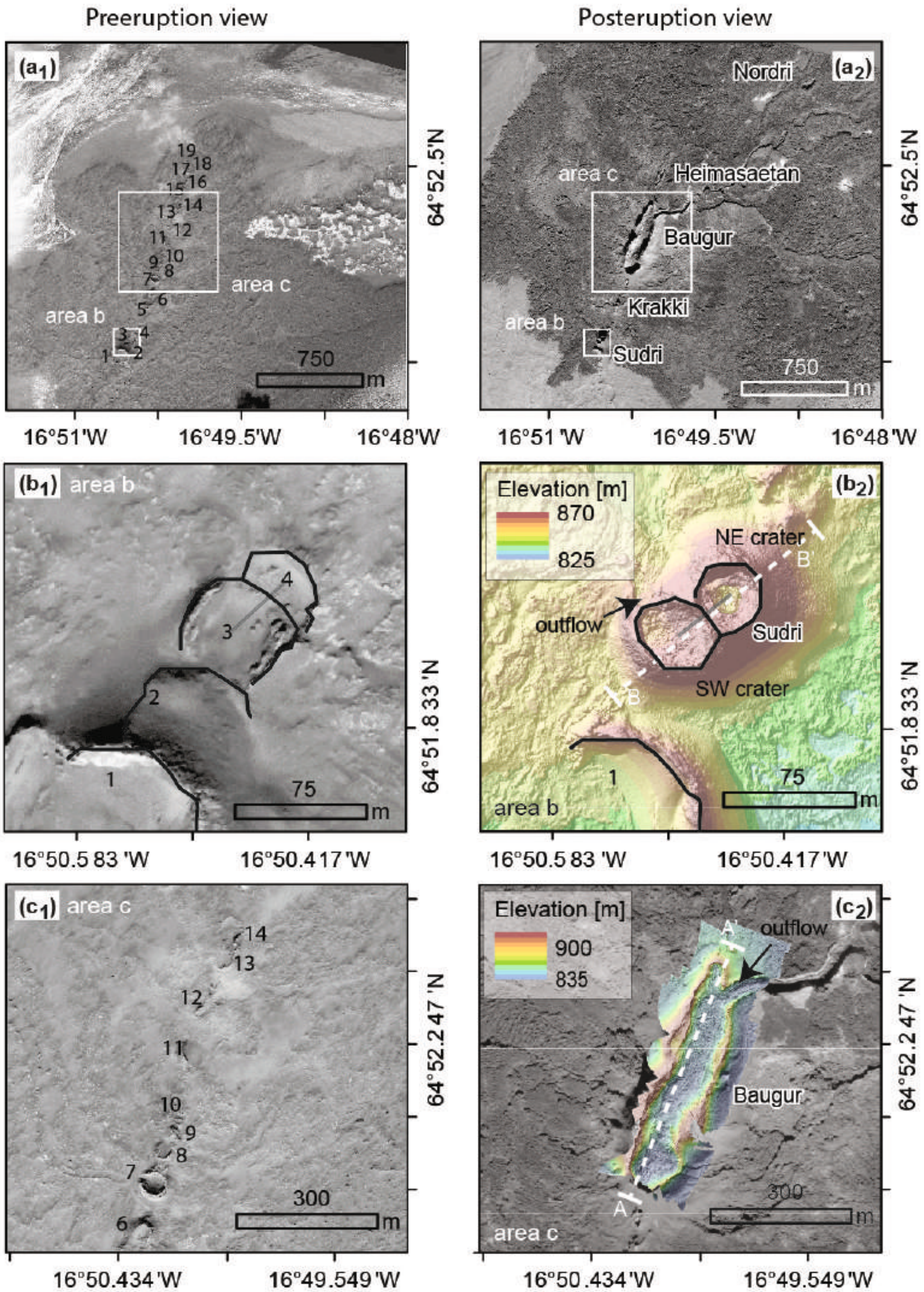

Figure 5.6: Morphology of the cones. a - The final topography of the Baugur and the Suðri cone generated by the Structure from Motion (SfM) algorithm with aerial photos of a field campaign in summer 2015. Right image (named with lowercase 2), based on DEM and hillshade, shows the topography after the eruption, and the left image (named with lowercase 1), based on WorldView-2, shows the topography before the eruption. The numbers indicate the different craters from previous eruptions, which were covered completely by the fresh lava. Closeup of the cones Suðri (b) and Baugur (c) using the same data. The profile lines of the cone morphology during the initial phase (Figure 5.7b_2 and c_2) are given in white. b - The outlines of the craters are given in black. The rim of the older cone 1 (b_1) can also be seen after the eruption (b_2). The orientation of cones 3 and 4 (b_1), and the SW and NE craters (b_2) are given in light gray. The orientation is the azimuth of the connecting line between the center points of the cone and craters. This orientation is similar for both situations. c - The Baugur cone (c_2) is located at the same place as the former cones 7 to 13 (c_1). The orientation of these row of cones (c_1) is the same as the elongation of the Baugur cone (c_2).

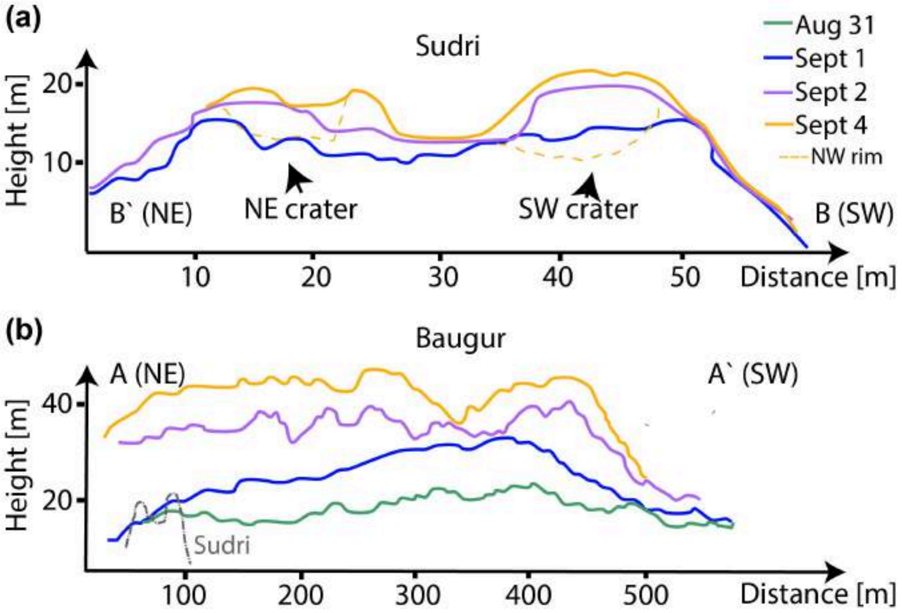

Figure 5.7: Evolution of the topography at the Suðri (a) and Baugur (b) cone during the initial phase. The height of the cones is calculated based on the baseline (see Figure 5.4 b). The days are color coded (green: Aug 31; blue: Sept 1; violet: Sept 2; orange: Sept 4). The location of the profile lines (A-A' and B-B') are shown in Figure 5.2 and Figure 5.6. The cone rim of the later Suðri crater on Sept 4 is shown in gray within the Baugur profiles (b) for better comparison. The dashed lines show the crater rim in the front, i.e., the crater rim in the NW.

2 to 4), the vents grew in height and width (see Table 5.3). At both vents, the rims were lower in the northwest (towards the camera position: see the dashed line in Figure 5.7) than in the southeast. The northeast slope was nearly constant at an angle of 57.4 ± 0.9°, whereas the slope in the southwest became steeper (58.2 ± 1.5°) (see Table 5.4). The southwestern vent grew faster than the northeastern vent. The depression between the vents was filled with erupted material from the fountains, establishing a shared crater rim. Therefore, the distance between the two vents decreased in length from 15.6 m to 7.1 m on Sept 4 (day 5 of the eruption). As the vents grew faster than the refilled depression, the vent height increased to 6.3 ± 1.0 m, even though the lower edge of the depression was higher (see Table 5.4 and Figure 5.7).

Table 5.4: Slope information of the flanks at Suðri The slopes are described as the angles with the corresponding standard deviation, general slope, and range of the slopes.

Date	**south-west cone**			**north-east cone**		
	$\angle_{SW}$ [°]	general [°]	range [°]	$\angle_{SW}$ [°]	general [°]	range [°]
4 Sept	58.2 ±		40.7 - 47.3	57.4 ±		51.9 - 64.7
Aug 2015 (final)	65.6	77.5 ± 4.0		SE: 73.4	79.7 ± 1.2	

Furthermore, an outflow of the southwest vent to the north-northwest can be observed starting on the evening of Sept 2 (day 3 of the eruption). The rim at the outflow is 16.9 m high, which is approximately 1 m lower than the rest of the cone rim. The next day, the difference between the outflow and the rim increased by up to 3 m.

The final morphologies of both Suðri vents as measured by UAV data are similar (see Figure 5.6). The cone rim is high in the southeastern part and decreases to the northwest. The depression is located to the southwest, and it is shifted closer to the cone wall between the two vents. The southwestern vent has an outflow in the northwest, resulting in a low cone rim height of 19.1 m. The mean slope of the flanks is high, 77.5 ± 4.0°, whereas we observe a lower slope at the southwestern flank. Both craters are symmetric and subelliptical (i.e., the min-to-max ratio of the basal diameter is 1.5) in map view, while the whole Suðri is an asymmetric, multiple superimposed cone.

In summary, by comparing the final topography with the initial eruption phase of Suðri, we can conclude that the main morphological features are established at the early stage of the eruption. The preferred outflow location at the southernmost cone can be identified in the initial phase. At the northern vent, the northwestern rim remains low during the whole eruption. The southwestern flank is steeper than the northwestern flank, both during the initial phase and after the eruption. During the eruption, the vents grow and become closer.

Baugur: The Baugur cone (see Figure 5.6) is elongated and has the largest expansion in the north-south direction (N18°E), aligned with the eruption fissure. Comparing the pre- and posteruption satellite data, we observe a consistent orientation between this eruption cone and previous cones (see Figure 5.6 c cone 7 - 12). The Baugur cone is the largest cone during the initial phase and during the whole eruption period (Pedersen et al., 2017), and the outflow at Baugur is the main feeder of the Holuhraun lava field (Figure 5.6 a). Baugur hosts a lava pond, which can be seen on aerial photos on Sept 1, 3 and 5 (see Chapter 6 Figure 6.1). Our camera data reveal that several fountains were active, which affected the cone morphology and the height might have been affected by the crater filling lava pond, which could be observed during the whole initial phase by flyovers.

Table 5.5: Cone morphology evolution of Baugur The basal diameter (2r), top diameter (2t), height (h), and slope in an orientation along the major axis (N-S) and the minor axis (E-W) of the elongated cone.

Date	**basal diameter** [m]	**top diameter** [m]	**height** [m]	**slope** [°]
31 Aug	456.24	392.92	8.92 ± 2.40	30 ± 7
1 Sept	465.80	250.82	21.74 ± 3.35	47 ± 8
2 Sept	467.10	332.80	25.36 ± 2.50	56 ± 13
4 Sept	467.94	377.29	33.36 ± 2.34	68 ± 7
Aug 2015 (final)	471.11	442.36	78.53 ± 1.00	69 ± 16

On days 1 and 2 of the eruption (Aug 31 – Sept 1, 2014), the cone was growing slowly. From days 2 to 3, we observed large morphology changes, as represented in Figure 5.7 (blue and green lines). During that period, the height grew from 11 % (47 ± 8 m) to 28 % (56 ± 13 m) of the final height (78.5 ± 1.0 m, see Table 5.5 for height values). On day 3, the cone rims in the south and north grew significantly and changed the shape from more hill-shaped to an elongated cone shape (Figure 5.7 b). Therefore, the basal diameter appeared quite stable, whereas the top diameter changed significantly. Due to the irregular growth of the cone over the length, the top diameter decreased between days 1 and 2 from 392.9 m to 250.8 m, respectively. After day 3, the main features appeared to be established, and the overall shape did not change much.

The final basal width and top diameter are irregular, as seen in the large range in the profiles from southwest to northeast (e.g., see Figure 5.11 and Table 5.6), with the northern region being slightly smaller than the southern region (see Figure 5.6 c). The height ranges from 51.4 to 105.5 m. Most of the variation in the Baugur height is hence found on the western and eastern flanks. The slopes in the east and west show large variations between 32° and 81°. The slopes in the north and south are very stable over the entire eruption. Baugur hosted a lava pond, which was the main feeder of the advancing lava flow through an outflow in the northeast (see Figure 5.6 c). The cone is a superelliptic, multiple coalescent cone.

Table 5.6: Final cone morphology of Baugur based on the drone surveys on Aug 14/15, 2015 The basal diameter (2r), top diameter (2t), and height (h) in an orientation along the major axis (N-S) and the minor axis (E-W) of the elongated cone.

Orien-tation	**basal diameter** mean [m]	range [m]	**top diameter** mean [m]	range [m]	**height** mean [m]	range [m]
E-W	195.30 ± 44.19	145.24 - 235.37	132.19 ± 29.27	75.55 - 185.67	65.02 ± 18.92	51.42 - 105.49
N-S	471.11		442.36		78.53 ± 1.0	

Baugur has an outflow channel located in the north and oriented to the northeast. This outflow has a basal diameter of 57.3 m, measured at the rim of Baugur, and a top diameter of 34.5 m. The height of the rim of the outflow is 63.7 ± 3.6 m above the surrounding lava fields and is 7 m higher in the north than in the south. Additionally, the slope in the north is 82°, which is much steeper than the slope of the outflow in the south, which is 65°.

In summary, the Baugur cone was the largest cone since the start of the eruption. During the eruption, the height of the cone increased significantly. Consequently, the final Baugur cone (Aug 2015) was approximate twice the height of the cone after the initial phase (Sept 4, 2014). The initial and final shapes of the Baugur cone show that it did not become significantly elongated. Overall, the spatial dimensions (width and elongation) and the large outflow could be identified on day 3 of the eruption. The video cameras viewing angles allowed the outflow channel morphology to be detected in the initial phase.

5.4.3 Comparison of the cone morphology at Suðri and Baugur

Suðri and Baugur both show a strong dependency on the preeruption morphology. Each of the cones hosts few vents. The orientation of the cones in the preexisting morphology was the same that in the posteruption cone morphology; the azimuths of the vents were N18°E (Baugur) and N57°E (Suðri).

The cones consisted of two small craters (Suðri) and one large crater (Baugur). Each crater hosted lava ponds (see Figure 5.1). The number of vents, i.e., lava fountains, for each crater changed with time. At Suðri, the vent number decreased to 2-3 during the first four days of the eruption, while Baugur hosted approximately 5 - 6 lava fountains on Sept 4.

The geomorphological shape of the cones is rather different. While at Suðri the vents are nearly circular, Baugur shows an elongated (superelliptical) vent with a clear orientation towards N18°E. Considering the growing vents, the overall shape of both cones is nearly stable, and many features and geometric characteristics are either found in the preeruption data (e.g., orientation) or formed at the beginning of the eruption (days 2-3; e.g., outflows and elongated cones/cones with two craters). At both cones, the growth of the crater rims was not equal, and the growth was remarkably faster at the some locations. This phenomenon can occur due to the position of the lava fountains (e.g., at Baugur) or due to the wind direction. One feature established during the first days of the eruption was a lava outflow (see Figure 5.6 b_2 and c_2). At Suðri, only one of the vents showed this outflow. Both flows were directed mainly northward but were released to different sides of the vents with Suðri to the NNW and Baugur to the NNE. Both show a slope steeper than 60° at the end of the initial phase and in the final morphology, but the slope at Baugur steepens later than that at Suðri.

5.4.4 Fountaining behavior - Height

The Holuhraun eruption started as a fissure eruption with an almost continuous line of 57 lava fountains. Our video monitoring data reveal that within the first 48 hours, the activity was focused at 4 main locations associated with the development of the cones. Commonly, the cones host 2 to 5 vents, which are partially separated in different craters (e.g., in 2 craters at Suðri). At each of the craters, we identify the highest and most active fountains. Over the whole time series, we observed pulses in fountaining, and consequently, we observed a strong short-term variation in the eruption height and width, which is mirrored in the large standard deviation of the mean height. The time between the pulses is shorter than the time the erupted material needs to fall down. Consequently, the lava fountain heights are always higher than zero.

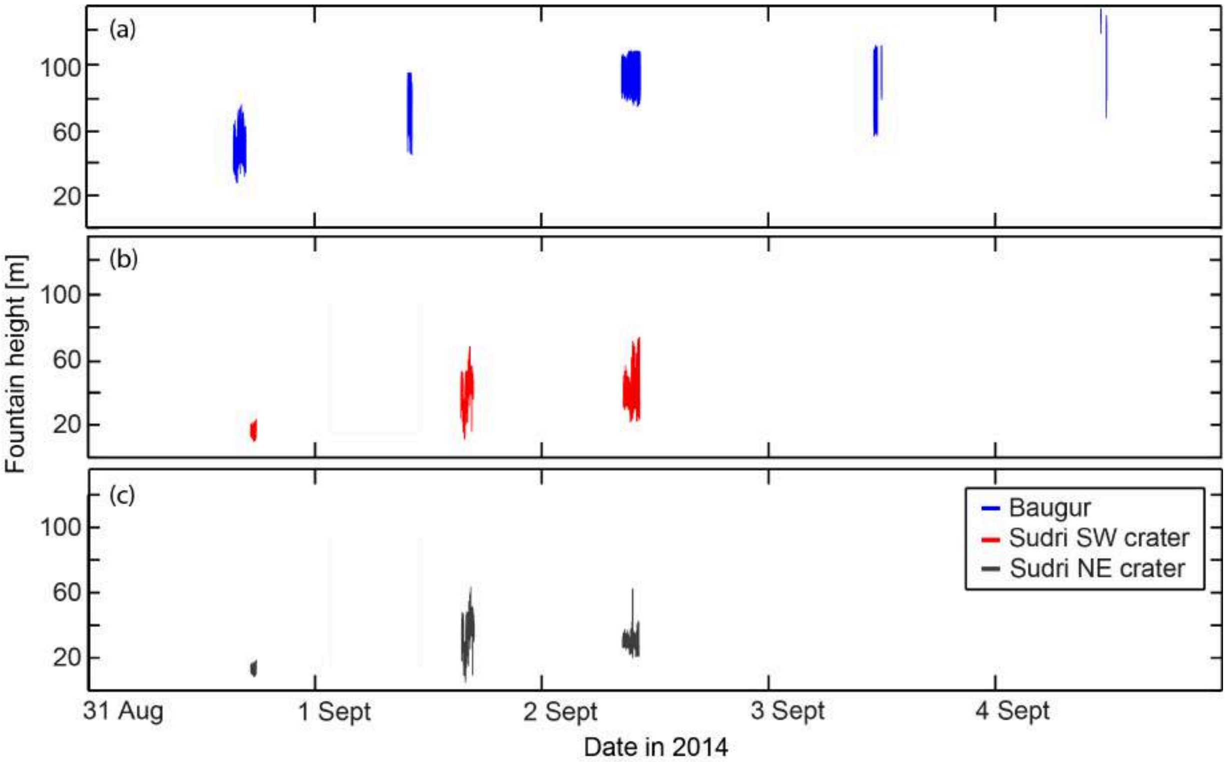

Figure 5.8: Fountain heights for Baugur (upper row) and Suðri (lower rows). Due to the pulsating behavior of the lava fountains the fountain height fluctuates. The time between the pulses is shorter than the time the erupted material needs to fall down. Therefore, the fountain heights at each vent do not go back to zero. The height is calculated as the difference between the highest fountain particles and the baseline b (see Figure 5.4a). Baugur and Suðri show an increase in the fountain height during the first three days of the eruption. On day 4, the mean height decreases. The lava fountain height at Baugur (a) shows the highest fountains with heights up to 130 m, while the fountains at Suðri reach heights up to 70 m (b, red line), with slightly lower heights at the northeast crater (c, black line).

Suðri: On the first day (Aug 31, 13:00 UTC), the lava fountain heights observed in the south were low. The mean height of these low fountains is 7.3 ± 2.7 m with a maximum height of 17.5 ± 0.3 m at the NE crater (see Figure 5.8 c) and slightly higher at the SW crater with mean fountain heights of 10.7 ± 3.6 m and a maximum height of 23.3 ± 0.3 m (see Figure 5.8 b). On day 2 (Sept 1), we observed a significant increase in the lava fountain heights reaching a mean height of 27.3 ± 13.7 m with a maximum height of 63.8 ± 0.5 m at the NE crater and a mean height of 29.3 ± 13.4 m with a maximum height of 67.5 ± 0.5 m at the SW crater. On day 3 (Sept 2), the lava fountain heights reached similar mean heights as the day before, and the activity was reduced to 4 fountains, with a mean height of 28.7 ± 7.1 m and a max height of 63.8 ± 0.6 m at the NE crater and a maximum height of 69.8 ± 0.6 m and a mean height of

31.5 ± 12.8 m at the SW crater (see Figure 5.8). The variation in the lava fountain heights at the NE crater is much smaller than that on Sept 1 and that at the SW crater, resulting in a more stable height. Two of four fountains at the Suðri cone are located at the multiple superimposed cone of Suðri, one fountain in each crater, and two fountains are between the Suðri cone and Baugur cone, close to the Suðri cone. The fountains in the SW crater are slightly larger than the fountains in the NE crater.

Baugur: The lava fountains at the location the Baugur cone forms during the next several days are the largest fountains in terms of height. On the first day (Aug 31), we observed fountains with heights up to 71.5 ± 0.4 m, with a mean height of 46.5 m and a standard deviation of 6.6 m (see Figure 5.8 a). These fountains were the highest in the line of fire on day 1 of the eruption. After focused venting began with fewer vents (day 2), the mean height of the main fountains further increased to 64.1 ± 12.4 m with occasional fountain pulses reaching a maximum height of 91.5 ± 0.3 m. On day 2, we observed 5 fountains, two in the northern part of Baugur, one in the southernmost part and two in the middle to southern part of the cone. The 2 in the middle appear dominant, much higher than the other three and increasing in intensity with time. The location of the highest fountains is between the middle and the southern parts of the Baugur cone. The fountain in the southernmost part appears separated from the others by up to 30 m and shows the smallest height, between 41 % and 58 % of the max fountain height. The two in the north are between 54 % to 75 % of the main fountains and 1.2 to 1.8 times higher than the southern fountains. The fountains in the middle are close together with a distance between them of 1.9 ± 0.9 m. On day 3 (Sept 2), the mean height has further increased to 92.2 ± 6.9 m with a pulsating maximum height of 105.7 ± 0.5 m. During day 4, the heights and fountain locations were nearly stable, with a mean height of 96.9 ± 13.3 m and a maximum height of 109.2 ± 0.2 m. On day 5 (Sept 4), the activity increased again to 126.4 ± 4.2 m and the highest fountain reached 133.0 ± 0.7 m. A slight decrease in heights was observed in the evening.

5.4.5 Height-to-Width Ratio

The height-to-width ratio is the maximum height of the lava fountain divided by its width at the same time. This height-to-width ratio clusters into two discrete groups - one for the fountains at Suðri (see triangles in Figure 5.9 a) and the other for those at Baugur (see squares in Figure 5.9 a). We find that the ratio is nonlinear; the height-to-width ratio of the fountains on the first day of the eruption is higher than that of the fountains at the end of the initial four days. In other words, the fountains first grow in height and then in width. Moreover, the ratio for each group becomes more stable with time, resulting in less scattering on the last day. We observe that the fountains at Baugur with the same width at those at Suðri are much greater than those at Suðri. The width of Suðri is clearly limited to the width of the craters (i.e., the inner radius of the cones), which are 24 m for the northeast vent and 32 m for the southwest vent. The mean height-to-width ratio (see Figure 5.9b) decreases at Suðri from 4.0 ± 0.8 (Aug 31) to 2.7 ± 0.5 (Sept 4), while at Baugur, we observe a decrease from 8.6 ± 1.8 (Sept 1) to 5.0 ± 0.9 (Sept 4), showing that at Baugur, the height-to-width ratio is 2.0 ± 0.2 times larger than the ratio at Suðri. The decrease in the ratio suggests that the relative increase in height is slower than the relative increase in width.

5.4.6 Comparison of the fountain dynamics between both cones

Both cones show an increase in the height of the fountains during the initial phase (see Figure 5.8) and a decrease in the number of fountains (see Figure 5.5 a). The variations at Suðri are smaller than those at Baugur, resulting in an unequal short-term fluctuation. The fountain

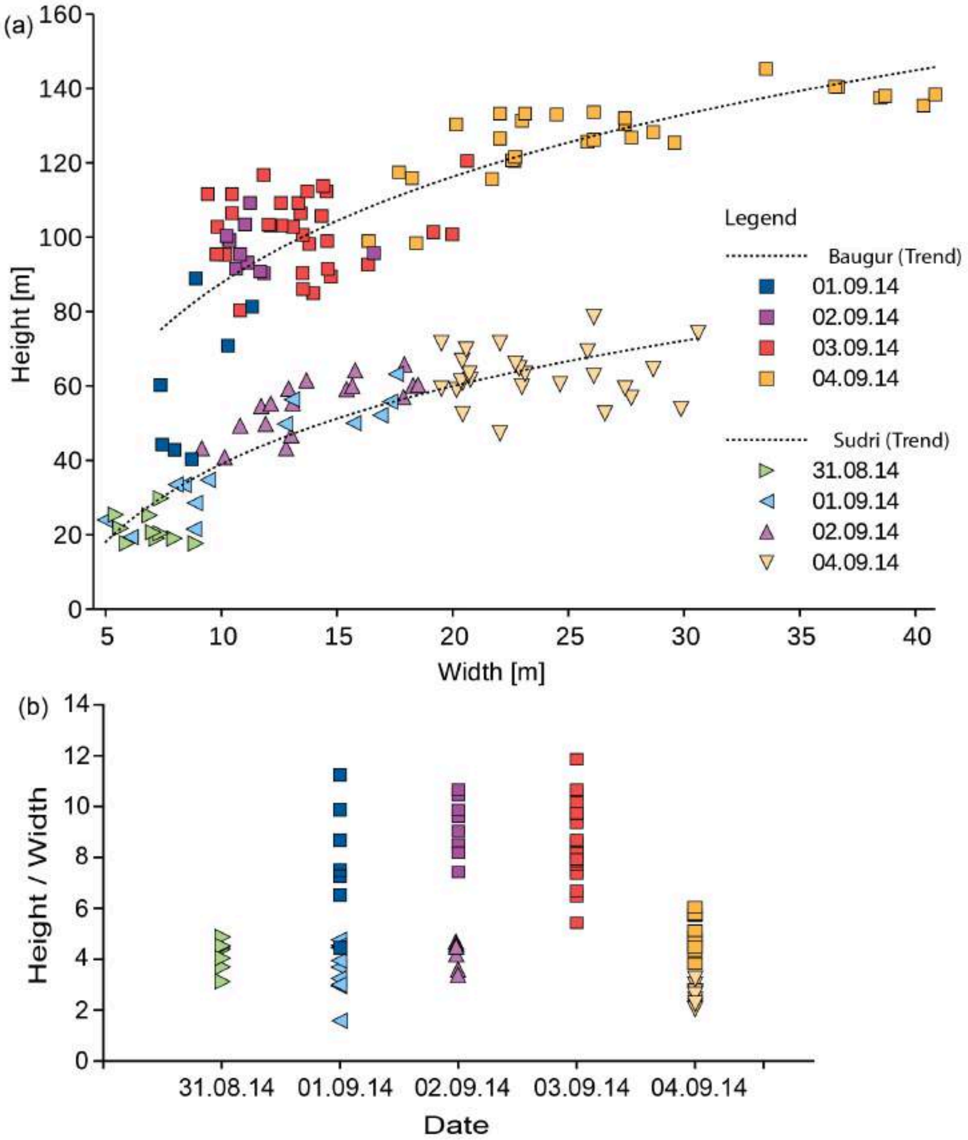

Figure 5.9: Height-to-width ratio of the lava fountains at Suðri and Baugur. a - The fountain height is the maximum height of the analyzed lava fountain pulse, and the width is the largest vertical extension at that time (see Figure 5.4). Each crater shows a specific cluster (Baugur as squares, Suðri as triangles and the time color coded). Both locations display an increase in height and width with time. b - The height divided by the width of the lava fountain for every day is plotted. Both cones (as in a: Suðri as triangles, Baugur as squares and the time color coded) show a decrease in the ratio over time. Furthermore, the ratio at Baugur is approximately twice the ratio at Suðri.

heights for the two craters at Suðri are similar to each other; however, the lava fountains at the SW crater are slightly higher. The lava fountains within the Baugur cone are much higher than those within the Suðri cone. Furthermore, the increase in the lava fountain height is stronger at Baugur. A similar behavior is seen in the comparison of the ratio between the height and width. We observe that the ratio at Baugur is twice the ratio at Suðri. In addition, both cones show a similar behavior as the ratio decreases with time.

5.4.7 Comparison of the morphology and the fountain dynamics

The lava fountain activity first occurred along a continuous fissure and then concentrated at distinct locations. We observed that the cones developed at locations where preexisting cones were located in the topography. As the fountains developed, their height increased and the number of fountains decreased. These fountains controlled the shape of the developing cones. We observed that lava ponds developed at the dominant fountain locations at both Baugur and Suðri. Moreover, we observed the largest changes in the spatter cone height and cone diameter in those areas for the most active and highest lava fountains. Additionally, near the outflow locations, the cone morphology appeared smoother (seen at Baugur and the NW vent of Suðri). At Suðri, we found that the SW vent grew faster than the other vents, where we observed slightly higher fountains during the whole eruption. At Baugur, several fountains formed in an elongated cone, while at Suðri, two fountains were hosted in two separated circular cones, which were connected. Therefore, at Baugur, we observed an interaction among the fountains, while at Suðri, the fountains were clearly separate. We conjecture that the differences in the fountaining behavior are induced by the different morphologies of the cones. However, the cones and craters allowed the generation of lava ponds, which in turn may have controlled the fountains as discussed in the following section.

5.5 Discussion

The 2014 – 2015 Holuhraun eruption in Iceland offered the unique opportunity to closely observe lava fountaining and measure topography at high resolution, allowing the study of the number and height of lava fountains and the changing morphology of associated spatter cones. Lava fountain eruptions show a characteristic evolution in their height and width at different cones during the first days of the eruption. Based on the ratio between width and height, we can distinguish between the different cones. Additionally, the cone morphologies evolved over the first 5 days, reaching a geometry that is similar to the final (posteruption) morphology, implying that the morphologic expression and focusing of fountains was established at the early stage of the eruption. We identified a large lava pond at the Baugur cone and smaller, separated vents at Suðri, including smaller lava ponds. Moreover, we observed the highest fountains at Baugur and smaller fountains at Suðri. Before discussing the possible interrelation between cone morphology, fountain height, and lava ponds, we will discuss the limitations of our data and analysis methods.

5.5.1 Limitation

The satellite data (WorldView-2) have a rather coarse resolution of ~ 0.5 m at best. The drone-based data, in turn, provide fine resolution at a 0.05 m scale but have the limitation that only dedicated areas could be mapped, such as the area of the spatter cone of Baugur. We selected key areas close to the two eruption sites: over these areas, we performed systematic surveys by drones and acquired video data. Therefore, while our database is robust for these key areas, other segments of the eruption site were not imaged by UAV. We could partially solve this problem by combining the UAV -based results with a TLS campaign. The TLS instrument had a scan range of up to 6 km, allowing even distant objects to be measured with high precision, although the point coverage decreases with distance. Consequently, we obtained a very good resolution for our two main cones.

In general, optical and infrared cameras transported on aircraft or on UAVs allow the detection of small-scale changes in topography and thermal anomalies (Nakano et al., 2014; Tiede et al., 2005). The analysis of volcanic areas based on cost-effective UAV data acquisition techniques is gaining importance (Amici et al., 2013b; Müller et al., 2017; Nakano et al., 2014). Nevertheless, some practical and technical problems may occur mainly due to complex terrain, wind (which may cause drone crashes), and changes in sun position (that may reduce the quality of the images). As the development of drones is quite rapid, newer UAVs that allow longer flight times and distances can possibly lead to improved data coverage for future campaigns. As the achievable quality of the DEMs depends critically on the quality of the photographs, systematic issues, such as oblique angles to the ground or coarse resolution, are directly transformed into geometric errors. As the SfM point could tend to bend at the edges, our data between the Sudri crater and the Baugur crater are quite limited. To minimize the effect of the bending and minimize camera internal errors (e.g., due to the use of uncalibrated cameras, James and Robson, 2014), we checked and corrected our UAV dataset using a TLS dataset. Nevertheless, for the crater, the accuracy is usually on the order of a few centimeters. Flight heights of 100 to 150 m limit the resolution and therefore, the accuracy of the 3D model reconstruction. This limitation has to be taken into account at very steep flanks.

Video monitoring data are simple to acquire during fissure eruptions and provide a unique data source, as demonstrated in this work. However, only very few videos exist for eruption fountains where the camera position was held constant for minutes or even hours. In most cases, handheld cameras or only a few tens of seconds of recordings are available (Spampinato et al., 2008; Witt and Walter, 2017). However, video monitoring contains various sources of systematic and nonsystematic errors. Potential error sources may arise from geometric effects (survey design and optics), temporal and spatial resolutions, random factors (such as atmospheric conditions, e.g., steam, ash or cloud cover), and operator errors occurring during recording (e.g., shaking or camera position) and/or during image analysis (Diefenbach et al., 2013; Major et al., 2009). One of the main sources of errors during data collection is the camera itself because of distortions in the images, which are also difficult to quantify (Formenti et al., 2003). The distortion is largest at the edges of the FOV; therefore, we concentrate the study on the fountains at the middle of the images. Here, the cameras were situated a few kilometers from the cones, which is why the resulting distortions of the important areas are assumed to be small. Areas that were too far for video recording were not investigated further, such as the northern part of the fissure. Therefore, the 57 identified vents may be an underestimate of the total number of vents.

The videos were not recorded continuously and at all cones simultaneously, and the timing and geometry of acquisition were not optimal. The videos are up to two hours long; thus, we can resolve only short temporal disparities and not the whole eruption development. Although we observe very stable results during the 5-day eruption episode, we cannot determine whether the variations described by our data remain stable, show daily variations or other interdependencies. The camera positions had to be changed repeatedly due to the lava field advancing towards us and due to the changing wind conditions exposing us to haze. As a result, the distance to the vents increased during the different recording days (see Figure 5.2). The most problematic aspect of changing recording position is the change in the FOV and viewing angle, which had to be recalculated for the comparison of the morphology analysis.

Due to windy weather conditions, the cameras were subject to small amounts ofshaking, even though we used robust and heavy tripods. Furthermore, high winds transported ash through the air. As a result, videos appear blurred and small fragmented particles are more difficult to detect on these days (Sept 1 and Sept 2 at the end of the recording). Additionally, due to hot air, the same blurring effect can occur (Aug 31 at the northern part). Consequently, the pulses of one vent may interfere with the pulses of adjacent vents, especially at Baugur, and the results of individual vents can be biased by spatters from adjacent vents. These interfering activities complicate the calculation of fountain widths, especially at Baugur. Here, we had to manually distinguish between the different fountains. At Suðri, the effect was negligible due to the separated vents.

Subpixel variability, related to changes in the surface characteristics (e.g., color or shape) and to rotational movements of the irregular spatters, can affect the results of our imaging technique (Walter et al., 2013b). With decreasing particle brightness (due to cooling of the lava), the pixels can be categorized as background and not as particles. Consequently, the size and height might be underestimated. To evaluate the impact of this underestimation, we performed a periodical manual check of the height, showing that this effect was less than the 2 % of the height.

5.5.2 Model of lava fountains

To discuss the observed variations in the height of lava fountains and the associated morphologic development of spatter cones and lava pools, we formulate a simple conceptual and physical model. The height of the lava fountains is a function of several factors (Parfitt et al., 1995): the content of exsolved gas within magma, the eruptive volume flux, the amount of re-entrainment of degassed lava, the magma rise speed, and the degree to which bubble coalescence effectively depletes gas from the magma. We calculated the lava fountain heights, which combines the results from 3 model parts: the first is based on a Poiseuille flow within the underlying dike, the second is based on magma and bubble ascent in the feeding conduit (Gonnermann and Manga, 2013) and the third part is a lava fountain model influenced by conduit diameter and lava pond depth (e.g., Wilson et al., 1995, 1980). The lava fountains of the 2014 – 2015 Holuhraun fissure eruption are thought to be fed by vertical conduits with a length of ~ 300 m (Eibl et al., 2017a), rooting at the dike beneath (Ruch et al., 2016; Sigmundsson et al., 2015). As we calculate the lava fountains after the channelling of the magma is established and after the seismic tremor is seen at that depth, this is a acceptable assumption. We use the Holuhraun eruption and dike parameters given in previous studies (see Table 6.1 in the Chapter 6), and the lateral magma flow velocity in a dike of length L is calculated by $v_z = \frac{\Delta P \cdot R^2}{4 \cdot \eta \cdot L}$, with an excess pressure driving the magma ΔP of approximately 1.6 MPa, a dynamic viscosity η of 100 Pa s and an average dike radius R of 7.5 ± 0.3 m (Ágústsdóttir et al., 2016). Magma propagation velocities of 2.3 m/s within the dike have been estimated based on an initial flow rate of 400 $\mathrm{m^3}$/s, which is in agreement with observed propagation rates (Ágústsdóttir et al., 2016). The above formulation suggests a flow velocity v_z of 2.58 ± 0.14 m/s within the lateral dike. This formulation is in good agreement with our calculation, although we expect a high Reynolds number (~ 310 ± 100), indicating the absence of pure laminar flow. Assuming laminar flow within the horizontal dike, a velocity v_z of 2.58 ± 0.14 m/s, a depth of vertical feeder conduits of 300 m (Eibl et al., 2017a) and a water vapor content of 0.5 wt% (Gíslason et al., 2015), we calculate the height of the expected fountains exceeding 300 m even for narrow vertical conduits (see eq. 5.4). The depth of the vertical feeder conduits is based on the analysis of the graben structure at the surface. The resulting lava fountain heights are much larger than the observed 133.0 ± 0.7 m height at the Baugur crater during the day 5 observations, although we note that the height might have increased later.

A slight decrease in the depth of the feeder conduit h (cf. Figure 5.10 a and Table 6.1 in the Chapter 6) would decrease the initial lava fountain height $H_{initial}$ (see eq. 4). An error of a few meters of h would affect the height change by less than 2 %. Therefore such an error could not explain the observed heights. The propagation velocity within the feeder dike with the given errors ($v_z = 2.58 \pm 0.14$ m/s), leads to a variation in the lava fountain heights of a few meters only. Compared to the absolute heights of hundreds of meters, this effect is minor. In comparison, a larger influence on the lava fountain height results from the variation in conduit radius r, which we investigated by varying this parameter. However, the range of radii investigated (2-3 m for both, Sudri and Baugur) produce lava fountain heights that are higher than the observed heights, implying that the radii are even smaller, or that another factor might reduce the eruption height. Altogether, for a constant magma pressure, the two factors that have largest influence on the fountain heights are (i) the conduit radius r, and (ii) the depth of the lava pond h_{pond} that is effectively reducing H as demonstrated in the following.

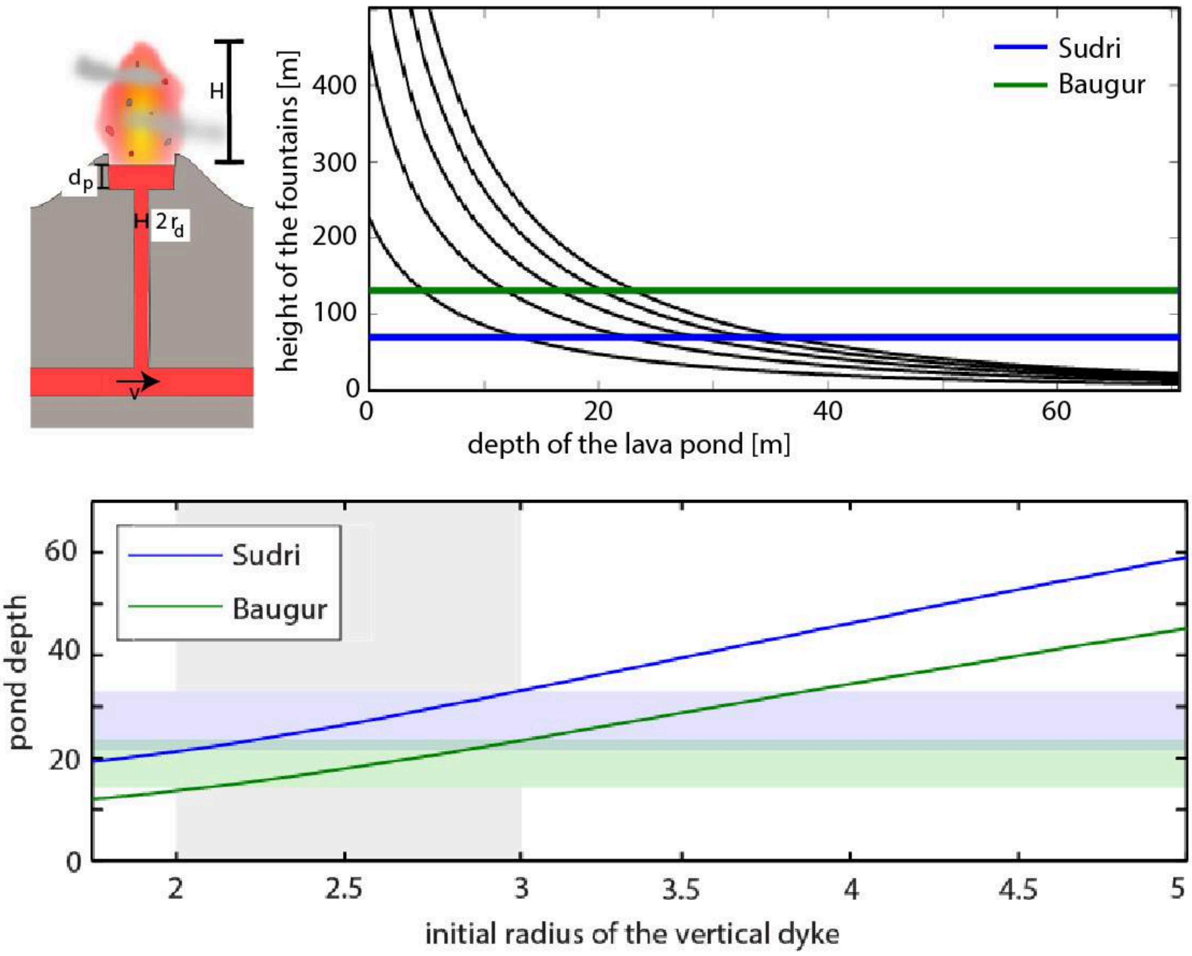

Figure 5.10: Model of fountain heights. a - Sketch of the model with fountain height H, pond depth d_p, dike radius r_d, and the velocity within the underlying feeder dike v. b - The height changes depending on the pond depth d_p are included as a model parameter. The different black lines are related to different initial lava fountain heights. The observed heights of the lava fountains at Baugur are shown in green and at Suðri in blue. The observed heights used are from Sept 2 and 4, when the channeling of the magma is already established. c - Resulting pond depth based on an initial radius of the vertical dike for Suðri (blue) and Baugur (green). The gray area highlights the range of opening of the underlying feeder dike and, therefore, assumed conduit diameters. The light blue and light green areas are the corresponding pond depth areas for Baugur and Suðri, respectively.

The development of lava ponds might strongly affect the height of fountains. As we showed earlier, the cones were growing as lava ponds were filling within their craters. Based on Wilson et al. (1980) and Wilson et al. (1995), we modified the fountain height formulas to account for a magma pond on top of the dike (see Figure 5.10 a). Consequently, the lava fountain height decreased. The initial height of the lava fountain, $H_{initial}$ (i.e., the height in a pond-free condition), is related to the radius of the feeding conduit r, the driving pressure $\partial p/\partial z$ and the viscosity of the magma η, where g is the acceleration of gravity and is calculated with the values given in the Chapter 6 by

$$H_{initial} = \frac{1}{2g} \cdot (\sqrt{\frac{\partial p}{\partial z} \cdot \frac{r^2}{4\eta}} + v_z)^2 \tag{5.4}$$

Comparing the model results with the actual height observation video data, we can infer the depth of the pond and the width of the conduit. As a first step, for a given conduit radius, we calculate the resulting magma ascent velocity in the conduit. Based on that velocity, we calculate the fountain height and the corresponding lava pond depth. The dike opening is well constrained by GPS and InSAR data and is between 4.5 m and 6 m (Ruch et al., 2016; Sigmundsson et al., 2015). However, the vertical connection to the vents is more difficult to constrain. The radius of the conduit in our model is between 2 and 3 m, which results in a mean radius of 2.5 ± 0.4 m for these conduits. The initial lava fountain height $H_{initial}$ is calculated based on the velocity within the conduit. For the different pond depths, we iteratively calculate the resulting velocity at the surface due to re-entrainment (see formulas in the Chapter 6). The deeper the pond is, the larger the entrainment is, and therefore, the lower the lava fountain is. By each iteration, the entrainment based on the pond depth and velocity is calculated. As the entrainment reduces the velocity, these steps have to be calculated several times until the entrainment and resulting velocity are stable. The formulas and parameters for the entrainment and height calculation can be seen in the Chapter 6 (equations and table with the model parameters) and in further detail in Wilson et al. (1980) and Wilson et al. (1995).

With the radii range for the cones, we obtain lava pond depths between 22.9 and 33.5 m at Suðri, and the pond depth at Baugur ranges between 13.6 and 24.2 m (see Figure 5.10 b and c). This result means that the ponds at the Suðri vents are approximately 1.6 times deeper than the pond at Baugur. The conduit radius correlates quadratically with the initial lava fountain height $\mathrm{H}_{initial}$ (see eq. 5.4). Therefore, for the same height, the higher the exit velocity is, the larger the pond depth d_p. If we set the feeding conduit radius for the different cones separately, we obtain pond depths ranging between 22.1 and 25.2 m at Suðri and between 16.9 and 24.2 m at Baugur, resulting in similar pond depths for both cones of 23.2 ± 1.0 m and 21.1 ± 2.9 m, respectively. Therefore, the feeding conduit radii range between 1.9 and 2.25 m at Suðri and between 2.3 and 3.1 m at Baugur. A larger conduit will furthermore result in a larger discharge rate at Baugur than at Suðri, which we can observe at the eruption site. The discharge rate can be estimated from the lava field fed by these conduits. Previous papers (Dirscherl, 2016; Müller et al., 2017; Pedersen et al., 2017) show that Baugur is the main feeder of the eruption. Therefore our result fits well with their results.

5.5.3 Implications of the study

Our observations show an increasing fountain height, growing cinder cones, and lava pond formation, while the number of eruption vents decreases. Similar behavior can also be observed elsewhere. At Kilauea, the eruption in 1969 (Parcheta et al., 2015) and the most recent eruption in 2018 (USGS, 2018) show the decrease and focusing of activity at few vents. This focusing occurs at the beginning of the eruption. This implies that the channeling of the magma emerges over time by solidification of less active parts of the fissure (Bruce and Huppert, 1990). It should be noted that the eruption activity ends first in the north, where the tip of the dike is located. From this, it can be deduced that the heat transport at the tip of the dikes decreases. Such a lower heat transport would lead to a higher cooling by the surrounding bedrock and thus support the formation of channels. This explains why the focusing and the stop of activity is seen first in the northern part. At the Kilauea eruption in 2018, the largest lava flow is fed by an outflow at the cone, where the initial fissure occurred, although a further propagation of the feeder dike can be observed. Due to this propagation new cones were formed. The activity at these newer cones stopped before the activity at the initial cone had decreased. This result shows the importance of studying the eruption behavior at the beginning of the eruption. The analysis of eruption behavior based on changes in lava fountain height and cone morphology (e.g. cone orientation and extension or outflow) can also be applied to eruptions at central vents, while the analysis of lava fountain activity focusing and channel formation is limited to fissure eruptions.

Based on our model calculations, a clear dependency exists between the fountain height and the initial exit velocity, the lava pond depth, and magma flux. Consequently, the differences between the observed craters Baugur and Suðri (i.e., higher fountains at Baugur) can either be explained by a higher initial velocity due to a wider conduit or by a lower pond depth. Based on inspection of the final geometry and the observation of a higher discharge rate at Baugur, we conjecture that at Baugur the lava fountains were higher due to a locally larger diameter of the conduit. As reported in Eibl et al. (2017a), the magma supply at Baugur occurs through different fingers of the dike. Variations in explosion behavior due to the complexity of the upper conduit system could also be observed at other volcanoes, e.g., Volcán de Colima. Therefore, the modelling of lava fountains at different times could give us information about changes in the complex conduit system or the lava pond depth within cones at fissure eruptions or central vents. We suggest that differences in the maximum height at the different lava fountains within the Baugur pond may occur due to different radii of these fingers.

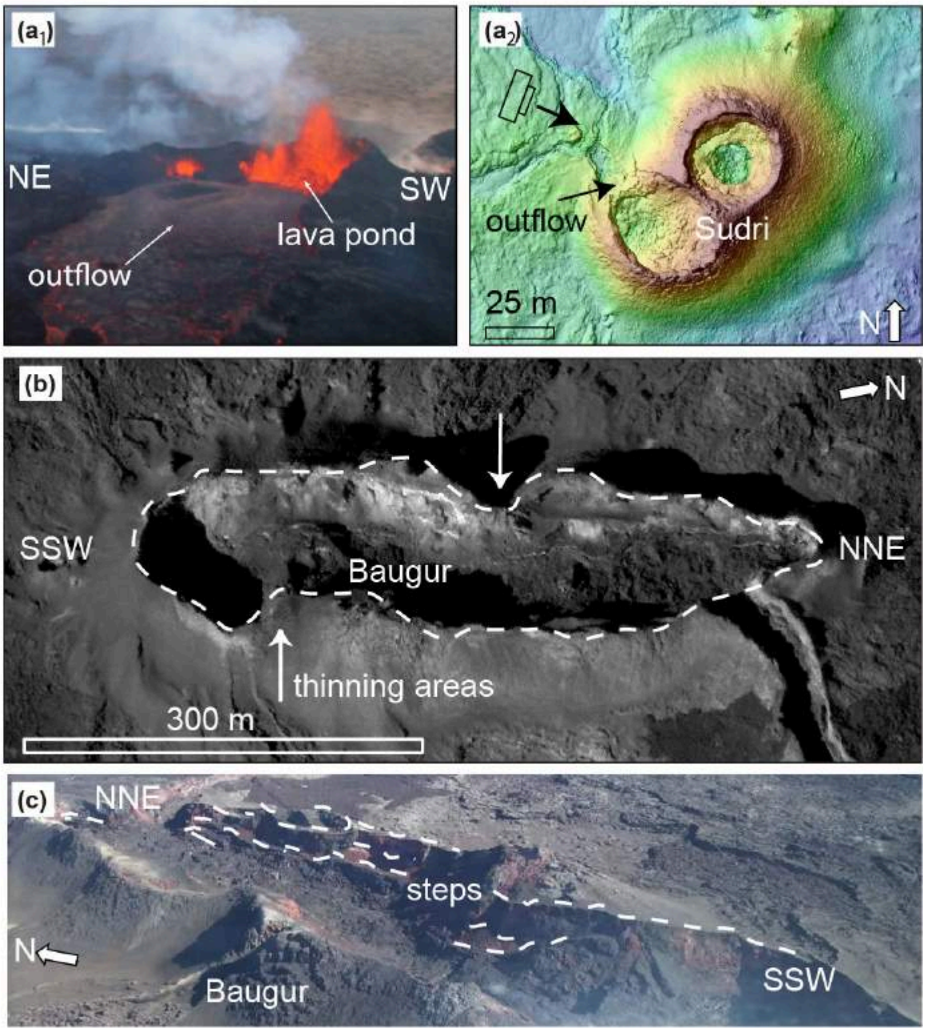

Figure 5.11: Features inside the different cones. a - Lava outflow at Suðri and the lava pond inside (a$_1$). The photo is taken by Tobias Dürig. Within the final cone morphology the outflow illustrated and the viewing direction of the camera in a$_2$ is shown. b - Thinning areas within the Baugur cone in the final cone morphology (Aug 2015). The crater rim is highlighted in white and shows variations in the width (in the WNW-ESE direction). c - Steps (dashed white lines) that form terraces within the final cone morphology of Baugur. The terraces are best seen on the inner slopes in the ESE direction.

A comparison with the final morphology of Baugur taken from the aerial photographs reveals morphologic steps resembling terraces (see Figure 5.11c, steps in dashed white). These terraces are seen at different locations and elevations, suggesting that the lava pond depth varied between 13.67 and 35.53 m (24.29 ± 6.96 m). Therefore, the results from the modeling of 21.1 ± 2.9 m are within a reliable range of values. The final morphology of Suðri does not show similar terraces. Therefore, direct validation of the pond depth computed for Suðri is not possible.

During the first two days of the eruption, we observed lava fountain heights smaller than those after focused venting at several vents. This result can be explained by our model, assuming deeper lava ponds or a thinner feeder conduit. However, a deeper lava pond does not seem reasonable, due to the morphology of the cones. The height of the lava pond is limited by the height of the vents. As we identify the outflow channels at the SW vent, the maximum depth is approximately 30 m and at the NE vent, the maximum height is approximately 32 m. Based on the model, we would expect a conduit radius of greater than 2.9 m. As a consequence, the limitation of the pond depth results in a radius that is smaller than the radius at Baugur. Therefore, the lower heights of Suðri cannot be caused by only a greater pond depth and might be mainly caused by a thinner feeder conduit.

An initial widening of the feeder conduit at the beginning of a fissure eruption at stable vents has been proposed earlier by Bruce and Huppert (1990). Furthermore, Eibl et al. (2017a) shows that the long-period (LP) tremor activity is focused during the early eruption days, and the tremor at Baugur increased on Sept 2 when we observed a significant change in the height data. This result can be due to changes beneath the surface, such as dike widening, conduit formation, or pressure changes. All these factors would result in a higher initial lava fountain height.

The main differences between the Baugur and the Suðri group can be explained by the feeder conduit diameter and pond depth. As we assume that both cones are fed by the same lateral dike, the overall characteristics should be determined by the same source. As the overall behavior of the fountains is similar (increase in the fountain heights) at all cones, we suggest here a mechanism that is routed deeper than the feeder conduit or the pond depth. A possible explanation may be a slowly increasing magma flux, due to stabilizing flow within the lateral dike or a small pressure increase within the lateral dike. Furthermore, a widening of the dike would increase the maximum flux velocity within the dike (v_z) and therefore the fountain heights.

The possible applications of this study can be divided into technical and scientific findings. The technical developments presented by us to study the lava fountain height and morphology of the cones can be similarly applied to other fissure eruptions and volcanoes with lava fountains, such as at Mount Etna. The scientific findings, i.e. the observation and analysis of a decrease of the number of vents, the focusing of the eruption activity and the formation of cones at these vents might be similarly found at other fissure eruptions, such as Mount Ulu (1969) or Kilauea (2018).

5.6 Conclusion

At the 2014 – 2015 Holuhraun fissure eruption site we carried out video monitoring of the lava fountains and recorded the evolving morphology of the scoria cones. We identified a decrease in the number of active vents producing lava fountains from 57 to 10 during the first five days of the eruption. The decrease occurs due to the establishment of magma channels from the dike to the surface. The channels are generated by solidification of the parts of the fissure that show lower activity and therefore have a lower heat transport. After two days the fountain activity became mainly focused at 10 vents located within 4 distinct craters (Norðri, Baugur and two at Suðri). The morphology of the cones was defined by preexisting topography characterized by cones and lava flows of the 1797/1798 eruption. Posteruption drone data showed that Suðri cone hosted two circular and separated craters, whereas the large and elongated Baugur cone hosted up to 5 fountains within one crater with a major lava pond that was changing in elevation with time. We can conjecture that the initial fountaining and the preexisting morphologic setting had a large influence on the final morphology of the eruption site, as the cones reactivated at the same locations as the previous eruption in 1797/1798.

Similar overall characteristics, such as an increase the height with time and pulsating behavior, were found at both cones, Suðri and Baugur, and the fountain pulses were not synchronized and displayed a small time shift. For each cone, we found a characteristic ratio between height and width. The ratio between height and width was nonlinear and was nearly double at Baugur compared to Suðri. During the first days of the eruption, the ratio decreased from 8.6 to 5.0 at Baugur, and from 4.0 to 2.7 at Suðri, indicating a faster increase in width than in height. We observed the greatest morphological changes within the cones at those sites where we observed the largest fountains. A single fountain occurred at circular vents that were classified as multiple superposed cones, whereas vents with multiple fountains were elongated and were classified as multiple coalescent cones.

From the modeling of the fountain heights, we estimated pond depths of $26.4 \pm 1.5\,\mathrm{m}$ at Suðri and $23.7 \pm 4.8\,\mathrm{m}$ at Baugur. These pond depths are consistent with the morphological steps seen within the Baugur cone and fit with the overall cone morphology. The resulting feeder conduit diameter was between 3.8 m and 4.5 m and between 4.4 m and 6.2 m for Suðri and Baugur, respectively. Long-term eruption behavior was controlled mainly by deeper eruption parameters, such as pressure changes in the dike, whereas smaller, local changes, as well as the maximum height of lava fountains, were mainly controlled by the feeder conduit diameter and the depth of the lava pond.

Conflict of Interest Statement

The authors declare that the research was conducted in the absence of any commercial or financial relationships that could be construed as a potential conflict of interest.

Author Contributions

TW collected and processed the dGPS data and video data, performed the analysis of data, and did the modelling of the lava fountains. She led the writing of the manuscript. DM collected the helikite data and processed the DEMs. TRW collected multicopter data and analyzed data. AS collected and processed TLS data. MG was involved in data interpretation and the writing of the manuscript.

Acknowledgments

This work contributed and was partially supported by the FUTURE-VOLC project. We especially thank the IMO for releasing detailed monitoring information from the Holuhraun eruption. Financial support came from an expedition fund of the GFZ Potsdam. This is a contribution to VOLCapse, a research project funded by the European Research Council under the European Union's H2020 Programme/ERC consolidator grant ERC-CoG 646858. We thank Ármann Höskuldsson for support during field works, and Francesco Maccaferri for improving our manuscript by commenting. Moreover, we thank the DLR for providing the TanDEM-X data set that was used to derive a topographic base map of the region. The Tandem-X data analysis in this work is considered as a contribution to the Helmholtz Alliance EDA. All data used is available on request.

Chapter 6

Supplementary Material for chapter 5

6.1 Equations for modelling the lava fountain heights

The development of lava ponds might strongly affect the height of fountains. Based on Wilson et al. (1980) and Wilson et al. (1995), we modified the fountain height formulas to account for a magma pond on top of the dike. Consequently, the lava fountain height decreased. The initial height of the lava fountain, H$_{initial}$ (i.e., the height in a pond-free condition), is related to the radius of the feeding conduit r, the driving pressure $\partial p/\partial z$ and the viscosity of the magma η, where g is the acceleration of gravity and is calculated with the values given in the Table 6.1 by

$$H_{initial} = \frac{1}{2g} \cdot (\sqrt{\frac{\partial p}{\partial z} \cdot \frac{r^2}{4\eta}} + v_z)^2 \tag{6.1}$$

The reduced lava fountain height in a vent with the pond depth h_{pond} is calculated by

$$\begin{aligned}
\beta_a^{-1} &= \frac{nQT}{mP_a} + \frac{1-n}{\rho_L} && (6.2)\\
u_a &= \sqrt{2gH_{initial} + (n-0.5)\cdot 1625} && (6.3)\\
r_a &= \sqrt{\frac{M}{\beta_a u_a \pi}} && (6.4)\\
P_{pond} &= P_a + \rho_{pond} g h_{pond} && (6.5)\\
\beta_{pond}^{-1} &= \frac{nQT}{mP_{pond}} + \frac{1-n}{\rho_L} && (6.6)\\
u &= \sqrt{2\left(u_a^2/2 + gh_{pond} - \frac{nQT}{m}\cdot\log(P_{pond}/P_a) - \frac{1-n}{\rho_l}(P_{pond}-P_a)\right)} && (6.7)\\
r_m &= \left(r_a + \sqrt{M/\beta_{pond}u\pi}\right)/2 && (6.8)\\
\rho_m &= (\beta_a + \beta_{pond})/2 && (6.9)
\end{aligned}$$

Now we iterate over following equations until we get negligible changes, starting with $u_m = (u_a + u)/2$:

$$\begin{aligned}
M_i &= 2\pi r_m h_{pond}\rho_{pond}\alpha u_m\sqrt{\rho_m/\rho_{pond}} && (6.10)\\
u_m &= (u + \frac{M}{M+M_i}u_a)/2 && (6.11)
\end{aligned}$$

The resulting height can than calculated by $H_{fount} = u_f^2/(2g)$

6.2 Supplementary Tables and Figures

6.2.1 Table of modelling parameters

Table 6.1: Parameters for the modelling Parameters used for the modelling of the lava fountain heights. The parameters are grouped general parameters, feeder dyke related parameter (exceeding dimension), spatial dimension, and magma specific parameters.

Symbol	Parameter	Value	Reference
g	acceleration of gravity	9.81 m/s^2	
m	molare mass of water	18.018 g/mol	
P_a	atmospheric pressure	0.1 Pas	
Q	gas constant	8.3145 J/K·mol	
ΔP	excess driving pressure	1.6 MPa	Ágústsdóttir et al. (2016)
v_z	flow velocity (feeder dyke)	2.58 ± 0.14 m/s	Ágústsdóttir et al. (2016)
h	depth of vertical feeder conduit	300 m	Eibl et al. (2017b)
L	feeder dyke length	48 km	Sigmundsson et al. (2015)
R	average dyke radius	7.5 ± 0.3 m	Ágústsdóttir et al. (2016)
r	radius of feeding conduit	4.5 - 6.5 m	after Sigmundsson et al. (2015); Ruch et al. (2016)
α	constant of proportionality	0.08	Wilson et al. (1995)
η	dynamic (magma) viscosity	100 Pas	Ágústsdóttir et al. (2016)
ρ	magma density	2500 kg/m^3	Ágústsdóttir et al. (2016)
ρ_{pond}	magma density within the pond	1000 kg/m^3	Wilson et al. (1995)
ρ_l	density of the bubble-free magmatic liquid	2600 kg/m^3	Wilson et al. (1995)
M	total magmatic flux	6.75e5	Gudmundsson et al. (2016)
n	water vapour content	0.5 wt%	Gíslason et al. (2015)
T_K	temperature of the magma	1173 - 1473 K	Gíslason et al. (2015)

6.2.2 Figures

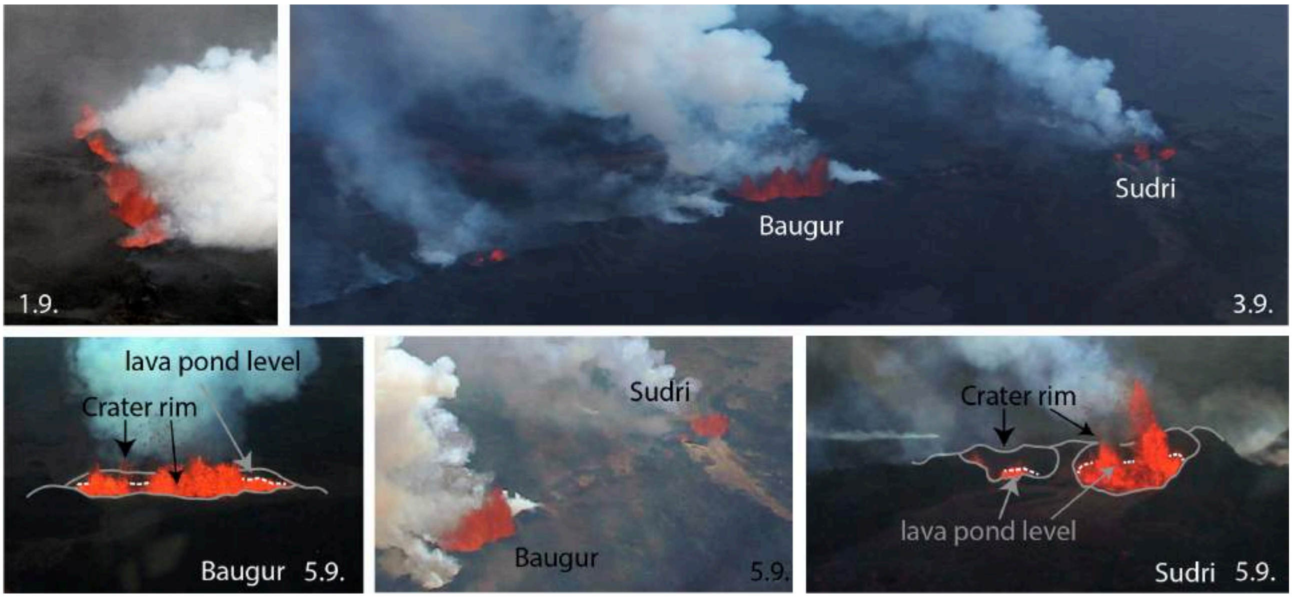

Figure 6.1: Lava pond within the cones The lava pond in the cones of Suðri and Baugur are clearly seen in the images. The magma level (red lines) is lower than the crater rim (gray lines). The images were taken during overflies by Tobias Dürig (Sept 1 and 3) and Magnus Tumi Gudmundson (Sept 5).

Chapter 7

Summary and Discussion

In this thesis I analysed the lava fountain dynamics of fissure eruptions, and compared the results with other geophysical and geological data, such as the geomorphologic and structural expression. I showed the potential of video analysis as part of a volcano monitoring system. This lava fountain dynamic analysis included the lava fountain height, the velocity and the relationship between aligned lava fountains. The study highlighted the complex relationship between focussed flow through dykes, morphology of the cones, and dynamics of the vents of an eruptive fissure.

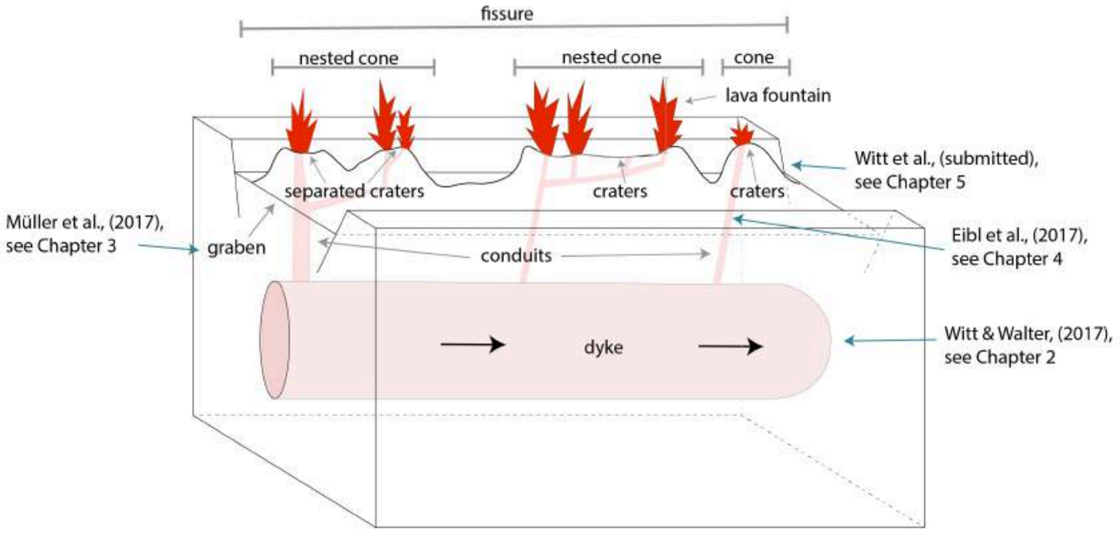

Figure 7.1: Area of a cone-building fissure eruption Similar illustration as in Figure 1.2, but highlighting the subject of each chapter in dark cyan. Chapter **??** analysed the velocity of pressure waves in the main dyke. In Chapter 4 the conduit and vent opening is studied. While, Chapter 3 and Chapter 5 discussed the morphology of the graben system and the morphology of the eruptive vents.

The method used for lava fountain monitoring is flexible and can also be used for the detection of the height of ash clouds or geyser eruptions. When using optical video data, the fountains can best be extracted from the red RGB colour channel of the images. By masking and using a Sobel edge detection, the height can be extracted frame by frame from the video data. This methodology enable me to determine the variations in an eruption plume, including its shape and width, and also, for the first time, to identify a time shift at adjacent vents.

When analysing the time-series data from lava fountains at Pu'u'Ō'ō (Hawai'i) and Holuhraun (Iceland), a pulsating behaviour of the eruptive vents was observed. The degree of similarity in the frequency pattern between adjacent vents decreased with the distance between vents. Lava fountains at the same vent or cone showed a high degree of similarity and I could also observe pronounced eruption peaks that appear to happen in chorus; whereas the similarity the frequency content and the time-series of the lava fountain height between fissure segments was lower. The overall correlation of the behaviour between adjacent vents revealed a small but systematic and significant phase shift, which increased with distance.

Based on this time shift, I hypothesized that there is a controlling process within the magma feeder system itself. That would mean the fountain behaviour at the surface was dominated by the underlying system. The fact that nearly the same propagation of changes in the height of lava fountains at all vent pairs was observed at the surface, implied that there is a hydraulic connection in the underlying system, which highlights a lateral flow of bubbly magma along the feeding dyke or pressure fluctuations at this dyke. Results in velocity of a pressure wave and dyke opening were found to be well in agreement with independent studies of geodetic and seismic data (Lundgren et al., 2013; Montagna and Gonnermann, 2013).

At the surface, a dyke can be recognized by complex topographic and structural surface expressions. The graben and fault system was both re-activated and formed during the eruption and its preceding dyke intrusion. The fracture system exhibited faults with over 80 % left-lateral component. These results were in agreement with those of independent studies and modelling (Ruch et al., 2016). Changes in expressions at the surface might be highlight a shallower upper edge of the feeder dyke.

Comparison of lava fountains on fissure eruptions and tremor signals generated at the vents showed that the processes at the vents influencing the lava fountains were one of the sources for tremor. The tremor was assumed to be generated by the bubble forming, which is responsible for the fountains at the surface. A simultaneous increase in tremor amplitude and lava fountaining activity revealed an opening of the vent and/or pressure change within the feeding system. The fast focusing from an elongated fissure to distinct vents was seen in the tremor and the video data, allowing one to speculate on local heterogeneities at these sites. There is no correlation between the effusive rate and the tremor amplitude. This means that the activity of the lava fountains is influenced by processes other than the degassing of magma in the underlying dyke as it was observed in other studies (Coppola et al., 2009).

The morphology was on one hand highly related to the pre-existing heterogeneous morphologic settings, as the fissure eruption occurred at the same position as previous eruptions. On the other hand, the fountaining behaviour itself had an influence on the morphology, as observed before at Hawaiian and Icelandic fissure eruptions (Parcheta et al., 2015; Reynolds et al., 2016). The largest changes in the cone morphology during the eruption were located at the position of the highest lava fountaining activity within the cone. The cone morphology itself regulates the lava fountains. In the Holuhraun case, the multiple superposed cones hosted separated lava fountains. Unlike interacting lava fountains within multiple coalescent cones, the multiple superposed cones in Holuhraun had fountains that had a larger width-to-height-ratio, than the interacting lava fountains within the multiple coalescent cone.

Modelling of the lava fountains and comparing the results to the fountain heights during an eruption revealed the influence of the conduit radius and the depth of the lava pond within the crater on the height of the lava fountains (Wilson et al., 1995). This modelling can help when the main eruption parameters are known or are similar for different vents, but variations in the fountains heights occurred. I showed that the long-term eruption behaviour at Holuhraun was controlled mainly by deeper eruption parameters, such as pressure changes in the dyke. While smaller, local changes and the maximum height were most likely mainly controlled by the vertical feeder dyke diameter and the depth of the lava pond. The pulses in the fountaining behaviour were likely associated with layers of bubbles reaching the surface.

7.1 Implications and Outlook

7.1.1 Video monitoring and the used methods

In video monitoring, methods can be separated into methods which detect changes in the structure (e.g., Amici et al., 2013c; Salzer et al., 2016), such as changes in the vent or dome growth (e.g., Darmawan et al., 2018; Diefenbach et al., 2013; James and Varley, 2012), and in ones which track eruption dynamics over time (e.g., Bagnardi et al., 2016; Gomez and Kennedy, 2017; Gomez and Purdie, 2016). Two areas are investigated, Kilauea and Holuhraun, showing an eruption which builds smaller cones and one that forms major cones, respectively. The presented work focused on the understanding of fissure eruptions. One of the main aspects thereby was the dynamics of the lava fountains. I showed how the photogrammetric methods provide important information on volcano activity and on the topography of the volcanic area.

The structural changes at volcanoes are well studied, and provide important information at fissure eruptions about the underlying feeder dyke (e.g., Lundgren et al., 2015; Ruch et al., 2016). These acquisitions are mainly based on InSAR data and GPS data. UAVs are used to monitor changes in the morphology. Unmanned aerial vehicle (UAV) measurements are becoming increasingly popular at volcanoes, and allow a high accuracy (Diefenbach et al., 2012). The disadvantage of ground-based measurements is that these measurements are limited in spatial resolution, as e.g., GPS data delivers information on one specific reference point. However, InSAR data covers large areas with lower grid resolution (Dirscherl, 2016). UAVs provide high-resolution data for a limited area. This thesis shows the high usability of UAV-based digital elevation models (DEMs) for the graben area above the dyke and the cones.

Ruch et al. (2016) model the Holuhraun graben over the propagated feeder dyke based on InSAR data, which had a grid resolution of 5 m. The DEMs, depicted in chapter 3 yield centimeter-scale resolutions, but do not cover the whole area of the 2014–2015 Holuhraun eruption. The higher resolution allows detection of very small fractures and faults, which are not seen by InSAR. Measurements by UAVs may facilitate monitoring of deformation in smaller time steps than InSAR and in greater detail.

Further work could combine high-resolution DEMs with thermal-cameras, as it is already done at geysers (Walter et al., 2018), to detect thermal changes and anomalies. This may provide new information about the heat transfer and heat distribution, which is most interesting in the first phase of an eruption and during decreasing activity level.

Lava fountains have been analysed at Etna (Scollo et al., 2014) and Kilauea (Orr et al., 2015), to calculate velocities of the pyroclasts (Taddeucci et al., 2012a,b) and to obtain physical eruption parameters, such as pyroclast velocity, ejection angle, size distribution, and the total mass of ejected bombs. The methods used range from manually picked velocities (e.g., Taddeucci et al., 2012b) to particle tracking velocity methods (PTV) based on optical flow equations (Gaudin et al., 2014). Thereby, the fountains are analysed using few images at the beginning of each explosion for the PTV (Gaudin et al., 2014; Taddeucci et al., 2012a), for the overall maximum height (Scollo et al., 2014), or to determine if fountains can be seen or not (Orr et al., 2015). This thesis provides a method to analyse the variation of the lava fountains during an eruption for a large dataset.

The provided fast algorithm can analyse the dynamics of the average activity and allows to study single eruption pulses in high temporal resolution. The edge detection was extended, commented to use additional information of one or more colour channels of the images. Based on the edges the height variations of single lava fountains are extracted. The resulting time-series of lava fountains enables us to identify single pulses. As the behaviour of adjacent lava fountains is poorly studied, an algorithm to compare the time-series in their frequency domain and to calculate a time-dependency correlation is generated. This time-dependency correlation between adjacent lava fountains allows detecting changes in their relation.

The uncommented code for the video analysis within the Ph.D. research was developed with MATLAB, and is available in Chapter 8. In the future, the source code should be extended, commented and be made publicly accessible in order to use video data of different wavelengths and also to make these methods available to other scientists. To have the algorithms and methods independent from existing licenses, rewriting the code in an open-source language, such as Python or C++, would be the next step. The lava fountain dynamics in this study mainly based on the variations in the lava fountain heights. Further dynamic data, such as initial velocity, can be extracted with the photogrammetric methods used during this Ph.D. research. Therefore, a further study of the fountain dynamics also based on the initial velocity and velocity variation within the fountains is recommended.

In summary, the presented methods can be used in several areas, not only volcanic ones. In case of morphology, UAV-based cameras provide important information on the morphology and the dyke in high precision, but in a smaller area than what is accessible by InSAR. Video analysis of lava fountains allows a study of the eruption dynamics in time-scales of seconds, as shown by pulses, up to days, as done to analyse the concentration of activity on several vents.

7.1.2 Dynamics of lava fountains

A pulsating behaviour of lava fountains, has been identified earlier (e.g., at Stromboli by Taddeucci et al., 2012a), but has not yet been studied in detail. I show that the pulses vary in their maximum height and duration. Most of the recent studies focus on single fountains (e.g., at Etna, see Andronico and Corsaro, 2011; Scollo et al., 2014) or on fountains as an indicator for activity (e.g., at Kilauea, see Lundgren et al., 2013; Orr et al., 2015). The interaction or chronologyof several fountains is normally not investigated. Based on video monitoring, the similar behaviour of adjacent vents is identified, and consequently, a close connection between them is shown in Chapters 2 and 5. Furthermore, it is demonstrated that fountains within one group or crater interact and influence each other. Consequently, the lava fountains of a fissure eruption can be simplified as one single eruption. Our detailed study of the interaction between single lava fountains, and the behaviour of single lava fountains provides new information. The time-dependency correlation shows that the eruption is stable over hours, and changes slightly over days.

Analysing the fountain distribution of a fissure eruption in the beginning of the eruption due to their overall activity, shows a concentration from a line of fire to several separated vents (e.g., at Laki Reynolds et al., 2016). Bruce and Huppert (1989) theoretically explained the concentration of fissure eruption to few vents by the thermostatic effects. These assumed vertical conduit-like structures suggest a formation of a magma pathway more or less from the beginning of the eruption. Tremor data and video data show that this interpretation is confirmed by observation in nature (see Chapter 4 and 5). The higher seismic tremor at the later cone positions supports the hypothesis that conduit-like structures are present right from the beginning. The conduit diameter changes that occur during the eruption due to temperature changes, can be inferred by seismic tremors and changes in the lava fountain height. The seismic tremor seems to be sensitive to conduit opening, which results in an increase in lava fountain heights. We were able to observe these changes in height by our video monitoring at the Holuhraun fissure eruption. The coupling of seismic tremor, fountain heights and structural changes in the underground is shown for the first time. This is one of the few cases where the initial phase of the eruption was studied in more detail, although the video data was limited to few hours at each day only.

Further work could include a continuous dataset over several days to investigate the impact of the granularity of the time-scales (hours, days). On the basis of such a dataset, the stopping of the activity at some of the lava fountains and the resulting change from a continuous line of fountains to discrete vents could be studied in more detailed. This methodology would also provide the opportunity to clarify whether the activity at different locations stops randomly. Therefore, a continuous long-term observation of a fissure eruption during the initial phase is necessary.

7.1.3 Dyke propagation and link to erupting vents

Dyke propagation is associated with earthquakes and deformations at the surface (Ágústsdóttir et al., 2016; Ruch et al., 2016; Sigmundsson et al., 2015). Earthquakes are commonly generated at the tip of the dyke, highlighting the propagation velocity of the dyke (Caudron et al., 2018). Based on InSAR data and deformation modelling, the opening of the dyke can be calculated (e.g., Lundgren et al., 2015; Sigmundsson et al., 2015). The surface deformation is characterised by a graben structure and can be clearly seen in InSAR (see Figure 7.1; e.g., Ruch et al., 2016). The propagation itself is influenced by the volcanic loading (Maccaferri et al., 2017).

After the dyke propagation stops and the dyke is established, the velocity can be calculated. This calculation is mainly based on InSAR, GPS and/or tilt data as well as using modelling. This provides an important overview about the velocities of the dyke (Ágústsdóttir et al., 2016; Montagna and Gonnermann, 2013). Thus, the velocity of the dyke as a whole can be calculated. Rarely, it included the irregular opening of the dyke, as seen at Kilauea or Bárðarbunga (e.g., Lundgren et al., 2013; Sigmundsson et al., 2015). In contrast to that, velocities based on the fountain behaviour are limited to the area of the fountains (see Chapter 2). This velocity is that of a pressure wave propagating through the dyke (Montagna and Gonnermann, 2013). In Chapter 2, based on the velocity of such a pressure wave, a calculation of the dyke opening is shown. Comparing the observed velocity with the average velocity might provide information about the inclination of the dyke under the fissure eruption itself. Similar concepts have been applied at Holuhraun (Gudmundsson et al., 2016) and at Tolbachik volcano (Frank et al., 2018) explaining the coupling between distant sources.

At the eruption site, erupting vents occur at locations where the dyke is the widest (Head et al., 1996) or where the erupting vents are fed by separated feeding conduits coming from the dyke (see Figure 7.1; Eibl et al., 2017a). Therefore, the dyke, the eruptive vents, and the volcanic load are linked together (Kervyn et al., 2009).

7.1.4 Interactions between fountain dynamics and morphology

The presented work methodically bridges gaps in our understanding of the two process categories of structural changes, as seen in the morphology, and the dynamics of lava fountains. It was observed that the eruption height and wind conditions influence the resulting cone morphology (Reynolds et al., 2016). Due to limited morphology data from the beginning of the eruptions, the study of the morphology concentrates on the final shape (Parcheta et al., 2015; Thordarson and Self, 1993). In Chapter 5, I presented an analysis of the changes in the morphology during the first days of a fissure eruption. Based on that data, the similarity between the initial morphology and the final morphology was observed. The largest changes occur where the highest lava fountains were observed, indicating the lava fountains have a large influence on the morphology. Furthermore, the pre-eruptive morphology seems to play an important rule, as the highest lava fountains are located at pre-existing cones. In further studies, it would be interesting to compare fissure eruptions with and without pre-existing cones to evaluate the effect of such a topography.

At fissure eruptions, fountains of different heights are observed. At Kilauea the fountains have nearly the same height (see Chapter 2), while at Bárðarbunga some of the lava fountains reach only half the height of the highest lava fountains (see Chapter 5). These varieties in eruption heights of adjacent lava fountains were not studied well before. In Chapter 2 and 5 I show that some of these lava fountains were fed by the same feeder dyke. Therefore the reason for such variations in height must be rooted deeper. By modelling, the different diameter of the conduits of one fissure eruption and the range in pond depth of adjacent cones were calculated (see Chapter 5). This showed that the eruption behaviour of different fountains of the same fissure eruption is influenced by the morphology of its cone, but also by the underlying feeding system. This feeding system can change due to thermal conditions (cf. Bruce and Huppert, 1990).

In summary, based on the methods used, the interaction between fountains and morphology can be analysed in more detail. Pre-existing cones are areas with higher fountains, which in turn changes the morphology at these locations the most. Despite these large changes, the shape is quite stable and influences the appearance of the lava fountains (see Chapter 5).

Further study of the relationship between lava fountains and morphology at other fissure eruptions and volcanoes would improve the understanding of the fountain dynamic. It may help to explain why some of the fountains are wider related to their height. I expect an influence of the radius of the inner rim as it limited the width, but also that interactions between lava fountains can play an important role. Therefore, video analysis of craters with several or single lava fountains compared with their cone morphology should be one of the next investigations.

7.1.5 Further outlook

For further work, one of the great opportunities of video monitoring is the range of cameras that can be used, such as optical, infra-red, SO_2 or cameras with higher temporal resolution (e.g., high-speed camera), and the combination of these cameras with other further methods. For example, the use of high-speed cameras makes it possible to see fast and small changes near the vents, whereas infra-red cameras provide additional information by contrasting apparent temperature. This could answer the question how changes in gas content or temperature influence the eruption behaviour at fissure eruptions.

Another unused data set is the videos recorded for non-scientific purposes. The video data used in Chapter 2 is from handheld videos recorded in the field. The data was affected by shaking and movement of the camera. Although the data is limited in time and resolution, it allows a better understanding of the dynamics and their connection to the depths. In future, video monitoring could be extended by an additional opportunity of using social network data. Nowadays, many people record volcanoes with mobile phones with high-resolution cameras and other cameras, producing thousands of photographs and videos. Many of them are georeferenced, resulting in a partially high coverage of many volcanoes, even at unmonitored ones. Most of the images are spread over the internet, and therefore scientists could gain access to a huge amount of data. An application for mobile phones and PC/tablets could provide an analysis of videos and photographs for the user. In the application the developed algorithm should be included, resulting in an analysis directly on the phone. Consequently, the user would get further formation about the eruption, such as height and in case of videos information of the eruption dynamics, such as velocity and variation in the heights. With such improvement the broad unused field of citizen science could increase in importance. This data could improve the knowledge of ongoing eruptions, and also be used to monitor changes at the volcano edifice.

Nowadays, the potential for the development of new drones and mini-satellite is enormous. Drones are becoming more powerful, and are capable flying longer and carrying heavier equipment. Using drones will become an option even for large areas. Mini-satellites might provide a new alternative to the normal satellite, as they collect a huge amount of photogrammetric data. Both allow a flexible usage specifically if a hazard occurs or is expected. Maybe mini-satellites in future are able to allow autonomous monitoring of volcanoes from above.

One interesting development in the last years in the field of video analysis is the *Video magnification*. It allows to see even small changes in colour and motion (Elgharib et al., 2015). One of the further goals would be to detect with an adjusted algorithm similar small changes and motions. This might provide information on small deformation at the vent during an eruption.

In addition to further used dataset, the described method is not limited to lava fountains. It can also be used to analyse also volcanic clouds by adjusting the edge detection. For lava fountains, the edge detection is based on the information in the red colour space, while for eruption clouds, a usage of the brightness information delivers good results (Dürig et al., 2018). For volcanic clouds, the atmospheric conditions are important, because wind influences the direction and dispersion of volcanic clouds. It could be interesting to integrate an analysis of volcanic cloud and lava fountains at volcano observatories, especially since the analysis of both are based on the similar algorithms applied to video data of the volcano. Although at many volcano observatories, web cameras are used as an optical surveillance method, a quantitative analysis of that data is not done yet. In Chapter 2 the potential of such an analysis of the lava fountains is shown. The importance of the cloud height calculation was shown already by Scollo et al. (2014).

In addition to its applications at volcanoes, video monitoring can also be used for example at landslides, mass movements or at geysers. The analysis provides continuous data about the height and timing of the geyser eruption. The method is equal to the one currently used for the lava fountains but uses the brightness instead of the red colour channel for the edge detection. I was able to test this during my Ph.D. research at Strokkur geyser, Iceland. Those results from video data are used to compare the height and timing of the water fountains to tilt and ground-based InSAR. There it could also be used to analyse the eruption dynamics, such as eruption height, rest time between eruptions and the distribution of the heights. This shows that the algorithm is not limited to volcanic regions, possibly improving monitoring at other geologic sites in the future.

Chapter 8

Supplementary information

8.1 MATLAB-Code

8.1.1 Main Code of the lava fountain analysis

```
%&&&&&&&&&&&&&&&&&&&&&&&&&&&&&&&&&&&&&&&&&&&&&&&&&&&&&&&&&&&&&&&&&&&&&&&&&&&&&&&&&&&&&
% prepostproc.m
% doing all things off the Postprocessing as load, shift, ...
%&&&&&&&&&&&&&&&&&&&&&&&&&&&&&&&&&&&&&&&&&&&&&&&&&&&&&&&&&&&&&&&&&&&&&&&&&&&&&&&&&&&&&
clear all;
close all;
%clc;
dbstop if error

disp('PREPROCESSING');

%%% STEP1: loading data %%%%%%%%%%%%%%%%%%%%%%%%%%%%%%%%%%%%%%%%%
filepath=uigetdir('/home/sysop/Documents/Data',...
    'Please choose the directory of your data');
while isequal(filepath, 0)
    err_dlg = errordlg('You must choose a dirctory!','File Error','modal');
    waitfor(err_dlg);
    filepath=uigetdir('/home/sysop/Documents/Data',...
    'Please choose the directory of your data');
end
 prompt='Where is the Data? ';
 filepath=input(prompt,'s');

str={'bmp';'BMP';'png';'PNG';'jpg';'jpeg';'JPG';'JPEG';...
    'tif';'tiff';'TIF';'TIFF';'gif';'GIF';'raw';'RAW'};
        [s,v] = listdlg('PromptString','What format has the data? ',...
                        'SelectionMode','single',...
                        'ListSize', [300 200],...
                    'Name','Format','ListString',str);
     while v~=1 %okay nicht gedrÃijckt
        err_dlg = errordlg('You must choose a format!','File Error','modal');
        waitfor(err_dlg);
        [s,v] = listdlg('PromptString','What format has the data? ',...
                    'SelectionMode','single',...
                    'ListString',str);
    end
        fileformat=str{s};

 prompt='What format has the data? ';
 fileformat=input(prompt,'s');

                            %Daten laden
rgb_data = load_data(filepath, fileformat);

clearvars('*','-except','rgb_data');

%%% STEP1-2: einbauen eines referenz Bildes %%%%%%%%%%%%%%%%%%%%%%%%%%%%%%
button = questdlg('Do you have a reference picture?','Referenz picture',...
    'yes','no','no');
switch button
    case ''
        ref='n';
    case 'yes'
        ref='y';
    case 'no'
        ref='n';
end

 prompt='Do you have a reference picture? y or n: ';
 ref=input(prompt,'s');

if ref=='y'
   prompt='What is the whole file path? ';
   filepath=input(prompt,'s');
   refi=imread(filepath);
   [~,~,~,img_ref]=size(rgb_data);
   rgb_data(:,:,:,img_ref) = refi;
else
    disp('pech gehabt');
end
```

```
 button = questdlg('Do you waqnt to convert into grey color?','Referenz picture',...
     'yes','no','no');
 switch button
     case ''
         ref='n';
     case 'yes'
         ref='y';
     case 'no'
         ref='n';
 end
 if ref=='y'
    prompt='What is the whole file path? ';
    filepath=input(prompt,'s');
    refi=imread(filepath);
    [~,~,~,img_ref]=size(rgb_data);
    rgb_data(:,:,:,img_ref) = refi;
 else
     disp('pech gehabt');
 end

rgb_data = rgb_data/255;

imshow(img_shift(:,:,:,1))

interest=FieldOfView([],rgb_data(:,:,:,1)); %noch unschÃűn

 prompt='Is this your field of interest? y or n: ';
 interest=input(prompt,'s');

if interest=='n'
   [~,b] = imcrop(rgb_data(:,:,:,1));
   b=round(b);
   img = rgb_data(b(2):(b(2)+b(4)-1),b(1):(b(1)+b(3)-1),:,:);
   clear('rgb_data');
   rgb_data=img;
   clear('img');
end

close all;
clearvars('*','-except','rgb_data','ref');

img_shift=shift_data(rgb_data,ref);

clearvars('*','-except','img_shift','ref');

imshow(img_shift(:,:,:,1))

interest=FieldOfView([],img_shift(:,:,:,1)); %noch unschÃűn

prompt='Is this your field of interest? y or n: ';
interest=input(prompt,'s');

if interest=='n'
   [~,b] = imcrop(img_shift(:,:,:,1));
   b=round(b);
   img = img_shift(b(2):(b(2)+b(4)-1),b(1):(b(1)+b(3)-1),:,:);
   clear('img_shift');
   img_shift=img;
   clear('img');
end

close all;
clearvars('*','-except','img_shift','ref');

disp('PROCESSING');

finish='n';

 [~,~,~,num]=size(img_shift);
 if ref=='y'
     for j=1:num-1
        img_shift(:,:,:,j)=abs(img_shift(:,:,:,j)-img_shift(:,:,:,num));
        img_shift(:,:,:,j)=img_shift(:,:,:,j)/max(max(max(img_shift(:,:,:,j))));
     end
 end
 img_shift=img_shift(:,:,:,1:num-1);

while finish=='n'
    close(gcf);
    button = questdlg('How do you want to do processing?'... %nur 3 AuswahlmÃűglichkeiten
        ,'Postprocessing',...
        'calculate the area, height or/and width (timing-plot)',...
        'save images',...
        'look at only one channel',...
        'calculate the area, height or/and width (timing-plot)'); %default
    switch button
        case ''
            process=1;
        case 'calculate the area, height or/and width (timing-plot)'
            process=1;
        case 'save images'
            process=2;
        case 'look at only one channel'
            process=3;
         case 'blubb or blubb'
             process=4;

    end

     prompt1=['How do you want to do processing?','\n' , ...
         '(1) calculate the area, height or/and width (timing-plot)','\n', ...
         '(2) nothing happen','\n', ...
         '(3) look at only one channel','\n', ...
```

```
         '(4) blubb or blubb','\n'];
     process=input(prompt1);

    %%% STEP1: finding edges and plot timing
    if process==1
        edgeplot(img_shift, ref);
    elseif process==2
        saveimg(img_shift)
    elseif process==3
        onechannel(img_shift, ref);
    end

    %%% Abfrage nach weiterem processing
    button = questdlg('Do you want to du further processing?','Further analysis',...
    'yes','no','no');
        switch button
            case ''
            case 'yes'
            case 'no'
                finish ='y';
        end

end
```

```
%&&&&&&&&&&&&&&&&&&&&&&&&&&&&&&&&&&&&&&&&&&&&&&&&&&&&&&&&&&&&&&
% Lava_Ana
% Einlesen der Daten und HÃűhen Tageweise abspeichern
% 30Frame per Second
%&&&&&&&&&&&&&&&&&&&&&&&&&&&&&&&&&&&&&&&&&&&&&&&&&&&&&&&&&&&&&&
% clear all;
%global feature;
%close all;
%clc;
dbstop if error;


%% Anlegen der Matrizen und Variablen
timestep_thres =  30;                    % Anzahl der Frames pro Durchlauf
max_vent = 11;                    % Anzahl der betrachteten Vents
scaling  =  0.025;                 % Scaling: pixel -> m   0.0932;
fa       =  30;                    % Abtastfrequenz
ask_roi  =  0;                    % 1 falls ca ROI abgefragt werden soll
ask_vent =  0;                    % 1 falls vents abgefragt werden soll
ask_vel  =  0;                    % 1 falls velocity berechnet werden soll
feat     =  0;                    % 1 falls precise roi
pic      =  0;                    % 1 falls bilder am Ende
wind     = 32;                    % window of piv
mask     = [];
passes   =  2;
int2     = wind/2;
roi      = [];
feature  = [];

if ask_vel==0
    wind = 0;
end

ref =   [  2   382   253     1   100   175   255   425   500   550   600
            1     1     1     1     1     1     1     1     1     1     1
          330   258   247    99    75    80    85    75    50    50    40
          300   300   300   300   300   300   300   300   300   300   300];


filepath  ='/home/sysop/Documents/Data/Vid/Hawaii/Hawaii_vid1';
fileformat='*.png';


filenames = dir(fullfile(filepath, fileformat));
filenames = {filenames.name};
max_file  = min(9999999+1,numel(filenames));                        % Anzahl der Bilder
timestep = gt_T(max_file-1,timestep_thres);
        runs=floor((max_file-1)/timestep);

d = filenames{1};
    f = fullfile(filepath , d);
    img=imread(f);

lava_img    =zeros(size(img,1),size(img,2),3,timestep+1);   % Images des Geysirs
lava_img_hsv=zeros(size(img,1),size(img,2),3,timestep+1);   % Images des Geysirs-ref
%ref         =zeros(size(img,1),size(img,2),max_vent);       % ref for vents
%ref         =zeros(4,max_vent);                              % ref for vents

daily = zeros(max_file-1,2,max_vent);       % daily heigth of the fountaine
daily_2 = zeros(max_file-1,max_vent);       % daily heigth of the fountaine
v_ini = zeros(max_file-1,max_vent-1);       % initial velocity of the fountaine
u_ini = zeros(max_file-1,max_vent-1);


%% Festlegen eines ungefaeren ROI
if ask_roi==1
    figure%close all;
    interest=FieldOfView([],img); %noch unschÃűn

    if interest=='n'
       [~,b] = imcrop(img);
       b=round(b);
       roi = [max(b(1)-wind,0)  min(b(2)+wind,size(img,2)) ...
           max(b(3)-wind,0)  min(b(4)+wind,size(img,1))];
    else
       roi=[];
    end
end
```

```
%% Festlegen der Refs fÃijr einzelne Vents
if ask_vent==1
    ref         =zeros(4,max_vent);
    for v_nr=1:max_vent
        figure%close all;
        [~,b] = imcrop(img);
        b=round(b);
        ref_a = [max(b(1)-0.5*wind,1)  max(b(2)-0.5*wind,1)  ... min(b(2)+wind,size(img,2))  ...max(b(3)-wind
            ,1)
              min((b(3)+wind-1),(size(img,2)-max(b(1)-0.5*wind,1)))  ...
              min((b(4)+wind-1),(size(img,1)-max(b(2)-0.5*wind,1)))];
        ref(:,v_nr)=ref_a;
        close(gcf);  % richtig???
     end
end

if feat==1
    subplot(2,2,1), imshow(rgb2gray(img)), title('gray');
        subplot(2,2,2), imshow(img(:,:,1)), title('red');
        subplot(2,2,3), imshow(img(:,:,2)), title('green');
        subplot(2,2,4), imshow(img(:,:,3)), title('blue');
    str={'gray';'red';'green';'blue'};

    [s,v] = listdlg('PromptString','Which color space do you want for the Feature? ',...
                    'SelectionMode','single',...
                    'ListSize', [300 200],...
                    'Name','Format','ListString',str);
     while v~=1 %okay nicht gedrÃijckt
        err_dlg = errordlg('You must choose a color space!','File Error','modal');
        waitfor(err_dlg);
        [s,v] = listdlg('PromptString','Which color space do you want? ',...
                    'SelectionMode','single',...
                    'ListString',str);
     end
     cs_feat=str{s};
end
%% Analyse der Daten

for run=1:runs
%%% Laden der Daten
    for k=(run-1)*timestep+1:run*timestep+1
        j=k-(run-1)*timestep;
        d = filenames{k};
        f = fullfile(filepath , d);
        img=imread(f);
        % take=sort_test(img);
        lava_img(:,:,:,j)=img;
        lava_img_hsv(:,:,:,j)=rgb2hsv(img);
    end

    for v_nr=1:max_vent
        for k=(run-1)*timestep+1:run*timestep
            j=k-(run-1)*timestep;
            refi=zeros(size(img,1),size(img,2));
            refi(ref(2,v_nr):ref(2,v_nr)+ref(4,v_nr),ref(1,v_nr):ref(1,v_nr)+ref(3,v_nr))=1;


            A=(lava_img(:,:,1,j));
            A(A<200) = 0;%-double(img_ref(:,:,1));%(lava_img(:,:,1,j+1));
            A(lava_img(:,:,3,j)>200)=0;
            A1=A;
            A(lava_img(:,:,2,j)>175)=0;
            A(155:end,:)=A1(155:end,:);
            A1=idealreject(A,128,2);

             A1=lava_img(:,:,1,j)/255;
             A1(A1<0.8)=0; %A1<0.1    0.5
             A2=lava_img(:,:,3,j)/255;
             A1(A2>0.7)=0;  %         0.3
            %figure,imagesc(A1);
            [~, threshold] = edge(A1, 'sobel');
            fudgeFactor=1.2;%1.2;0.95
            BWs = edge(A1,'sobel', threshold * fudgeFactor);

            se90 = strel('line', 3, 90);
            se0 = strel('line', 3, 0);
            BWsdil = imdilate(BWs, [se90 se0]);

            BWdfill = imfill(BWsdil, 'holes');
            BWdfill = im2bw(A1);
            BWdfill = BWdfill.*refi;

            BWdfill2=zeros(360,642);
            BWdfill2(:,2:641)=BWdfill;
            BWnobord = imclearborder(BWdfill2, 4);
            BWnobord = BWnobord(:,2:641);

            seD = strel('diamond',1);
            BWfinal = imerode(BWnobord,seD);
            BWfinal = imerode(BWfinal,seD);

            A2=A1;
            A2(A2>0)=1;
            A2=A2.*refi;
            %%% Referencebild
             if k==1
                 ref1=BWfinal.*A1;
             else
                 BWfin=BWfinal.*A1-ref1;
                 BWfin = logical(BWfin);
             end
```

```
[B,L] = bwboundaries(BWfinal,'noholes');
[B,L] = bwboundaries(A2,'noholes');
stats = regionprops(L,'Area','BoundingBox');

if isempty(B)
    allHeight = 0;
    totHeight = zeros(1,2);
else
    allHeight = zeros(length(B),1);
    totHeight = zeros(length(B),2);
    if v_nr==1
        totHeight(:,1)=230;%99999;
    else
        totHeight(:,1)=216;%99999;
    end
end

for l=1:length(B)
    area = stats(l).Area;

    y_begin=max(floor(stats(l).BoundingBox(2)),1);
    x_begin=max(floor(stats(l).BoundingBox(1)),1);
    mean_sum=mean(mean(lava_img_hsv(y_begin:y_begin+stats(l).BoundingBox(4) ,...
        x_begin:x_begin+stats(l).BoundingBox(3) ,2,j)));
    if v_nr <=3
        if y_begin+stats(l).BoundingBox(4)<=245 &&  y_begin+stats(l).BoundingBox(4)>=210
            allHeight(l) = stats(l).BoundingBox(4);
            totHeight(l,2) = -(floor(stats(l).BoundingBox(2))-totHeight(l,1));
        else
            allHeight(l) = 0;
            totHeight(l,2) = -(floor(stats(l).BoundingBox(2))-totHeight(l,1));
        end
    elseif v_nr <=7
        if y_begin+stats(l).BoundingBox(4)<=250 &&  y_begin+stats(l).BoundingBox(4)>=210
            allHeight(l) = stats(l).BoundingBox(4);
            totHeight(l,2) = -(floor(stats(l).BoundingBox(2))-totHeight(l,1));
        else
            allHeight(l) = 0;
            totHeight(l,2) = -(floor(stats(l).BoundingBox(2))-totHeight(l,1));
        end
    else
        if y_begin+stats(l).BoundingBox(4)<=223 &&  y_begin+stats(l).BoundingBox(4)>=210%mean_sum
            <1%0.475
            allHeight(l) = stats(l).BoundingBox(4);
            totHeight(l,2) = -(floor(stats(l).BoundingBox(2))-totHeight(l,1));
        else
            allHeight(l) = 0;
            totHeight(l,2) = -(floor(stats(l).BoundingBox(2))-totHeight(l,1));
        end
    end

end

if isempty(B)
    allHeight=0;
end
daily_2(k,v_nr)= max(totHeight(:,2))*scaling;

daily(k,2,v_nr)= max(allHeight)*scaling;
if max(allHeight)==0
    daily(k,2,v_nr)=0;
else
    index=find(allHeight==max(allHeight),1);
    daily(k,1,v_nr)=floor(stats(index).BoundingBox(2));
end
 if v_nr==2 && mod(k,25)==0 %max_file<25 %&& j==1
     figure;
     subplot(2,2,1), imagesc(A1)
     labeledImage = bwlabel(BWfinal, 8);     % Label each blob so we can make measurements of it
     coloredLabels = label2rgb (labeledImage, 'hsv', 'k', 'shuffle'); % pseudo random color
         labels
     subplot(2,2,2), imshow( lava_img(:,:,:,j)/255);
     title('Labeled Image, from bwlabel()');
     subplot(2,2,3),imagesc(coloredLabels);
     caption = sprintf('Pseudo colored labels, from label2rgb().\nBlobs are numbered from top to
         bottom, then from left to right.');
     title(caption);
     blobMeasurements = regionprops(labeledImage,A1, 'all');
     numberOfBlobs = size(blobMeasurements, 1);
     subplot(2, 2, 4); imagesc(A1);
     title('Outlines, from bwboundaries()');
     hold on;
     boundaries = bwboundaries(BWfinal);
     numberOfBoundaries = size(boundaries);
     for m = 1 : numberOfBoundaries
         thisBoundary = boundaries{m};
         plot(thisBoundary(:,2), thisBoundary(:,1), 'g', 'LineWidth', 2);
     end
     hold off;
 end

if ask_vel==1 && daily(k)~=0
    if feat==1
        img1=rgb2cs(lava_img(:,:,:,j),cs_feat);
        feature = masc_precise(img1);  %How to implement this?
    else
        feature = [];
    end
    roi=ref(:,v_nr);
    im1=rgb2gray(lava_img(:,:,:,j)/255);
    im2=rgb2gray(lava_img(:,:,:,j+1)/255);
    if passes==2
        [xi,yi,iu,iv,typevector]=piv_multi(im1,im2, wind, 0.5*wind,1, ...
```

```
                         mask,roi,passes,int2,0,0,'spline',feature,fid);
                elseif passes==3
                    [xi,yi,iu,iv,typevector]=piv_multi(im1,im2, wind, 0.5*wind,1, ...
                         mask,roi,passes,int2,int2/2,0,'spline',feature,fid);
                else
                    warning('passes is reduce/set to 2!')
                    [xi,yi,iu,iv,typevector]=piv_multi(im1,im2, wind, 0.5*wind,1, ...
                         mask,roi,passes,int2,0,0,'spline',feature,fid);
                end
                v_ini(k,v_nr)= -min(min(iv));
                u_ini(k,v_nr)= iu(find(iv==min(min(iv)),1,'first'));
            end
        end
    end
    str=['Process: ' num2str(run/runs*100) ' %'];
    disp(str);
end

for v_nr=1:max_vent
    Freq_ana(:,v_nr) = spectrum(squeeze(daily(:,2,v_nr)),length(squeeze(daily(:,2,v_nr))),fa);
end


% fclose(fid);
if pic==1
    for j=1:3*6%numel(filenames)
        figure(1), subplot(3,6,j), imagesc(lava_img_hsv(:,:,1,j)/255), title('H')
        figure(2), subplot(3,6,j), imagesc(lava_img_hsv(:,:,2,j)/255), title('S')
        figure(3), subplot(3,6,j), imagesc(lava_img_hsv(:,:,3,j)/255), title('V')
        figure(4), subplot(3,6,j), imagesc(lava_img(:,:,:,j)/255), title('RGB')
    end

    for j=1:max_vent-1
        for k=j+1:max_vent
            [corri,lags]=xcorr(daily(:,j),daily(:,k),'coeff');

        end
    end
    title('Correlation daily')
    figure,
    u_ini(isnan(u_ini))=0;
    for j=1:max_vent-1
        for k=j+1:max_vent
            [corri,lags]=xcorr(u_ini(:,j),u_ini(:,k),'coeff');
        end
    end
    title('Correlation u')
    v_ini(isnan(v_ini))=0;
    figure,
    for j=1:max_vent-1
        for k=j+1:max_vent
            [corri,lags]=xcorr(v_ini(:,j),v_ini(:,k),'coeff');
        end
    end
    title('Correlation v')

    mean_daily=zeros(size(daily));
    mean_vini=zeros(size(v_ini));
    for i=1:size(daily,2)
        mean_daily(:,i)=daily(:,i)-mean(daily(:,i));
        mean_vini(:,i)=v_ini(:,i)-mean(v_ini(:,i));
    end
    fft_time2(mean_daily,fa);
    fft_time2(mean_vini,fa);
end
```

8.1.2 Code for Correlation, smoothing and velocity

```
%&&&&&&&&&&&&&&&&&&&&&&&&&&&&&&&&&&&&&&&&&&&&&&&&&&&&&&&&&&&&&&&&&&&&&&&&&&&&&&&&&
% Corr
%&&&&&&&&&&&&&&&&&&&&&&&&&&&&&&&&&&&&&&&&&&&&&&&&&&&&&&&&&&&&&&&&&&&&&&&&&&&&&&&&&
clear all;
global feature;
close all;
clc;
dbstop if error;

load('ref_vid19.mat')
lava_ana
try_mean_vid19
% Correlation           %smoothen, interpolieren
close all;
fa=50;
dai_test=dai_mean';
fft_time2(dai_test(:,1:4),fa);

data=squeeze(daily(:,2,:));
data(:,4:11)=dai_mean(:,1:865)';
data=data_full(50001:125000,:);
data = dai_all(:,4:11);
data = fsdf2;
% Power-Spektrum
 N = size(data,1); % number of points
 T = N/fa; % define time of interval, 3.4 seconds
for k=1:size(data,2)
      p = abs(fft(data(:,k)))/(N/2); % absolute value of the fft
      p = p(1:N/2).^2; % take the power of positve freq. half
      freq = [0:N/2-1]/T; % find the corresponding frequency in Hz
      semilogy(freq,p); % plot on semilog scale
      axis([0 20 0 1]); % zoom in
      hold all
end

clear('corr_lag');
thres=0.5;
corr_length=50;
corr_shift=ceil(corr_length/2);
mean_corr=[];
multi_max_corr=[];
max_corr_ges = [];most_05=[];
for l=1:size(data,2)
    for k=1:size(data,2)
        %if k~=l
             max_corr=[];
             for i=corr_shift+1:length(data)-(corr_shift+corr_length)
                  ori=zeros(1,2*corr_shift+corr_length);
                  ori(corr_shift+1:corr_shift+corr_length)=...
                       data(i:i+corr_length-1,l)-mean(data(i:i+corr_length-1,l));
                  ori = ori./max(ori);
                  test=data(i-corr_shift:i+corr_shift+corr_length-1,k)...
                      -mean(data(i-corr_shift:i+corr_shift+corr_length-1,k));
                  test=test./max(test);
                  if all(test==0) || all(ori==0)
                        %disp('blubb!!!')
                        corri=zeros(1,199);
                  else
                       [corri,lags]=xcorr(ori,test,'coeff');
                         lag_corrMax=lags(corri>=max(corri));
                         max_corr_i=[corri(lags==lag_corrMax(1)) ...
                              lags(corri>=max(corri))/15 0 0];
                         corri(corri>=max(corri))=0;
                         lag_corrMax2=lags(corri>=max(corri));
                         max_corr_i(3:4)=[corri(find(lags==lag_corrMax2(1),1)) ...
                              lags(find(corri>=max(corri),1))/15];
                         while length(max_corr_i)~=4
                              lag_corrMax=lags(corri>=max(corri));
                              max_corr_i=[corri(lags==lag_corrMax(1)) ...
                                   lags(corri>=max(corri))/15 0 0];
                              corri(corri>=max(corri))=0;
                              lag_corrMax2=lags(corri>=max(corri));
                              max_corr_i(3:4)=[corri(find(lags==lag_corrMax2(1),1)) ...
                                   lags(find(corri>=max(corri),1))/15];
                         end
                         max_corr=[max_corr;max_corr_i];
                  end
                  corr_lag(:,i,k,l)=corri;

             end
             I=find(max_corr(:,1)==max(max_corr(:,1)),1);
             I2=find(max_corr(:,3)==max(max_corr(:,3)),1);
             mean_corr=[mean_corr; ...
                  l k mean(max_corr(:,1)) sum(max_corr(:,2).*max_corr(:,1))/sum(max_corr(:,1)) ...
                  mean(max_corr(:,3)) mean(max_corr(:,4))];

              A1=find(max_corr(:,1)>=thres);
              A2=find(max_corr(:,3)>=thres);
              A=[A1;A2];
              B=zeros(length(A),2);
              for i=1:length(A1)
                   B(i,1)=max_corr(A1(i),1);
                   B(i,2)=max_corr(A1(i),2);
              end
             most_05=[most_05; l-3 k-3 mean(B(:,1)) sum(B(:,2).*B(:,1))/sum(B(:,1))];
        %end

    end

end
```

```
for i=0:7
     maxxi=0;gessi =0;
     for k=1:7
         if k>i+1
         maxxi = maxxi + (max_corr_ges((k-1)*8+i+1,3)*max_corr_ges((k-1)*8+i+1,4));
         else
         maxxi = maxxi - (max_corr_ges((k-1)*8+i+1,3)*max_corr_ges((k-1)*8+i+1,4));
         end
         gessi = gessi + max_corr_ges((k-1)*8+i+1,3);
     end
     maxxi = maxxi/gessi;
end

dist=[100; 141;180; 234;508;559;597;633];
corr_dist=[];
for i=1:64
 corr_dist=[corr_dist; abs(dist(max_corr_ges(i,1))-dist(max_corr_ges(i,2))) max_corr_ges(i,3)];
end
P=polyfit(corr_dist(:,1),corr_dist(:,2),1)

corr_lag(corr_lag==0)=1;
for k=1:2
    figure
    for l=1:2
        subplot(8,1,l),imagesc([1:size(corr_lag,2)]/fa/60,lags/fa/60,corr_lag(:,:,k,l),[-1 1])
        title([num2str(l) ' and ' num2str(k)])
    end
end
```

```
%&&&&&&&&&&&&&&&&&&&&&&&&&&&&&&&&&&&&&&&&&&&&&&&&&&&&&&&&&&&&&&&&&&&&&&&&&&&&&&&&&&&&&
% VelIni_Ana
%&&&&&&&&&&&&&&&&&&&&&&&&&&&&&&&&&&&&&&&&&&&&&&&&&&&&&&&&&&&&&&&&&&&&&&&&&&&&&&&&&&&&&
dbstop if error;
global feature;  % feature blubb
global refi;

timestep_thres =  30;                   % Anzahl der Frames pro Durchlauf
max_vent = 1;                   % Anzahl der betrachteten Vents
wind     = 16;                   % window of piv
name = {'WUE_JVC' 'WUE_HS' 'GFZ1' 'GFZ2' 'I_HD'};
ly=9;

filepath  = ['/home/sysop/Data/Lauf_' num2str(ly) '/Run_' num2str(ly) '_GFZ2_test2'];
if ly==3 || ly==5 || ly==6
    timerate= 1/50;  % Vid 3,5,6
    scaling =1/115; % GFZ Vid   3,   5, 6
    roi = [820 826 967 1002]; % GFZ1
else
    timerate= 1/250*5; % Vid 1,2,  4,     7,8,9,10,clean
    scaling = 1/30; % GFZ 1 und 2
end

fileformat='*.jpg';

filenames = dir(fullfile(filepath, fileformat));
filenames = {filenames.name};

max_file  = min(75+1,numel(filenames));                     % Anzahl der Bilder
timestep = gt_T(max_file-1,timestep_thres);
runs=floor((max_file-1)/timestep);
time_sqrt=ceil(sqrt(timestep));

d = filenames{1};
    f = fullfile(filepath , d);
    ref=imread(f);

lava_img    =zeros(size(ref,1),size(ref,2),3,timestep+1);   % Images des Geysirs
daily = zeros(max_file-1,max_vent);      % daily heigth of the fountaine

fa       =  1;                  % Abtastfrequenz
ask_roi  =  1;                  % 1 falls ca ROI abgefragt werden soll
ask_vent =  0;                  % 1 falls vents abgefragt werden soll
ask_vel  =  1;                  % 1 falls velocity berechnet werden soll
feat     =  0;                  % 1 falls precise roi
pic      =  0;                  % 1 falls bilder am Ende
mask     = [];
passes   =  2;
int2     = wind/2;
%roi      = [];

if ask_vel==0
    wind = 0;
end

file = '/log_vector.txt'; % Name der Ausgabedatei
fid = fopen([filepath file],'w');
fprintf(fid,'method: FFT multi \n');

daily = zeros(max_file-1,3,max_vent);      % daily heigth of the fountaine
daily_2 = zeros(max_file-1,max_vent);      % daily heigth of the fountaine
v_ini = zeros(max_file-1,max_vent-1);      % initial velocity of the fountaine
u_ini = zeros(max_file-1,max_vent-1);

if ask_roi==1
    figure%close all;
    interest=FieldOfView([],ref); %noch unschĂČÂűn

    if interest=='n'
       [~,b] = imcrop(ref);
       b=round(b);
       roi = [max(b(1)-wind,1)  max(b(2)-wind,1) ...
```

```
           min(b(1)+b(3)+wind,size(ref,2))  min(b(2)+b(4)+wind,size(ref,1))];
    else
        roi=[1 1 size(ref,2) size(ref,1)];
    end
end

if ask_vent==1
   ref          =zeros(4,max_vent);
   for v_nr=1:max_vent
        figure%close all;
        [~,b] = imcrop(img);
        b=round(b);
        ref_a = [max(b(1)-0.5*wind,1)  max(b(2)-0.5*wind,1)  ... min(b(2)+wind,size(img,2))  ...max(b(3)-wind
            ,1)
              min((b(3)+wind-1),(size(img,2)-max(b(1)-0.5*wind,1)))  ...
              min((b(4)+wind-1),(size(img,1)-max(b(2)-0.5*wind,1)))];
        ref(:,v_nr)=ref_a;
        close(gcf);  % richtig???
    end
end

if feat==1
    subplot(2,2,1), imshow(rgb2gray(img)), title('gray');
        subplot(2,2,2), imshow(img(:,:,1)), title('red');
        subplot(2,2,3), imshow(img(:,:,2)), title('green');
        subplot(2,2,4), imshow(img(:,:,3)), title('blue');
    str={'gray';'red';'green';'blue'};
    [s,v] = listdlg('PromptString','Which color space do you want for the Feature? ',...
                    'SelectionMode','single',...
                    'ListSize', [300 200],...
                    'Name','Format','ListString',str);
     while v~=1 %okay nicht gedrÃČÂijckt
        err_dlg = errordlg('You must choose a color space!','File Error','modal');
        waitfor(err_dlg);
        [s,v] = listdlg('PromptString','Which color space do you want? ',...
                    'SelectionMode','single',...
                    'ListString',str);
     end
     cs_feat=str{s};
end
referenz=double(ref);

v_nr=1;
for run=1:runs
    %%% Laden der Daten
    figure(1)

    for k=(run-1)*timestep+1:run*timestep+1
        j=k-(run-1)*timestep;
        d = filenames{k};
        f = fullfile(filepath , d);
        img=imread(f);
        lava_img(:,:,:,j)=img;
        if j~=timestep+1
            subplot(time_sqrt,ceil(timestep/time_sqrt),j),imagesc(img)
        end
    end

    figure(2)
    for k=(run-1)*timestep+1:run*timestep
        j=k-(run-1)*timestep;

        % Maske erstellen
        Im_6=lava_img(:,:,:,j)/255;
        A=double(ref(:,:,3))/255;
        B=double(Im_6(:,:,3));
        F=(A-B)*15;
        thres=max(1,max(max(F)));
        F(abs(F)<thres/10)=0;
        F(F~=0)=1;
        figure(2),subplot(time_sqrt,ceil(timestep/time_sqrt),j),imagesc(F)%imagesc(rgb2gray(A1.*Im_6))

        [B,L] = bwboundaries(F,'noholes');
        stats = regionprops(L,'Area','BoundingBox');

        if isempty(B)
            allHeight = 0;
            totHeight = zeros(1,2);
        else
            allHeight = zeros(length(B),1);
            totHeight = zeros(length(B),2);
        end

        area_total = [];
        for l=1:length(B)
            area_total = [area_total; stats(l).Area];
        end
        area_max=max(area_total);
        for l=1:length(B)
            area = stats(l).Area;
            if area==area_max
                y_begin=max(floor(stats(l).BoundingBox(2)),1);
                x_begin=max(floor(stats(l).BoundingBox(1)),1);
                %l
                allHeight(l) = stats(l).BoundingBox(4);
                %totHeight(l,2) = -(floor(stats(l).BoundingBox(2))-325);
                totHeight(l,2) = stats(l).BoundingBox(3);
            else
                allHeight(l) = 0;
                totHeight(l,2) = 0;
            end
        end
```

```
        if isempty(B)
            allHeight=0;
        end
        daily_2(k,v_nr)= max(allHeight)*scaling;

        daily(k,2,v_nr)= max(allHeight)*scaling;
        if daily(k,2,v_nr)==0
            daily(k,3,v_nr)= 0;
        else
            ind = find(allHeight>=floor(daily(k,2,v_nr)/scaling),1);
            daily(k,3,v_nr)= totHeight(ind,2)*scaling;
        end
        if max(allHeight)==0
            daily(k,2,v_nr)=0;
        else
            index=find(allHeight==max(allHeight),1);
            daily(k,1,v_nr)=floor(stats(index).BoundingBox(2));
        end

        if ask_vel==1 && daily(k,2,v_nr)~=0
            if feat==1
                img1=rgb2cs(lava_img(:,:,:,j),cs_feat);
                feature = masc_precise(img1);  %How to implement this?
            else
                feature = [];
            end
            roi=[1 1 size(img,2)-1 size(img,1)-1];
            F1=F(roi(2):roi(4),roi(1):roi(3));
            im1=rgb2gray(lava_img(roi(2):roi(4),roi(1):roi(3),:,j)/255);
            im2=rgb2gray(lava_img(roi(2):roi(4),roi(1):roi(3),:,j+1)/255);
            F1=F(875-wind:940+wind,940-wind:990+wind);
            im1=rgb2gray(lava_img(875-wind:940+wind,940-wind:990+wind,:,j)/255).*F1;
            im2=rgb2gray(lava_img(875-wind:940+wind,940-wind:990+wind,:,j+1)/255);

%              im1=rgb2gray(lava_img(:,:,:,j)/255);
%              im2=rgb2gray(lava_img(:,:,:,j+1)/255);
            if passes==2
                [xi,yi,iu,iv,typevector]=piv_multi(im1,im2, wind, 0.5*wind,1, ...
                     mask,roi,passes,int2,0,0,'spline',feature,fid);
                 (image1,image2,interrogationarea, step, subpixfinder,
                 mask_inpt, roi_inpt,passes,int2,int3,int4,imdeform,feature, fid)
                feature = F1; % feature for the calculation
                refi = rgb2gray(ref(roi(2):roi(4),roi(1):roi(3),:));
                figure(3)
                [xi,yi,iu,iv]=mpiv_try(im1,im2, wind,wind, 0.5,0.5, ...
                     ceil(wind/10)*10,ceil(wind/10)*10, timerate, 'mqd', 0, 1, 1);

                [x,y] = meshgrid(xi,yi);

            elseif passes==3
                [xi,yi,iu,iv,typevector]=piv_multi(im1,im2, wind, 0.5*wind,1, ...
                     mask,roi,passes,int2,int2/2,0,'spline',feature,fid);
            else
                warning('passes is reduce/set to 2!')
                [xi,yi,iu,iv,typevector]=piv_multi(im1,im2, wind, 0.5*wind,1, ...
                     mask,roi,passes,int2,0,0,'spline',feature,fid);
            end
            iv(abs(iv)>size(im1,1))=0;
            iu(abs(iu)>size(im1,2))=0;
            v_ini(k,v_nr)= -min(min(iv));
            u_ini(k,v_nr)= iu(find(iv==min(min(iv)),1,'first'));
        end

    end
    str=['Process: ' num2str(run/runs*100) ' %'];
    disp(str);
end

figure, plot([1:size(u_ini)]*timerate, u_ini)
figure, plot([1:size(u_ini)]*timerate, v_ini)
height=daily(:,2);
height(v_ini==0)=0;
width=daily(:,3);
width(v_ini==0)=0;
figure, plot([1:size(u_ini)]*timerate,height,[1:size(u_ini)]*timerate,width)
```

```
dai=squeeze(daily_2);
X_mags = abs(fft(dai(:,1)));
 num_bins = length(X_mags);
 [b, a] = butter(7, 0.2, 'low');
 [b2, a2] = butter(7, 0.02, 'high');
 H1 = freqz(b,a, floor(num_bins/2));
 H2 = freqz(b2,a2, floor(num_bins/2));
max_vent=size(dai,2);
y_all=[];
for i=1:max_vent
     x = dai(:,i);

     x_filtered = filter(b,a,x);
     %x_filtered2 = filter(b2,a2,x_filtered);

     y_all=[y_all x_filtered];

end
dai=squeeze(daily_2);

data2=y_all';%dai';%ly_2;%dai_all2;
clearvars -except da* y_all

wname ='bior3.3';
level  = 2;
dirDec = 'r';
```

```
FontSizeTitle = 20;
FontSize = 18;

X=data2';
decROW = mdwtdec(dirDec,X,level,wname);
data_wav   = mdwtrec(decROW,'a',level);

data_wav=data_wav';
leng=size(data_wav,2);
data_1=data_wav(:,1:4000);
data_2=data_wav(:,4000:end);
data_3=data_wav(:,2001:6000);
data1=zeros(size(data_1,2),9);
data2=zeros(size(data_2,2),9);
data3=zeros(size(data_2,2),9);
data_1=data_1';
data_2=data_2';
data_3=data_3';
for k=1:9
    i=k;
    max1=max(data_1(:,i));
    data1(:,k)=data_1(:,i)/max1-mean(data_1(:,i)/max1);
    data2(:,k)=data_2(:,i)/max(data_2(:,i))-mean(data_2(:,i)/max(data_2(:,i)));
    data3(:,k)=data_3(:,i)/max(data_3(:,i))-mean(data_3(:,i)/max(data_3(:,i)));
end

corriplott2=zeros(9,9);
for i=1:8
    ori=data1(:,i);
    %ori=data_1(i,:)/max(data_1(i,:))-mean((data_1(i,:)/max(data_1(i,:))));
    for k=i:8
        test=data1(:,k);
        %test=data_1(k,:)/max(data_1(k,:))-mean((data_1(k,:)/max(data_1(k,:))));
        [corri,lags]=xcorr(ori,test,'coeff');
            max_corr_i=max(corri);
        corriplott2(i,k)=max_corr_i(1);
        corriplott2(k,i)=max_corr_i(1);
    end
end
```

8.1.3 Fountain height calculation

```
%%%%%%%%%%%%%%%%%%%%%%%%%%%%%%%%%%%%%%%%%%%%%%%%%%%
% Calculating Fountains height
% Modell of lava fountains based on Poiseuille flow
%%%%%%%%%%%%%%%%%%%%%%%%%%%%%%%%%%%%%%%%%%%%%%%%%%%%
 clear all;
 close all;

%% Initialise the parameters
dP_dike       = 4e6;     % driving pressure [1.6e6Pa]/ [4e1bar]
r_Baugur =  15.6/2;     % radius dike of Baugur
r_Sudri  =  7.5;     % radius dike of Baugur
eta      = 100;     % dynamic viscosity of the fluid [Pa s]
L        = 40e3;    % length of the dike

g        =   9.81;  % Constant Erdbeschleunigung
h        = 3e2;
rho      = 2500;    %magma density [kg/m3] ref: Augustsdottir et al
%% Anlegen der benÃűtigten Matrizen

dP = -dP_dike-rho*g*h;
dz = h;

R = [r_Baugur; r_Sudri];

for k=1:length(R)
    %% Calculate the velocity within the circular dike as a function of the radial position
    r_vent = R(k);
    r=[-r_vent:0.5:r_vent];

    vel_max = (-dP*r_vent.^2)/(4*eta*(L+h));
    vel_R   = vel_max*(1-(r./r_vent).^2);
    vel_mean = vel_max/2;
    figure(1), plot(r,vel_R)
        title('Poiseuille flow within circular dike')
        hold all;
end

r_cond=[0:0.1:15.6];
u_g = 3*(-dP*r_cond.^2)/(4*eta*(L+h))%sqrt(2*g*r_cond);
h_cond = u_slug_g.^2/(2*g);

% magma ascent in conduit
for a = 2:0.02:3
    u_z((a-2)*50+1) = 1/(4*eta)*dP/dz*a^2;
        %% Calculating the resulting height based on vertical throw
    H((a-2)*50+1) = u_z.^2/(2*g);   % vertical throw with air drag
end
```

```
%%%%%%%%%%%%%%%%%%%%%%%%%%%%%%%%%%%%%%%%%%%%%%%%%%%
% Calculating Fountains height
% Modell of lava fountains based on pond depth Wilson et al.
%%%%%%%%%%%%%%%%%%%%%%%%%%%%%%%%%%%%%%%%%%%%%%%%%%%%

% clear all;
 close all;

%% Initialise the parameters
dP_dike  = 1.6e6;           % driving pressure [1.6e6Pa]/ [4e1bar]
r_Baugur =  15.6/2;         % radius dike of Baugur
r_Sudri  =  7.5;            % radius dike of Baugur
eta      = 100;             % dynamic viscosity of the fluid [Pa s]
L        = 40e3;            % length of the dike

g        =   9.81;          % Constant Erdbeschleunigung
h        = 3e2;
rho      = 2500;            % magma density [kg/m3] ref: Augustsdottir et al

rho_l = 2600;               %
n_all     = [0.5:0.05:0.75];  % gas content 0.5 wt% up to 0.75?
Q     = 8.3145;
T_K     = [1173, 1200, 1250, 1300, 1400, 1423, 1473];  % between 1173 and 1473 (1423.15) [K]
m     = 18.018;             % molare mass of water
Pa    = 0.1e6;              % atmosphaeric pressure
M     = 6.75e5;%8.75e5;
rho_pond = 1000;
alpha = 0.08;
r_full=[2:0.1:30];
d_pond=[0:0.1:80];
h =load('/home/sysop/Documents/MATLAB/Scripte/Daten/morph_H.mat');%[630:5:775]; % HÃűhe nach Head&Wilson,
     1987 up to 775
H_all=h(1,1,1).H_all;
H_all=[225:225:1125];%[630:5:775];
h =load('/home/sysop/Documents/MATLAB/Scripte/Daten/morph_r.mat');
r=h(1,1,1).r;
%% Anlegen der benÃűtigten Matrizen
H_fount=zeros(9,length(T_K), length(n_all),length(H_all));
H_fount2=zeros(length(d_pond),length(r_full), length(n_all));
r_all=zeros(length(d_pond),length(T_K), length(n_all),length(H_all),3);
r_all2=zeros(9, length(r_full),length(n_all),3);
H_130=zeros(size(H_all));
H_70=zeros(size(H_all));
%% Calculation depending on the pond depth
for p=1:length(T_K)
    T=T_K(p);

    for q=1:length(n_all)
        n=n_all(q);
        beta_a = 1/((n*Q*T/(m/1000*Pa))+(1-n)/rho_l)*100;
        for s=1:length(H_all)
```

```
            ua = sqrt(2*g*(H_all(s)+(n-0.5)*1625));
            r_a = sqrt(M/(beta_a*ua*pi));

            P = 1/0.4*n/(1-n)*(Q*T*rho_l)/m;
            h_frac = (P-Pa)/(g*rho_pond);
            H_fount(1,p,q,s)=H_all(s)+(n-0.5)*1625;
            for k=2:length(d_pond)
                h_pond = d_pond(k);
                P_pond = Pa + rho_pond*g*h_pond;

                beta_pond = 1/((n*Q*T/(m/1000*P_pond))+(1-n)/rho_l)*100;
                u = real(sqrt(2*(ua^2/2+g*h_pond-(n*Q*T/m)*log(P_pond/Pa)-((1-n)/rho_l)*...
                    (P_pond-Pa))));
                r_pond = real(sqrt(M/(beta_pond*u*pi)));

                rm = real((r_a+r_pond)/2);
                um = real(ua+u)/2;
                rho_m = (beta_a+beta_pond)/2;

                for l=1:100
                    Mi=real(2*pi*rm*h_pond*rho_pond*alpha*um*sqrt(rho_m/rho_pond));
                    uf=M/(M+Mi)*ua;
                    um=real(u+uf)/2;
                end
                H_fount(k,p,q,s)=uf^2/(2*g);
                r_all(k,p,q,s,:)=[r_pond rm r_a];
                r_all(1,p,q,s,:)=r_a;

                 if H_fount(k,p,q,s)>130
                     H_130(s) = d_pond(k);
                 elseif H_fount(k,p,q,s)>70
                     H_70(s)  = d_pond(k);
                 end
            end
        end
    end
end

T=1423;
for q=1:length(n_all)
    n=n_all(q);
    beta_a = 1/((n*Q*T/(m/1000*Pa))+(1-n)/rho_l)*100;

    for t=1:length(r_full)
        r_a = r_full(t);
        ua = M/(r_a^2*beta_a*pi);

        H_0=ua^2/(2*g);

        P = 1/0.4*n/(1-n)*(Q*T*rho_l)/m;
        h_frac = (P-Pa)/(g*rho_pond);
        H_fount2(1,t,q)=H_0;
        for k=9:16
            h_pond = d_pond(k);
            P_pond = Pa + rho_pond*g*h_pond;

            beta_pond = 1/((n*Q*T/(m/1000*P_pond))+(1-n)/rho_l)*100;
            u = sqrt(2*(ua^2/2+g*h_pond-(n*Q*T/m)*log(P_pond/Pa)-((1-n)/rho_l)*...
                (P_pond-Pa)));
            r_pond = sqrt(M/(beta_pond*u*pi));

            rm = (r_a+r_pond)/2;
            um = (ua+u)/2;
            rho_m = (beta_a+beta_pond)/2;

            for l=1:100
                Mi=2*pi*rm*h_pond*rho_pond*alpha*um*sqrt(rho_m/rho_pond);
                uf=M/(M+Mi)*ua;
                um=(u+uf)/2;
            end
            H_fount2(k-8,t,q)=uf^2/(2*g);
            r_all2(k-8,t,q,:)=[r_pond rm r_a];
            r_all2(1,t,q,:)=r_a;
        end
    end
end
```

Bibliography

Acocella, V., Gudmundsson, A., and Funiciello, R. (2000). Interaction and linkage of extension fractures and normal faults: examples from the rift zone of Iceland. *Journal of Structural Geology*, 22(9)(9):1233–1246.

Acocella, V. and Neri, M. (2003). What makes flank eruptions? The 2001 Etna eruption and its possible triggering mechanisms. *Bulletin of Volcanology*, 65(7)(7):517–529.

Acocella, V. and Neri, M. (2009). Dike propagation in volcanic edifices: overview and possible developments. *Tectonophysics*, 471(1-2)(1-2):67–77.

Acocella, V. and Trippanera, D. (2016). How diking affects the tectonomagmatic evolution of slow spreading plate boundaries: Overview and model. *Geosphere*, 12(3)(3):867.

Ágústsdóttir, T., Woods, J., Greenfield, T., Green, R. G., White, R. S., Winder, T., Brandsdóttir, B., Steinthórsson, S., and Soosalu, H. (2016). Strike-slip faulting during the 2014 Bárðarbunga-Holuhraun dike intrusion, central Iceland. *Geophysical Research Letters*, 43(4):1495–1503.

Ágústsdóttir, T., Woods, J., Greenfield, T., Green, R. G., White, R. S., Winder, T., Brandsdóttir, B., Steinthórsson, S., and Soosalu, H. (2016). Strike-slip faulting during the 2014 Bárðarbunga-Holuhraun dike intrusion, central Iceland. *Geophysical Research Letters*, 43(4):1495–1503.

Aki, K. and Koyanagi, R. (1981). Deep volcanic tremor and magma ascent mechanism under Kīlauea, Hawai'i. *Journal of Geophysical Research: Solid Earth*, 86(B8):7095–7109.

Allard, P., Burton, M., and Muré, F. (2005). Spectroscopic evidence for a lava fountain driven by previously accumulated magmatic gas. *Nature*, 433(7024)(7024):407.

Allard, P., La Spina, A., Tamburelllo, G., Aiuppa, A., Coquet, A., Brenguier, F., Coppola, D., Di Muro, A., Burton, M., and Staudacher, T. (2011). First cross-correlated measurements of magma dynamics and degassing during a dyke eruption at Piton de la Fournaise hot spot volcano, Reunion island. In *AGU Fall Meeting Abstracts*.

Alparone, S., Andronico, D., Lodato, L., and Sgroi, T. (2003). Relationship between tremor and volcanic activity during the Southeast Crater eruption on Mount Etna in early 2000. *Journal of Geophysical Research: Solid Earth*, 108(B5).

Amici, S., Piscini, A., Buongiorno, M. F., and Pieri, D. (2013a). Geological classification of volcano Teide by hyperspectral and multispectral satellite data. *International journal of remote sensing*, 34(9-10)(9-10):3356–3375.

Amici, S., Turci, M., Giammanco, S., Spampinato, L., and Giulietti, F. (2013b). UAV thermal infrared remote sensing of an italian mud volcano. *Advances in Remote Sensing*, 2(4)(4):358–364.

Amici, S., Turci, M., Giulietti, F., Giammanco, S., Buongiorno, M., La Spina, A., and Spampinato, L. (2013c). Volcanic environments monitoring by drones mud volcano case study. *International Archives of the Photo-grammetry, Remote Sensing and Spatial Information Sciences, UAV*, 1:W2.

Andronico, D. and Corsaro, R. (2011). Lava fountains during the episodic eruption of South–East Crater (Mt. Etna), 2000: insights into magma-gas dynamics within the shallow volcano plumbing system. *Bulletin of volcanology*, 73(9):1165–1178.

Andronico, D., Corsaro, R., Cristaldi, A., and Polacci, M. (2008). Characterizing high energy explosive eruptions at Stromboli volcano using multidisciplinary data: an example from the 9 January 2005 explosion. *Journal of Volcanology and Geothermal Research*, 176(4):541–550.

Andronico, D., Taddeucci, J., Cristaldi, A., Miraglia, L., Scarlato, P., and Gaeta, M. (2013). The 15 March 2007 paroxysm of Stromboli: video-image analysis, and textural and compositional features of the erupted deposit. *Bulletin of volcanology*, 75(7):733.

Árnadóttir, T., Geirsson, H., and Jiang, W. (2008). Crustal deformation in Iceland: Plate spreading and earthquake deformation. *Jökull*, 58:59–74.

Bagnardi, M., González, P. J., and Hooper, A. (2016). High-resolution digital elevation model from tri-stereo Pleiades-1 satellite imagery for lava flow volume estimates at Fogo Volcano. *Geophysical Research Letters*, 43(12):6267–6275.

Baldi, P., Bonvalot, S., Briole, P., and Marsella, M. (2000). Digital photogrammetry and kinematic GPS applied to the monitoring of Vulcano Island, Aeolian Arc, Italy. *Geophysical Journal International*, 142(3):801–811.

Battaglia, J., Aki, K., and Staudacher, T. (2005). Location of tremor sources and estimation of lava output using tremor source amplitude on the Piton de la Fournaise volcano: 2. Estimation of lava output. *Journal of volcanology and geothermal research*, 147(3-4):291–308.

Behncke, B., Branca, S., Corsaro, R. A., De Beni, E., Miraglia, L., and Proietti, C. (2014). The 2011–2012 summit activity of Mount Etna: Birth, growth and products of the new SE crater. *Journal of Volcanology and Geothermal Research*, 270:10–21.

Behncke, B., Neri, M., Pecora, E., and Zanon, V. (2006). The exceptional activity and growth of the Southeast Crater, Mount Etna (Italy), between 1996 and 2001. *Bulletin of Volcanology*, 69(2)(2):149–173.

Belousov, A., Belousova, M., Edwards, B., Volynets, A., and Melnikov, D. (2015). Overview of the precursors and dynamics of the 2012–13 basaltic fissure eruption of Tolbachik Volcano, Kamchatka, Russia. *Journal of Volcanology and Geothermal Research*, 307:22–37.

Belousov, A., Walter, T. R., and Troll, V. R. (2005). Large-scale failures on domes and stratocones situated on caldera ring faults: sand-box modeling of natural examples from Kamchatka, Russia. *Bulletin of Volcanology*, 67(5):457–468.

Bemis, K., Walker, J., Borgia, A., Turrin, B., Neri, M., and Swisher III, C. (2011). The growth and erosion of cinder cones in Guatemala and El Salvador: models and statistics. *Journal of Volcanology and Geothermal Research*, 201(1-4)(1-4):39–52.

Bemis, K. G. (1995). *A morphometric study of volcanoes in Guatemala, Iceland, the Snake River Plain, and the South Pacific.* PhD thesis, Rutgers University, New Brunswick.

Benson, P. M., Vinciguerra, S., Meredith, P. G., and Young, R. P. (2008). Laboratory simulation of volcano seismicity. *Science*, 322(5899)(5899):249–252.

Bernard, B., Battaglia, J., Proaño, A., Hidalgo, S., Vásconez, F., Hernandez, S., and Ruiz, M. (2016). Relationship between volcanic ash fallouts and seismic tremor: quantitative assessment of the 2015 eruptive period at Cotopaxi volcano, Ecuador. *Bulletin of Volcanology*, 78(11):80.

Beyreuther, M., Barsch, R., Krischer, L., Megies, T., Behr, Y., and Wassermann, J. (2010). ObsPy: A Python toolbox for seismology. *Seismological Research Letters*, 81(3)(3):530–533.

Björnsson, A. (1985). Dynamics of crustal rifting in NE Iceland. *Journal of Geophysical Research: Solid Earth*, 90(B12):10151–10162.

Björnsson, A., Johnsen, G., Sigurdsson, S., Thorbergsson, G., and Tryggvason, E. (1979). Rifting of the plate boundary in North Iceland 1975–1978. *Journal of Geophysical Research: Solid Earth*, 84(B6):3029–3038.

Björnsson, H. and Einarsson, P. (1990). Volcanoes beneath Vatnajökull, Iceland: Evidence from radio echo-sounding, earthquakes and jökulhlaups. *Jökull*, 40:147–168.

Björnsson, H., Magnusson, S., Arason, P., and Petersen, G. (2013). Velocities in the plume of the 2010 Eyjafjallajökull eruption. *Journal of Geophysical Research: Atmospheres*, 118(20)(20).

Bluth, G. J. and Rose, W. I. (2004). Observations of eruptive activity at Santiaguito volcano, Guatemala. *Journal of Volcanology and Geothermal research*, 136(3-4)(3-4):297–302.

Brown, S. K., Auker, M., and Sparks, R. (2015). *Populations around Holocene volcanoes and development of a Population Exposure Index*, pages 223–232. Cambridge University Press.

Bruce, P. M. and Huppert, H. E. (1989). Thermal control of basaltic fissure eruptions. *Nature*, 342(6250)(6250):665–667.

Bruce, P. M. and Huppert, H. E. (1990). Solidification and melting along dykes by the laminar flow of basaltic magma. *Magma transport and storage*, edited by MP Ryan, Chichester, England, John Wiley:87–101.

Budd, L., Griggs, S., Howarth, D., and Ison, S. (2011). A fiasco of volcanic proportions? Eyjafjallajökull and the closure of European airspace. *Mobilities*, 6(1):31–40.

Calvari, S., CannavÃš, F., Bonaccorso, A., Spampinato, L., and Pellegrino, A. G. (2018). Paroxysmal explosions, lava fountains and ash plumes at etna volcano: Eruptive processes and hazard implications. *Frontiers in Earth Science*, 6:107.

Calvari, S. and Pinkerton, H. (2004). Birth, growth and morphologic evolution of the âĂŸLaghettoâĂŹcinder cone during the 2001 Etna eruption. *Journal of Volcanology and Geothermal Research*, 132(2-3)(2-3):225–239.

Cannata, A., Di Grazia, G., Montalto, P., Ferrari, F., Nunnari, G., Patanè, D., and Privitera, E. (2010). New insights into banded tremor from the 2008–2009 Mount Etna eruption. *Journal of Geophysical Research: Solid Earth*, 115(B12)(B12).

Carey, S. and Sparks, R. (1986). Quantitative models of the fallout and dispersal of tephra from volcanic eruption columns. *Bulletin of volcanology*, 48(2-3)(2-3):109–125.

Carrivick, J. L., Smith, M. W., and Quincey, D. J. (2016). Background to structure from motion. *Structure from Motion in the Geosciences*, Chichester: John Wiley & Sons, Ltd.:37–59.

Caudron, C., White, R. S., Green, R. G., Woods, J., Ágústsdóttir, T., Donaldson, C., Greenfield, T., Rivalta, E., and Brandsdóttir, B. (2018). Seismic Amplitude Ratio Analysis of the 2014–2015 Bárðarbunga-Holuhraun Dike Propagation and Eruption. *Journal of Geophysical Research: Solid Earth*, 123(1)(1):264–276.

Cecchi, E., de Vries, B. v. W., Lavest, J.-M., Harris, A., and Davies, M. (2003). N-view reconstruction: a new method for morphological modelling and deformation measurement in volcanology. *Journal of volcanology and geothermal research*, 123(1-2)(1-2):181–201.

Chouet, B. (1988). Resonance of a fluid-driven crack: Radiation properties and implications for the source of long-period events and harmonic tremor. *Journal of Geophysical Research: Solid Earth*, 93(B5)(B5):4375–4400.

Chouet, B. A. (1996). Long-period volcano seismicity: its source and use in eruption forecasting. *Nature*, 380(6572)(6572):309.

Coppola, D., Laiolo, M., Cigolini, C., Delle Donne, D., and Ripepe, M. (2016). Enhanced volcanic hot-spot detection using MODIS IR data: results from the MIROVA system. *Geological Society, London, Special Publications*, 426(1)(1):181–205.

Coppola, D., Laiolo, M., Piscopo, D., and Cigolini, C. (2013). Rheological control on the radiant density of active lava flows and domes. *Journal of Volcanology and Geothermal Research*, 249:39–48.

Coppola, D., Piscopo, D., Staudacher, T., and Cigolini, C. (2009). Lava discharge rate and effusive pattern at Piton de la Fournaise from MODIS data. *Journal of Volcanology and Geothermal Research*, 184(1-2)(1-2):174–192.

Coppola, D., Ripepe, M., Laiolo, M., and Cigolini, C. (2017). Modelling satellite-derived magma discharge to explain caldera collapse. *Geology*, 45(6)(6):523–526.

Coppola, D., Staudacher, T., and Cigolini, C. (2005). The May-July 2003 eruption at Piton de la Fournaise (La Reunion): Volume, effusion rates, and emplacement mechanisms inferred from thermal imaging and Global Positioning System (GPS) Survey. *Special papers - Geological Society of America*, 396:103.

Corazzato, C. and Tibaldi, A. (2006). Fracture control on type, morphology and distribution of parasitic volcanic cones: An example from Mt. Etna, Italy. *Journal of Volcanology and Geothermal Research*, 158(1-2):177–194.

Cronin, S. J. (2013). Stratovolcanoes. In *Encyclopedia of Natural Hazards*, pages 941–947. Springer.

Darmawan, H., Walter, T. R., Brotopuspito, K. S., Nandaka, I. G. M. A., et al. (2018). Morphological and structural changes at the Merapi lava dome monitored in 2012–15 using unmanned aerial vehicles (UAVs). *Journal of Volcanology and Geothermal Research*, 349:256–267.

Delaney, P. T. and Pollard, D. D. (1982). Solidification of basaltic magma during flow in a dike. *American Journal of Science*, 282(6):856–885.

DeMets, C., Gordon, R. G., and Argus, D. F. (2010). Geologically current plate motions. *Geophysical Journal International*, 181(1):1–80.

Diefenbach, A. K., Bull, K. F., Wessels, R. L., and McGimsey, R. G. (2013). Photogrammetric monitoring of lava dome growth during the 2009 eruption of Redoubt Volcano. *Journal of Volcanology and Geothermal Research*, 259:308–316.

Diefenbach, A. K., Crider, J. G., Schilling, S. P., and Dzurisin, D. (2012). Rapid, low-cost photogrammetry to monitor volcanic eruptions: an example from Mount St. Helens, Washington, USA. *Bulletin of volcanology*, 74(2)(2):579–587.

Dirscherl, M. C. (2016). Topographic change quantification and DEM uncertainty assessment using TanDEM-X and F-SAR DEM time series and quality maps: Application to the 2014-2015 Bárðarbunga volcanic eruption, Iceland. Master's thesis, University College London, https://elib.dlr.de/109037.

Dóniz-Páez, J. (2015). Volcanic geomorphological classification of the cinder cones of Tenerife (Canary Islands, Spain). *Geomorphology*, 228:432–447.

Dürig, T., Gudmundsson, M. T., Dioguardi, F., Woodhouse, M., Björnsson, H., Barsotti, S., Bonadonna, C., Witt, T., and Walter, T. R. (2018). REFIR- An multi-parameter system for estimating plume height and mass eruption rate during explosive eruptions operationally in near real-time . *submitted to Journal of Volcanology and Geothermal Research*.

Dürig, T., Gudmundsson, M. T., Karmann, S., Zimanowski, B., Dellino, P., Rietze, M., and Büttner, R. (2015). Mass eruption rates in pulsating eruptions estimated from video analysis of the gas thrust-buoyancy transition - a case study of the 2010 eruption of Eyjafjallajökull, Iceland. *Earth, Planets and Space*, 67(1):180.

Dzurisin, D. (2007). *Volcano deformation: Geodetic monitoring techniques*. Springer-Praxis Books in Geophysical Sciences, Berlin.

Dzurisin, D., Koyanagi, R. Y., and English, T. T. (1984). Magma supply and storage at Kīlauea Volcano, Hawai'i, 1956–1983. *Journal of Volcanology and Geothermal Research*, 21(3-4):177–206.

Eaton, J. P., Richter, D. H., and Krivoy, H. L. (1987). Cycling of magma between the summit reservoir and Kīlauea Iki lava lake during the 1959 eruption of Kīlauea volcano. *US Geol. Surv. Prof. Pap*, 1350:1307–1335.

Eibl, E. P., Bean, C. J., Jónsdóttir, I., Höskuldsson, A., Thordarson, T., Coppola, D., Witt, T., and Walter, T. R. (2017a). Multiple coincident eruptive seismic tremor sources during the 2014–2015 eruption at Holuhraun, Iceland. *Journal of Geophysical Research: Solid Earth*, 122(4)(4):2972–2987.

Eibl, E. P., Bean, C. J., Vogfjörd, K. S., Ying, Y., Lokmer, I., Möllhoff, M., O'Brien, G. S., and Pálsson, F. (2017b). Tremor-rich shallow dyke formation followed by silent magma flow at Bárðarbunga in Iceland. *Nature Geoscience*, 10(4)(4):299.

Einarsson, Þ. and Douglas, G. (1994). *Geology of Iceland: rocks and landscape*. Mál og menning.

Elgharib, M., Hefeeda, M., Durand, F., and Freeman, W. T. (2015). Video magnification in presence of large motions. In *Proceedings of the IEEE Conference on Computer Vision and Pattern Recognition*, pages 4119–4127.

Fagents, S. and Wilson, L. (1993). Explosive volcanic eruptions - VII. The ranges of pyroclasts ejected in transient volcanic explosions. *Geophysical Journal International*, 113(2):359–370.

Falsaperla, S., Alparone, S., D'Amico, S., Grazia, G., Ferrari, F., Langer, H., Sgroi, T., and Spampinato, S. (2005). Volcanic tremor at Mt. Etna, Italy, preceding and accompanying the eruption of July–August, 2001. *pure and applied geophysics*, 162(11)(11):2111–2132.

Favalli, M., Fornaciai, A., Mazzarini, F., Harris, A., Neri, M., Behncke, B., Pareschi, M. T., Tarquini, S., and Boschi, E. (2010). Evolution of an active lava flow field using a multitemporal LIDAR acquisition. *Journal of Geophysical Research: Solid Earth*, 115(B11):B11203.

Favalli, M., Karátson, D., Mazzarini, F., Pareschi, M. T., and Boschi, E. (2009). Morphometry of scoria cones located on a volcano flank: a case study from Mt. Etna (Italy), based on high-resolution LiDAR data. *Journal of Volcanology and Geothermal Research*, 186(3-4)(3-4):320–330.

Fedotov, S. (1981). Magma rates in feeding conduits of different volcanic centres. *Journal of Volcanology and Geothermal Research*, 9(4)(4):379–394.

Ferguson, D. J., Barnie, T. D., Pyle, D. M., Oppenheimer, C., Yirgu, G., Lewi, E., Kidane, T., Carn, S., and Hamling, I. (2010). Recent rift-related volcanism in Afar, Ethiopia. *Earth and Planetary Science Letters*, 292(3)(3):409–418.

Field, L., Blundy, J., Brooker, R., Wright, T., and Yirgu, G. (2012). Magma storage conditions beneath Dabbahu Volcano (Ethiopia) constrained by petrology, seismicity and satellite geodesy. *Bulletin of Volcanology*, 74(5)(5):981–1004.

Floricioiu, D., Jaber, W. A., Minet, C., Rossi, C., and Eineder, M. (2015). Tandem-X for mass balance of glaciers and subglacial volcanic activities. In *Geoscience and Remote Sensing Symposium (IGARSS), 2015 IEEE International*, pages 2903–2906. IEEE.

Flóvenz, Ó. G. and Gunnarsson, K. (1991). Seismic crustal structure in Iceland and surrounding area. *Tectonophysics*, 189(1-4)(1-4):1–17.

Formenti, Y., Druitt, T., and Kelfoun, K. (2003). Characterisation of the 1997 Vulcanian explosions of Soufrière Hills Volcano, Montserrat, by video analysis. *Bulletin of Volcanology*, 65(8)(8):587–605.

Fornaciai, A., Bisson, M., Landi, P., Mazzarini, F., and Pareschi, M. T. (2010). A LiDAR survey of Stromboli volcano (Italy): Digital elevation model-based geomorphology and intensity analysis. *International Journal of Remote Sensing*, 31(12)(12):3177–3194.

Francis, P., Wadge, G., and Mouginis-Mark, P. (1996). Satellite monitoring of volcanoes. In *Monitoring and Mitigation of Volcano Hazards*, pages 257–298. Springer.

Frank, W. B., Shapiro, N. M., and Gusev, A. A. (2018). Progressive reactivation of the volcanic plumbing system beneath Tolbachik volcano (Kamchatka, Russia) revealed by long-period seismicity. *Earth and Planetary Science Letters*, 493:47–56.

Garel, F., Kaminski, E., Tait, S., and Limare, A. (2012). An experimental study of the surface thermal signature of hot subaerial isoviscous gravity currents: implications for thermal monitoring of lava flows and domes. *Journal of Geophysical Research: Solid Earth*, 117(B2)(B2).

Gaudin, D., Taddeucci, J., Scarlato, P., Moroni, M., Freda, C., Gaeta, M., and Palladino, D. M. (2014). Pyroclast Tracking Velocimetry illuminates bomb ejection and explosion dynamics at Stromboli (Italy) and Yasur (Vanuatu) volcanoes. *Journal of Geophysical Research: Solid Earth*, 119(7)(7):5384–5397.

Geiger, H., Mattsson, T., Deegan, F. M., Troll, V. R., Burchardt, S., Gudmundsson, Ó., Tryggvason, A., Krumbholz, M., and Harris, C. (2016). Magma plumbing for the 2014–2015 Holuhraun eruption, Iceland. *Geochemistry, Geophysics, Geosystems*, 17(8)(8):2953–2968.

Gíslason, S. R., Stefánsdóttir, G., Pfeffer, M., Jóhannsson, T., Galeczka, I. M., Bali, E., Sigmarsson, O., Stefansson, A., Keller, N. S., Sigurðsson, Á., et al. (2015). Environmental pressure from the 2014–15 eruption of Bárðarbunga volcano, Iceland. *Geochemical Perspectives Letters*, 1(0):84–93.

Gomez, C. and Kennedy, B. (2017). Capturing volcanic plumes in 3D with UAV-based photogrammetry at Yasur Volcano–Vanuatu. *Journal of Volcanology and Geothermal Research*.

Gomez, C. and Purdie, H. (2016). UAV-based Photogrammetry and Geocomputing for Hazards and Disaster Risk Monitoring–A Review. *Geoenvironmental Disasters*, 3(1):23.

Gonnermann, H. M. and Manga, M. (2013). Dynamics of magma ascent in the volcanic conduit. In Fagents, S., Gregg, T., and Lopes, R., editors, *Modeling of volcanic processes*, chapter 4, pages 55–84. Cambridge, United Kingdom, Cambridge University Press.

Grant, J. V. and Kattenhorn, S. A. (2004). Evolution of vertical faults at an extensional plate boundary, southwest Iceland. *Journal of Structural Geology*, 26(3)(3):537–557.

Grosse, P., van Wyk de Vries, B., Petrinovic, I. A., Euillades, P. A., and Alvarado, G. E. (2009). Morphometry and evolution of arc volcanoes. *Geology*, 37(7):651–654.

Gudmundsson, A. (1992). Formation and growth of normal faults at the divergent plate boundary in Iceland. *Terra Nova*, 4(4):464–471.

Gudmundsson, A. and Brenner, S. L. (2005). On the conditions of sheet injections and eruptions in stratovolcanoes. *Bulletin of Volcanology*, 67(8)(8):768–782.

Gudmundsson, A., Friese, N., Galindo, I., and Philipp, S. L. (2008). Dike-induced reverse faulting in a graben. *Geology*, 36(2)(2):123–126.

Gudmundsson, A. and Loetveit, I. F. (2005). Dyke emplacement in a layered and faulted rift zone. *Journal of Volcanology and Geothermal Research*, 144(1-4)(1-4):311–327.

Gudmundsson, M. T. and Högnadóttir, T. (2007). Volcanic systems and calderas in the Vatnajökull region, central Iceland: Constraints on crustal structure from gravity data. *Journal of Geodynamics*, 43(1)(1):153–169.

Gudmundsson, M. T., Jónsdóttir, K., Hooper, A., Holohan, E. P., Halldórsson, S. A., Ófeigsson, B. G., Cesca, S., Vogfjörd, K. S., Sigmundsson, F., Högnadóttir, T., et al. (2016). Gradual caldera collapse at Bárðarbunga volcano, Iceland, regulated by lateral magma outflow. *Science*, 353(262)(262):262.

Harris, A. (2013). *Thermal remote sensing of active volcanoes: a user's manual*. Cambridge University Press.

Hartley, M. E. and Thordarson, T. (2013). The 1874–1876 volcano-tectonic episode at Askja, North Iceland: Lateral flow revisited. *Geochemistry, Geophysics, Geosystems*, 14(7)(7):2286–2309.

Head, J. W. and Wilson, L. (1987). Lava fountain heights at Pu'u'Ō'ō, Kīlauea, Hawai'i: Indicators of amount and variations of exsolved magma volatiles. *Journal of Geophysical Research: Solid Earth*, 92(B13)(B13):13715–13719.

Head, J. W., Wilson, L., and Smith, D. K. (1996). Mid-ocean ridge eruptive vent morphology and substructure: Evidence for dike widths, eruption rates, and evolution of eruptions and axial volcanic ridges. *Journal of Geophysical Research: Solid Earth*, 101(B12)(B12):28265–28280.

Head III, J. W. and Wilson, L. (1989). Basaltic pyroclastic eruptions: influence of gas-release patterns and volume fluxes on fountain structure, and the formation of cinder cones, spatter cones, rootless flows, lava ponds and lava flows. *Journal of Volcanology and Geothermal Research*, 37(3-4):261–271.

Hibert, C., Mangeney, A., Polacci, M., Muro, A. D., Vergniolle, S., Ferrazzini, V., Peltier, A., Taisne, B., Burton, M., Dewez, T., et al. (2015). Toward continuous quantification of lava extrusion rate: Results from the multidisciplinary analysis of the 2 January 2010 eruption of Piton de la Fournaise volcano, La Réunion. *Journal of Geophysical Research: Solid Earth*, 120(5)(5):3026–3047.

Hildreth, W., Christiansen, R. L., and O'Neil, J. R. (1984). Catastrophic isotopic modification of rhyolitic magma at times of caldera subsidence, Yellowstone Plateau volcanic field. *Journal of Geophysical Research: Solid Earth*, 89(B10):8339–8369.

Hjartardóttir, Á. R., Einarsson, P., Gudmundsson, M. T., and Högnadóttir, T. (2016). Fracture movements and graben subsidence during the 2014 Bárðarbunga dike intrusion in Iceland. *Journal of Volcanology and Geothermal Research*, 310:242–252.

Honda, K. and Nagai, M. (2002). Real-time volcano activity mapping using ground-based digital imagery. *ISPRS Journal of Photogrammetry and Remote Sensing*, 57(1-2):159–168.

Hotovec, A. J., Prejean, S. G., Vidale, J. E., and Gomberg, J. (2013). Strongly gliding harmonic tremor during the 2009 eruption of Redoubt Volcano. *Journal of Volcanology and Geothermal Research*, 259:89–99.

Houghton, B. and Gonnermann, H. (2008). Basaltic explosive volcanism: constraints from deposits and models. *Chemie der Erde-Geochemistry*, 68(2)(2):117–140.

Houghton, B. and Schmincke, H. (1989). Rothenberg scoria cone, East Eifel: a complex Strombolian and phreatomagmatic volcano. *Bulletin of Volcanology*, 52(1)(1):28–48.

Ida, Y. (1996). Cyclic fluid effusion accompanied by pressure change: implication for volcanic eruptions and tremor. *Geophysical research letters*, 23(12):1457–1460.

Jackson, D. B., Swanson, D. A., Koyanagi, R. Y., and Wright, T. L. (1975). The August and October 1968 east rift eruptions of Kīlauea volcano, Hawai'i. Technical report, US Govt. Print. Off.

James, M. and Varley, N. (2012). Identification of structural controls in an active lava dome with high resolution DEMs: Volcán de Colima, Mexico. *Geophysical Research Letters*, 39(22)(22).

James, M. R., Lane, S. J., Wilson, L., and Corder, S. B. (2009). Degassing at low magma-viscosity volcanoes: Quantifying the transition between passive bubble-burst and Strombolian eruption. *Journal of Volcanology and Geothermal Research*, 180(2-4)(2-4):81–88.

James, M. R., Pinkerton, H., and Robson, S. (2007). Image-based measurement of flux variation in distal regions of active lava flows. *Geochemistry, Geophysics, Geosystems*, 8(3)(3).

James, M. R. and Robson, S. (2014). Mitigating systematic error in topographic models derived from UAV and ground-based image networks. *Earth Surface Processes and Landforms*, 39(10)(10):1413–1420.

James, M. R., Robson, S., Pinkerton, H., and Ball, M. (2006). Oblique photogrammetry with visible and thermal images of active lava flows. *Bulletin of Volcanology*, 69(1)(1):105–108.

Jaupart, C. and Vergniolle, S. (1988). Laboratory models of Hawaiian and Strombolian eruptions. *Nature*, 331(6151):58.

Jaupart, C. and Vergniolle, S. (1989). The generation and collapse of a foam layer at the roof of a basaltic magma chamber. *Journal of Fluid Mechanics*, 203:347–380.

Jin-Yu, Z., Yan, C., and Xian-Xiang, H. (2009). Edge detection of images based on improved Sobel operator and genetic algorithms. In *Image Analysis and Signal Processing, 2009. IASP 2009. International Conference on*, pages 31–35. IEEE.

Julian, B. R. (1994). Volcanic tremor: nonlinear excitation by fluid flow. *Journal of Geophysical Research: Solid Earth*, 99(B6)(B6):11859–11877.

Julio Miranda, P. and Granados, H. D. (2003). Fast hazard evaluation employing digital photogrammetry: Popocatépetl glaciers, Mexico. *Geofísica Internacional*, 42(2):275–283.

Karlstrom, L., Dufek, J., and Manga, M. (2009). Organization of volcanic plumbing through magmatic lensing by magma chambers and volcanic loads. *Journal of Geophysical Research: Solid Earth*, 114(B10).

Kedar, S., Kanamori, H., and Sturtevant, B. (1998). Bubble collapse as the source of tremor at Old Faithful Geyser. *Journal of Geophysical Research: Solid Earth*, 103(B10)(B10):24283–24299.

Kervyn, M., Ernst, G., van Wyk de Vries, B., Mathieu, L., and Jacobs, P. (2009). Volcano load control on dyke propagation and vent distribution: Insights from analogue modeling. *Journal of Geophysical Research: Solid Earth*, 114(B3)(B3).

Koyanagi, R. Y., Chouet, B., and Aki, K. (1987). Origin of volcanic tremor in Hawai'i: Part I. Data from the Hawaiian Volcano Observatory, 1969–1985. *US Geological Survey Professional Paper*, 2(1350)(1350):pp. 1221–1257.

Krüger, F. and Weber, M. (1992). The effect of low-velocity sediments on the mislocation vectors of the GRF array. *Geophysical journal international*, 108(1)(1):387–393.

La Rocca, M., Galluzzo, D., Malone, S., McCausland, W., Saccorotti, G., and Del Pezzo, E. (2008). Testing small-aperture array analysis on well-located earthquakes, and application to the location of deep tremor. *Bulletin of the Seismological Society of America*, 98(2)(2):620–635.

Langer, H., Falsaperla, S., Messina, A., Spampinato, S., and Behncke, B. (2011). Detecting imminent eruptive activity at Mt Etna, Italy, in 2007–2008 through pattern classification of volcanic tremor data. *Journal of Volcanology and Geothermal Research*, 200(1-2)(1-2):1–17.

Lara, L., Naranjo, J., and Moreno, H. (2004). Rhyodacitic fissure eruption in Southern Andes (Cordón Caulle; 40.5 S) after the 1960 (Mw: 9.5) Chilean earthquake: a structural interpretation. *Journal of Volcanology and Geothermal Research*, 138(1-2)(1-2):127–138.

Leet, R. C. (1988). Saturated and subcooled hydrothermal boiling in groundwater flow channels as a source of harmonic tremor. *Journal of Geophysical Research: Solid Earth*, 93(B5)(B5):4835–4849.

Lipman, P. (1980). Rates of volcanic activity along the southwest rift zone of Mauna Loa volcano, Hawai'i. *Bulletin Volcanologique*, 43(4)(4):703–725.

Lister, J. R. and Kerr, R. C. (1991). Fluid-mechanical models of crack propagation and their application to magma transport in dykes. *Journal of Geophysical Research: Solid Earth*, 96(B6)(B6):10049–10077.

Lockwood, J., Banks, N., English, T., Greenland, P., Jackson, D., Johnson, D., Koyanagi, B., McGee, K., Okamura, A., and Rhodes, M. (1985). The 1984 eruption of Mauna Loa Volcano, Hawai'i. *Eos, Transactions American Geophysical Union*, 66(16):169–171.

Lundgren, P., Kiryukhin, A., Milillo, P., and Samsonov, S. (2015). Dike model for the 2012–2013 Tolbachik eruption constrained by satellite radar interferometry observations. *Journal of Volcanology and Geothermal Research*, 307:79–88.

Lundgren, P., Poland, M., Miklius, A., Orr, T., Yun, S.-H., Fielding, E., Liu, Z., Tanaka, A., Szeliga, W., Hensley, S., et al. (2013). Evolution of dike opening during the March 2011 Kamoamoa fissure eruption, Kīlauea Volcano, Hawai'i. *Journal of Geophysical Research: Solid Earth*, 118(3)(3):897–914.

Maccaferri, F., Bonafede, M., and Rivalta, E. (2011). A quantitative study of the mechanisms governing dike propagation, dike arrest and sill formation. *Journal of Volcanology and Geothermal Research*, 208(1):39–50.

Maccaferri, F., Richter, N., and Walter, T. R. (2017). The effect of giant lateral collapses on magma pathways and the location of volcanism. *Nature Communications*, 8(1)(1):1097.

Major, J., Dzurisin, D., Schilling, S., and Poland, M. P. (2009). Monitoring lava-dome growth during the 2004–2008 Mount St. Helens, Washington, eruption using oblique terrestrial photography. *Earth and Planetary Science Letters*, 286(1-2)(1-2):243–254.

Mancini, F., Dubbini, M., Gattelli, M., Stecchi, F., Fabbri, S., and Gabbianelli, G. (2013). Using unmanned aerial vehicles (UAV) for high-resolution reconstruction of topography: The structure from motion approach on coastal environments. *Remote Sensing*, 5(12)(12):6880–6898.

Manga, M. (1996). Waves of bubbles in basaltic magmas and lavas. *Journal of Geophysical Research: Solid Earth*, 101(B8):17457–17465.

Mangan, M. T., Cashman, K. V., and Newman, S. (1993). Vesiculation of basaltic magma during eruption. *Geology*, 21(2)(2):157–160.

McBirney, A. R. and Murase, T. (1984). Rheological properties of magmas. *Annual Review of Earth and Planetary Sciences*, 12(1):337–357.

McGuire, W. and Pullen, A. (1989). Location and orientation of eruptive fissures and feeder dykes at Mount Etna; influence of gravitational and regional tectonic stress regimes. *Journal of Volcanology and Geothermal Research*, 38(3-4):325–344.

McNutt, S. R. (1987). Volcanic tremor at Pavlof Volcano, Alaska, October 1973–April 1986. *pure and applied geophysics*, 125(6)(6):1051–1077.

McNutt, S. R. (1992). Volcanic tremor. *Encyclopedia of earth system science*, 4:417–425.

McNutt, S. R. (1994). Volcanic Tremor Amplitude Correlated with Eruption Explosivity and its Potential Use in Determining Ash Hazards to Aviation. *US Geological Survey Bulletin*, 2047:377.

McNutt, S. R. (1996). Seismic monitoring and eruption forecasting of volcanoes: a review of the state-of-the-art and case histories. In *Monitoring and mitigation of volcano hazards*, pages 99–146. Springer.

Medynski, S., Pik, R., Burnard, P., Dumont, S., Grandin, R., Williams, A., Blard, P.-H., Schimmelpfennig, I., Vye-Brown, C., France, L., et al. (2016). Magmatic cycles pace tectonic and morphological expression of rifting (Afar depression, Ethiopia). *Earth and Planetary Science Letters*, 446:77–88.

Medynski, S., Pik, R., Burnard, P., Williams, A., Vye-Brown, C., Ferguson, D., Blard, P.-H., France, L., Yirgu, G., Seid, J., et al. (2013). Controls on magmatic cycles and development of rift topography of the Manda Hararo segment (Afar, Ethiopia): insights from cosmogenic 3He investigation of landscape evolution. *Earth and Planetary Science Letters*, 367:133–145.

Megies, T., Beyreuther, M., Barsch, R., Krischer, L., and Wassermann, J. (2011). ObsPy–What can it do for data centers and observatories? *Annals of Geophysics*, 54(1)(1):47–58.

Michon, L., Staudacher, T., Ferrazzini, V., Bachèlery, P., and Marti, J. (2007). April 2007 collapse of Piton de la Fournaise: a new example of caldera formation. *Geophysical Research Letters*, 34(21).

Montagna, C. P. and Gonnermann, H. M. (2013). Magma flow between summit and Pu'u'Ō'ō at Kīlauea Volcano, Hawai'i. *Geochemistry, Geophysics, Geosystems*, 14(7)(7):2232–2246.

Mori, N. and Chang, K.-A. (2003). Introduction to MPIV. *Review of Reviewed Item.*

Müller, D., Walter, T. R., Schöpa, A., Witt, T., Steinke, B., Gudmundsson, M. T., and Dürig, T. (2017). High-Resolution Digital Elevation Modeling from TLS and UAV Campaign Reveals Structural Complexity at the 2014/2015 Holuhraun Eruption Site, Iceland. *Frontiers in Earth Science*, 5:59.

Nadeau, P. A., Palma, J. L., and Waite, G. P. (2011). Linking volcanic tremor, degassing, and eruption dynamics via SO2 imaging. *Geophysical Research Letters*, 38(1)(1).

Nakano, T., Kamiya, I., Tobita, M., Iwahashi, J., and Nakajima, H. (2014). Landform monitoring in active volcano by UAV and SfM-MVS technique. *The International Archives of Photogrammetry, Remote Sensing and Spatial Information Sciences*, 40(8)(8):71.

Németh, K. (2010). Monogenetic volcanic fields: Origin, sedimentary record, and relationship with polygenetic volcanism. In Canon-Tapia, E. and Szakács, A., editors, *What is a Volcano?*, volume 470, chapter 4, pages 43–66. Geological Society of America.

Németh, K., Risso, C., Nullo, F., and Kereszturi, G. (2011). The role of collapsing and cone rafting on eruption style changes and final cone morphology: Los Morados scoria cone, Mendoza, Argentina. *Central European Journal of Geosciences*, 3(2)(2):102–118.

Neuberg, J., Luckett, R., Baptie, B., and Olsen, K. (2000). Models of tremor and low-frequency earthquake swarms on Montserrat. *Journal of Volcanology and Geothermal Research*, 101(1-2)(1-2):83–104.

Opheim, J. A. and Gudmundsson, A. (1989). Formation and geometry of fractures, and related volcanism, of the Krafla fissure swarm, northeast Iceland. *Geological Society of America Bulletin*, 101(12)(12):1608–1622.

Oppenheimer, C., Pyle, D. M., and Barclay, J. (2003). *Volcanic degassing*. Geological Society of London.

Orr, T. R., Heliker, C., and Patrick, M. R. (2013). The ongoing Pu'u'Ō'ō eruption of Kīlauea Volcano, Hawai'i: 30 years of eruptive activity. Technical report, US Geological Survey.

Orr, T. R., Poland, M. P., Patrick, M. R., Thelen, W. A., Sutton, A. J., Elias, T., Thornber, C. R., Parcheta, C., and Wooten, K. M. (2015). Kīlauea's 5–9 March 2011 Kamoamoa fissure eruption and its relation to 30+ years of activity from Pu'u'Ō'ō. *Hawaiian Volcanoes: From Source to Surface*, 208:393.

Palma, J. L., Calder, E. S., Basualto, D., Blake, S., and Rothery, D. A. (2008). Correlations between SO2 flux, seismicity, and outgassing activity at the open vent of Villarrica volcano, Chile. *Journal of Geophysical Research: Solid Earth*, 113(B10)(B10).

Parcheta, C., Fagents, S., Swanson, D. A., Houghton, B. F., and Ericksen, T. (2015). Hawaiian fissure fountains: quantifying vent and shallow conduit geometry, Episode 1 of the 1969–1974 Mauna Ulu eruption. *Hawaiian Volcanoes: From Source to Surface (American Geophysical Union Geophysical Monograph)*, 208:369–391.

Parcheta, C. E., Houghton, B., and Swanson, D. A. (2013). Contrasting patterns of vesiculation in low, intermediate, and high Hawaiian fountains: a case study of the 1969 Mauna Ulu eruption. *Journal of Volcanology and Geothermal Research*, 255:79–89.

Parfitt, E. and Wilson, L. (1995). Explosive volcanic eruptions - IX. The transition between Hawaiian-style lava fountaining and Strombolian explosive activity. *Geophysical Journal International*, 121(1):226–232.

Parfitt, E. A. (2004). A discussion of the mechanisms of explosive basaltic eruptions. *Journal of Volcanology and Geothermal Research*, 134(1-2):77–107.

Parfitt, E. A. and Wilson, L. (1994). The 1983–86 Pu'u'Ō'ō eruption of Kīlauea Volcano, Hawai'i: a study of dike geometry and eruption mechanisms for a long-lived eruption. *Journal of Volcanology and Geothermal Research*, 59(3)(3):179–205.

Parfitt, E. A. and Wilson, L. (1999). A Plinian treatment of fallout from Hawaiian lava fountains. *Journal of Volcanology and Geothermal Research*, 88(1-2):67–75.

Parfitt, E. A., Wilson, L., and Neal, C. A. (1995). Factors influencing the height of Hawaiian lava fountains: implications for the use of fountain height as an indicator of magma gas content. *Bulletin of Volcanology*, 57(6)(6):440–450.

Patrick, M., Wilson, D., Fee, D., Orr, T., and Swanson, D. (2011a). Shallow degassing events as a trigger for very-long-period seismicity at Kīlauea Volcano, Hawai'i. *Bulletin of Volcanology*, 73(9):1179–1186.

Patrick, M. R., Harris, A. J., Ripepe, M., Dehn, J., Rothery, D. A., and Calvari, S. (2007). Strombolian explosive styles and source conditions: insights from thermal (FLIR) video. *Bulletin of volcanology*, 69(7)(7):769–784.

Patrick, M. R., Kauahikaua, J. P., and Antolik, L. (2010). MATLAB tools for improved characterization and quantification of volcanic incandescence in Webcam imagery: Applications at Kīlauea Volcano, Hawai'i. *US Geol. Surv. Tech. Methods*, 13:1–16.

Patrick, M. R., Orr, T., Wilson, D., Dow, D., and Freeman, R. (2011b). Cyclic spattering, seismic tremor, and surface fluctuation within a perched lava channel, Kīlauea Volcano. *Bulletin of volcanology*, 73(6)(6):639–653.

Peacock, D. and Parfitt, E. (2002). Active relay ramps and normal fault propagation on Kīlauea Volcano, Hawai'i. *Journal of structural geology*, 24(4)(4):729–742.

Pedersen, G., Höskuldsson, A., Dürig, T., Thordarson, T., Jonsdottir, I., Riishuus, M. S., Óskarsson, B., Dumont, S., Magnússon, E., Gudmundsson, M. T., et al. (2017). Lava field evolution and emplacement dynamics of the 2014–2015 basaltic fissure eruption at Holuhraun, Iceland. *Journal of Volcanology and Geothermal Research*, 340:155–169.

Pieri, D. C. and Baloga, S. M. (1986). Eruption rate, area, and length relationships for some Hawaiian lava flows. *Journal of Volcanology and Geothermal Research*, 30(1-2)(1-2):29–45.

Pioli, L., Bonadonna, C., Azzopardi, B., Phillips, J., and Ripepe, M. (2012). Experimental constraints on the outgassing dynamics of basaltic magmas. *Journal of Geophysical Research: Solid Earth*, 117(B3).

Polacci, M., Corsaro, R. A., and Andronico, D. (2006). Coupled textural and compositional characterization of basaltic scoria: Insights into the transition from Strombolian to fire fountain activity at Mount Etna, Italy. *Geology*, 34(3):201–204.

Poland, M., Miklius, A., Orr, T., Sutton, J., Thornber, C., and Wilson, D. (2008). New episodes of volcanism at Kīlauea Volcano, Hawai'i. *Eos, Transactions American Geophysical Union*, 89(5):37–38.

Poland, M. P. (2014). Time-averaged discharge rate of subaerial lava at Kīlauea Volcano, Hawai'i, measured from TanDEM-X interferometry: Implications for magma supply and storage during 2011–2013. *Journal of Geophysical Research: Solid Earth*, 119(7):5464–5481.

Porter, S. C. (1972). Distribution, morphology, and size frequency of cinder cones on Mauna Kea volcano, Hawai'i. *Geological Society of America Bulletin*, 83(12)(12):3607–3612.

Project, G. V. (2016. (updated: 27.9.2016)). http://volcano.si.edu/. Technical report, Smithsonian Institute.

Raffel, M., Willert, C. E., Kompenhans, J., et al. (2007). *Particle image velocimetry: a practical guide*. Springer Science & Business Media.

Reynolds, P., Brown, R., Thordarson, T., and Llewellin, E. (2016). The architecture and shallow conduits of Laki-type pyroclastic cones: Insights into a basaltic fissure eruption. *Bulletin of Volcanology*, 78(5):36.

Richter, D. H., Eaton, J., Murata, K., Ault, W., and Krivoy, H. (1970). Chronological narrative of the 1959-60 eruption of Kīlauea volcano, Hawai'i. Technical report.

Richter, N., Favalli, M. E., de Zeeuw-van Dalfsen, E., Fornaciai, A., da Silva Fernandes, R. M., Pérez, N. M., and Walter, T. R. (2016). Lava flow hazard at Fogo Volcano, Cabo Verde, before and after the 2014-2015 eruption. *Natural Hazards and Earth System Sciences*, 16(8)(8):1925.

Richter, N., Poland, M. P., and Lundgren, P. R. (2013). TerraSAR-X interferometry reveals small-scale deformation associated with the summit eruption of Kīlauea Volcano, Hawai'i. *Geophysical Research Letters*, 40(7)(7):1279–1283.

Riggs, N. and Duffield, W. (2008). Record of complex scoria cone eruptive activity at Red Mountain, Arizona, USA, and implications for monogenetic mafic volcanoes. *Journal of Volcanology and Geothermal Research*, 178(4)(4):763–776.

Ripepe, M., Delle Donne, D., Lacanna, G., Marchetti, E., and Ulivieri, G. (2009). The onset of the 2007 Stromboli effusive eruption recorded by an integrated geophysical network. *Journal of Volcanology and Geothermal Research*, 182(3-4)(3-4):131–136.

Ripepe, M. and Gordeev, E. (1999). Gas bubble dynamics model for shallow volcanic tremor at Stromboli. *Journal of Geophysical Research: Solid Earth*, 104(B5)(B5):10639–10654.

Rossi, C., Minet, C., Fritz, T., Eineder, M., and Bamler, R. (2016). Temporal monitoring of subglacial volcanoes with TanDEM-X - Application to the 2014–2015 eruption within the Bárðarbunga volcanic system, Iceland. *Remote Sensing of Environment*, 181:186–197.

Rowland, S. K. and Walker, G. P. (1990). Pahoehoe and aa in Hawaii: volumetric flow rate controls the lava structure. *Bulletin of Volcanology*, 52(8)(8):615–628.

Rubin, A. M. (1990). A comparison of rift-zone tectonics in Iceland and Hawai'i. *Bulletin of Volcanology*, 52(4)(4):302–319.

Rubin, A. M. (1995). Propagation of magma-filled cracks. *Annual Review of Earth and Planetary Sciences*, 23(1):287–336.

Rubin, A. M. and Pollard, D. D. (1988). Dike-induced faulting in rift zones of Iceland and Afar. *Geology*, 16(5)(5):413–417.

Ruch, J., Wang, T., Xu, W., Hensch, M., and Jónsson, S. (2016). Oblique rift opening revealed by reoccurring magma injection in central Iceland. *Nature communications*, 7:12352.

Rymer, H. (1996). Microgravity monitoring. In *Monitoring and mitigation of volcano hazards*, pages 169–197. Springer.

Salzer, J. T., Thelen, W. A., James, M. R., Walter, T. R., Moran, S., and Denlinger, R. (2016). Volcano dome dynamics at Mount St. Helens: Deformation and intermittent subsidence monitored by seismicity and camera imagery pixel offsets. *Journal of Geophysical Research: Solid Earth*, 121(11)(11):7882–7902.

Scarpa, R. and Gasparini, P. (1996). A review of volcano geophysics and volcano-monitoring methods. In *Monitoring and mitigation of volcano hazards*, pages 3–22. Springer.

Schneider, D. J., Vallance, J. W., Wessels, R. L., Logan, M., Ramsey, M. S., Sherrod, D., Scott, W., and Stauffer, P. (2008). Use of thermal infrared imaging for monitoring renewed dome growth at Mount St. Helens, 2004. *A volcano rekindled*, pages 2004–2006.

Schweitzer, J. (2001). Slowness corrections - One way to improve IDC products. *pure and applied geophysics*, 158(1-2)(1-2):375–396.

Scollo, S., Prestifilippo, M., Pecora, E., Corradini, S., Merucci, L., Spata, G., and Coltelli, M. (2014). Eruption column height estimation of the 2011-2013 etna lava fountains. *Annals of Geophysics*, 57(2):0214.

Segall, P., Cervelli, P., Owen, S., Lisowski, M., and Miklius, A. (2001). Constraints on dike propagation from continuous GPS measurements. *Journal of Geophysical Research: Solid Earth*, 106(B9):19301–19317.

Senyukov, S., Nuzhdina, I., Droznina, S. Y., Garbuzova, V., Kozhevnikova, T. Y., Sobolevskaya, O., Nazarova, Z., and Bliznetsov, V. (2015). Reprint of" Seismic monitoring of the Plosky Tolbachik eruption in 2012–2013 (Kamchatka Peninsula Russia)". *Journal of Volcanology and Geothermal Research*, 307:47–59.

Siebert, L., Simkin, T., and Kimberly, P. (2011). *Volcanoes of the World*. Univ of California Press.

Sigmundsson, F. (2006). *Iceland geodynamics: crustal deformation and divergent plate tectonics*. Springer Science & Business Media.

Sigmundsson, F., Hooper, A., Hreinsdóttir, S., Vogfjörd, K. S., Ófeigsson, B. G., Heimisson, E. R., Dumont, S., Parks, M., Spaans, K., Gudmundsson, G. B., et al. (2015). Segmented lateral dyke growth in a rifting event at Bárðarbunga volcanic system, Iceland. *Nature*, 517(7533)(7533):191.

Sigurdsson, H. and Sparks, R. (1978). Rifting episode in north Iceland in 1874–1875 and the eruptions of Askja and Sveinagja. *Bulletin Volcanologique*, 41(3):149–167.

Sinton, J. M. and Detrick, R. S. (1992). Mid-ocean ridge magma chambers. *Journal of Geophysical Research: Solid Earth*, 97(B1):197–216.

Slezin, Y. B. (2003). The mechanism of volcanic eruptions (a steady state approach). *Journal of Volcanology and Geothermal Research*, 122(1-2):7–50.

Smith, D. K. and Cann, J. R. (1992). The role of seamount volcanism in crustal construction at the Mid-Atlantic Ridge (24–30 N). *Journal of Geophysical Research: Solid Earth*, 97(B2)(B2):1645–1658.

Soosalu, H., Einarsson, P., and Þorbjarnardóttir, B. S. (2005). Seismic activity related to the 2000 eruption of the Hekla volcano, Iceland. *Bulletin of volcanology*, 68(1)(1):21–36.

Spampinato, L., Calvari, S., Oppenheimer, C., and Boschi, E. (2011). Volcano surveillance using infrared cameras. *Earth-Science Reviews*, 106(1-2)(1-2):63–91.

Spampinato, L., Calvari, S., Oppenheimer, C., and Lodato, L. (2008). Shallow magma transport for the 2002–3 Mt. Etna eruption inferred from thermal infrared surveys. *Journal of Volcanology and Geothermal Research*, 177(2)(2):301–312.

Sparks, R. (2003). Forecasting volcanic eruptions. *Earth and Planetary Science Letters*, 210(1-2):1–15.

Spence, D. and Turcotte, D. (1985). Magma-driven propagation of cracks. *Journal of Geophysical Research: Solid Earth*, 90(B1):575–580.

Stevenson, J. A. and Varley, N. (2008). Fumarole monitoring with a handheld infrared camera: Volcán de Colima, Mexico, 2006–2007. *Journal of Volcanology and Geothermal Research*, 177(4)(4):911–924.

Sumner, J. M. (1998). Formation of clastogenic lava flows during fissure eruption and scoria cone collapse: the 1986 eruption of Izu-Oshima Volcano, eastern Japan. *Bulletin of Volcanology*, 60(3)(3):195–212.

Swanson, D. A., Duffield, W. A., and Fiske, R. S. (1976). Displacement of the south flank of Kīlauea Volcano; the result of forceful intrusion of magma into the rift zones. Technical report, US Govt. Print. Off.,.

Taddeucci, J., Alatorre-Ibargüengoitia, M., Moroni, M., Tornetta, L., Capponi, A., Scarlato, P., Dingwell, D., and De Rita, D. (2012a). Physical parameterization of Strombolian eruptions via experimentally-validated modeling of high-speed observations. *Geophysical Research Letters*, 39(16):L16306.

Taddeucci, J., Scarlato, P., Capponi, A., Del Bello, E., Cimarelli, C., Palladino, D., and Kueppers, U. (2012b). High-speed imaging of strombolian explosions: The ejection velocity of pyroclasts. *Geophysical Research Letters*, 39(2):L02301.

Tárraga, M., Martí, J., Abella, R., Carniel, R., and López, C. (2014). Volcanic tremors: Good indicators of change in plumbing systems during volcanic eruptions. *Journal of Volcanology and Geothermal Research*, 273:33–40.

Thordarson, T., Hoskuldsson, A., Jónsdottir, I., Pedersen, G., Gudmundsson, M., Dürig, T., Riishuus, M., Moreland, W., Gudnason, J., Gallagher, C., et al. (2015). Emplacement and growth of the August 2014 to February 2015 Nornahraun Lava flow field North Iceland. In *AGU Fall Meeting Abstracts*, pages abs–id V13D–01.

Thordarson, T. and Larsen, G. (2007). Volcanism in Iceland in historical time: Volcano types, eruption styles and eruptive history. *Journal of Geodynamics*, 43(1)(1):118–152.

Thordarson, T. and Self, S. (1993). The Laki (Skaftár Fires) and Grímsvötn eruptions in 1783–1785. *Bulletin of Volcanology*, 55(4):233–263.

Thordarson, T. and Self, S. (1998). The Roza Member, Columbia River Basalt Group: A gigantic pāhoehoe lava flow field formed by endogenous processes? *Journal of Geophysical Research: Solid Earth*, 103(B11)(B11):27411–27445.

Tiede, C., Camacho, A., Gerstenecker, C., Fernández, J., and Suyanto, I. (2005). Modeling the density at Merapi volcano area, Indonesia, via the inverse gravimetric problem. *Geochemistry, Geophysics, Geosystems*, 6(9)(9).

Trippanera, D., Acocella, V., Ruch, J., and Abebe, B. (2015a). Fault and graben growth along active magmatic divergent plate boundaries in Iceland and Ethiopia. *Tectonics*, 34(11)(11):2318–2348.

Trippanera, D., Ruch, J., Acocella, V., and Rivalta, E. (2015b). Experiments of dike-induced deformation: insights on the long-term evolution of divergent plate boundaries. *Journal of Geophysical Research: Solid Earth*, 120(10)(10):6913–6942.

Tron, V. and Brun, J.-P. (1991). Experiments on oblique rifting in brittle-ductile systems. *Tectonophysics*, 188(1-2)(1-2):71–84.

Tu, R., Wang, R., Ge, M., Walter, T., Ramatschi, M., Milkereit, C., Bindi, D., and Dahm, T. (2013). Cost-effective monitoring of ground motion related to earthquakes, landslides, or volcanic activity by joint use of a single-frequency GPS and a MEMS accelerometer. *Geophysical Research Letters*, 40(15):3825–3829.

USGS (2018). Kīlauea's lower East Rift Zone lava flows and fissures (between June and August 2018), URL *https://volcanoes.usgs.gov/volcanoes/kilauea/multimedia_maps.html* (2018-10-12).

Valentine, G. and Gregg, T. (2008). Continental basaltic volcanoes-processes and problems. *Journal of Volcanology and Geothermal Research*, 177(4)(4):857–873.

Vergniolle, S. and Jaupart, C. (1986). Separated two-phase flow and basaltic eruptions. *Journal of Geophysical Research: Solid Earth*, 91(B12):12842–12860.

Vergniolle, S. and Jaupart, C. (1990). Dynamics of degassing at Kīlauea volcano, Hawai'i. *Journal of Geophysical Research: Solid Earth*, 95(B3):2793–2809.

Vergniolle, S. and Mangan, M. (2000). Hawaiian and Strombolian eruptions. *Encyclopedia of volcanoes*, pages 447–461.

Vergniolle, S. and Ripepe, M. (2008). From Strombolian explosions to fire fountains at Etna Volcano (Italy): what do we learn from acoustic measurements? *Geological Society, London, Special Publications*, 307(1)(1):103–124.

Vincent, O. R. and Folorunso, O. (2009). A descriptive algorithm for sobel image edge detection. In *Proceedings of Informing Science & IT Education Conference (InSITE)*, volume 40, pages 97–107. Informing Science Institute California.

Voight, B., Janda, R., Glicken, H., Douglass, P., et al. (1983). Nature and mechanics of the Mount St. Helens rockslide-avalanche of 18 May 1980. *Geotechnique*, 33(3):243–273.

Walker, G. P. (1993). Basaltic-volcano systems. *Geological Society, London, Special Publications*, 76(1):3–38.

Walker, G. P. and Sigurdsson, H. (2000). Basaltic volcanoes and volcanic systems. In Sigurdsson, H., Houghton, B. F., McNutt, S., Rymer, H., and Stix, J., editors, *Encyclopedia of volcanoes*, pages 283–289. Academic Press San Diego.

Walter, T. R. (2011). Low cost volcano deformation monitoring: optical strain measurement and application to Mount St. Helens data. *Geophysical Journal International*, 186(2)(2):699–705.

Walter, T. R. and Amelung, F. (2006). Volcano-earthquake interaction at Mauna Loa volcano, Hawai'i. *Journal of Geophysical Research: Solid Earth*, 111(B5)(B5).

Walter, T. R., Jousset, P., Allahbakhshi, M., Witt, T., Gudmundsson, M. T., and Hersir, G. P. (2018). Underwater and drone based photogrammetry reveals structural control at Geysir geothermal field in Iceland. *Journal of Volcanology and Geothermal Research*.

Walter, T. R., Legrand, D., Granados, H. D., Reyes, G., and Arambula, R. (2013a). Volcanic eruption monitoring by thermal image correlation: Pixel offsets show episodic dome growth of the Colima volcano. *Journal of Geophysical Research: Solid Earth*, 118(4)(4):1408–1419.

Walter, T. R., Ratdomopurbo, A., Aisyah, N., Brotopuspito, K. S., Salzer, J., Lühr, B., et al. (2013b). Dome growth and coulée spreading controlled by surface morphology, as determined by pixel offsets in photographs of the 2006 Merapi eruption. *Journal of Volcanology and Geothermal Research*, 261:121–129.

Weertman, J. (1970). The creep strength of the Earth's mantle. *Reviews of Geophysics*, 8(1):145–168.

Westerweel, J. (1997). Fundamentals of digital particle image velocimetry. *Measurement science and technology*, 8(12):1379.

Westoby, M., Brasington, J., Glasser, N., Hambrey, M., and Reynolds, J. (2012). “Structure-from-Motion” photogrammetry: A low-cost, effective tool for geoscience applications. *Geomorphology*, 179:300–314.

Wilson, Lionel; Parfit, E. A. (1993). The formation of perched lava ponds on basaltic volcanoes: the influence of flow geometry on cooling-limited lava flow lengths. *Journal of Volcanology and Geothermal Research*, 56:113–123.

Wilson, L., Parfitt, E. A., and Head III, J. (1995). Explosive volcanic eruptions - VIII. The role of magma recycling in controlling the behaviour of Hawaiian-style lava fountains. *Geophysical Journal International*, 121(1)(1):226–232.

Wilson, L., Sparks, R. S. J., and Walker, G. P. (1980). Explosive volcanic eruptions - IV. The control of magma properties and conduit geometry on eruption column behaviour. *Geophysical Journal International*, 63(1)(1):117–148.

Witt, T. and Walter, T. R. (2017). Video monitoring reveals pulsating vents and propagation path of fissure eruption during the March 2011 Pu’u’Ō’ō eruption, Kīlauea volcano. *Journal of Volcanology and Geothermal Research*, 330:43–55.

Wolfe, E. W., Garcia, M. O., Jackson, D. B., Koyanagi, R. Y., and Neal, C. A. (1987). Volcanism in Hawai’i. *US Geol. Surv. Prof. Pap*, 1350:471–508.

Woods, A. (2013). Sustained explosive activity: volcanic eruption columns and Hawaiian fountains. *Modeling Volcanic Processes: The Physics and Mathematics of Volcanism*, 153–172.

Wright, R., Blake, S., Harris, A. J., and Rothery, D. A. (2001). A simple explanation for the space-based calculation of lava eruption rates. *Earth and Planetary Science Letters*, 192(2)(2):223–233.

Wright, T. J., Ebinger, C., Biggs, J., Ayele, A., Yirgu, G., Keir, D., and Stork, A. (2006). Magma-maintained rift segmentation at continental rupture in the 2005 Afar dyking episode. *Nature*, 442(7100)(7100):291–294.

Wylie, J. J., Helfrich, K. R., Dade, B., Lister, J. R., and Salzig, J. F. (1999a). Flow localization in fissure eruptions. *Bulletin of Volcanology*, 60(6)(6):432–440.

Wylie, J. J., Voight, B., and Whitehead, J. (1999b). Instability of magma flow from volatile-dependent viscosity. *Science*, 285(5435)(5435):1883–1885.